

DISS. ETH No. 21494

THE FIRST SEMICONDUCTOR-BASED  
CAMERA FOR IMAGING ATMOSPHERIC  
CHERENKOV TELESCOPES

Dissertation submitted to  
ETH Zurich

for the degree of  
Doctor of Sciences

Thomas Krähenbühl  
Dipl. Phys. ETH Zürich  
born February 25, 1984  
from Zäziwil, BE

Accepted on the recommendation of  
Prof. Dr. Felicitas Pauss, examiner  
Prof. Dr. Rainer Wallny, co-examiner  
Prof. Dr. Adrian Biland, co-examiner  
2013



Eidgenössische Technische Hochschule Zürich  
Swiss Federal Institute of Technology Zurich



# Abstract

The systematic exploration of our environment and its underlying principles is a fundamental human characteristic to satisfy our curiosity. Precise observations and their thorough analysis depend in general on technological aids, either initiating their specific development or pushing technologies to their limits and enhancing their application. The tight coupling of scientific progress to technological advancements requires the regular review of the currently used techniques and the evaluation of new developments from industry and other fields of research for new applications.

The begin of the industrial production of Geiger-mode Avalanche Photodiodes (G-APD) for the measurement of light on the single photon level a few years ago implied the need for an evaluation of the currently used Photomultiplier Tubes (PMT) for the detection of weak Cherenkov light flashes initiated by high-energetic particles from galactic and extra-galactic sources. The field of Very High Energy (VHE) astrophysics measures and analyses gamma rays with energies above 30 GeV, which are emitted by cosmic objects such as supernova remnants, pulsars or Active Galactic Nuclei (AGN). When these gamma rays arrive at the earth's atmosphere, they initiate a shower of secondary particles, which in turn emit Cherenkov light. The measurement of this light using Imaging Atmospheric Cherenkov Telescopes (IACT) requires cameras with fast and single-photon sensitive photosensors. All major experiments in this field currently use PMTs for this task. The availability of semiconductor photosensors in the form of G-APDs with the potential of a facilitated implementation and improved performance with the drawbacks of a strong temperature and voltage dependence, slower signals and a completely different noise characteristic, raised the question of their applicability in IACT cameras. The First G-APD Cherenkov Telescope (FACT) collaboration designed and built the first camera based on this novel technology, which is operational since autumn 2011 and shows excellent performance characteristics.

At the start of this PhD thesis in 2008, many questions concerning the characteristics and correct usage of G-APDs were not yet answered, and it was my task in the collaboration to find and evaluate potential problems. Through laboratory measurements, computer simulations and analytic calculations I characterized the behavior of G-APDs under the viewpoint of their application in an IACT camera. The voltage dependencies of gain, crosstalk probability and photon detection efficiency were measured and combined with a mathematical model of the sensor response. The various components influencing the precision of measured signals were identified and characterized, allowing to compare their relevance quantitatively. Based on these investigations, the optimal G-APD type for the FACT camera was identified.

In summer 2009, the construction of a prototype camera was finished and successfully used for the first measurement of Cherenkov air showers in a self-triggering mode using G-APDs. A full camera with 1440 pixels and in-camera digitization electronics for the operation in a refurbished telescope mount of the pioneering HEGRA Cherenkov telescope array was subsequently constructed. Besides tests and characterization measurements of camera electronics I participated in the development of optical light guides

(“light-collecting cones”) and established measurements for the quality assurance in their production. The optical light guides were glued onto the photosensors, which required the evaluation of cleaning and gluing procedures. I participated in the development of these procedures and ensured the gluing quality and correct administration of the photosensors and pixels during the assembly of the sensor compartment.

After extensive laboratory tests, the final camera was installed in the telescope on the Roque de los Muchachos on La Palma, Spain, and switched on in the evening of October 11, 2011. The camera was instantly operational and shows excellent performance parameters. Using laboratory and telescope measurements I characterized the homogeneity of the photon detection efficiency and the gain of the camera, which have an RMS of  $<7\%$  and  $<5\%$  without fine-tuning, respectively. For the analysis software, I contributed algorithms for the calibration step, in particular an algorithm which allows the in-situ calibration of observation data without additional information. This allowed to evaluate the stability of the FACT camera under various observation conditions, where it proved to be exceptionally stable using a real-time bias voltage regulation system. The regular remote observations since summer 2012 and the planned robotic observations are only possible due to the high reliability of the camera. The advantages of the photosensors could be fully exploited while keeping the drawbacks well under control.

The successful observation of three sources (Crab, Markarian 421, Markarian 501) with FACT was communicated to the astrophysics community half a year after recording the first air showers. Regular updates on the experience with the new camera established G-APDs as an excellent alternative to PMTs and FACT as an excellent monitoring instrument for variable galactic and extra-galactic sources.



# Zusammenfassung

Die systematische Erforschung unserer Umgebung und der ihr zugrunde liegenden Prinzipien ist eine grundlegende menschliche Eigenart zur Befriedigung unserer Neugierde. Präzise Beobachtungen und ihre sorgfältige Analyse benötigen im Allgemeinen technologische Hilfsmittel, welche entweder spezifisch entwickelt werden oder die auf vorhandenen Technologien basieren und diese an ihre Grenzen bringen und ihre Anwendung weiterentwickeln. Die enge Kopplung von wissenschaftlichem Fortschritt und technologischen Verbesserungen bedingt die regelmässige Überprüfung der gegenwärtig verwendeten Verfahren sowie die Evaluierung neuer Entwicklungen aus Industrie und anderen Forschungszweigen auf neue Anwendungen.

Der Beginn der industriellen Produktion von Geiger-mode Avalanche Photodiodes (G-APD) zur Lichtdetektion auf Einzelphotonenlevel vor einigen Jahren machte die Evaluation der gegenwärtig verwendeten Photomultiplier Tubes (PMT) zur Detektion von schwachen Lichtblitzen nötig, welche durch hochenergetische Teilchen von galaktischen und extra-galaktischen Quellen ausgelöst werden. Das Forschungsgebiet der Very High Energy (VHE) Astrophysik misst und analysiert Gammateilchen mit einer Energie über 30 GeV, welche von kosmischen Quellen wie Supernova-Überresten, Pulsaren oder Aktiven Galaxienkernen ausgestossen werden. Wenn diese Gammastrahlen auf die Erdatmosphäre treffen, initiieren sie einen Schauer von Sekundärteilchen, welche wiederum Cherenkovlicht aussenden. Dieses Licht wird von Imaging Atmospheric Cherenkov Telescopes (IACT) aufgefangen und detektiert, was Kameras mit schnellen und sehr sensitiven Lichtsensoren benötigt. Sämtliche grossen Experimente in diesem Feld benutzen dazu PMTs. Die Verfügbarkeit von Halbleiter-Lichtsensoren in der Form von G-APDs mit dem Potential einer vereinfachten Anwendung und verbesserter Leistung mit den Nachteilen einer starken Temperatur- und Spannungsabhängigkeit, langsameren Signalen und komplett andersartiger Rauschcharakteristik warf die Frage auf, ob sie in IACTs anwendbar seien. Die "First G-APD Cherenkov Telescope" (FACT) Kollaboration plante und baute die erste Kamera basierend auf dieser neuartigen Technologie, welche seit Herbst 2011 in Betrieb ist und exzellente Leistungsmerkmale aufweist.

Beim Beginn dieser Doktorarbeit in 2008 waren noch viele Fragen bezüglich der Eigenschaften und korrekten Verwendung von G-APDs offen, und es war meine Aufgabe innerhalb der Kollaboration, potentielle Probleme zu finden und zu evaluieren. Durch Labormessungen, Computersimulationen und analytische Berechnungen charakterisierte ich das Verhalten von G-APDs unter dem Gesichtspunkt ihrer Anwendung in einer IACT-Kamera. Die Spannungsabhängigkeit ihrer Lawinenverstärkung, Übersprech-Rauschwahrscheinlichkeit sowie Lichtdetektionseffizienz wurde gemessen und in ein mathematisches Modell der Sensorsignale eingebaut. Die verschiedenen Komponenten welche die Präzision der gemessenen Signale beeinflussen wurden gemessen und charakterisiert, was den Vergleich ihrer quantitativen Relevanz ermöglicht. Basierend auf diesen Untersuchungen wurde die optimale G-APD für die FACT-Kamera ausgewählt.

Im Sommer 2009 wurde die Konstruktion einer Prototypenkamera abgeschlossen und erfolgreich für die erste Messung von Cherenkov-Luftschauern mit G-APDs in einem un-

abhängig ausgelösten Messmodus verwendet. Daraufhin wurde eine komplette Kamera mit 1440 Pixeln und integrierter Digitalisierung der Sensorsignale konstruiert, welche zur Verwendung in einem instandgesetzten Teleskop des HEGRA-Experiments vorgesehen war. Nebst Tests und Messungen an der Kameraelektronik war ich an der Entwicklung der optischen Lichtleiter beteiligt und entwickelte Messmethoden zur Qualitätssicherung in deren Produktion. Die optischen Lichtleiter wurden auf die Lichtsensoren aufgeklebt, was die Evaluation von Reinigungs- und Klebprozeduren benötigte. Ich entwickelte diese Methoden mit und war für die Qualität der Klebungen sowie die korrekte Administration der Lichtsensoren und Pixel während der Konstruktion des Sensorabteils verantwortlich.

Nach ausführlichen Labortests wurde die Kamera im Teleskop auf dem Roque de los Muchachos auf La Palma (Spanien) installiert, und am Abend des 11. Oktobers 2011 eingeschaltet. Die Kamera war sofort betriebsbereit und weist exzellente Leistungswerte auf. Mit Hilfe von Labor- und Teleskop-Messungen charakterisierte ich die Homogenität der Detektionseffizienz und Signalgrösse der Kamera, welche ohne Feintuning direkt nach Inbetriebnahme ein RMS von  $<7\%$  respektive  $<5\%$  aufwiesen. Für die Analyse-Software entwickelte ich Algorithmen zur Datenkalibration, welche insbesondere die Kalibration aus den Daten selbst ohne weitere Hilfsmittel ermöglicht. Dies erlaubte die Untersuchung der Stabilität der FACT-Kamera unter verschiedensten Beobachtungsbedingungen, wobei sie sich unter Verwendung einer Echtzeit-Spannungsregulierung als ausserordentlich stabil erwies. Der regelmässige ferngesteuerte Betrieb seit Sommer 2012 und die geplante robotische Teleskop-Steuerung sind nur möglich dank der hohen Zuverlässigkeit der Kamera. Die Vorteile der Lichtsensoren konnten voll ausgenutzt werden, während ihre Nachteile gut unter Kontrolle gehalten werden konnten.

Die erfolgreiche Beobachtung dreier Quellen (Krebs-Nebel, Markarian 421, Markarian 501) durch FACT wurde der Astrophysik-Gemeinschaft ein halbes Jahr nach der Beobachtung der ersten Luftschauern mitgeteilt. Regelmässige Aktualisierungen über die Erfahrungen mit der neuen Kamera etablierten G-APDs als hervorragende Alternative zu PMTs, und FACT als exzellentes Beobachtungsinstrument für variable galaktische und extragalaktische Quellen.

# Contents

<b>1. Why build a new camera type?</b>	<b>1</b>
1.1. A bit of history . . . . .	1
1.2. The technology of Imaging Atmospheric Cherenkov Telescopes . . . . .	2
1.2.1. Interaction of high energy photons with the atmosphere . . . . .	2
1.2.2. Background signals: hadronic showers . . . . .	2
1.2.3. Cherenkov radiation . . . . .	3
1.2.4. Cherenkov radiation: formulas . . . . .	5
1.2.5. Background light . . . . .	5
1.2.6. Mirror design . . . . .	6
1.2.7. Camera requirements . . . . .	7
1.2.8. Data analysis principle . . . . .	8
1.3. Observation of variable sources . . . . .	9
1.4. The current status of the field . . . . .	10
1.5. A short introduction to the FACT project . . . . .	12
1.6. Thesis outline . . . . .	15
<b>2. Geiger-mode Avalanche Photodiodes</b>	<b>17</b>
2.1. Properties of photosensors . . . . .	17
2.1.1. Principle of photomultiplier tubes . . . . .	18
2.1.2. History of semiconductor photosensors . . . . .	18
2.1.3. Naming . . . . .	20
2.2. Working principle of G-APDs . . . . .	21
2.2.1. Voltage definitions . . . . .	21
2.2.2. Photon detection efficiency . . . . .	22
2.2.3. Saturation . . . . .	24
2.2.4. Gain . . . . .	24
2.2.5. Equivalent circuit and pulse form . . . . .	24
2.2.6. Dead time and cell recovery . . . . .	24
2.2.7. Crosstalk . . . . .	26
2.2.8. Dark counts . . . . .	26
2.2.9. Afterpulses . . . . .	26
2.3. Measurements of G-APD properties . . . . .	27
2.3.1. Geometrical properties . . . . .	27
Package size . . . . .	28
Chip position . . . . .	28
Surface profile . . . . .	28
2.3.2. Voltage dependence of gain and crosstalk probability . . . . .	29
2.3.3. Measurement of the average number of cells triggered by crosstalk . . . . .	30
2.3.4. Avalanche fluctuations (peak widths) . . . . .	32
Expectation . . . . .	32

Measurement . . . . .	32
2.3.5. Dependence of avalanche fluctuations on the over-voltage . . . . .	33
2.3.6. Angle dependence of the PDE . . . . .	33
Expectation . . . . .	34
Setup . . . . .	34
Analysis method . . . . .	35
Method . . . . .	37
Results / discussion . . . . .	37
2.4. Mathematical modeling of the response . . . . .	39
Calculation requirements . . . . .	41
2.4.1. Dependence of the Geiger-mode Avalanche Photodiode (G-APD) response on the over-voltage . . . . .	41
2.4.2. Calculation of $N_{pe}$ from a number of triggered cells $\tilde{N}$ . . . . .	43
2.4.3. Variations in the saturation process . . . . .	43
2.4.4. Excess Noise Factor . . . . .	44
2.4.5. Relative ENF for different PDE . . . . .	47
2.5. Statistical simulation of G-APDs . . . . .	48
2.5.1. Relation of $\mu_{ct}$ and $p_{ct}$ in the simulation . . . . .	48
2.5.2. Variations in the saturation process . . . . .	49
2.5.3. Combination of processes . . . . .	49
2.5.4. Summary of the statistical properties . . . . .	50
2.5.5. ENF dependency on the over-voltage . . . . .	52
2.6. Choosing the right G-APD type for the camera . . . . .	53
<b>3. Construction of the FACT camera</b>	<b>55</b>
3.1. The prototype module M0 . . . . .	55
3.1.1. Hollow light guides . . . . .	56
3.1.2. Sensor unit mechanics . . . . .	58
3.1.3. Electronics . . . . .	59
Data acquisition . . . . .	59
3.1.4. Front window and internal LED pulser . . . . .	60
3.1.5. First air shower measurements . . . . .	60
3.1.6. Rate scans . . . . .	61
3.1.7. Temperature stabilization . . . . .	63
3.2. The FACT camera: overview . . . . .	64
Integrated digitization . . . . .	65
Mechanics . . . . .	65
3.2.1. Photon rate estimates . . . . .	67
Rate estimate using a hand-held light meter and a literature reference	67
Current prediction . . . . .	68
Comparison PMT-G-APD . . . . .	68
3.3. Solid light-collecting cones . . . . .	71
3.3.1. Concept . . . . .	71
3.3.2. Simulation: basic designs . . . . .	71
3.3.3. Simulation: setup . . . . .	73
3.3.4. Simulation: final cone geometry . . . . .	75
3.3.5. Light-absorbing grid . . . . .	76
3.3.6. Cone prototypes . . . . .	76
Cone prototypes: ripples and bulge . . . . .	76

Cone prototypes: rim . . . . .	78
Cone prototypes: surface contaminations . . . . .	78
3.3.7. Transmission measurements . . . . .	79
Measurement at 380 nm with a pulsed LED . . . . .	79
Spectrometer measurements . . . . .	79
3.3.8. Cone prototype evaluation: laser measurements . . . . .	80
Cone alignment . . . . .	80
Transmission measurement: method . . . . .	82
Transmission results . . . . .	82
Reflection measurements . . . . .	84
Reflection measurement results . . . . .	85
3.3.9. Cone batch tests . . . . .	85
Simple transmission test . . . . .	85
Batch spectrometer measurements . . . . .	87
3.3.10. Laser transmission: bubbles . . . . .	88
3.4. The sensor compartment . . . . .	89
3.4.1. Gluing of G-APDs to cones . . . . .	90
Tools and methods . . . . .	91
Amount of glue . . . . .	93
Gluing tests and bubble reduction . . . . .	93
Glue preparation . . . . .	94
Cone and G-APD cleaning . . . . .	94
Stability test of the gluing . . . . .	96
Gluing batch tests . . . . .	98
Test patches . . . . .	98
3.4.2. Focal plane layout and pixel ordering . . . . .	98
Bubble types . . . . .	100
G-APD operation voltage distribution . . . . .	100
3.4.3. Gluing of the pixels to the front window . . . . .	102
Glue optimization . . . . .	104
Cleaning tests . . . . .	105
Load tests . . . . .	105
Capillary effect between the cones . . . . .	106
Gluing administration . . . . .	106
3.4.4. Cable soldering and baffle plate installation . . . . .	108
3.4.5. Pixel repairs . . . . .	108
3.4.6. Final front window . . . . .	111
3.5. Electronics . . . . .	114
3.5.1. Pixel organization . . . . .	114
3.5.2. Electronics: front-end layout . . . . .	117
3.5.3. Pre-amplifier and trigger system . . . . .	117
3.5.4. Digitization . . . . .	120
3.5.5. Bias voltage supply . . . . .	120
3.5.6. Light pulser . . . . .	121
3.6. Calibration . . . . .	121
3.6.1. The case with Photomultiplier Tubes (PMTs) . . . . .	122
3.6.2. Advantages and disadvantages using G-APDs . . . . .	123
3.6.3. FACT-specific issues . . . . .	123
3.6.4. Available real-time information and calibration concept . . . . .	124

<b>4. Operation and performance of the FACT camera</b>	<b>127</b>
4.1. Camera tests at ETH Zurich	127
4.1.1. DRS charge calibration and sample signals	127
4.1.2. First dark count spectrum	127
4.1.3. Relative photon detection efficiency	129
Setup	131
Data analysis	131
Results and discussion	132
Summary	132
4.2. Camera installation and first operation	134
4.2.1. First operation	134
4.2.2. Rate scans	136
4.2.3. Crab occultation observation	140
4.3. Camera performance	141
4.3.1. Gain homogeneity	143
4.3.2. Broken pixels	144
4.3.3. Extraction of calibration information from data runs	145
4.4. Telescope PSF measurement	146
Measurement	146
Analysis	148
Result and discussion	149
4.5. Observations of sources	151
4.5.1. First detections of strong sources	151
4.5.2. Monitoring of variable sources	151
<b>5. Summary and future prospects of the FACT technology</b>	<b>153</b>
5.1. Project summary	153
5.2. G-APD summary	154
5.3. Desired improvements of G-APDs for Imaging Atmospheric Cherenkov Telescope (IACT) cameras	155
5.4. Improvements of the FACT technology	155
5.5. Future of the FACT project	156
Technology and knowledge transfer to CTA	156
Closing words	157
<b>Acknowledgements</b>	<b>159</b>
<b>Appendices</b>	<b>161</b>
<b>A. Calculations</b>	<b>161</b>
A.1. On the statistics of Cherenkov photon counting	161
A.2. Two-dimensional PSF	162
A.3. PSF widening for light sources in infinite distance	163
A.4. Noise characteristic of random background events	163
A.5. Unit transformations to photon rates	165
A.6. Generalized mean value and variance for combined distributions	166
Norm	167
Average	167
Variance	167
A.7. Equivalence of the ENF definitions	168

A.8. Explicit calculation of the ENF of a Poisson distribution with noise . . . . .	168
A.8.1. Definitions . . . . .	168
A.8.2. Only Poisson statistics . . . . .	168
Sum . . . . .	169
Average . . . . .	169
Variance . . . . .	169
A.8.3. Including noise . . . . .	169
Integral . . . . .	169
Average . . . . .	170
Variance . . . . .	170
Excess noise factor . . . . .	170
<b>B. Linearity of digital photo camera measurements</b>	<b>171</b>
B.1. Camera settings . . . . .	171
B.2. Image processing . . . . .	172
B.2.1. Conversion of raw files to TIFF image files using dcraw . . . . .	172
B.2.2. TIFF image processing in Matlab . . . . .	172
B.2.3. Python image processing . . . . .	172
B.3. Result . . . . .	173
<b>Glossary</b>	<b>175</b>
<b>References</b>	<b>183</b>
<b>Curriculum Vitae</b>	<b>197</b>





# 1. Why build a new camera type?

## 1.1. A bit of history

The quest to explore and explain our universe is as old as humanity itself, and may well be considered a distinguishing criterion to define humans. The first systematic studies are reported from the ancient Egyptians, and since then every culture searched the sky for systematic occurrences and the consequences for life here on Earth [1]. In all these years, astronomy was an important pillar of fundamental research. As such, it was not only contributing to the cultural heritage of each generation, but also boosted the evolution of other fields of science (starting with geometry in Ancient Egypt) and brought forward technical inventions.

For the predominant part of history, the only available sensor to detect light was the human eye, which restricted our view on the universe to the very narrow band of optical wavelengths. A major breakthrough was the invention of the optical telescope in the early 17th century. The number of observable objects was immensely increased, but still the observations were limited to light which the eye can see.

The first astronomical observation outside the visible spectrum came with the discovery of infrared light. On March 18, 1800, Sir William Herschel published a measurement where he used a blackened thermometer and measured its heating in various parts of the solar spectrum, which was split into its wavelengths using a prism [2]. To his surprise, the temperature increase was fastest outside the visible spectrum beyond the red colors. He concluded, that *“there are rays coming from the sun [...] with a high power of heating bodies, but with none of illuminating objects”* [3]. Similarly, the sun was used as an “astronomical source” in an experiment using silver chloride for the first detection of ultra-violet (UV) light shortly thereafter [4, 5].

More than a hundred years passed until the first non-optical signal from outside our solar system was detected. Karl G. Jansky was investigating the static noise on short wave frequencies in 1932, when he detected a faint background signal. Due to its periodicity of 24 hours, it was at first described as being *“somehow associated to the sun”* [6], but later found to come from a location *“fixed in space; i.e., that the waves come from some source outside the solar system”* or more precisely from the direction of the Milky Way [7].

In the past century, thousands of scientists were crawling through the immense amount of data which was accessible from radio to X-ray wavelengths. Scientific findings were usually based on looking at a large number of cosmic objects, or by looking closely at single objects over a large wavelength range (multi-wavelength approach). It was thus at hand to look at photons with even higher energies than X-rays<sup>(1)</sup>. Photons at such energies interact with the Earth’s atmosphere and thus do not reach its surface. However, one of the products of these interactions are Cherenkov photons, which reach the Earth’s surface and can be detected using special telescopes. This technique allows to observe

---

<sup>1</sup>When going to high frequencies, it is often more convenient to use the energy carried by a single photon rather than its frequency. Energy  $E_\gamma$ , wavelength  $\lambda$  and frequency  $\nu$  of a photon are related via the speed of light  $c$  and the Planck constant  $h$ :  $E_\gamma = h\nu = \frac{hc}{\lambda}$

high-energetic photons in the TeV<sup>(2)</sup> range, i.e. photons which carry a trillion times the energy of visible light. In 1989, the first source of this high energy radiation was identified by the WHIPPLE collaboration. Using a telescope with a 10 m diameter reflector and a camera with 37 pixels, they detected gamma rays with photon energies above 0.7 TeV from the direction of the Crab nebula [8].

This was the beginning of astronomy with photons in the Very High Energy (VHE) range, defined as having photon energies above  $\sim 30$  GeV. Combining all observation technologies, the total observable range now spreads over about 20 orders of magnitude, from lowest radio observations around 10 MHz [9] up to gamma ray energies above 10 TeV ( $2.4 \times 10^{21}$  MHz).

## 1.2. The technology of Imaging Atmospheric Cherenkov Telescopes

The observation of photons with high energies has to address two main problems: the flux of these photons is very low compared to photons of lower energies, and due to their interactions with the atmosphere, they do not reach the surface of the earth. The second problem can be addressed by using spaceborne experiments, as it is done e.g. with the Fermi satellite<sup>(3)</sup>. Its main instrument is the Large Area Telescope (LAT), which covers photon energies from about 20 MeV to more than 300 GeV [10]. Unfortunately, the effective area in which photons are detected is less than one square meter<sup>(4)</sup>, which is for most sources too small to collect statistically significant data at large photon energies. A possibility would be to increase the size of the satellites, but due to the very high costs of space experiments, this approach is unreasonable. Directly detecting the photons on the surface of the Earth is not possible due to the aforementioned interactions with the atmosphere. The breakthrough was to make a virtue out of necessity and, instead of directly capturing the high energy photons, to observe the products of these interactions.

### 1.2.1. Interaction of high energy photons with the atmosphere

High-energetic photons induce in the atmosphere a process which is called an air shower. At energies above some tens of MeV, the main interaction of photons with matter is pair production (see figure 1.1): the photon interacts with the electric field of a nucleus of the atmosphere and produces an electron and a positron. The energy of the primary photon is transferred into the mass of the two particles and their kinetic energy.

These two particles may then emit high energy photons via bremsstrahlung: the electron or positron is deflected in the electric field of a nucleus, and produces a photon while losing part of its kinetic energy. Those photons may again create electron-positron pairs, and by iterating these steps a “shower” of secondary particles is produced.

### 1.2.2. Background signals: hadronic showers

Unfortunately, high energy photons are not the only source of such air showers. Much more common are hadrons which enter the atmosphere and induce showers. Since hadrons

---

<sup>2</sup>The energy unit eV, electron volt, denotes the energy an electron gains when passing a voltage difference of 1 Volt. It is approximately  $1.602 \times 10^{-19}$  Joule. Visible light has a wavelength from 400 nm to 800 nm, corresponding to photon energies from 1.5 eV to 3 eV.

<sup>3</sup><http://fermi.gsfc.nasa.gov>

<sup>4</sup>Maximal effective area as a function of the energy is  $9500 \text{ cm}^2$  at an energy around 1 GeV to 10 GeV [10].

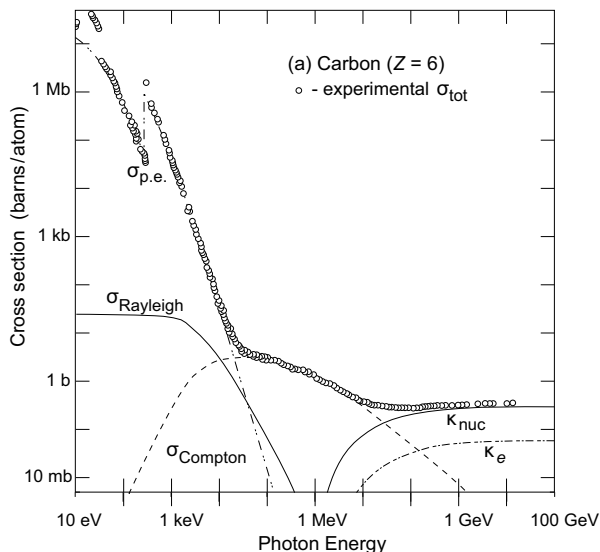


Figure 1.1.: Contributions to the total cross section of the interaction of photons with carbon ( $Z = 6$ ). The cross sections for nitrogen ( $Z = 7$ ) and oxygen ( $Z = 8$ ) are similar. Pair production in the nuclear field is denoted with  $\kappa_{\text{nuc}}$ , and is the dominant contribution for photon energies above some tens of MeV. Figure adapted from [11].

can interact over the strong nuclear force, additional interactions are possible which can produce other particles such as charged or uncharged pions [12, 13]. They either undergo again hadronic interactions, or decay into particles including muons, photons and electrons/positrons. Additional photons can be produced by bremsstrahlung. The secondary photons and electrons/positrons can start electromagnetic sub-showers.

For the analysis of gamma-induced electromagnetic showers, these hadronic showers must be sorted out. This is achieved by taking advantage of the different topology and temporal structure in the shower development on a statistical basis (see figure 1.2).

### 1.2.3. Cherenkov radiation

Most of these particles in both electromagnetic and hadronic showers are produced with very high energy. In the case of massive particles, their velocity is as a consequence highly relativistic<sup>(5)</sup>. If the velocity of a charged particle is larger than the speed of light in a medium (here: the atmosphere), Cherenkov photons are emitted [15]. These photons have wavelengths in the optical and UV range. They are partly absorbed when traveling through the atmosphere [16], such that the resulting spectrum has a peak wavelength around 320 nm (see figure 1.3). The Cherenkov photons can be detected by optical sensors.

The Cherenkov photons from air showers arrive on the surface of the Earth within some nanoseconds, and illuminate a circular area with a radius around 100 m to 200 m with a photon density of  $\sim 100 \text{ photons m}^{-2} \text{ TeV}^{-1}$  [16, 17]. An Imaging Atmospheric Cherenkov Telescope (IACT) somewhere in this circle can detect this air shower, which in turn gives the IACT a huge effective collection area for VHE photons.

<sup>5</sup>Close to the vacuum speed of light  $c=299792458 \text{ m s}^{-1}$ .

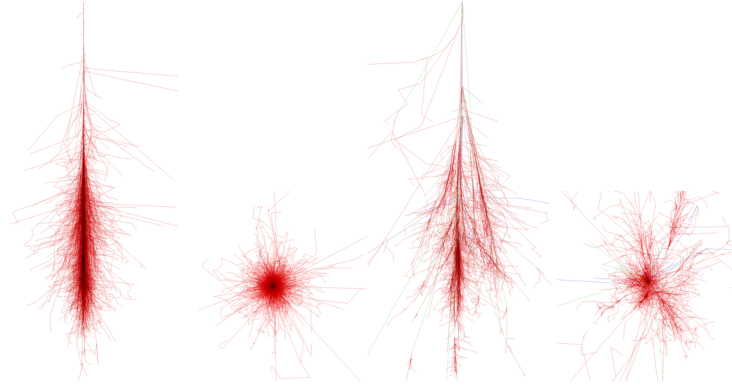


Figure 1.2.: Comparison of air showers initiated by a 100 GeV photon (left) and a proton with the same energy (right), in projections to the  $xz$ - and  $xy$ -plane. The red lines show tracks from electrons, positrons or high-energetic photons. Image courtesy of F. Schmidt [14].

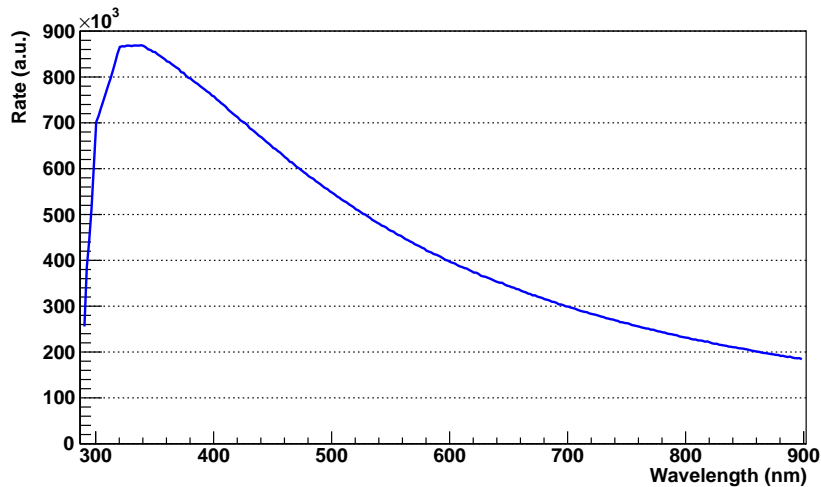


Figure 1.3.: Simulated Cherenkov spectrum on ground. The electromagnetic air showers were simulated between 100 GeV and 50 TeV with a spectral index of  $-2.7$ . The Cherenkov spectrum peaks in the UV range around 320 nm. The simulation data was provided by T. Bretz.

### 1.2.4. Cherenkov radiation: formulas

The number of emitted Cherenkov photons  $N_c$  per path length  $ds$  of the charged particle is given by

$$\frac{dN_c}{ds} = 2\pi\alpha \int \frac{\sin^2 \theta_c}{\lambda^2} d\lambda \quad [13]. \quad (1.1)$$

$\alpha$  is the fine-structure constant,  $\lambda$  the wavelength of the emitted photons, and  $\theta_c$  their angle relative to the direction of the charged particle. This angle is given by

$$\cos \theta_c = \frac{1}{n\beta}. \quad (1.2)$$

$n$  is the refractive index of the medium in which the particle travels and  $\beta$  its velocity ( $v = \beta c$ ). This formula contains the radiation condition  $\beta > 1/n$ <sup>(6)</sup>, defining the lower limit for the particle velocity. The integral in equation (1.1) seems to diverge for small wavelengths  $\lambda$ , but since the refractive index  $n$  depends on the wavelength and becomes smaller than one for X-ray energies [18, 19], the radiation condition cannot be satisfied for such energies and the integral does not diverge.

### 1.2.5. Background light

The Cherenkov photons from the air showers are embedded in background light coming from various sources. To ensure a low level of artificial light, the locations for Cherenkov observations must be carefully selected. For one of these locations, the Observatorio del Roque de los Muchachos (ORM) on the Canary Island of La Palma, Spain, the different components and the total background photon flux were investigated. According to C. Benn and S. Ellison [20] and S. Preuss *et al.* [17], the main contributions in moonless nights are

- starlight, which varies significantly between the galactic plane and other regions of the sky,
- diffuse galactic light, which is star light scattered in the interstellar dust,
- zodiacal light, which has a similar origin, but contains of solar light scattered in the interplanetary dust,
- airglow, the light produced by chemical reactions in the atmosphere and the decay of excited atoms,
- and artificial light sources such as the light by street lamps or house illuminations<sup>(7)</sup>.

Outside the galactic plane a mean flux of  $2.6 \times 10^{12}$  photons sr<sup>-1</sup> s<sup>-1</sup> m<sup>-2</sup> in the range from 300 nm to 650 nm was measured.

The amount of background light and its spectrum and intensity are highly variable. The decay time of excited oxygen atoms contributing to airglow is about one hour [22], and is thus most relevant shortly after nightfall. Scattered sunlight disturbs the observations during twilight. Moonlight is reflected sunlight, and has thus a similar spectrum except for the wavelength dependence of its reflection<sup>(8)</sup>. If the moon is visible, its light usually

---

<sup>6</sup>The condition for Cherenkov radiation is that the particle speed  $v = \beta c$  is faster than the speed of light in the medium, i.e.  $\beta c > c/n$ .

<sup>7</sup>It is worth mentioning that there is a law dedicated to the protection of the quality of astronomical observations on La Palma. Subject of the law are outdoor lighting installations, activities and services producing atmospheric contamination and other factors which degrade the atmospheric quality for the observations [21].

<sup>8</sup>The reflectivity of the moon increases by a factor 2.5 from 300 nm to 800 nm [23–25].

dominates the spectrum and intensity (and thus also the variability) of the background light. See section 3.2.1 for a quantitative comparison of the Cherenkov and background photon rates.

### 1.2.6. Mirror design

Due to the small signal size from an individual shower compared to the large background rate, it is of crucial importance to collect as many signal photons as possible with precise timing: the photons of the air showers arrive within some nanoseconds, whereas the background photons arrive randomly and independent of each other. When designing a telescope for the observation of air showers, the various design parameters must be optimized to balance the various goals:

- The number of collected signal photons  $N_\gamma$  should be as large as possible, while keeping the number of background photons  $N_{\text{bg}}$  low. The significance of the signal is (approximately) the number of signal photons divided by the square root of the number of background photons, i.e.  $N_\gamma/\sqrt{N_{\text{bg}}}$ .
- The timing of the air shower photons should be conserved, i.e. the mirror should be isochronous (small time dispersion).
- The Point Spread Function (PSF) describes the light distribution of a pointlike source at the camera entrance window, i.e. how much the image is “smeared out”, and should be small<sup>(9)</sup>.
- The PSF is usually best at the center of the camera and degrades towards the outer pixels (see e.g. [26]). These optical aberrations at off-axis points are often asymmetric and complicate the analysis of the images.

These parameters are optimized by varying the design of the mirror dish:

**Mirror area:** In first order, both the number of signal photons  $N_\gamma$  and the number of collected background photons  $N_{\text{bg}}$  scale linearly with the mirror area. The significance is then proportional to the square root of the mirror area. A large mirror allows to observe fainter air showers, i.e. ones with lower energy of the primary photon.

**Mirror reflectivity:** For the same reason as in the previous item, the overall reflectivity of the mirrors is maximized. Due to the differing spectral distributions of signal and background photons, it is favorable to optimize the reflectivity only in the main wavelength range of Cherenkov photons, and reduce it outside this region.

**Mirror curvature:** The curvature is mainly defined by the focal ratio  $f/D$ , where  $f$  is the focal length of the telescope (the distance between the mirror and the camera) and  $D$  is the diameter of the mirror dish. A large  $f/D$  reduces the aberration effects and time dispersion of the mirror. However, increasing the focal length requires to enlarge the size of the camera (see next section), which increases its cost.

**Mirror shape:** Besides the curvature, the exact shape of the mirror dish influences the aberration effects and the time dispersion, but cannot be optimized for both properties at the same time (see below).

The two basic mirror shapes in discussion for IACTs are the Davies-Cotton design<sup>(10)</sup> or a parabolic shape. Since the total mirror area is usually large (today’s IACTs have mirror

---

<sup>9</sup>The size of the PSF is usually compared to the pixel size of the camera of the telescope.

<sup>10</sup>This design was not originally developed for astrophysical observations but rather “for the purpose of producing a radiation flux sufficiently high to destroy materials” for the U.S. Army [27].

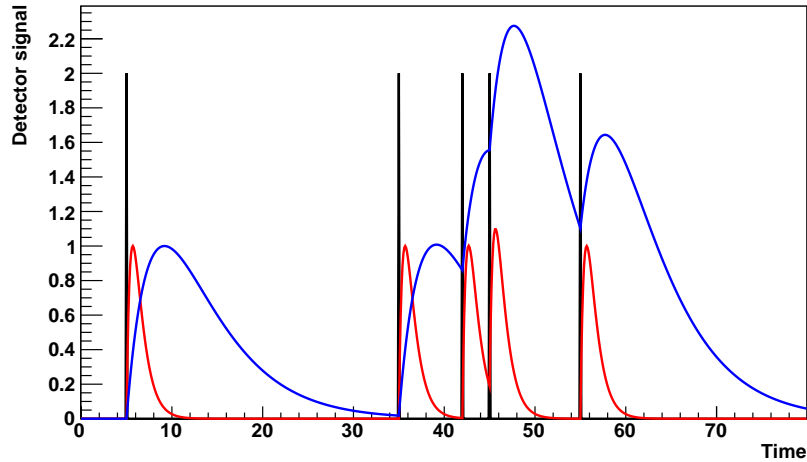


Figure 1.4.: Illustration of pile-up: while the photon arrival times (black) can be well distinguished for fast signals (red), they are difficult to separate for slower signals (blue).

areas  $> 100 \text{ m}^2$ ), the mirror is segmented into multiple smaller mirrors. In the Davies-Cotton design, the single mirrors have a spherical shape (with radius  $2f$ ) and are arranged on a sphere of radius  $f$ . Compared to parabolic mirrors this design has smaller and more symmetrical aberration effects. Its main disadvantage is the larger time dispersion, which is negligible in the case of parabolic mirrors. See M. Actis *et al.* [28] and the references therein for a more complete discussion on mirror designs.

### 1.2.7. Camera requirements

The task of the camera in an IACT is in principle quite simple: to translate the Cherenkov photons which arrive at the focal plane into electrical signals, with an efficiency as high as possible and without losing the timing information. The focal plane is divided into pixels to get information on the location of the photon arrivals. The performance parameters are similar to those of the mirror dish:

- As many of the Cherenkov photons which arrive at the entrance window of the camera should be collected, if possible while rejecting background photons.
- The timing of the photons should be passed on to the electrical signal.
- The signal created by single photons should be short enough to avoid pile-up effects<sup>(11)</sup> from the high background photon rate (see figure 1.4).
- As few photons as possible should be assigned to the wrong pixel (no inter-pixel crosstalk).
- The created signals should be accurate and allow a precise reconstruction of the number of photons (see later explanations on the Excess Noise Factor (ENF)).
- The occurrence of fake signals from noise should be rare.

Two additional issues have a significant advantage in the analysis of the data: homogeneity and stability. Homogeneity means that all pixels have a similar behavior in converting

<sup>11</sup>If several events occur at the same time or shortly after each other (here: several photons arrivals), it can become difficult to disentangle the detector signal into the separate events. This problem is called pile-up.

photon signals to electrical signals and similar noise characteristics. Stability considerations are divided into short-term changes in the observation conditions (e.g. temperature or background light), and long-term effects such as performance changes over the years the camera is in operation (e.g. optical degradation).

The next step in the observation of air showers is the digitization of the electrical signals. This step is either done inside the camera, or the electrical signals are transmitted out of the camera and digitized elsewhere. Integrated digitization has the disadvantages of space and power requirements, that the maintenance is more difficult, and that produced heat must be dissipated. External digitization has to address the weight of the large number of necessary cables and the signal quality losses in the transmission.

The size of the camera's pixels must match the desired angular resolution of the telescope. For a focal length of  $f$  and an angular resolution of  $\alpha$ , the pixel size  $s$  is approximately

$$s = 2f \cdot \sin(\alpha/2). \quad (1.3)$$

The advantage of smaller pixels in the data analysis saturates for angular resolutions around  $0.1^\circ$  [28]<sup>(12)</sup>. Due to intrinsic fluctuations of the air shower development in the atmosphere, a better angular resolution only increases the amount of data, but does not provide additional information for the data analysis (in particular for the gamma-hadron separation). The complexity (and cost) of a camera scales approximately with the number of pixels and thus with the inverse square of the pixel size for a fixed field of view (FOV) of the camera. The FOV of the camera determines how many showers can be observed. The upper limit on the useful FOV for a single telescope and point-like sources<sup>(13)</sup> can be estimated as follows: the area homogeneously illuminated by Cherenkov light has approximately a radius of 100 m to 200 m [16], with the center of the shower in a height around 10 km. This contributes to the radius of the camera with  $1.15^\circ$ . The common observation mode directs the telescope around  $0.6^\circ$  beside the source direction<sup>(14)</sup>, and the showers may extend up to  $1^\circ$  in the camera, resulting in a total diameter of  $2 \cdot (1.15 + 0.6 + \frac{1}{2})^\circ = 4.5^\circ$  of the camera. Larger cameras only observe showers from a location outside the homogeneously illuminated radius, which are almost impossible to analyze with a single telescope<sup>(15)</sup>.

### 1.2.8. Data analysis principle

The analysis of IACT data has two main purposes: first to decide whether there is a source of high energy photons at a certain location, and, if this is the case, to characterize the flux and energy spectrum of the source.

The digitized data is saved event by event. The first step in the analysis is to extract the calibrated number, timing and distribution of photons from the digitized signal. Since most of the observed air showers are initiated by charged particles instead of high energy photons, these events where a hadron shower was observed must be sorted out.

The parameters used for this are usually based on the ones proposed by A. M. Hillas in 1985 [30]. They describe the geometrical and temporal distributions of shower images,

---

<sup>12</sup>The simulation was performed for an array of nine telescopes. The values for a single telescope are comparable.

<sup>13</sup>For extended sources or extended regions of interest (off-axis observations) the FOV needs to be increased.

<sup>14</sup>This so-called wobble mode allows to estimate the background rate without taking separate datasets, which increases the effective observation time of a telescope [29].

<sup>15</sup>For more precise estimates a complete simulation is necessary. If multiple telescopes are connected in an array, even telescopes in the non-homogeneously illuminated area outside the 200 m radius can contribute information for the analysis, making larger cameras reasonable [28].



which are different for the two shower types. This allows to statistically classify the events, either based on cuts on the various parameters, or by using random forest or neural network approaches [31–33].

When the gamma shower candidates are selected, the orientations and locations of the showers in the camera are analyzed and compared to data of a region in the sky where no source is expected. The comparison allows to determine the probability whether the observed flux from the (supposed) source position is compatible with the null hypothesis that the source does not emit high energy photons. The standard formulas for the statistical analysis are the ones by Li & Ma [34], but newer and more accurate statistical descriptions are proposed (e.g. by S. Klepser [35]) and are currently being investigated.

Source detections are quantified in units of standard deviations or “sigma” ( $\sigma$ )<sup>(16)</sup>. It denotes the probability that the observed signal is not from a source of high-energetic radiation, but a statistical fluctuation of the background. The standard limit to claim a detection is 5 sigma, corresponding to a probability of 99.99997%, or, in other words, 3.5 million to 1.

The next step is the determination of the energies of the observed photons. Since no reference data e.g. from a test beam is available, the energy has to be estimated by comparing the shower images with computer simulations. This allows to create a spectrum of the observed photons and draw conclusions on the emission processes of the source.

A description of the full analysis chain for the MAGIC telescope can be found in J. Albert *et al.* [36]. Alternative analysis principles are used e.g. in the H.E.S.S. experiment [37].

### 1.3. Observation of variable sources

Besides the energy spectrum, another characteristic of the photon flux is important for many sources: its variability. Many sources do not show a steady flux, but are highly irregular by showing a flaring behavior. The time-scale of the flux changes ranges from minutes [38, 39] to days [40–42] to years [43].

One particular class of sources often shows a highly variable photon emission: in some galaxies, the central region is brighter than the rest of the galaxy in some part of the electromagnetic spectrum. Such galaxies are said to have an Active Galactic Nucleus (AGN) at their center. The most used categorization of AGNs attributes the characteristics in the various wavelengths to the observation angle of the galaxy (see e.g. the introduction by C. Tadhunter [44]). Most of the extragalactic sources which are observable with IACTs belong to the blazar class, i.e. are active in radio frequencies and have a jet<sup>(17)</sup> (see figure 1.5) pointing towards the Earth [47, 48].

An important question is the process which produces the high-energetic photons. The most simple model is the Synchrotron Self-Compton (SSC) model, where relativistic leptons in the jet emit photons via synchrotron radiation, and the same photons are then pushed to higher energies via Inverse Compton (IC) scattering. The synchrotron photons and the “upscattered” high-energy photons lead to a characteristic double-peak structure in the spectral energy distribution of such sources [50]. Changes in the lepton flux lead to

---

<sup>16</sup>A probability of  $n$  sigma is defined as

$$p(n\sigma) = \int_{-\infty}^{n\sigma} \frac{1}{\sigma\sqrt{2\pi}} e^{-\frac{x^2}{2\sigma^2}} dx. \quad (1.4)$$

<sup>17</sup>A jet is a stream of particles which is emitted by an object in a constrained angular direction. Even for astronomical scales their length can be huge, as an example the jet of the galaxy M87, which is about 6000 light years long [45]. See e.g. E. M. de Gouveia Dal Pino [46] for more information on jets.

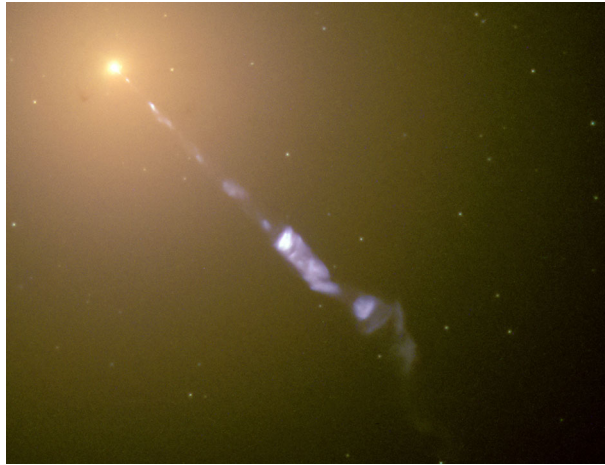


Figure 1.5.: Hubble image of the galaxy M87: its well-visible jet is about 6000 light years long. Image source: [49].

correlated changes of both peaks in the spectrum. In other models the second peak comes from external photons, which are boosted in energy via IC scattering.

The third group of models are based on hadronic interactions, where the high-energetic photons are produced in the decay of neutral pions [48]. The investigation of these models and the underlying characteristics of the source are based on parallel observations of different telescope types to cover a large wavelength range. The observations must also cover various flux states of the source to investigate correlations between the wavelengths and possible changes in the spectrum [51, 52]. Most sources are usually in a ground state, and show times of higher flux, so-called flares.

In order to observe those flares and characterize their commonness and properties compared to the ground state, long-term observations are necessary. For such observations, the telescope's stability is of special importance. If the telescope or camera performance changes over time, the analysis has to correct these changes in the calibration stage of the data analysis. This makes the analysis both more complicated (and thus more error-prone) and less precise. Every step towards more stable telescopes is a major step forward in the attempt to establish observations of VHE photons as a key player in astronomy.

## 1.4. The current status of the field

Up to the end of the 20th century, only a handful of sources in the VHE range were known. In the last decade this number increased drastically and is now around 150<sup>(18)</sup>. The best-observed target is the radiation from the direction of the Crab nebula, a supernova remnant with a pulsar at its center<sup>(19)</sup>. The photon flux at energies which is observable with IACTs is considered stable, even though it was recently found to show flares at gamma ray energies just below this range [53]. The Crab nebula defines the simplified standard unit for the photon flux in VHE astronomy: one Crab unit (CU) is the flux which is necessary to observe a source with the same statistical significance as an observation of the Crab nebula under identical conditions. The drawback of this unit is the fact that

---

<sup>18</sup>Most known sources are collected in the TeVCat catalog by the University of Chicago: <http://tevcat.uchicago.edu>.

<sup>19</sup>A supernova is the explosion of a massive star at the end of its lifetime. A pulsar is a rotating neutron star with a strong magnetic field.

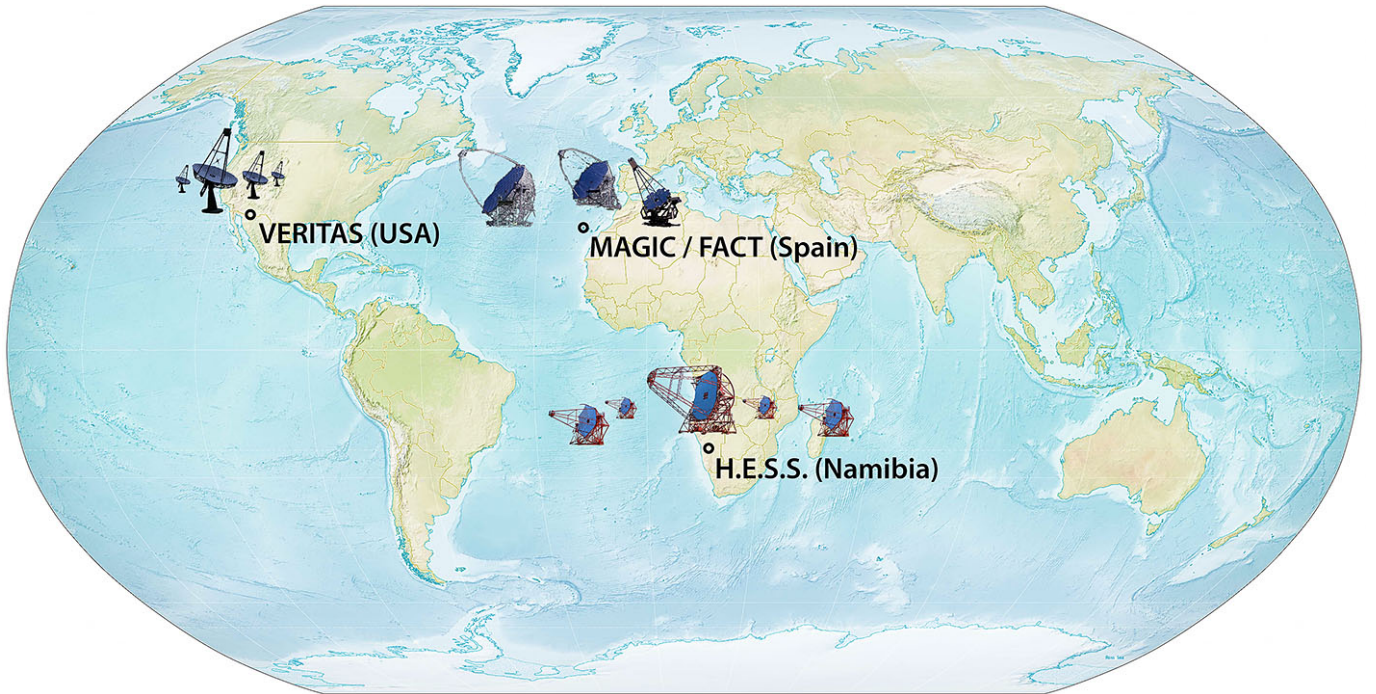


Figure 1.6.: Location of the major IACT experiments VERITAS, H.E.S.S. and MAGIC. The latter is located on the Roque de los Muchachos on the island La Palma (Spain), where also FACT can be found. Image sources: [59].

sources with a different energy spectrum might need more or fewer photons for the same significance, making the unit only an indirect indicator for the photon flux of a source.

The unit is also used in the primary performance criterion for IACTs: if a source has a similar energy spectrum as the Crab nebula and the telescope observes the source for 50 h, what is the minimal flux the source must have for a detection with a significance of  $5\sigma$ ?

The two most observed variable sources are Markarian 501 (Mrk 501) and Markarian 421 (Mrk 421). Both are AGNs of the blazar class, and show a strong variability, with flares reaching fluxes of several CU [39, 41].

Currently there are several collaborations worldwide operating IACTs. The most important ones are H.E.S.S.<sup>(20)</sup>, MAGIC<sup>(21)</sup> and VERITAS<sup>(22)</sup> (see figure 1.6). A more detailed introduction to the field of IACTs can be found in one of the numerous overviews by one of the pioneers of the field, T. C. Weekes [54–56], the review report by R. A. Ong [57] or one of the PhD theses on the topic (e.g. by M. Rissi [58]).

All of these telescopes use Photomultiplier Tubes (PMTs) as photosensors in their cameras. These devices are known since the middle of the last century and feature the speed and sensitivity necessary for the challenging application in IACTs. In the last years, their sensitivity underwent a remarkable progress and was more than doubled [60]. However, they also have some properties which are challenging, from the production of large fake pulses to significant aging effects [61].

Geiger-mode Avalanche Photodiodes (G-APDs) are semiconductor photosensors which

<sup>20</sup>High Energy Stereoscopic System (H.E.S.S.): <http://www.mpi-hd.mpg.de/HESS>

<sup>21</sup>Major Atmospheric Gamma-Ray Imaging Cherenkov (MAGIC) telescopes: <http://magic.mppmu.mpg.de>

<sup>22</sup>Very Energetic Radiation Imaging Telescope Array System (VERITAS): <http://veritas.sao.arizona.edu>

have only recently become commercially available in reasonable quantities. Their sensitivity is already in the first generation comparable to PMTs, and the electronics design is facilitated by the absence of high voltage components. Furthermore, G-APDs are mechanically and electrically more robust and show no aging effects [62], making them appear predestined to replace PMTs in Cherenkov telescope cameras. The improved ease of use and higher reliability are of particular importance if multiple telescopes are operated in parallel, as it is planned in the Cherenkov Telescope Array (CTA) project. CTA plans to build and operate over a hundred IACTs in parallel and is currently in its design phase [28].

Unfortunately the main disadvantages of G-APDs are especially challenging in the outdoor and high background conditions of an IACT: many device parameters depend strongly on the temperature, and their output pulses are a bit slower than those of PMTs. This led to skepticism on the practicability of using G-APDs in IACTs. The challenge of overcoming these disadvantages with the prospect of a major leap forward in the performance, stability and reliability was reason enough to call the First G-APD Cherenkov Telescope (FACT) project into life.

## 1.5. A short introduction to the FACT project

One of the first tests to use G-APDs in Cherenkov telescopes was conducted in 2007, when an array of four G-APDs was mounted in the camera of the MAGIC telescope with very promising outcome [63]. After this test, the project was started with the proposal to build a full camera in a modular design. Groups of four G-APDs are summed up and form one pixel of the camera.  $6 \times 6$  pixels arranged in a square form one module, multiple modules would be stacked to increase the size of the camera (see figure 1.7). The signals of the light sensors are amplified directly in the camera close to the sensors to minimize noise collection. The dead space between the active area of the sensors is eliminated using light guides which concentrate the light onto the active area of the photosensors. The camera was planned to be installed in a refurbished telescope mount of one of the HEGRA<sup>(23)</sup> telescopes on the Roque de los Muchachos on the island of La Palma, Spain, first for tests of the technology and its performance, and later for the long-term monitoring of bright blazars.

We built the first of these modules in winter 2008/2009. It followed the design of the proposal, using 144 G-APDs<sup>(24)</sup> with an active area of  $3 \times 3 \text{ mm}^2$  each. On top of each sensor, simple light-collecting cones consisting of a reflective foil increased the sensitive area per device to  $7.2 \times 7.2 \text{ mm}^2$ , such that each of the 36 pixels had a size of  $14.4 \times 14.4 \text{ mm}^2$ . The light sensor signals were amplified directly at the sensors. The signals were then led to a NIM electronics crate<sup>(25)</sup>, where the signals were split into two identical signals. One signal was led to the trigger logic, whereas the other was temporarily stored in a ring buffer pipeline for the digitization.

In summer 2009, the module was mounted on top of a mirror with a focal length of 80 cm on the roof of a building at the Campus Honggerberg of the ETH Zurich. Using this setup, we could for the first time obtain images of air showers with a self-triggering camera based on G-APDs. This result was reported by the collaboration at the International Cosmic Ray Conference (ICRC) 2009 in Łódź, Poland, and later published [65]. The plan to install

---

<sup>23</sup>The High Energy Gamma-Ray Astronomy (HEGRA) experiment was an array of six Cherenkov telescopes on La Palma, Spain. They were replaced in 2002 by the MAGIC telescopes.

<sup>24</sup>MPPC S10362-33-050C [64] by Hamamatsu Photonics K.K., Japan.

<sup>25</sup>The Nuclear Instrumentation Module (NIM) standard defines an interface for a wide range of electronics modules used for the processing of analog and digital signals.



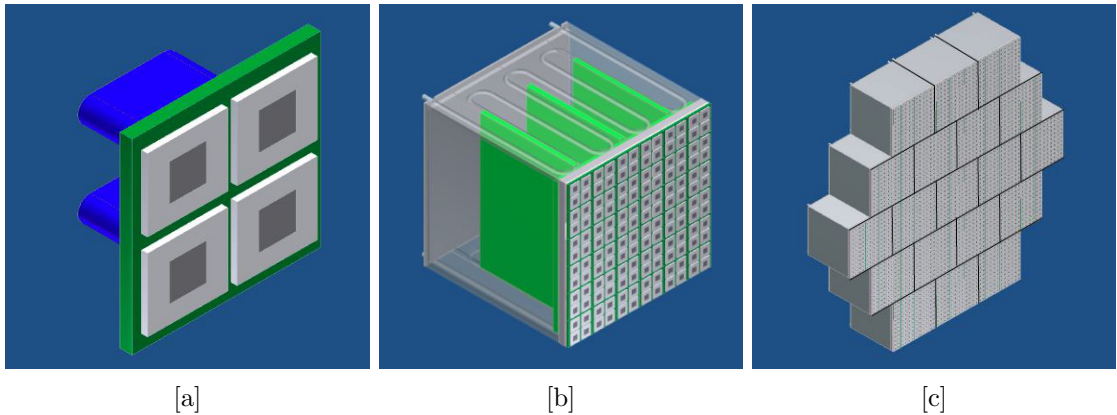


Figure 1.7.: Early CAD drawings for the FACT project as of March 2008: [a] four G-APDs are summed up and form one pixel. [b] 36 pixels form one module. [c] 19 modules combined form the full camera. Images courtesy of the FACT collaboration.

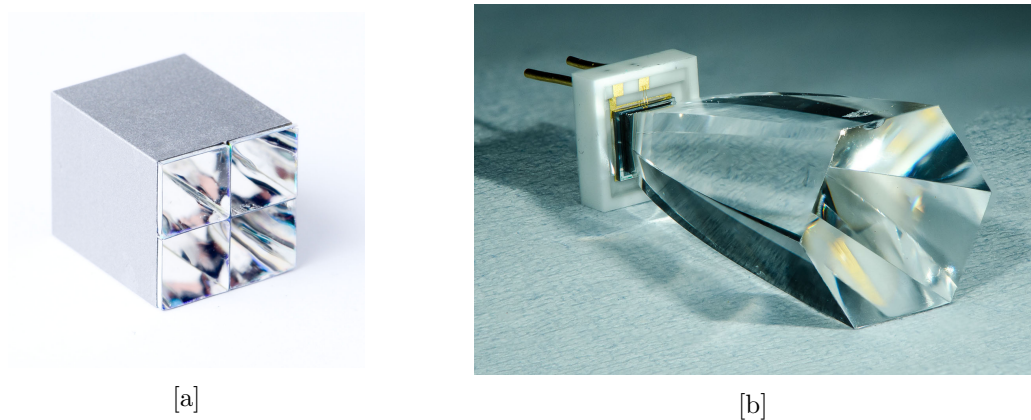


Figure 1.8.: Comparison of the pixels for [a] the prototype module M0 and [b] the FACT camera. The M0 pixels are quadratic with light guides made of a folded reflective foil and consist of four G-APDs, whereas the FACT pixels are hexagonal with a solid cone and only one G-APD.

M0 in the former Cherenkov Telescope 3 (CT3) of the HEGRA experiment was abandoned since the necessary manpower and administrative requirements were not justified by the expected additional insights: due to the limited number of pixels, it would not have been possible to separate hadron shower images from gamma ray images. Without gamma-hadron separation the detection of a source would have been impossible or at least very improbable (see previous sections). Moreover, most studies were found to be also possible with the setup at ETH Zurich.

The original plan was to extend this camera with identical modules. Based on the experience gained during the construction of M0 and computer simulations, it was decided to abandon this idea and make some fundamental improvements to the design of the camera. Instead of summing four G-APDs in a square arrangement to form one pixel, it was decided to arrange the sensors in a hexagonal array and read out each device. The reflective light guides were replaced by solid cones where the light is concentrated using total internal reflection (see figure 1.8). The trigger and readout electronics were designed from scratch and integrated in the camera.

The camera construction was finished in early summer 2011 and was followed by extensive

tests in the laboratory at ETH Zurich. Studies on the noise performance, stability and interplay of the many electronics components with each other and the control software were made. End of September 2011 the camera was moved to the telescope, and two weeks later, on October 11, the last cables were connected. Already in the following night the very first air showers were recorded, an achievement which not only proves the thoroughness of the laboratory tests in Zurich but also the ease of operation of the FACT camera. Incidentally, the first operation was during full moon, where other, PMT based Cherenkov telescopes usually do not operate due to the high level of background light. In parallel to the following commissioning of the telescope, the first astrophysical sources were observed. The detection of the three first sources (Crab nebula, Mrk 501, Mrk 421) with the FACT telescope was reported at the Gamma2012 conference [66].

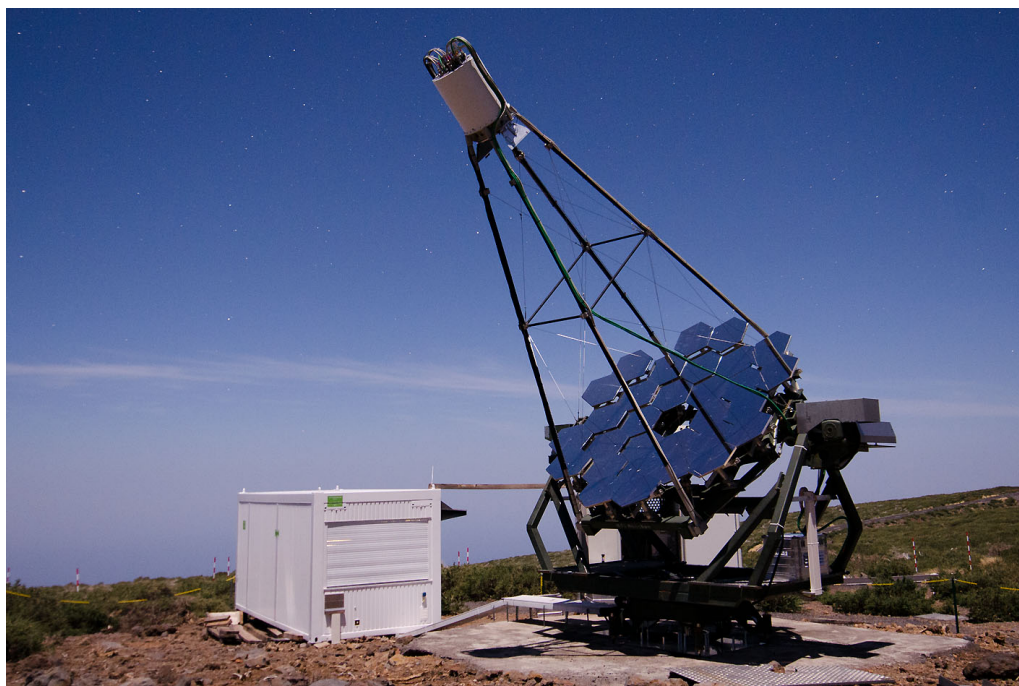


Figure 1.9.: The FACT telescope on the Roque de los Muchachos on La Palma, Spain, during its first operation in the full-moon night from October 11-12, 2011.

## 1.6. Thesis outline

In the course of my thesis, I had the opportunity to participate in every phase of the FACT project:

### **Evaluation – Design – Construction – Commissioning – Operation**

As the general baseline, I was responsible for the photosensors of the camera: the G-APDs. This went from early tests and their characterization to the administration of the pixels during the construction of sensor compartment and the development of the calibration system and the best operation mode for the devices.

It started with the investigation of G-APDs, a work which was continued from my diploma thesis on the use of G-APDs for medical applications [67]. The laboratory tests were made together with D. Renker at PSI Villigen. Their function principle and important characteristics were investigated, in particular their dependence on temperature and voltage variations, and the various noise components and their characteristics. This is described in chapter 2 of this thesis.

The construction of the FACT camera is documented in chapter 3. Optical light guides (“cones”) were developed which concentrate the light onto the sensor area. The development was centered around the optical simulation by I. Braun, for which I provided input properties of the G-APDs and helped with calculations. When the cones were finally produced, I tested the cone prototypes to provide feedback to the manufacturer and obtain realistic values for the cone simulation, described in section 3.3. The tools and methods for the construction of the sensor compartment were developed together with J.-P. Stucki (see section 3.4). More than 1500 pixels were constructed and had to be administered, of which 1440 were finally installed in the camera.

When the camera construction was finished, it was tested in the laboratory at ETH Zurich and finally installed on La Palma. I participated in the debugging of the camera during the lab tests and was on site when the camera was operated for the first time to observe air showers. For the commissioning of the FACT camera I traveled to the telescope three times at the end of the year 2011 and January 2012. The operation and performance of the camera is described in chapter 4.

In the last chapter, a summary on the FACT project is given, possible improvements discussed and the future potential of the FACT technology estimated.





## 2. Geiger-mode Avalanche Photodiodes

### 2.1. Properties of photosensors

At the heart of each Cherenkov telescope is the camera, which translates the incoming light into electrical signals. The conversion inside the camera is performed by its photosensors. There are dozens of different types of photosensors, and the choice for a specific type is based on a complex set of characteristics<sup>(1)</sup>:

**Sensitivity:** Not every photon arriving at the surface of the photosensor can be converted into an electrical signal. In Cherenkov astronomy every single photon counts, which makes the sensitivity a crucial issue in the choice of the photosensor.

**Speed:** Often the interesting signal photons are embedded in a continuous trickle of background signals, which emanate from either the sensor itself (see fake signals) or from external photons (in our case e.g. from scattered starlight). Depending on the temporal shape of the signal a photon produces, the signals might smear out and disappear in the background. Faster and sharper signals avoid such pile-up effects (see figure 1.4).

**Timing:** Between the arrival of the photon at the detector and the production of an output signal there is a delay. Two properties of this delay are of importance, how long and how stable it is. Variations in the delay are called jitter.

**Gain:** The photons arriving at the surface of the detector are converted into electrical signals. The amount of charge released per photon divided by the elementary charge  $e$ <sup>(2)</sup> is called the gain of the detector.

**Fake signals:** Photosensors create fake pulses, which may look similar or identical to signals produced by external photons. Fake pulses appearing randomly in time independent of each other are called dark counts. Often the probability for fake pulses is increased after an initial pulse, such pulses are denoted afterpulses.

**Accuracy and precision:** The signals produced for a fixed number of photons can include two types of uncertainty. The accuracy of the signals concerns the deviation of the average value from the real value (systematic error), whereas the precision describes the spreading of a single measurement versus the mean value (statistical error).

**Dynamic range:** Most sensors have lower and upper limits on the number of photons which can be detected simultaneously. The ratio of these limits is called its dynamic range.

**Ease of use:** The simplicity of using a photosensor in an experiment depends on its specification, both for the design/construction and their operation. The design parameters include for example their size, weight, power consumption, high voltage requirements,

---

<sup>1</sup>Note that this selection is tailored for photosensors delivering a continuous signal stream. While some items are also relevant for integrating sensors such as CCDs or CMOS sensors, others are not.

<sup>2</sup>The charge carried by a single electron, which is  $1.602 \times 10^{-19}$  C.

operation temperature (e.g. the need for cryogenic conditions), and mechanical robustness. For the operation of the photosensors other effects are more important, such as temperature or magnetic field dependencies, aging effects, or the robustness against accidental light exposure.

**Cost:** Especially if many sensors are necessary, the cost of a device is important. Besides the price per piece often the price per sensitive area is considered.

The detection of light on the level of few photons with fast instruments was long dominated by the use of Photomultiplier Tubes (PMTs). PMTs were used in a wide variety of fields ranging from particle physics to astrophysics and applications in medical physics and biological research. In the last years, G-APDs have become the most discussed alternative due to their ease of use and high performance with the promise of further improvements.

In the course of this thesis, many properties of G-APD were studied. In this chapter an introduction to G-APDs is given, and the measurements, calculations and simulations on G-APDs presented.

### 2.1.1. Principle of photomultiplier tubes

The detection of photons with optical wavelengths usually starts with the photoelectric effect [68]. The incoming photon interacts with an electron of the so-called cathode and transfers its energy into kinetic energy of the electron which is removed from its location and leaves a positively charged hole. This charge separation is too small to be electronically registered, so an amplification is necessary.

In PMTs, this amplification is divided into steps. The photoelectric conversion with the emission of a primary electron takes place in the photocathode. This electron is accelerated in an electric field and conducted onto the first dynode. The kinetic energy of the electron is sufficient to release multiple electrons from the dynode, which are accelerated and conducted to the second dynode, where the number of electrons is again multiplied. This process is repeated several times, such that the total number of electrons gets in the range  $10^5$  to  $10^7$ , depending on the design of the PMT and the applied operation voltage. The electrons are collected at the anode of the photomultiplier, the resulting electric pulse is the output signal of the PMT, which can be further amplified and processed (see figure 2.1).

More details on the performance and properties of PMTs can be found e.g. in one of the reference handbooks by Flyckt and Marmonier [69] or Hakamata et al. [70].

### 2.1.2. History of semiconductor photosensors

The first semiconductor photosensors were used in space experiments [71]. One of the simplest and oldest forms is the PIN diode: a p-type and an n-type semiconductor are separated by a layer of intrinsic material, forming an electrical diode. A reverse bias is applied, producing a depletion zone with few electric carriers. The photon detection starts as in PMTs with the photoelectric effect. If the electron and the hole do not recombine, they move towards the cathode and anode, respectively, and thus create a photocurrent. See e.g. [71–73] for more information about photodiodes.

The main problem in the application of PIN diodes is that there is only one electron-hole pair produced per photon. In order to detect light pulses, the number of photons must be large enough such that the produced electrical pulse exceeds the noise of the detector and all following electronics. This requires the use of low-noise charge-sensitive amplifiers [71]. Nonetheless, the smallest detectable pulses need to contain several hundred photons [74].

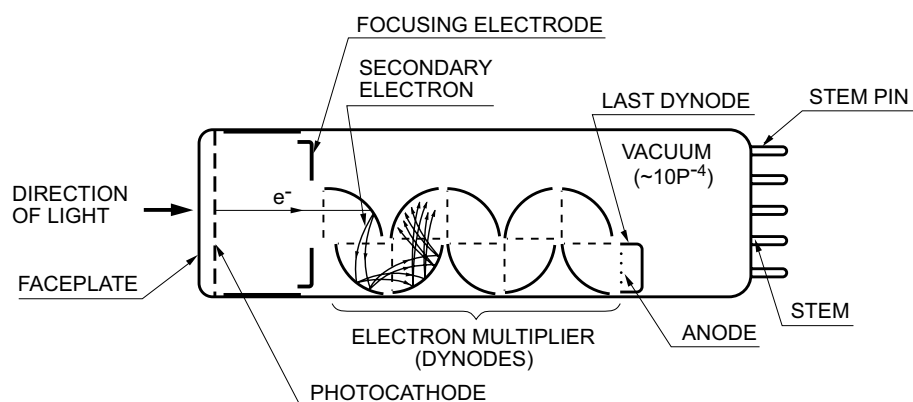


Figure 2.1.: Schematic drawing of a PMT: the incoming photons (left side) produce free electrons via photoelectric effect, which are focused and guided to the first dynode. In several steps, the number of electrons is multiplied, and the total resulting signal collected at the last dynode (anode). Figure from [70].

The electric field in PIN diodes is only strong enough to separate the two charges, and accelerate them towards the electrical contacts. If the acceleration is large enough, the charge carriers start to produce new electron-hole pairs by impact ionization, which is more efficient for electrons than for holes as initiating charge carrier [75]. This allows to build and operate Avalanche Photodiodes (APDs) in a linear mode: the electrons produce electron-hole pairs by ionization, of which the new electron iteratively makes another ionization, producing an avalanche where the ionizations move mostly in the direction of the electrons. The avalanche stops when the charge carriers reach an area of lower electric field strength [74]. The mode is called linear because the total charge is proportional to the number of photons arriving on the surface. The multiplication factor (gain) can be chosen within some limits, and is typically in the range 50 to 200, though larger gains up to  $10^4$  are possible. The larger charge per photon compared to PIN diodes simplifies the electronics design and allows the detection of fainter light pulses. The downside of the charge multiplication is that it induces a statistical fluctuation to the signal since the avalanche formation is a stochastic process.

The number of charge carriers is a function of the applied voltage. When increasing the voltage above a limit, the number of charge carriers diverges [76] and the avalanche does not stop by itself (see figure 2.2). This voltage is called “breakdown voltage”. To stop the avalanche, the applied voltage must be reduced below the breakdown voltage. One way is to detect the avalanche and actively lower the applied voltage. The other possibility is passive quenching by placing a resistor in series to the diode: the avalanche induces a current in the resistor, and the resulting potential difference according to Ohm’s law reduces the voltage over the diode, stopping the avalanche process.

This operation mode is called Geiger mode. The total released charge and its temporal distribution is defined by the exact doping structure of the semiconductor and the quenching resistor, and is independent of the number of photons arriving at the photosensor. As a consequence, only a single photon can be detected at a time.

At the end of the last century, the capabilities of such photosensors were extended by dividing the sensitive area into small cells, each of them operating in Geiger mode with its own quenching resistor. The cells are connected in parallel, effectively summing up the signals of the single cells, an idea first proposed independently by two Russian scientists, Z. Sadygov [77] and V. Golovin [78]. It is now possible to detect multiple photons if they

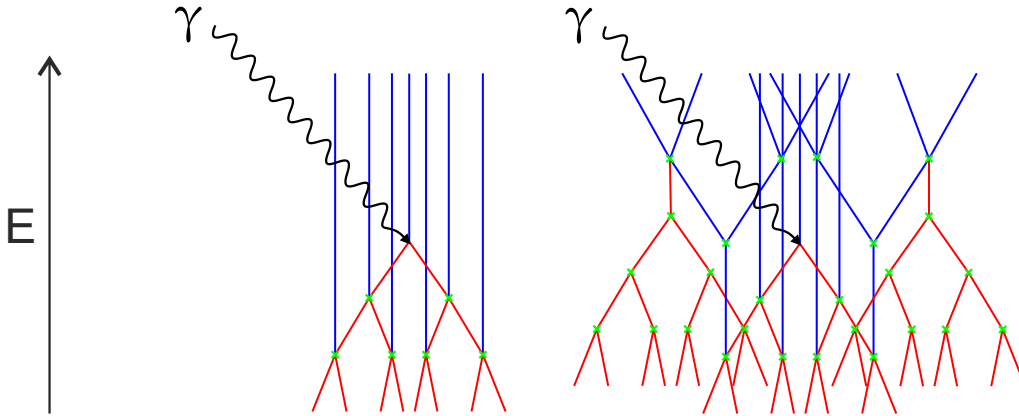


Figure 2.2.: Schematic comparison of the avalanche development below (left) and above the breakdown voltage (right): below the breakdown voltage mostly the electrons (red) start ionizations (green), resulting in an avalanche development only in the opposite direction of the electric field  $E$ . The holes (blue) have a lower ionization rate. Above the breakdown voltage the contribution of hole ionizations becomes large enough such that the avalanche process becomes self-sustaining. The avalanche must be stopped externally by lowering the bias voltage.

arrive in different cells of the sensor. In the following years the production processes were improved, such that commercial mass production of the devices is now possible.

### 2.1.3. Naming

In this thesis, the name G-APD is used for a device consisting of an array of cells, each of which is operated in Geiger mode. G-APDs are known under a wide variety of other names, usually stressing a particular property of the devices. The two most important properties are the characteristics of the Geiger discharge, and the pixelisation of the sensor surface into cells. While the name G-APD focuses on the semiconductor and avalanche property of the device, the most common alternative is Silicon Photomultiplier (SiPM) in reference to the similarity of the applications of G-APDs and PMTs.

However, the name SiPM is misleading in various aspects. Most properties of PMTs are dominated by the efficiency of the photoelectric effect in the cathode and the electron multiplication. The same processes are also important for G-APDs, but with two addenda: the main component of the signal is produced in a Geiger discharge, which dominates the previous electron multiplication. The pixelisation is the defining characteristic in the response of G-APDs. The term SiPM is misleading both in the usage and in the interpretation of signals<sup>(3)</sup>.

Both important characteristics are included in the term Geiger-mode multi pixel photon device, which is rarely used due to its extent. The focus on the pixelisation is in the names PPD (Pixelised Photon Detector), MPPC (Multi-Pixel Photon Counter, brand name by Hamamatsu K.K.) or MAPD (Micro-pixel Avalanche Photo Diodes, brand name by Zecotek). For historical reasons within the FACT project, the term G-APD is used in this thesis.

<sup>3</sup>This applies in particular if the noise properties (e.g. afterpulses) and the statistical variations of signals are investigated.

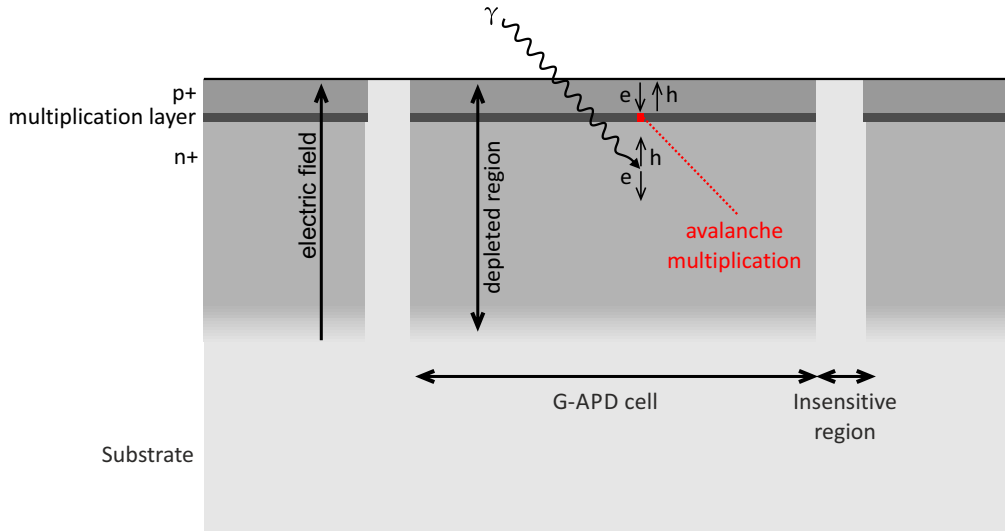


Figure 2.3.: Schematic view of the layer structure of a G-APD. An electric field is applied on a p-n junction, creating a depleted zone. Charge carriers produced by the photoelectric effect of external photons drift to the multiplication layer, where (most of the) avalanche multiplication occurs. Photons which are absorbed above the multiplication layer produce so-called electron-seeded avalanches, those absorbed below hole-seeded avalanches. Illustration based on [79].

## 2.2. Working principle of G-APDs

The commonly used layer structure is of a p-on-n type. A heavily doped  $p+$  layer containing an excess of holes is closest to the surface of the device, followed by a  $n+$  layer with an excess of electrons. When the semiconductor is reverse biased, the charge carriers are pulled away from the p-n junction, creating a depleted layer free of charge carriers.

If a photon enters this depleted region and creates a free charge carrier due to the photoelectric effect, the electron and hole are separated and accelerated towards the cathode and anode of the diode, respectively (see figure 2.3). The charge carriers cause ionizations, the electrons with a higher probability than the holes due to their higher mobility in the semiconductor. The electric field is strongest around the junction, and in consequence the majority of the multiplications take place there, effectively forming a multiplication layer [79].

The entrance depth of photons depends on their wavelength, and is shorter for blue ( $0.6 \mu\text{m}$  at  $470 \text{ nm}$ ) than for red light ( $3.6 \mu\text{m}$  at  $650 \text{ nm}$ ) [80]. If the initial ionization takes place above the multiplication layer, the avalanche is seeded by the electron, for ionizations below the multiplication layer by the hole. If the charge carrier recombines before reaching the multiplication layer and no avalanche is started, the signal is lost. The probability to initiate avalanches (“avalanche probability”) is thus wavelength dependent, and peaks for p-on-n structures in the blue wavelength range.

### 2.2.1. Voltage definitions

In the operation of G-APDs, four voltages are of importance: the bias voltage  $V_b$  (also called operation voltage) is the external voltage which is applied to the G-APD. The aforementioned breakdown voltage  $V_{bd}$  is the voltage at which the avalanche process be-

comes self-perpetuating, above which Geiger discharges occur. It depends on the layer structure and the temperature of the semiconductor. The temperature affects the mobility of electrons and holes, the mobility is lower for higher temperatures. The breakdown voltage is thus larger for higher temperatures. For the current devices by Hamamatsu, the dependence is linear with a coefficient around 55 mV/K [64, 67, 74]. The diode voltage  $V_d$  is the effective voltage over the diode: due to the quenching resistor, this voltage may differ from the bias voltage during the discharge when a current is flowing.

The difference between the diode voltage and the breakdown voltage is called over-voltage  $V_{ov}$ :

$$V_{ov} = V_d - V_{bd} \quad (2.1)$$

Many device parameters only depend on the over-voltage, and depend little on other parameters (such as the temperature) if the over-voltage is kept constant. Since the diode voltage may differ from cell to cell in one device, the term over-voltage is usually used for the difference between bias voltage and breakdown voltage:

$$V_{ov} = V_b - V_{bd} \quad (2.2)$$

### 2.2.2. Photon detection efficiency

The total probability that a single incoming photon triggers a Geiger discharge is called Photon Detection Efficiency (PDE). It is the product of three factors:

$$\text{PDE} = \epsilon_{\text{geo}} \cdot \text{QE} \cdot p_{\text{trigger}} \quad (2.3)$$

- The geometrical factor  $\epsilon_{\text{geo}}$ : the surface of the a G-APD is divided into cells, which are separated by some dead space in between which is not sensitive. It is typically in the order of 30 % to 80 % [64].
- The quantum efficiency (QE) is the probability that a photon creates an electron hole pair in the depleted region of the G-APD. It depends on the layer structure of the device and the wavelength of the incoming photons.
- The trigger probability  $p_{\text{trigger}}$  is the probability, that the initial ionization triggers a Geiger discharge of the G-APD cell. It depends on the layer structure, the photon wavelength and the voltage which is applied to the diode [81].

The number of cells which would trigger without additional effects (such as saturation and crosstalk, see below) is often called “number of photons detected by the G-APD” or “photon equivalents”. It is denoted  $N_{\text{pe}}$  and is given by

$$N_{\text{pe}} = \text{PDE} \cdot N_{\gamma}. \quad (2.4)$$

The voltage dependence of the PDE is dominated by the trigger probability, which becomes one for large over-voltages, and has approximately the shape  $k(1 - e^{-V_{ov}/\alpha})$  (see figure 2.4). A detailed analysis shows that the saturation behavior of the trigger probability is wavelength dependent [82]. The PDE does not depend on the temperature [83].

The PDE depends strongly on the wavelength of the incoming photon. Depending on the layer structure, the peak wavelength is in the blue wavelength range for p-on-n structures (see figure 2.5) or in the green range for n-on-p structures.

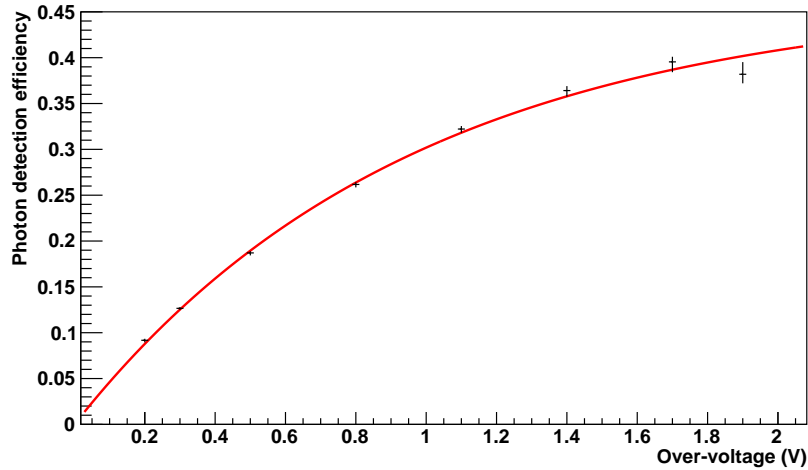


Figure 2.4.: Measured dependence of the PDE on the over-voltage for a Hamamatsu device with  $50\ \mu\text{m}$  cell spacing: the data points can be well fitted with an exponential saturation curve  $k(1 - e^{-V_{ov}/\alpha})$  with  $k = 0.47$  and  $\alpha = 0.96\ \text{V}$ . Plot based on my diploma thesis [67].

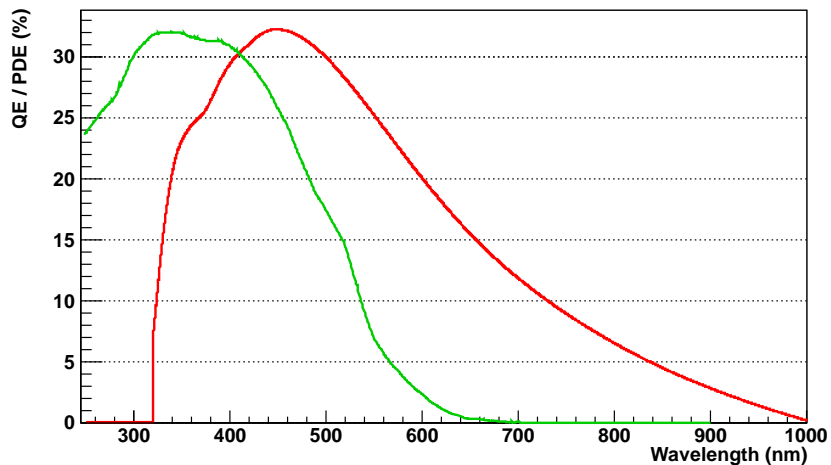


Figure 2.5.: Comparison of the quantum efficiency of the Hamamatsu R10408 PMT which is used in the MAGIC II telescope [84] (green, left curve) to the PDE of a G-APD (red, right curve). The G-APD values are taken from the manufacturer’s datasheet [64] and linearly scaled to match the measurement (see figure 2.4) at the standard operation voltage of  $1.1\ \text{V}$  at  $450\ \text{nm}$ . The original datasheet values “include effects of crosstalk and afterpulses”, resulting in an over-estimation of the PDE. Due to the peak wavelength range in the blue region, it can be concluded that Hamamatsu G-APDs are based on a p-on-n layer structure. While the values are comparable for those devices, recently developed G-APDs have peak PDE values  $> 50\%$  [85].

### 2.2.3. Saturation

The division of the sensor surface into cells, each of them operating in Geiger-mode, introduces a form of statistical saturation: if a light pulse contains several photons, more than one might arrive on the same cell and initiate the Geiger discharge. The signal of such a cell is identical to the case where the discharge is initiated by a single photon. The average number of initially triggered cells is approximately

$$N_0 = N_{\text{cells}} \left( 1 - e^{-\frac{N_{\text{pe}}}{N_{\text{cells}}}} \right) \quad (2.5)$$

See the section 2.4 for details.

### 2.2.4. Gain

The gain (released electron-hole pairs per Geiger discharge) of a G-APD depends linearly on the over-voltage:

$$G = \frac{C}{e} (V_b - V_{\text{bd}}) = \frac{C}{e} V_{\text{ov}} \quad [74], \quad (2.6)$$

where  $e$  is the elementary charge. This linear behavior can be explained with a simple model: the depleted region separates charges and forms a capacitance which is charged at the bias voltage. The total charge of the capacitance is hence  $Q_C = C \cdot V_b$ . When the cell is triggered, charge carriers are exchanged in the avalanche between the cathode and the anode, until the voltage drop over the quenching resistor lowered the voltage over the diode down to the breakdown voltage. The charge in the capacitance is then  $Q_C = C \cdot V_{\text{bd}}$ , so the charge needed to refill the capacitance is  $Q = C(V_b - V_{\text{bd}})$ .

The capacitance depends on the cell size and the width of the depletion region. It has a small dependence on the temperature of about 0.1% increase per degree at constant over-voltage [83].

### 2.2.5. Equivalent circuit and pulse form

There are various descriptions of G-APDs as an equivalent circuit (see figure 2.6). Most are based on the model above, with some variations in the number and size of stray capacitances (see e.g. [86, 87]). The pulse form which is observable outside the device consists of a fast rising edge and a pulse decay which is often described by one or two exponential functions.

### 2.2.6. Dead time and cell recovery

After the Geiger discharge of a cell, the capacitance needs to be recharged. The recharging is basically an exponential process, in which the voltage over the diode is reestablished. During this process, the PDE and the gain are reduced according to the above-mentioned dependencies on the over-voltage.

Several measurements suggested that the cell does not start immediately with recharging, but only after some dead time. This would imply that the voltage over the diode  $V_d$  goes below the breakdown voltage. This was reproduced in various simulations, e.g. the one by H. Otono *et al.* [86] (see figure 2.7). In their simulation, “the avalanche process is terminated due to the internal physics: charge transportation, impact ionization and circuit equation”.



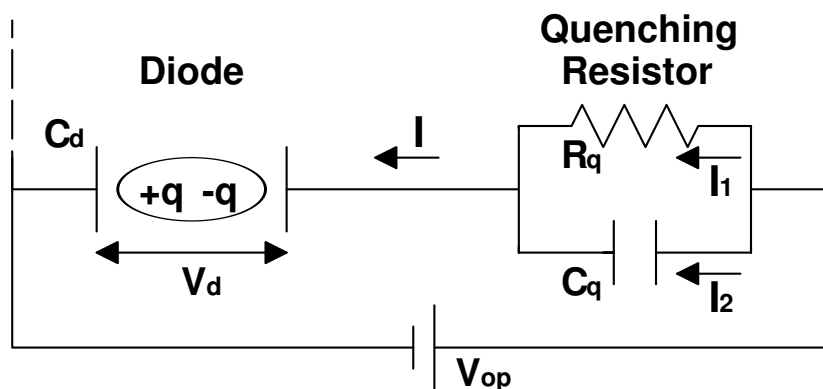


Figure 2.6.: Model for the equivalent circuit of a G-APD: the diode capacitance  $C_d$  is charged by the diode voltage  $V_d$ . In this model, the quenching resistor  $R_q$  has a parallel quenching capacitance  $C_q$ , which changes the waveform of the resulting G-APD signal. Figure from [86].

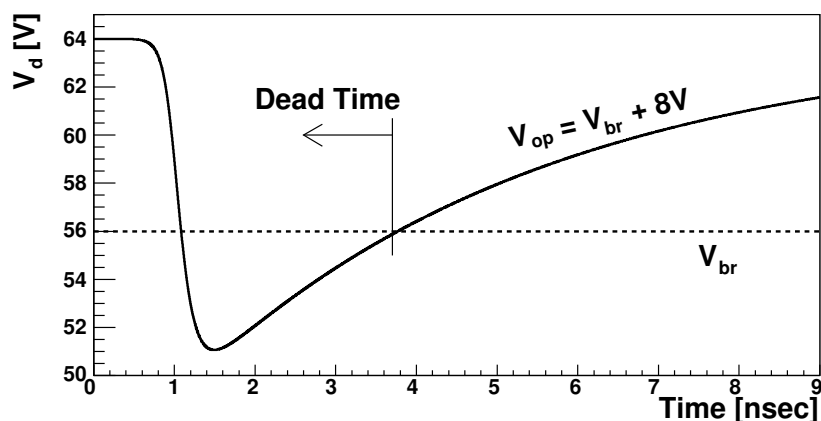


Figure 2.7.: In some models, the voltage over the diode  $V_d$  drops below the breakdown voltage  $V_{bd}$ , which results in a dead time where the cell is completely insensitive. As soon as the diode voltage is above the breakdown voltage, the diode exponentially restores its PDE and may trigger again. Figure from [86].

The time constant of the exponential recharging process is dominated by the quenching resistor and cell capacitance:  $\tau \approx R_q C$ . The time constant is independent of the over-voltage [88].

### 2.2.7. Crosstalk

During the Geiger discharge in the multiplication layer of the G-APD, optical and infrared photons are created in the avalanche region: per  $10^5$  charge carriers, on average 2.9 photons with an energy above 1.14 eV are created [89]. Such photons may propagate to a neighboring cell and trigger it, an effect called (optical) crosstalk. See e.g. A. N. Otte [90] for more details.

Due to crosstalk, a single external photon may trigger two or even more cells instead of one, which introduces an additional statistical uncertainty to the output signal of a G-APD. The crosstalk probability  $p_{ct}$  is defined as the probability that one or more additional cells are triggered if initially exactly one cell is triggered<sup>(4)</sup>. The average number of cells triggered by crosstalk is denoted  $\mu_{ct}$ . The statistical properties of crosstalk were studied in the course of this thesis and found to dominate the noise behavior for our devices (see section 2.4.4).

The temperature dependence of the crosstalk probability was investigated in the course of my diploma thesis, and no dependence was found [67]. However, there is a strong dependence on the over-voltage (see section 2.3.2).

### 2.2.8. Dark counts

A G-APD cell can also be triggered by charge carriers which are thermally generated or by tunneling. The thermal component doubles for every 8 °C, whereas the tunneling component is independent of the temperature [74]. Compared to other photosensors, the dark count rate of G-APDs is high, with values around some 100 kHz per mm<sup>2</sup> of sensitive area [64]. Note that for our application, this dark count rate is negligible during the operation of the telescope camera, since the diffuse photon rate from the night sky is much larger (see section 3.2.1).

### 2.2.9. Afterpulses

During the Geiger discharge of a G-APD cell, charge carriers can be trapped in the silicon and released with some delay, when the initial discharge was already quenched. These delayed carrier releases may trigger the cell again, which is called afterpulsing. The time distribution of these delayed releases I measured in the course of my diploma thesis and is exponentially decreasing after the initial pulse (see figure 2.8). The measured distributions are usually described by two components, in the case of my measurement with time constants  $(50 \pm 6)$  ns and  $(138 \pm 22)$  ns. A more detailed analysis of afterpulses including the dependence on the over-voltage was made in [87]. It is important to note that charge carriers released too shortly after the initial pulse are lost due to the dead-time of the cell, or have a reduced amplitude due to the cell recovery (see previous section 2.2.6).

---

<sup>4</sup>Often this is considered equivalent to the ratio of the dark count rate with a threshold of 1.5 p.e. by the rate at 0.5 p.e. This definition requires low noise in the measurement, since otherwise the rate at 1.5 p.e. contains events with only one triggered cell and vice versa. Further the dead-time of the rate measurement must be precisely known to get the actual event rates from the measured rates.

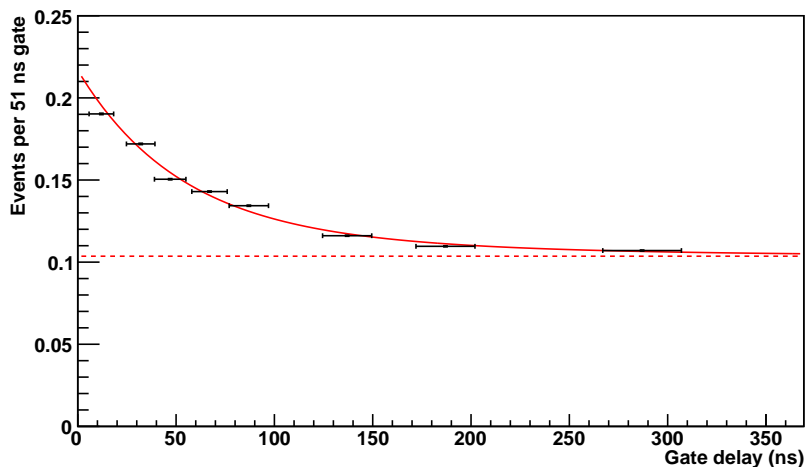


Figure 2.8.: Measurement of afterpulses: after an initial pulse, the probability for a second pulse within a delayed gate was measured: the afterpulses cause an increased probability shortly after the initial pulse, the dotted line marks the dark counts. The red line is a fitted sum of two exponentials, the resulting time constants are  $(50 \pm 6)$  ns and  $(138 \pm 22)$  ns. Plot from my diploma thesis [67].

### 2.3. Measurements of G-APD properties

The measurements described in this section were performed in the design phase of the FACT project. They served as a basis for the decision on the G-APD type to be used and were implemented both in the telescope simulation and the simulation used for the design of the light-collecting cones. Most measurements I carried out in the laboratory of D. Renker at the Paul Scherrer Institute (PSI)<sup>(5)</sup>. Many characteristics of G-APDs were previously measured in the course of my diploma thesis [67].

For the measurement, the G-APDs were mounted on a low-noise amplifier in a light-tight box which was electro-magnetically shielded. Its signal was further amplified and shaped in a ORTEC Timing Filter Amplifier and recorded with a LeCroy WaveRunner 64Xi oscilloscope. The implemented "Area" function of the oscilloscope was used for the integration [91].

For most measurements the dark counts of the G-APDs were used. Only for the angle dependence measurement, a light pulser was used (see section 2.3.6). All measurements were made with Multi-Pixel Photon Counter (MPPC) from Hamamatsu<sup>(6)</sup>. The two versions used had square cells with side lengths of 50  $\mu\text{m}$  and 100  $\mu\text{m}$ , respectively, both with a chip size of  $3 \times 3 \text{ mm}^2$ .

#### 2.3.1. Geometrical properties

For most commercial devices available during the FACT design phase, the sensitive chip is embedded in a metallic or ceramics package and coated with an epoxy resin. For the devices from Hamamatsu with a chip size of  $3 \times 3 \text{ mm}^2$ , the size of the ceramics package, the position of the chip within the package and the surface profile of the epoxy was measured (see figure 2.9).

<sup>5</sup>Paul Scherrer Institute, 5232 Villigen PSI, <http://www.psi.ch>.

<sup>6</sup>Hamamatsu Photonics K.K., Japan, <http://www.hamamatsu.com>.

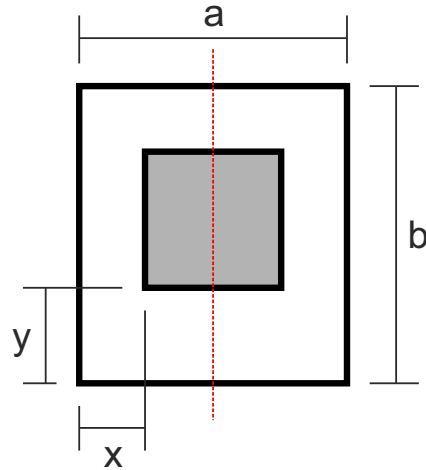


Figure 2.9.: Overview of the geometry measurements of G-APDs: the package size ( $a, b$ ) and the position of the chip within the package ( $x, y$ ) were measured. The dashed (red) line shows the position of the surface profile measurement.

### Package size

The size of the ceramics package is  $a \times b = (5.90 \pm 0.15) \times (6.55 \pm 0.15) \text{ mm}^2$  according to the data sheet [64] provided by the manufacturer. For a sample of 29 pieces the package was measured with a digital caliper with a precision of 0.005 mm. The mean package size of this sample was  $(5.905 \pm 0.020) \times (6.553 \pm 0.017) \text{ mm}^2$  in accordance with the data sheet values. The spread was much smaller than specified, facilitating the design of the tools for the camera construction.

### Chip position

As with the surface curvature, also the position of the chip within the ceramics package is of importance: if the light guide is not perfectly aligned with the chip, the relative light loss is in first order proportional to the displacement. The position of the chip within the package was measured relatively to a corner of the package (see figure 2.9).

The measured distances were  $x = 1.14 \text{ mm}$  and  $y = 1.84 \text{ mm}$ . The standard deviation of the measurement was  $45 \text{ }\mu\text{m}$ , with maximal deviations from the mean value up to 0.1 mm. If a light guide is off by that distance, we lose approximately  $100/3000 = 3.3\%$  of the light just from the displacement. The consequence for the construction is that the position of the cones cannot be fixed to the ceramics package, but has to be adapted individually to each G-APD.

### Surface profile

Knowledge on the geometrical surface curvature of the devices is a necessity if any form of light guide is mounted on the sensor. This may be a scintillating crystal as for PET applications (as e.g. in the AX-PET project [92]), or, as in our case, light-collecting cones. The geometry is both important for the simulation of the light transmission and the mechanical contact of mounted cones.

Two different methods were used to measure the surface curvature: the first method was

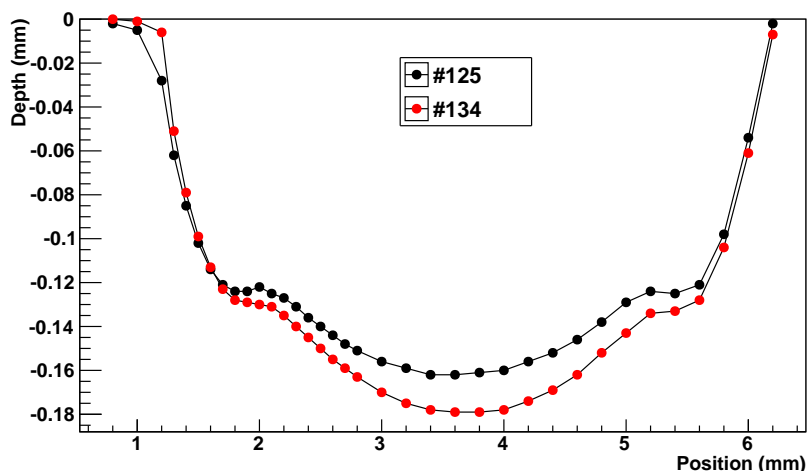


Figure 2.10.: Surface profile of two Hamamatsu MPPCs of type S10362-33-050C (ceramics package). 0 mm is at the height of the ceramics package. A flatter profile is expected for the SMD version of the device.

to scan the surface with a solid sphere of radius 5 mm. This rather crude method leads of course to offsets in non-horizontal areas. The more precise second method was to use a microscope with an x-y table. To determine the z-component, the microscope was focused onto the center of the field of view of the microscope which was denoted with cross-hairs. Since the surface of G-APDs consists of a transparent epoxy layer, a black line was drawn onto the surface with a non-permanent marker. The location of the measured profiles can be seen in figure 2.9.

The measurements results are shown in figure 2.10. The surface of the epoxy is 0.15 mm to 0.18 mm lower than the edge of the ceramics package. The central region of the G-APD above the sensitive area (innermost 3 mm) is not flat, the center is 0.04 mm to 0.05 mm lower than at the edge.

This behavior is not surprising due to the surface tension of the protective layer. The measured profiles were used to estimate the necessary amount of glue for the contact to the optical light guides (see section 3.4.1). A flatter surface can be expected from SMD versions<sup>(7)</sup>, since the epoxy is not filled into ceramic boxes but distributed over a flat area which is cut into the single devices after the hardening.

### 2.3.2. Voltage dependence of gain and crosstalk probability

The linearity of the gain with the over-voltage is one of the most basic and most important properties of G-APDs. The crosstalk probability is the product of several factors, most importantly the number and positions of the emitted photons and the photon detection efficiency of the adjacent cells. If we assume that the distribution of the emission points is independent of the over-voltage, the number of photons arriving at a neighboring cell is proportional to the number of emitted photons. This number is proportional to the charge released in a cell breakdown, i.e. the gain [89]. The probability that one of these photons triggers the cell correlates with the PDE.

Since both gain and PDE depend on the over-voltage, also the crosstalk depends on it. In a simple measurement the dark counts at various operation voltages was recorded for

<sup>7</sup>Surface Mount Device (SMD). The G-APD chip is attached to a piece of conductor board and has no ceramics package.

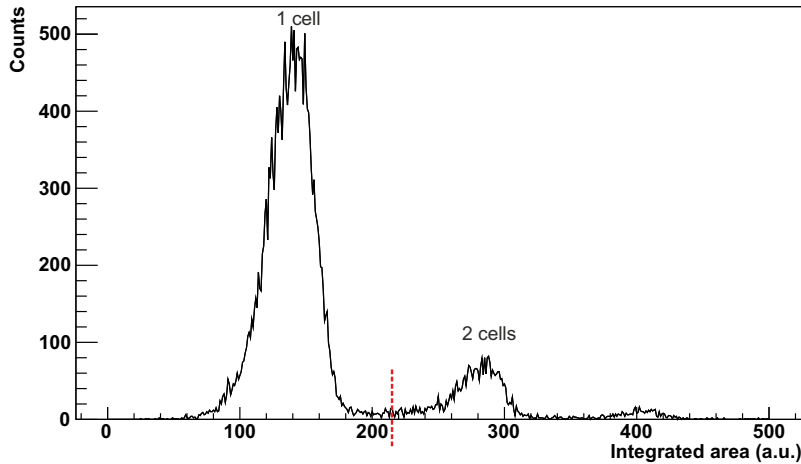


Figure 2.11.: Example of a dark counts spectrum: the readout is triggered on dark counts of the G-APD and the pulse integrated in a time window of 6 ns around the peak. The dashed line (red) shows the cut for the determination of the crosstalk probability, which is the number of events on the right side of the cut divided by the total number of triggered events. The plot shows data from the gain/crosstalk measurement of a Hamamatsu device with a cell spacing of 50  $\mu\text{m}$  at an over-voltage of 1.5 V, where the crosstalk probability is 14.7 %. The standard over-voltage is around 1.1 V with a crosstalk probability of  $\sim 10\%$ .

Hamamatsu devices with 50  $\mu\text{m}$  and 100  $\mu\text{m}$  cell spacing and a histogram of the charge in an integration window of 6 ns length recorded (see figure 2.11). The gain is proportional to the distance between the peaks in the spectrum. A cut was applied between the peaks corresponding to one and two cells in the spectrum. The crosstalk probability is the number of events to the right of the cut divided by the total number of recorded events (see my diploma thesis [67] for more details on the measurement principle).

The measurement confirmed the expectation of the linear dependence of the gain on the over-voltage (see figure 2.12). For the crosstalk probability (figure 2.13), the measured dependence on the over-voltage can be well fitted with a quadratic polynomial which is fixed at 0 for both devices:  $p_{\text{ct}} = a \cdot V_{\text{ov}} + b \cdot V_{\text{ov}}^2$ . The fit parameters are  $a = 0.035$ ,  $b = 0.044$  for the 50  $\mu\text{m}$  devices and  $a = 0.076$ ,  $b = 0.224$  for the 100  $\mu\text{m}$  devices, respectively.

### 2.3.3. Measurement of the average number of cells triggered by crosstalk

From the same dataset that was used in the previous section, the average charge per dark count including crosstalk can be determined: if we neglect saturation effects (which we can do in good approximation since we only use a handful of the 3600 cells), the average number of triggered cells  $\tilde{N}$  for one initial cell is  $\tilde{N} = 1 + \mu_{\text{ct}}$ .

From a charge spectrum as the one in figure 2.11, the average charge can be extracted as follows:

- We start by determining the positions of the peaks corresponding to one and two triggered cells by fitting Gaussian curves to the data. The two positions are denoted with  $q_1$ ,  $q_2$ , respectively.
- The difference is proportional to the gain of the G-APD at this voltage.
- We now read the full histogram  $(\tilde{q}_i, k_i)$  where  $\tilde{q}_i$  is the bin center and  $k_i$  the number of entries. The charge in this bin is normalized to the gain and summed up using

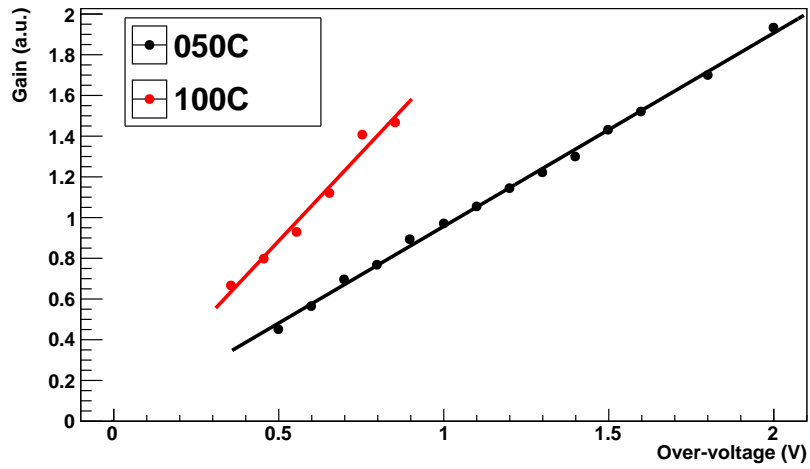


Figure 2.12.: Gain versus over-voltage for devices with 50  $\mu\text{m}$  (black, Hamamatsu S10362-33-050C) and 100  $\mu\text{m}$  cell spacing (red, Hamamatsu S10362-33-100C), respectively. The lines show linear fits to the data points.

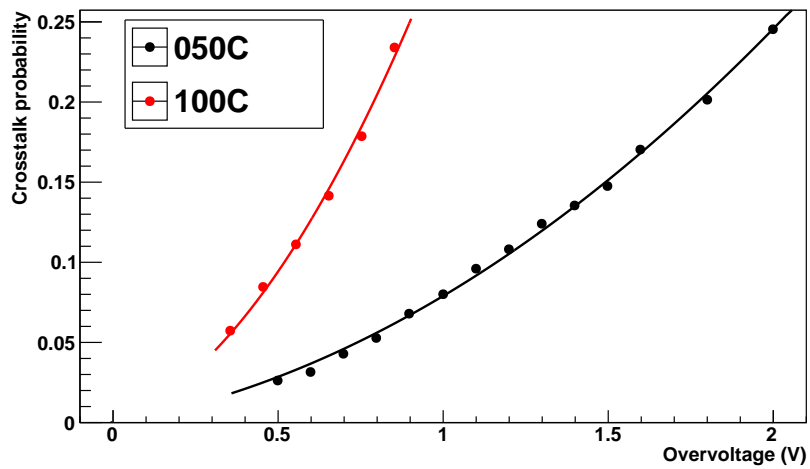


Figure 2.13.: Crosstalk probability for varying over-voltage for devices with 50  $\mu\text{m}$  (black) and 100  $\mu\text{m}$  (red) cell spacing, respectively. The lines show quadratic fits fixed at (0/0).

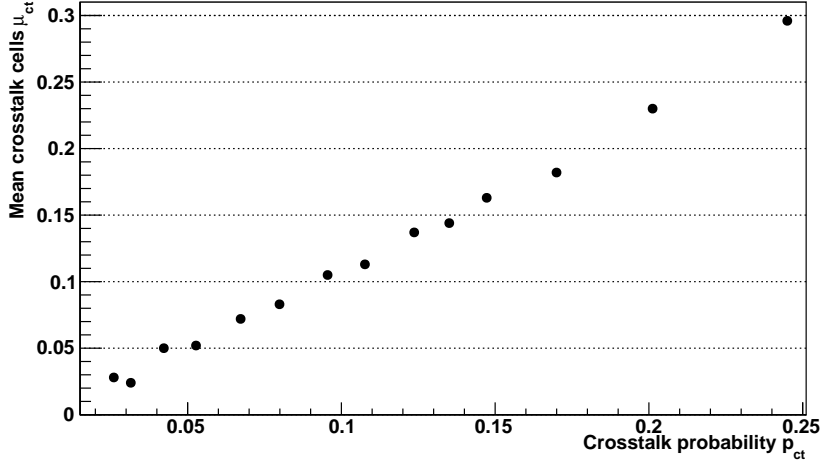


Figure 2.14.: Average number of cells triggered by crosstalk  $\mu_{ct}$  vs. crosstalk probability  $p_{ct}$ . The average number of triggered cells is of course slightly larger than the crosstalk probability, since one *or more* cells are triggered. The G-APD used for this measurement has a cell spacing of  $50 \mu\text{m}$ .

the weights of the number of entries:

$$\tilde{N} = N_0 + N_{ct} = \frac{1}{\sum k_i} \sum_i k_i \left( 1 + \frac{\tilde{q}_i - q_1}{q_2 - q_1} \right) \quad (2.7)$$

$$\approx 1 + \mu_{ct} \quad (2.8)$$

We can now plot  $\mu_{ct}$  versus the crosstalk probability  $p_{ct}$  (see figure 2.14). The dependence is approximately linear in this probability range.

### 2.3.4. Avalanche fluctuations (peak widths)

#### Expectation

The width of the peaks in a pulse spectrum is determined by the noise of the electronics and the variations in the charge which is released in the avalanche. The standard deviation of the width of the peak corresponding to  $n$  cells is expected to be

$$\sigma_n^2 = \sigma_{ped}^2 + n \cdot \sigma_{av}^2, \quad (2.9)$$

where  $\sigma_{ped}$  is the width of the pedestal peak, and  $\sigma_{av}$  corresponds to the variation in the charge released in one avalanche. If the variations in the released charge were correlated, the peak widths would add up as follows:

$$\sigma_{n,correlated}^2 = \sigma_{ped}^2 + n^2 \cdot \sigma_{av}^2, \quad (2.10)$$

#### Measurement

The pulsed light source was used to produce a Poisson spectrum of triggered cells, with about  $\mu = 5.5$  cells triggered on average. Peaks up to 13 triggered cells could be distinguished. A sum of 14 Gaussian peaks was fitted to the data and the peak widths noted. The fitting was made using the program “fityk” [93] using a superposition of “GaussianA” functions which optimize the area.



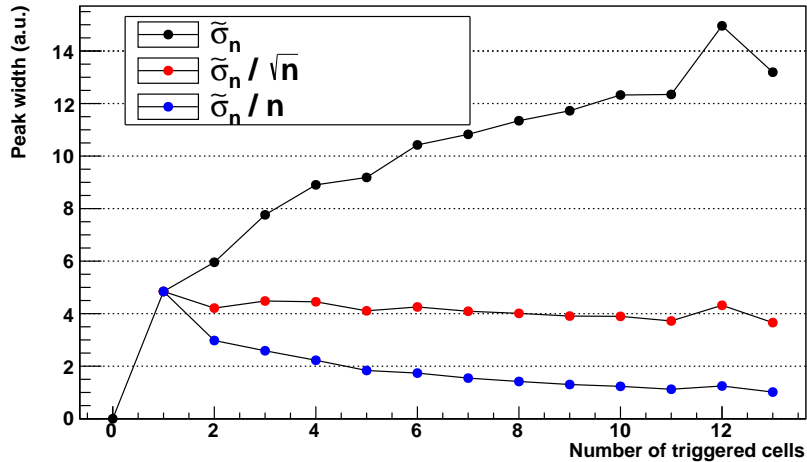


Figure 2.15.: Charge variations for 1-13 triggered cells (black). The contribution of the pedestal  $\sigma_{\text{ped}}$  was (quadratically) subtracted. The corrected peak widths are divided by  $\sqrt{n}$  (red) and  $n$  (blue), where  $n$  is the number of triggered cells. Only the division by  $\sqrt{n}$  leads to constant values, thus confirming our expectation.

Figure 2.15 shows the widths of the peaks with the pedestal subtracted, i.e.  $\tilde{\sigma}_n = \sqrt{\sigma_n^2 - \sigma_{\text{ped}}^2}$ . The measurement confirms the expectation according to formula (2.9), i.e. the fluctuations in multiple cells are not correlated. The measurement also allows to determine  $\sigma_{\text{av}}$  by dividing the peak width by the gain (peak difference) of the measurement: the relative value of the avalanche fluctuations is  $\sigma_{\text{av}} \approx 10\%$ .

### 2.3.5. Dependence of avalanche fluctuations on the over-voltage

For this measurement, the same setup as in the previous section was used. A Poisson spectrum for a range of operation voltages was created and the peak widths and positions of the pedestal and the one-cell peak determined. The relative amount of avalanche fluctuations is given as

$$\sigma_{\text{av,rel}} = \frac{\sigma_{\text{av}}}{x_1 - x_0} = \frac{\sqrt{\sigma_1^2 - \sigma_0^2}}{x_1 - x_0}, \quad (2.11)$$

with  $x_0, x_1$  and  $\sigma_0, \sigma_1$  the positions and standard deviations of the pedestal and one-cell peak, respectively.

The measurement was made for 13 voltages between 0.2 V and 1.6 V over-voltage. The relative avalanche fluctuations are decreasing for rising over-voltage down to a value of  $\sigma_{\text{av}} = 12\%$  at an over-voltage around 1.1 V to 1.2 V (see figure 2.16). Within the measurement error this is in agreement with the value  $\sigma_{\text{av}} = 10\%$  stated in section 2.3.4.

### 2.3.6. Angle dependence of the PDE

Typically, measurements of the PDE are made with light which arrives perpendicular to the surface. For PMTs, the PDE depends both on the angle and the position on the photocathode [70]. Both properties are important for the design of the light guides. In the case of G-APDs, the homogeneity of the PDE over the area was reported e.g. in P. Eckert *et al.* [94], while I measured the angular dependence of G-APDs in a setup by D. Renker at PSI. The results were first published at the PD09 conference [95].

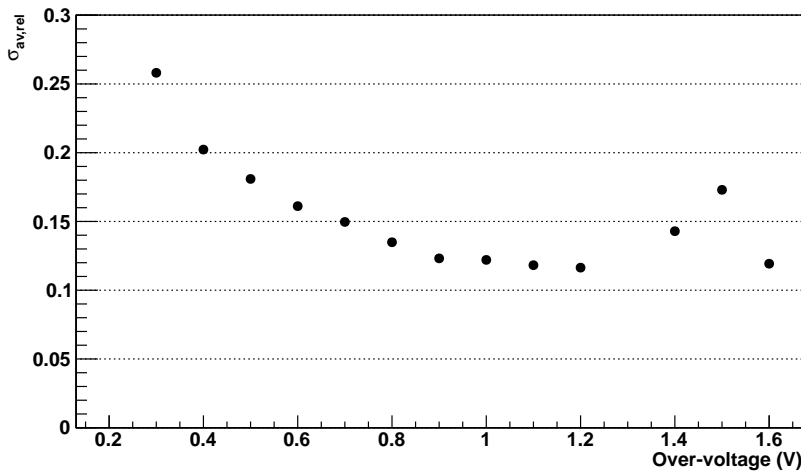


Figure 2.16.: Dependence of the avalanche fluctuations on the over-voltage:  $\sigma_{av}$  divided by the gain (i.e. the relative avalanche fluctuation) shows a minimum at the operation voltage around 1.1 V.

### Expectation

The angle dependence of the PDE is the product of a number of effects. The first important effect are surface Fresnel reflections. The amount of these reflections is a function of the refractive indices of the two materials at the boundary  $n_1$  and  $n_2$  (air and silicon in our case) and the incidence angle  $\alpha$ . Since the transmitted light is bent towards smaller angles according to Snell's law, an additional angle dependence is expected if the quantum efficiency or the trigger efficiency depend on the depth in the chip: photons impinging at an angle  $\alpha$  are refracted to an angle

$$\alpha' = \arcsin[\sin(\alpha) \cdot n_1/n_2] \quad (2.12)$$

which is smaller than  $\alpha$  for  $n_2 > n_1$ .

The layers and their exact refractive indices are usually subject to restrictive information policies of the manufacturers and thus not well known. For our devices, it was confirmed by the manufacturer that there is an insulation layer with a refractive index around 2 at the surface [96]. The refractive index  $n$  of intrinsic silicon is  $n > 4$  in the range 300 nm to 500 nm [80]. In between an additional layer of silicon oxide with a refractive index around 1.5 is expected [85].

Photons impinging at a large angle of  $\alpha = 85^\circ$  on the chip from air ( $n_1 = 1$ ) are refracted to an angle of  $\alpha' = 29.9^\circ$  for  $n_2 = 2$ . The entrance depth is thus only reduced by  $1 - \cos(\alpha') = 13.3\%$  compared to perpendicular light. For  $n_2 = 4$  (silicon), the effect is even smaller (3.2%). Based on this estimate, no additional angle dependence of the PDE is expected.

### Setup

The G-APD and the low-noise amplifier were installed on a pivotable mount (see figure 2.17). The center of the sensitive area was adjusted to the rotation center. A commercial LED light pulser<sup>(8)</sup> which emits light pulses with a duration of 1 ns was used. The metal sides of the box were covered with black paper to reduce reflections. The light pulser

<sup>8</sup>HORIBA Jobin Yvon NanoLED, <http://www.horiba.com>.

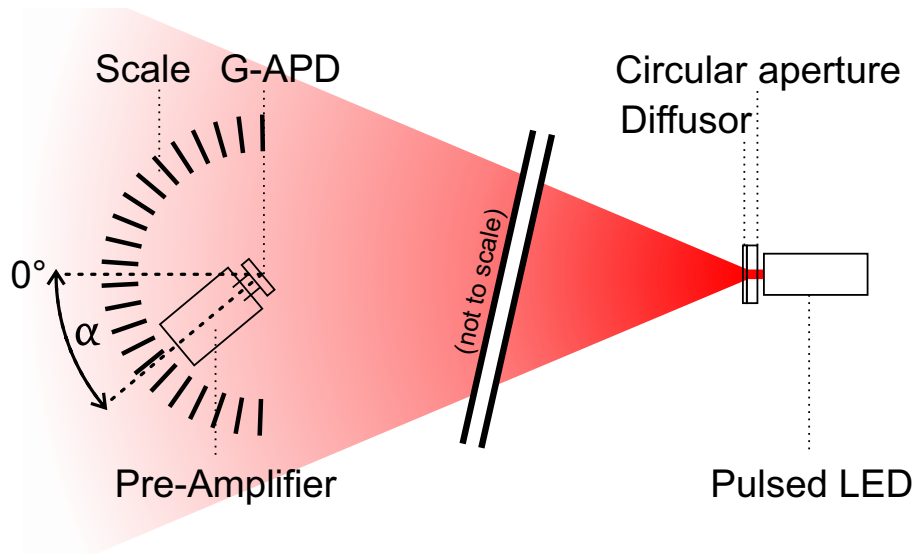


Figure 2.17.: Setup for the angle dependence measurement: a G-APD is homogeneously illuminated with a pulsed LED. The angle of the G-APD relative to the light beam can be adjusted. The distance between the diffuser and the G-APD is  $> 40$  cm, so the direction of the photons at the G-APD is approximately parallel.

contained an internal clock generator which was used to trigger both the light pulser and our readout system. This allowed to trigger the readout also if no photon was detected by the G-APD, and thus to record the Poisson spectrum of the light pulses.

The light of the LED pulser was collimated using a circular aperture with a diameter of 1 mm and then diffused such that the area of the sensor was homogeneously illuminated. To avoid alignment effects the illuminated area was much larger than the sensor. The distance between the diffuser and the G-APD is  $> 40$  cm, so the beam is approximately parallel: if the light source is assumed point-like at the diffuser, the maximal angle between of photons at the G-APD to the perpendicular direction is  $\arcsin(0.5 \times d/400 \text{ mm}) = 0.2^\circ$ , where  $d$  is the width of our sensor (3 mm).

### Analysis method

The number of photons arriving at the surface of the G-APD per pulse follows a Poisson statistics. If we neglect saturation and crosstalk, also the probability that exactly  $i$  cells are triggered is Poissonian, i.e.

$$p_i = \frac{\mu^i e^{-\mu}}{i!}. \quad (2.13)$$

$\mu$  is the average number of triggered cells, i.e. the number of photons multiplied by the PDE:  $\mu = N_\gamma \cdot \text{PDE}$ . Saturation and crosstalk change these probabilities for  $i \neq 0$ : the probabilities are shifted to higher values by crosstalk and reduced by saturation. Since  $p_0$  is not changed, it is thus possible to calculate  $\mu$  if  $p_0$  is known:

$$\mu = -\ln(p_0) \quad (2.14)$$

The number of photons is proportional to the intensity of the light flash and the perpendicular projection of the sensitive area to the beam direction. Including the angle dependence of the Fresnel transmission at the chip surface and a potential angle dependence of the G-APD, the average number of measured photons  $\mu$  per pulse at an angle  $\alpha$

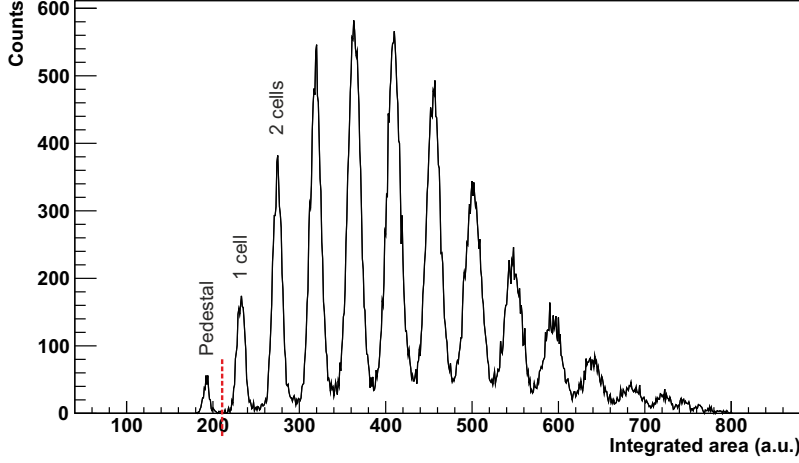


Figure 2.18.: Example of a Poisson spectrum. The plot shows data from the angle dependence measurement at  $0^\circ$ . The dashed line (red) is the cut necessary for the determination of the number of events in the pedestal: on the left of the cut are the pedestal events, to the right of the line the events where one or more G-APD cells triggered.

is

$$\mu(\alpha) = \underbrace{I}_{\text{Beam intensity}} \cdot \underbrace{A \cdot \cos(\alpha)}_{\text{Projected sensitive area}} \cdot \underbrace{F(\alpha)}_{\text{Fresnel transmission}} \cdot \underbrace{\text{AD}(\alpha)}_{\text{G-APD angle dependence}} \quad (2.15)$$

To ensure that the intensity of the LED pulses was constant during the measurement, the same angles were measured both at the beginning and the end of the measurement series and the resulting values compared.

The measurement errors are on one hand the statistical errors on the measured numbers. On the other hand we have a systematic error since our pedestal is not Gaussian due to random dark counts, and also because there may be spill-over of events at the cut. An estimate on the systematic error in the determination of  $\mu$  is made by calculating  $p_0$  for  $(1 \pm k)N_{\text{ped}}$ , with  $k$  the estimate on the systematic error of the cut:

$$\mu_{\text{systematic}} = -\ln((1 \pm k) \cdot N_{\text{ped}}/N_{\text{tot}}) = \mu - \ln(1 \pm k) \approx \mu \mp k \quad (2.16)$$

The approximation is valid for small  $k$ .  $N_{\text{ped}}$  and  $N_{\text{tot}}$  have a Poissonian error, so the total error on  $\mu$  is

$$\Delta\mu = \sqrt{\left(\Delta N_{\text{ped}} \frac{\partial\mu}{\partial N_{\text{ped}}}\right)^2 + \left(\Delta N_{\text{tot}} \frac{\partial\mu}{\partial N_{\text{tot}}}\right)^2} + k \quad (2.17)$$

$$= \sqrt{\frac{1}{N_{\text{ped}}} + \frac{1}{N_{\text{tot}}}} + k \quad (2.18)$$

$k$  corresponds to the correction for the non-Gaussian pedestal, i.e. the fact that random triggers also might contain a dark count. In P. Eckert *et al.* [94], it corresponds to the term  $\ln\left(\frac{N_{\text{ped}}^{\text{dark}}}{N_{\text{tot}}^{\text{dark}}}\right)$  of equation (2).

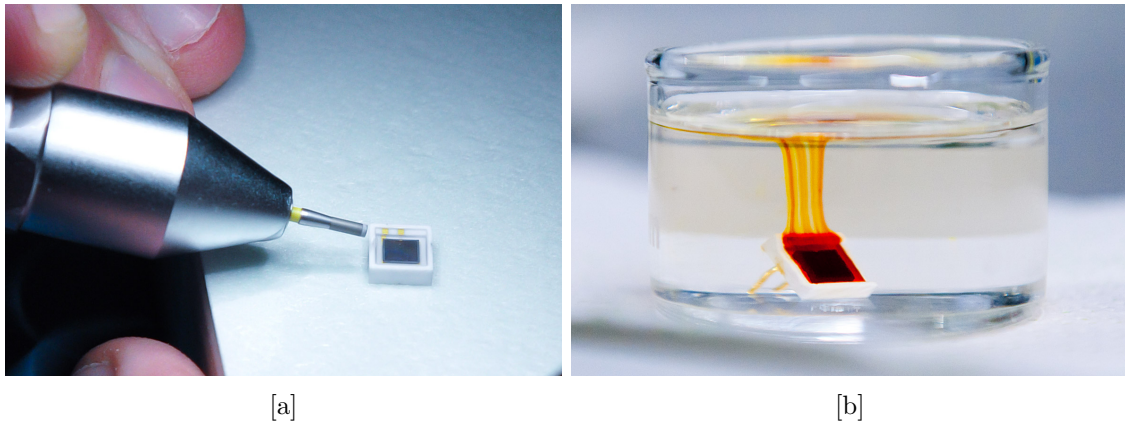


Figure 2.19.: Preparation of the G-APD for the angle dependence measurement: [a] The sides of the ceramics package were removed using a dental drill. [b] The epoxy on the surface was dissolved in sulfuric acid to expose the bare chip.

### Method

We wanted to measure the angle dependence of the bare G-APD chip without the influence of the protective Epoxy layer and the package shadow. The ceramics package was removed at the sides with a dental drill<sup>(9)</sup>.

The Epoxy layer was dissolved in concentrated sulfuric acid, afterwards the chip was washed with distilled water. See figure 2.19 for photos of these two steps. Great care was taken that the chip surface is only exposed to the acid for as short as possible. The dark current and the PDE for perpendicular light were measured before and after the procedure and were identical within the measurement precision.

About 70000 to 100000 events are taken per position. The positioning precision of the angle was about  $1^\circ$ , with a small systematic offset  $\alpha_0$  of unknown size which can be estimated by the symmetry of the measurement.

The measured values can be found in table 2.1 and figure 2.20. A function was fitted to the data which included the angular dependence and Fresnel transmission for unpolarized light. The open parameters were the refractive index of the material, the systematic offset of the angle  $\alpha_0$  and an intensity constant. When dividing the data by  $\cos(\alpha - \alpha_0)$  to get rid of the geometric projection, only the Fresnel transmission and the potential angular dependence of the G-APD remains (see figure 2.21).

### Results / discussion

When all data points are included, the fit yields a systematic offset of  $\alpha_0 = (1.0 \pm 0.3)^\circ$  and a refractive index of  $n = 2.3 \pm 0.3$  with a reduced  $\chi^2$  of 1.1. The systematic offset is as expected. The fitted refractive index is consistent with the information by the manufacturer. Having  $\chi^2$  close to one indicates that there is no additional angle dependence of the G-APD besides the Fresnel reflections at the chip surface.

The two values at large angles (around  $\pm 85^\circ$ ) are significantly larger than the expectation (see figure 2.21). This may have two reasons: first the light is not fully parallel, which results in slightly more light at large angles, and second a systematic deviation towards smaller angles of around  $1^\circ$  can be explained by the mechanical force from the readout

<sup>9</sup>Many thanks to Silvan Streuli (PSI) for his help in this step.

Angle ( $^{\circ}$ )	$N_{\text{tot}}$	$N_{\text{ped}}$	$\mu$	$\Delta\mu$
0	70177	352	5.295	0.063
10	70857	421	5.126	0.059
-10	73615	441	5.118	0.058
-20	70548	591	4.782	0.051
20	70188	508	4.928	0.055
30	88563	1032	4.452	0.041
-30	75753	902	4.431	0.043
-40	77221	1692	3.821	0.035
40	76706	1521	3.921	0.036
50	73323	2717	3.295	0.030
-50	71589	3224	3.100	0.028
-60	78530	8267	2.251	0.022
60	88344	7321	2.490	0.022
70	102774	21408	1.569	0.018
-70	76630	19351	1.376	0.018
-75	97192	37422	0.954	0.016
75	73932	23913	1.129	0.017
80	83687	40295	0.731	0.016
-80	99100	57176	0.550	0.015
-85	94456	73623	0.249	0.015
85	85246	56679	0.408	0.015

Table 2.1.: Measured values of the angle dependence measurement:  $N_{\text{tot}}$  is the total number of registered events,  $N_{\text{ped}}$  were pedestal events with no photon triggering a cell. The value  $\mu$  is a measure on the sensitivity of the G-APD at this angle (see equation (2.15)).

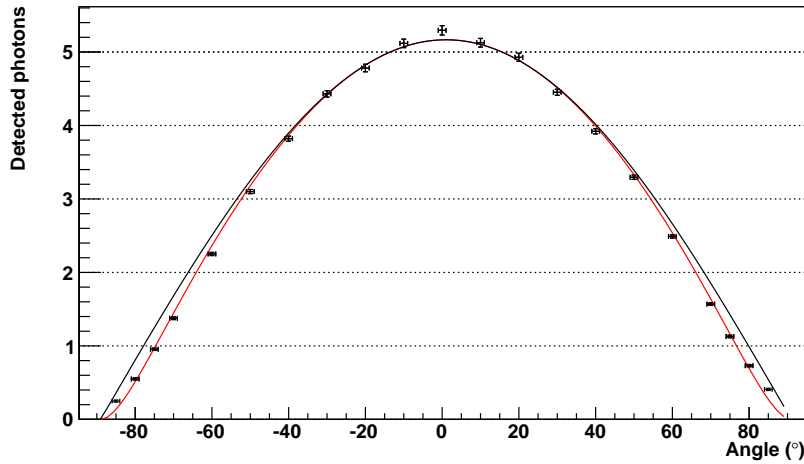


Figure 2.20.: Plot of the values in table 2.1. The number of detected photons  $\mu$  decreases with the cosine of the angle since the area rectangular to the photon beam decreases. A function combining the geometric effect and Fresnel transmission was fitted to the data (red), yielding a refractive index of the surface material of  $2.3 \pm 0.3$ . If only the geometric dependence is plotted (black), the data points do not match for large angles.

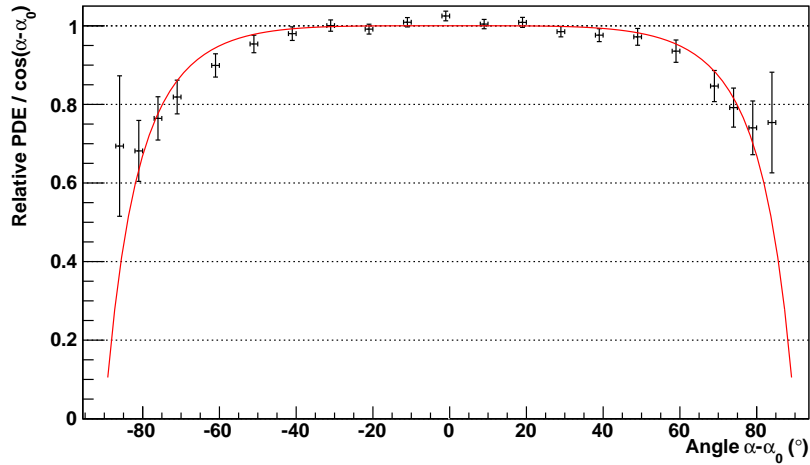


Figure 2.21.: When the geometric dependence and the intensity constant are eliminated, only the Fresnel transmission (red curve) and a potential angular dependence of the G-APD remain. Since the measurement matches the angle dependence of Fresnel reflections within the measurement error, no additional angle dependence of the G-APD is assumed.

cables attached to the setup. If the two data points are omitted in the fit, the resulting parameters are  $\alpha_0 = (1.0 \pm 0.3)^\circ$  and  $n = 1.9 \pm 0.4$  with a reduced  $\chi^2$  of 0.73.

As a summary, the angular dependence of a G-APD was measured and tested for effects additional to surface Fresnel reflections. The measurement was consistent with Fresnel transmission of a material with refractive index  $n = 2.3 \pm 0.3$ , so no angle dependence of the PDE of G-APDs was found. This means in particular that there are no additional losses at large incidence angles, which is of particular interest in our case: if light-collecting cones are placed on the G-APD, a large fraction of photons impinges on the surface at large angles  $> 60^\circ$ . The result of this measurement was included in the optical simulation by I. Braun (ETH Zurich), which was used to design the cones for the FACT project.

## 2.4. Mathematical modeling of the response

A simplified calculation of the number of triggered cells for light pulses including effects of crosstalk and saturation was presented in my diploma thesis [67]. The principle is as follows (see figure 2.22 for an overview):

1. A certain number of photons  $N_\gamma$  arrive on the surface of the G-APD.
2. If every photon would arrive in a different cell, they would initially trigger  $N_{pe} = \text{PDE} \cdot N_\gamma$  cells.  $N_{pe}$  is called “number of photons detected by the G-APD” or number of “photon equivalents”.
3. Since this is not the case, they only trigger  $N_0$  cells on average, where  $N_0$  is a function of the total number of cells  $N_{\text{cells}}$  and  $N_{pe}$  according to the equations (2.23) and (2.24) (see below). We denote this function  $S(N, N_{\text{tot}})$ .
4. Every of these effectively triggered cells may trigger other cells by crosstalk. On average, every cell triggers  $\mu_{ct}$  other cells if no saturation was present.
5. A part of these cells coincides with cells that already triggered. The other ones are distributed over the remaining  $(N_{\text{cells}} - N_0)$  free cells and may partly overlap, in the

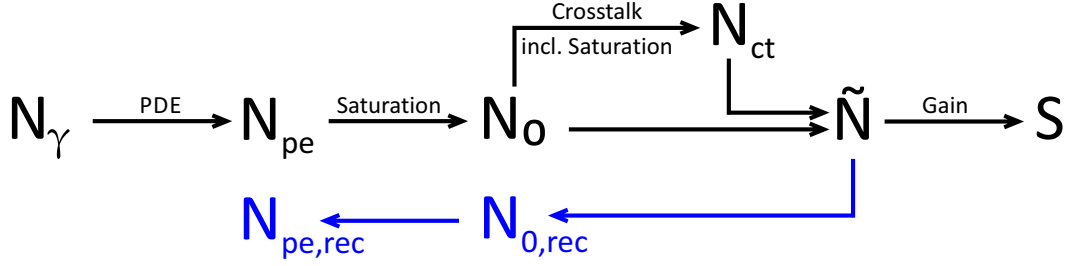


Figure 2.22.: Overview on the notation used for the calculations: the total number of triggered cells  $\tilde{N}$  is the sum of the cells triggered by external photons  $N_0$  and the cells triggered by crosstalk  $N_{ct}$ . For the calculation of  $N_0$ , the PDE and saturation must be considered. The measured signal  $S$  is proportional to the gain, and is for example the amplitude of a pulse. When a signal is measured and the number of detected photons for this signal is calculated (blue), the additional index “rec” (reconstructed) is added.

same way the external photons may arrive at the same cell. The total number of cells triggered by crosstalk is denoted  $N_{ct}$ .

6. The total number of triggered cells  $\tilde{N}$ , is the sum of the initially triggered cells and the cells triggered by crosstalk.
7. These pixels create a signal pulse of size  $S$ , which is proportional to the gain of the diode.

If all effects are included, the total number of triggered cells  $\tilde{N}$  is

$$\tilde{N} = N_0 + N_{ct} \quad (2.19)$$

$$\text{with } N_0 = S(N_{pe}, N_{\text{cells}}), \quad (2.20)$$

$$N_{ct} = S\left(\frac{N_{\text{cells}} - N_0}{N_{\text{cells}} - 1} \mu_{ct} N_0, N_{\text{cells}} - N_0\right), \quad (2.21)$$

$$\text{and } N_{pe} = \text{PDE} \cdot N_\gamma. \quad (2.22)$$

The saturation function  $S(N, N_{\text{cells}})$  can be calculated as

$$S(N_{pe}, N_{\text{cells}}) = N_{\text{cells}} \left( 1 - \left( 1 - \frac{1}{N_{\text{cells}}} \right)^{N_{pe}} \right), \quad (10) \quad (2.23)$$

which for large  $N_{\text{cells}}$  is approximated as

$$N_0 = N_{\text{cells}} \left( 1 - e^{-\frac{N_{pe}}{N_{\text{cells}}}} \right). \quad (2.24)$$

We denote these functions  $S_{\text{exact}}(N_{pe}, N_{\text{cells}})$  and  $S_{\text{approx}}(N_{pe}, N_{\text{cells}})$ , respectively. The combined equations are plotted in figure 2.23.

Please note that I published the formula for the crosstalk cells  $N_{ct}$  (2.21) without the  $-1$  in the denominator [67, 95], which was neglected since usually  $N_{\text{cells}} \gg 1$ <sup>(11)</sup>. If we look

<sup>10</sup>The probability that a cell is *not* triggered by a specific photon is  $(N_{\text{cells}} - 1)/N_{\text{cells}}$ .

<sup>11</sup>It is further noted that an additional approximation is made in the averaging: in principle we have  $N_{ct} = \sum_i p_i \cdot S(i, N_{\text{cells}} - N_0)$ .  $p_i$  is the probability distribution of the number of cells triggered by crosstalk if no saturation is present, where the mean of the distribution is  $\sum_i p_i \cdot i = \frac{N_{\text{cells}} - N_0}{N_{\text{cells}} - 1} \mu_{ct} N_0$ . The approximation is least precise for small mean values, i.e. for few triggered cells, and gets more precise for values  $\gg 1$ .



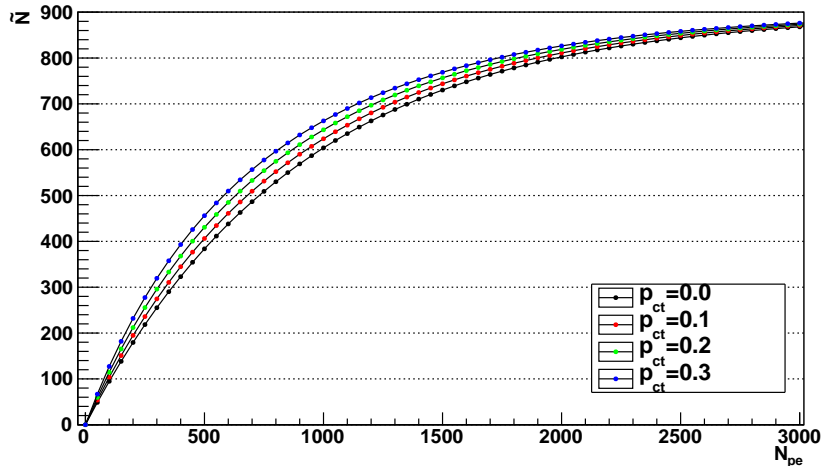


Figure 2.23.: Effect of saturation and different crosstalk probabilities  $p_{ct}$  for a G-APD with 900 cells: the number of triggered cells  $\tilde{N}$  is saturating at the number of cells for large numbers of detected photons  $N_{pe}$ . Crosstalk triggers additional cells and changes the shape of the saturation curve, but not its maximum.

at the situation for small photon numbers, we can neglect the saturation function, i.e.

$$N_{ct} = \frac{N_{\text{cells}} - N_0}{N_{\text{cells}} - 1} \mu_{ct} N_0. \quad (2.25)$$

If one cell is initially triggered ( $N_0 = 1$ ), the average number of crosstalk cells must be  $\mu_{ct}$ , thus requiring the  $-1$  in the denominator. However, as  $N_{\text{cells}}$  is typically large, the difference is small.

### Calculation requirements

This model holds for time-coincident photons, i.e. when the spread of the arrival times is small compared to the dead time/recovery time of the device. In that case, the influence of afterpulses can be neglected. If the arrival time spread is moreover small compared to the rise time of the single cell signals, the number of cells is proportional to the amplitude of the resulting signal<sup>(12)</sup>.

#### 2.4.1. Dependence of the G-APD response on the over-voltage

This calculation can be used to determine the dependence of the G-APD signal on the over-voltage for light pulses of constant intensity. For the response of a G-APD, three parameters are dominant: the PDE, the crosstalk probability  $p_{ct}$  and the gain. All three depend strongly on the over-voltage (see figure 2.24).

Even though the gain is linear in the over-voltage, this is not the case for the total response due to the non-linearity of the PDE and crosstalk probability. To get the dependence of the response on the over-voltage, fits on the measured data for a Hamamatsu device with 50  $\mu\text{m}$  cell spacing are used (see figures 2.4, 2.12 and 2.13) and combined using equation (2.19).

The dependence of the G-APD signal  $S$  on the over-voltage is plotted in figure 2.25. The dependence is strongly non-linear: in the range from 0.6 V to 1.7 V an exponential function  $k \cdot V^\alpha$  is fitted to the data points. The resulting exponent is  $\alpha = 1.69$ .

<sup>12</sup>Of course this requires that the rise time is smaller than the recovery time, which is usually the case.

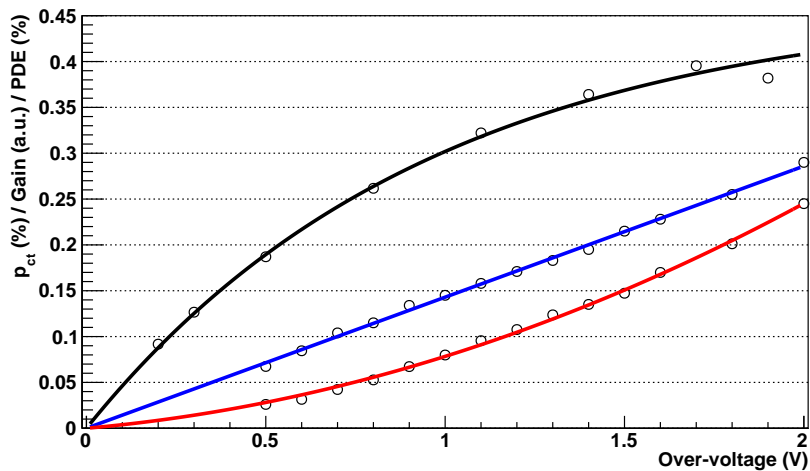


Figure 2.24.: Overview on the voltage dependence of gain (blue), crosstalk probability (red) and PDE (black) for a Hamamatsu 50  $\mu\text{m}$  device. All parameters show a strong voltage dependence. The circles are measured values, the lines are fitted curves.

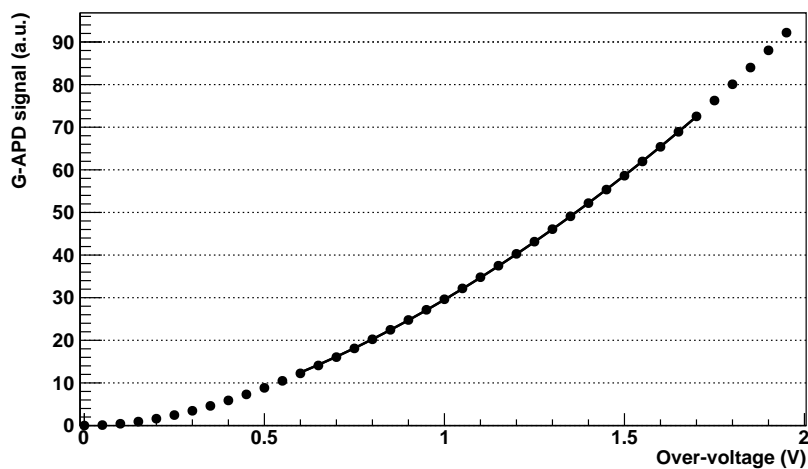


Figure 2.25.: When the dependencies of PDE, crosstalk probability and gain are combined, the total dependence of the G-APD signal on the over-voltage can be calculated. The plot above shows the response of a Hamamatsu 50  $\mu\text{m}$  device for a pulse of 100 photons. The dependence is strongly non-linear: a fitted exponential function  $\propto V^\alpha$  results in an exponent  $\alpha = 1.69$ .

### 2.4.2. Calculation of $N_{\text{pe}}$ from a number of triggered cells $\tilde{N}$

When a signal  $S$  from a G-APD is measured, the corresponding number of triggered cells  $\tilde{N}$  can be calculated by dividing the signal by the signal from a single cell. However, this value is influenced by saturation and crosstalk, which are not present in other photosensors such as PMTs. For the comparison of G-APD properties to other photosensors, it makes thus sense to consider saturation and crosstalk as additional sources of noise, and compare on the level of  $N_{\text{pe}}$ . It would also be possible to go back to  $N_\gamma$ , but the PDE is a quantity relevant for all types of photosensors.

If saturation and crosstalk are present,  $N_{\text{pe}}$  can only be approximately calculated from the actual measured signal  $\tilde{N}$ . We denote the calculated number of  $N_{\text{pe}}$  as “reconstructed”:  $N_{\text{pe,rec}}$ . Without crosstalk ( $\mu_{\text{ct}} = 0$ ), we only have to invert the saturation function  $S_{\text{exact}}$  or  $S_{\text{approx}}$  and can define the inverse functions  $S_{\text{exact}}^{-1}(N_0, N_{\text{cells}})$  and  $S_{\text{approx}}^{-1}(N_0, N_{\text{cells}})$ :

$$N_{\text{pe,rec}} = S_{\text{exact}}^{-1}(N_0, N_{\text{cells}}) = \frac{\log\left(\frac{N_{\text{cells}} - N_0}{N_{\text{cells}}}\right)}{\log\left(\frac{N_{\text{cells}} - 1}{N_{\text{cells}}}\right)} \quad (2.26)$$

$$S_{\text{approx}}^{-1}(N_0, N_{\text{cells}}) = -N_{\text{cells}} \ln\left(\frac{N_{\text{cells}} - N_0}{N_{\text{cells}}}\right) \quad (2.27)$$

If we also include crosstalk, we would have to invert equation (2.19), which can only be calculated approximately. If we neglect the saturation of the crosstalk cells and only include the loss of crosstalk cells identical to a previously triggered cell,  $\tilde{N}$  simplifies to

$$\tilde{N} = N_0 + \frac{N_{\text{cells}} - N_0}{N_{\text{cells}} - 1} \mu_{\text{ct}} N_0. \quad (2.28)$$

This is a simple quadratic equation, which can be solved by  $N_0$ :

$$N_{0,\text{rec}} = \frac{1}{2\mu_{\text{ct}}} \left( [N_{\text{cells}}(1 + \mu_{\text{ct}}) - 1] - \sqrt{[N_{\text{cells}}(1 + \mu_{\text{ct}}) - 1]^2 - 4\mu_{\text{ct}}(N_{\text{cells}} - 1)\tilde{N}} \right) \quad (2.29)$$

The number of detected photons  $N_{\text{pe}}$  can be calculated as before according to equation (2.26).

### 2.4.3. Variations in the saturation process

Since the variation is a statistical process, even for a fixed number of detected photons the number of triggered cells may vary. The standard deviation of this variation can be found e.g. in [97]:

$$\sigma_{N_0}^2 = N_{\text{cells}}(N_{\text{cells}} - 1) \left(1 - \frac{2}{N_{\text{cells}}}\right)^{N_{\text{pe}}} + N_{\text{cells}} \left(1 - \frac{1}{N_{\text{cells}}}\right)^{N_{\text{pe}}} - N_{\text{cells}}^2 \cdot \left(1 - \frac{1}{N_{\text{cells}}}\right)^{2N_{\text{pe}}} \quad (2.30)$$

$$\approx N_{\text{cells}} e^{-\frac{N_{\text{pe}}}{N_{\text{cells}}}} \left(1 - \left(1 + \frac{N_{\text{pe}}}{N_{\text{cells}}}\right) e^{-\frac{N_{\text{pe}}}{N_{\text{cells}}}}\right) \quad (2.31)$$

Both formulas show an important property of saturation: its standard deviation becomes zero in the limit of a lot of light  $N_{\text{pe}} \rightarrow \infty$  (see figure 2.26). This is intuitively clear when looking at a very strong light flash which always triggers (almost) all cells of the G-APD: the variation of the signal is then (almost) zero. This means that the variations in the

detector signal  $\Delta(S)/S$  can be even smaller than the incoming distribution of photons (which is e.g. Poisson distributed). However, the determination of the number of initially triggered cells  $N_{\text{pe,rec}}$  is only possible with a large statistical error, which must have the limit  $\sigma_{\text{pe,rec}} \rightarrow \infty$  for  $N_{\text{pe}} \rightarrow \infty$ <sup>(13)</sup>. The effect of  $\Delta(S)/S \rightarrow 0$  is a consequence of the non-linearity of the sensor.

If we want to calculate the standard deviation  $\sigma_{\text{pe,rec}}$  we can use Gaussian error propagation on equation (2.26) as an approximation:

$$\sigma_{\text{pe,rec}}^2 = \left( \frac{\partial N_{\text{pe,rec}}}{\partial N_0} \right)^2 \sigma_{N_0}^2 \quad (2.32)$$

$$\frac{\partial N_{\text{pe,rec}}}{\partial N_0} = \frac{1}{(N_{\text{cells}} - N_0) \cdot \ln \left( \frac{N_{\text{cells}}}{N_{\text{cells}} - 1} \right)} \quad (2.33)$$

$$\approx \frac{N_{\text{cells}}}{N_{\text{cells}} - N_0} \quad (2.34)$$

For an approximate calculation, we can insert the equations (2.24), (2.31) and (2.34) into (2.32) and get<sup>(14)</sup>:

$$\sigma_{\text{pe,rec}}^2 \approx N_{\text{cells}} \left( e^{\frac{N_{\text{pe}}}{N_{\text{cells}}}} - 1 \right) - N_{\text{pe}} \quad (2.35)$$

In contrast to the standard deviation of the number of triggered cells  $\sigma_{N_0}$ , the standard deviation of the reconstructed number of photons  $\sigma_{\text{pe,rec}}$  goes to infinity for  $N_{\text{pe}} \rightarrow \infty$ .

Its Taylor approximation up to the 3rd order is

$$\sigma_{\text{pe,rec}}^2 \approx \frac{N_{\text{pe}}^2}{2N_{\text{cells}}} + \frac{N_{\text{pe}}^3}{6N_{\text{cells}}^2} + \dots \quad (2.36)$$

i.e. the standard deviation is approximately linear to  $N_{\text{pe}}$ , with a linearity constant  $\frac{1}{\sqrt{2N_{\text{cells}}}}$  (see figure 2.27). Usually the standard deviation is proportional to the square root of the input signal (see e.g. section 2.3.4), as it is the case for uncorrelated noise. However, saturation is a prime example of correlated noise, thus the proportionality to  $N_{\text{pe}}$ .

#### 2.4.4. Excess Noise Factor

Every detector adds some sort of statistical variations to its output signals: for a well-defined input signal, its output is not always exactly identical. In the case of G-APDs, the following items contribute to those variations:

- Not every photon triggers an avalanche: the average probability is the PDE, and for a fixed number of photons we get a binomial distribution of the number of avalanches (i.e. detected photons).
- Some photons may hit the same cell (saturation). Of course this occurs stochastically, inducing fluctuations in the number of initially triggered cells.
- Also crosstalk is only characterized by a probability, and the number of effectively triggered cells by crosstalk may vary.

<sup>13</sup>Please note that the G-APDs in FACT are operated with small photon numbers compared to the cell number. The dynamic range is limited by the readout electronics. See also section 2.6.

<sup>14</sup>Using the exact formulas (2.23), (2.30) and (2.33) in (2.32), the calculation becomes rather complicated but does not provide additional insights.

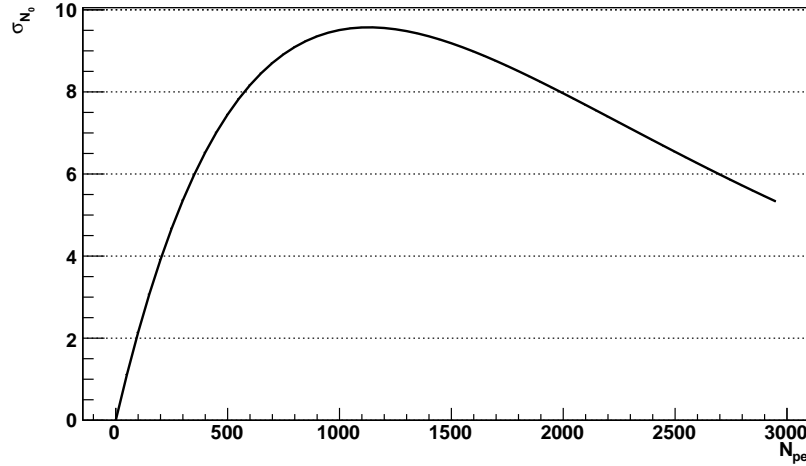


Figure 2.26.: Plot of the standard deviation of the number of triggered cells for a device with 900 cells due to statistical saturation: even if a fixed number of photons are registered by the G-APD, the number of triggered cells varies. The variations are increasing up to approximately  $N_{pe} = N_{cells}$ , the following decrease is a consequence of the non-linearity of the sensor.

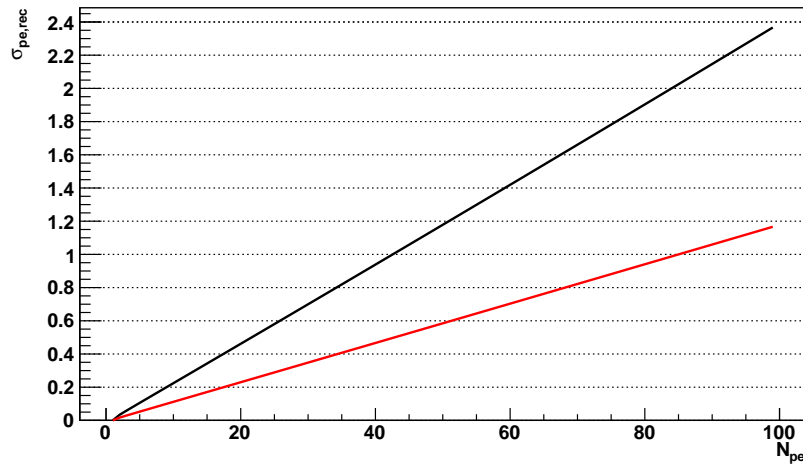


Figure 2.27.: Standard deviation of the reconstructed number of photons due to saturation effects for 900 cells (black) and 3600 cells (red), according to the exact formulas (2.23), (2.30), (2.32) and (2.33). The effect of saturation is approximately linear (see equation (2.36)) for small photon numbers.

- And finally the charge released per cell has some fluctuations (see section 2.3.4).

Since different sensors have different noise characteristics, a measure is necessary to quantify the noise and be able to compare it. Furthermore, a quantification allows to compare various noise components, which is important when choosing a specific type of a genre of photosensors.

The number of photons arriving at the photosensor has usually a Poisson distribution. The standard deviation of a Poisson distribution with mean value  $\mu$  is its square root  $\sqrt{\mu}$ . The idea of the ENF is to quantify the noise by comparing the width of the signal distribution with the distribution at the entrance of the photosensor: the relative width of the distribution of photons is

$$\frac{\Delta(N_\gamma)}{N_\gamma} = \sqrt{\frac{1}{N_\gamma}}. \quad (2.37)$$

The number of detected photons has a broader distribution, since only a fraction of all arriving photons are detected. Though it is a Binomial process, the distribution is still Gaussian (see appendix A.1). The relative width of this distribution is analogously

$$\frac{\Delta(N_{\text{pe}})}{N_{\text{pe}}} = \sqrt{\frac{1}{N_{\text{pe}}}} = \sqrt{\frac{1}{\text{PDE} \cdot N_\gamma}} > \sqrt{\frac{1}{N_\gamma}}. \quad (2.38)$$

A noise-free detector would keep the width of this distribution, such that the relative width of the output signals had the same relative width. However, noise components make the distribution wider. If the processing of the single photons inside the detector is independent of other photons arriving at the same time, the total noise is proportional to the square root of the number of processed photons:

$$S = \sum_{i=1}^{N_{\text{pe}}} S_i \quad (2.39)$$

$$\Delta(S) = \sqrt{\sum_{i=1}^{N_{\text{pe}}} \Delta(S_i)^2} \quad \text{with } \Delta(S_i) = \Delta_S \quad (2.40)$$

$$= \sqrt{N_{\text{pe}}} \Delta_S \quad (2.41)$$

This is the same behavior as Gaussian distribution. It lies thus at hand to define the ENF as

$$\frac{\Delta(S)}{S} = \sqrt{\frac{\text{ENF}}{N_{\text{pe}}}} \quad (2.42)$$

if the number of detected photons  $N_{\text{pe}}$  is Poisson distributed. The ENF is then a value larger than one, which contains the additional (thus “excess”) variations of the width of the output signals. This definition is used e.g. in [98].

Often the ENF is defined as the “normalized second moment of the gain random variable when a single photocarrier initiates the multiplication” [99]:

$$\text{ENF} = \langle S^2 \rangle / \langle S \rangle^2 = 1 + [\text{Var}(S) / \langle S \rangle^2] \quad (2.43)$$

Note that in some publications this value is denoted as  $F^2$ , and  $F$  is called ENF (i.e. the definitions differ by a square). This often complicates the comparison of values.

The two definitions (2.42) and (2.43) are equivalent under some conditions on the distribution of the signals (see appendix A.7). These conditions are met for the signals of PMTs, but for G-APDs only if the number of initially triggered cells is Poisson distributed, which is the case without saturation (i.e. low-light limit:  $N_0 = N_{pe}$ ).

In this case, two components of the ENF remain:

- For a crosstalk probability of  $p_{ct}$  and no other noise sources, the ENF is reported as

$$\text{ENF} \approx 1 + p_{ct} \quad [74] \quad (2.44)$$

- If we neglect crosstalk and only look at the noise induced by charge variations with a standard deviation  $\sigma_{av}$  (see section 2.3.4), we get for the ENF

$$\text{ENF} = 1 + \sigma_{av}^2. \quad (2.45)$$

See appendix A.8 for the explicit calculation according to definition (2.42).

The ENF for APDs was calculated e.g. by R. McIntyre [100]. It depends strongly on multiplication factor in the avalanche process (i.e. the gain), which can be adjusted via the bias voltage. For the APDs used in the CMS experiment at CERN<sup>(15)</sup>, the ENF was measured in dependence of the voltage, and are operated at a gain of 50 where they have an ENF of 2 [101].

Based on the formulas (2.44) and (2.45), the ENF for G-APDs can be estimated. For small photon numbers relative to the total number of cells of the G-APD where saturation can be neglected, crosstalk is the dominating contribution to the noise and the ENF.

However, the quantitative effect of saturation is not clear, as well as the combination of various noise components. These phenomena are investigated using a toy Monte Carlo simulation (see next section).

### 2.4.5. Relative ENF for different PDE

When comparing two photosensors with different PDE, the effective difference in the Poisson variations can be expressed as a relative excess noise factor. We denote the two PDEs with  $k_1$  and  $k_2$ , with  $k_1 > k_2$ . The widths of the distributions of detected photons are then

$$\frac{\sigma_1}{N_{pe,1}} = \sqrt{\frac{1}{k_1 N_\gamma}} \quad (2.46)$$

$$\frac{\sigma_2}{N_{pe,2}} = \sqrt{\frac{1}{k_2 N_\gamma}} = \sqrt{\frac{k_1/k_2}{k_1 N_\gamma}} \quad (2.47)$$

$$= \sqrt{\frac{\text{ENF}_{rel}}{k_1 N_\gamma}} \quad (2.48)$$

$$\Rightarrow \text{ENF}_{rel} = \frac{k_1}{k_2} > 1 \quad (2.49)$$

The relative ENF scales inversely proportional to the PDE. As an example, using a photosensor with a 20% higher PDE improves the noise behavior in the same way as using a perfect sensor with an ENF of one compared to a photosensor with an ENF of 1.2.

---

<sup>15</sup><http://cms.web.cern.ch>

## 2.5. Statistical simulation of G-APDs

In order to investigate the effect of the various noise components and in particular the effect of saturation on the resolution of reconstructed signals, I wrote a simple statistical simulation of G-APDs. The aim was to simulate the number of triggered cells  $\tilde{N}$  and its standard deviation, and get distributions of the reconstructed number of photons. The simulation is (as the calculations in the previous sections) valid for pulses of photons with an arrival time spread small compared to the dead time/recovery time of the device.

The following parameters can be adjusted in the simulation:

- The input distribution of the number of detected photons  $N_{\text{pe}}$ : either a fixed number is used, or the mean value for a Poisson distribution is specified<sup>(16)</sup>.
- The number of cells  $N_{\text{cells}}$  of the G-APD.
- The crosstalk probability  $p_{\text{ct}}$ .
- The amount of avalanche fluctuations  $\sigma_{\text{av}}$ .
- The amount of pedestal fluctuations  $\sigma_0$ .
- The number of iterations, i.e. how many light pulses are simulated.

A two-dimensional Boolean array represents the G-APD, each value corresponding to one cell which is either active (true) or inactive (false). Initially, all cells are set to inactive. The number of detected photons is either fixed or selected from a Poisson distribution<sup>(17)</sup>. These photons are handled iteratively: first a random cell is selected from all cells. If the cell was previously true, nothing happens. Else the cell state is switched to true, and with a certain probability  $p_{\text{ct}}$  another cell is triggered by crosstalk. This crosstalk cell can trigger other cells, which is repeated iteratively.

When no further cells are triggered by crosstalk, the next photon is handled. At the end, the number of triggered cells  $\tilde{N}$  is counted. The amplitude of the total signal  $S$  is determined by a random distribution with average  $\tilde{N}$  and width  $\sigma_{\tilde{N}} = \sqrt{\sigma_0^2 + \tilde{N}^2 \sigma_{\text{av}}^2}$  (see section 2.3.4). The gain itself is normalized to 1.

The reconstructed number of triggered cells  $\tilde{N}_{\text{rec}}$  is equal to the signal, since we have no information on the avalanche fluctuations. We use equation (2.29) to get  $N_{0,\text{rec}}$  and equation (2.26) to obtain our number of detected photons  $N_{\text{pe,rec}}$ . The first calculation requires the average number of cells triggered by crosstalk  $\mu_{\text{ct}}$ , and not the crosstalk probability  $p_{\text{ct}}$ . The first step was thus to correlate the crosstalk probability to the average number of triggered cells.

### 2.5.1. Relation of $\mu_{\text{ct}}$ and $p_{\text{ct}}$ in the simulation

The analysis is similar to the one in section 2.3.3, except that the normalization on the gain can be omitted since the gain in the simulation is one. We start the simulation with a crosstalk probability of  $p_{\text{ct}}$ , and set  $N_{\text{pe}}$  to one (no Poisson spectrum!). The average signal is then  $\tilde{N} = 1 + \mu_{\text{ct}}$ . The simulation is repeated for several values of  $p_{\text{ct}}$  and compared to the measurement from section 2.3.3. The measurement and the simulation show an excellent agreement (see figure 2.28).

<sup>16</sup>It would also be possible to start with a number of external photons, but the detection is a binomial process which is statistically simple: the width from the distribution changes from  $\sigma_{\gamma} = 1/\sqrt{N_{\gamma}}$  to  $\sigma_{\text{pe}} = 1/\sqrt{N_{\text{pe}}} = 1/\sqrt{\text{PDE} \cdot N_{\gamma}}$ , i.e. it becomes a wider corresponding to the PDE, but remains a Poisson distribution (see also appendix A.1).

<sup>17</sup>The ROOT library TRandom3 was used, which implements a Mersenne twister pseudo-random number generator [102].



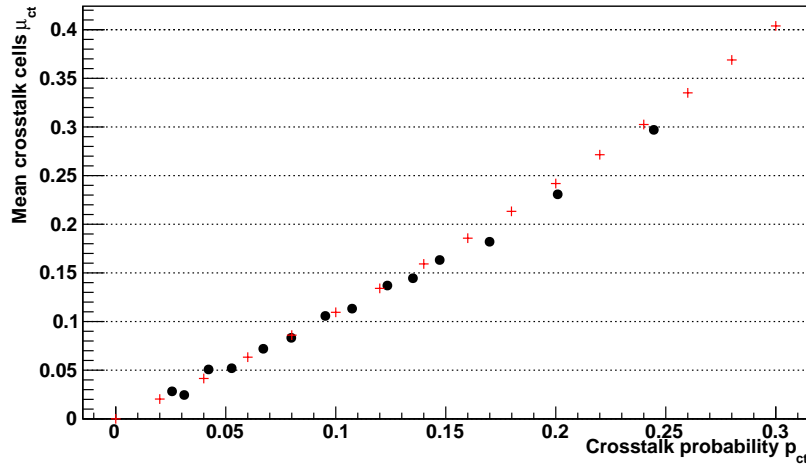


Figure 2.28.: Average number of cells triggered by crosstalk  $\mu_{ct}$  vs. crosstalk probability  $p_{ct}$  according to the simulation (crosses, red). The comparison with the measurement (dots, black) shows a good agreement.

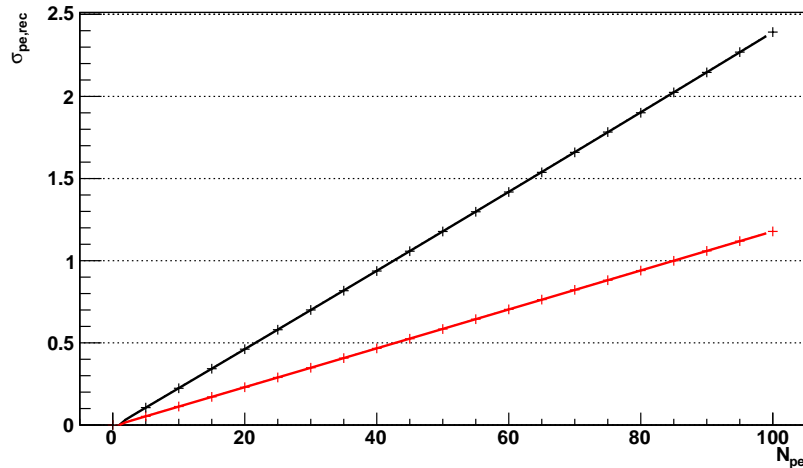


Figure 2.29.: Standard deviation of the reconstructed number of photons due to saturation effects for 900 cells (black, upper curve) and 3600 cells (red, lower curve): the markers show the simulation, the lines the calculation from section 2.4.3.

### 2.5.2. Variations in the saturation process

To compare the effect of saturation on the width of the reconstructed number of detected photons  $N_{pe,rec}$ , the simulation was run with an input range from 0 to 100 detected photons which are not Poisson distributed, and the widths of the distributions of the reconstructed number of photons determined. As expected from the calculation in section 2.4.3, the dependence is linear for small photon numbers (see figure 2.29).

### 2.5.3. Combination of processes

In the application of pixelated sensors, the previously described effects always occur combined. As for the average values as in figure 2.22, we can analyze the variations by looking at a series of distributions, where the average is given by the previous calculations, and the standard deviations can be combined using the calculation in appendix A.6. Since the definition of the ENF is only reasonable for variations which are independent for mul-

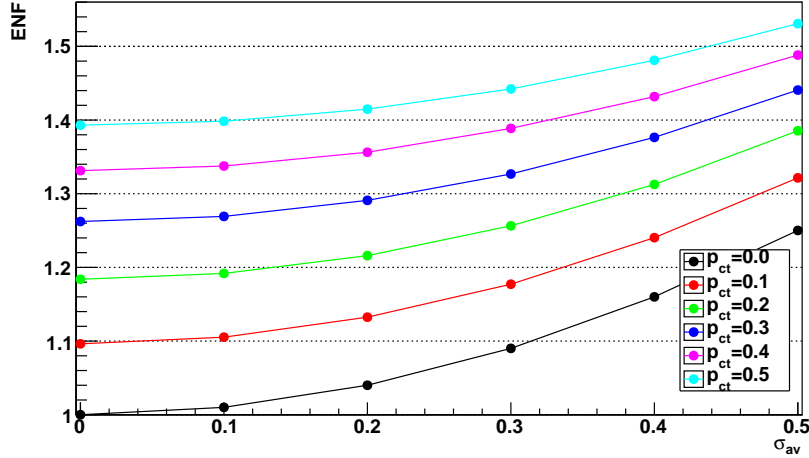


Figure 2.30.: ENF for distributions combining the effect of avalanche fluctuations  $\sigma_{av}$  and crosstalk  $p_{ct}$ .

multiple photons, we only look at the combination of the effect of crosstalk and avalanche fluctuations. Pedestal noise ( $\sigma_0$ , see section 2.3.4) and saturation (see section 2.4.3) are not considered due to their independence or quadratical dependence on the number of photons, respectively. The PDE is set to one.

Since we have uncorrelated noise, we can take the definition (2.43), which is based on the resulting signal for one single incoming photon. Due to crosstalk, we get a distribution of the number of triggered cells with an average of  $\mu_D = 1 + \mu_{ct}$  and variance  $\sigma_D^2 = \sigma_{ct}^2$  (from the simulation / measurement and/or the calculation in S. Vinogradov [103]). This distribution is then combined with the (Gaussian) avalanche fluctuations:  $\sigma_{lin} = \sigma_{av}$ , and  $\sigma_0 = \sigma_{sq} = 0$ .

For the resulting width of the output signal distribution  $S$  we get according to formula (A.60)

$$\sigma_S^2 = (1 + \mu_{ct})\sigma_{av}^2 + S_1^2\sigma_{ct}^2. \quad (2.50)$$

The size of the single cell signal  $S_1$  is often set to one for simplicity.

Without saturation, the reconstructed number of photons  $N_{pe,rec}$  is linear to the signal  $S$ :

$$N_{pe,rec} = \frac{S}{S_1(1 + \mu_{ct})} \quad (2.51)$$

Due to the linearity, the ENF in the number of photons can be calculated using the width of the signal distribution<sup>(18)</sup>, thus:

$$ENF = 1 + \frac{\sigma_S^2}{S^2} = 1 + \frac{(1 + \mu_{ct})\sigma_{av}^2 + S_1^2\sigma_{ct}^2}{S_1^2(1 + \mu_{ct})^2} = 1 + \frac{1}{1 + \mu_{ct}} \frac{\sigma_{av}^2}{S_1^2} + \frac{\sigma_{ct}^2}{(1 + \mu_{ct})^2} \quad (2.52)$$

This equation was confirmed using the statistical simulation (see figure 2.30).

#### 2.5.4. Summary of the statistical properties

The processes leading from a number of incoming photons to an electrical signal can be analyzed by considering a series of distributions (as illustrated in figure 2.22). The averages of the distributions can be calculated from the basic properties of the G-APDs,

<sup>18</sup>The linearity factor just cancels out in the formula of the ENF.

and the inverse calculations allow to estimate the number of initial photons from a certain measured signal.

The other interesting question is the development of the standard deviation of these distributions, which allows to estimate the amount of “randomness” in the electrical G-APD signal for a certain number of photons. The various processes which contribute variations to the output signal can be classified depending on whether the fluctuations are independent of other photons or not. Independent processes are the PDE, crosstalk, and the variations in the released charge per G-APD cell, whereas the variations in the statistical saturation are based on the overlap of multiple photons and thus belongs to the other category.

For the independent processes, the extent of variation inducing processes can be compared by looking at a measurable quantity, the ENF. It compares the signal fluctuations of a sensor output with a Poisson distribution at its entrance. The ENF is defined such that the received number is independent of the Poissonian mean of the number of incoming photons (which is of course only possible if the noise processes are independent for each photon). In order to compare the relative relevance of noise processes, one can look at the ENF if only this process was present.

For the three distribution-widening processes PDE, crosstalk and avalanche fluctuations, the corresponding ENFs are (see previous sections)

$$\text{ENF}_{\text{PDE}} = \frac{k_1}{k_2} \quad (2.53)$$

$$\text{ENF}_{\text{ct}} = 1 + p_{\text{ct}} \quad (2.54)$$

$$\text{ENF}_{\text{av}} = 1 + \sigma_{\text{av}}^2. \quad (2.55)$$

For the PDE, only a relative ENF of two photosensors with a PDE of  $k_1$  and  $k_2$ , respectively, can be defined. The crosstalk probability is  $p_{\text{ct}}$ , whereas  $\sigma_{\text{av}}$  is the relative width of the signal of one G-APD cell. For the G-APDs that we evaluated (Hamamatsu), typical values for both the crosstalk probability and the avalanche fluctuations are in the range 10 % to 15 % for the recommended operation voltage. Since the avalanche fluctuations only enter the ENF squared, the crosstalk dominates.

However, the effect of the PDE can be dominant, if two photosensors with different PDE are compared. In order to get a relative ENF of 1.15 (comparable to the one induced by crosstalk), the PDE of a photosensor with a PDE of 20 % only needs an improvement to 23 %.

For PMTs the ENF depends strongly on the specific device and the operation conditions. It ranges from 1.15 for low-noise devices [83] up to 1.32 for the devices used in the MAGIC experiment [104]<sup>(19)</sup> or higher.

The ENF of G-APDs is thus already in the first generation comparable to the very best available PMTs. The efforts by the device manufacturers to reduce the crosstalk probability will lower the ENF of G-APDs further, though it must be emphasized that the changes in the sensor structure must not deteriorate the PDE, since any loss there will linearly increase the ENF.

---

<sup>19</sup>The definition  $F = \sqrt{1 + \sigma^2/Q^2}$  used in the MAGIC experiment is the square root of the one used in this thesis. There is a reference to  $\sigma_Q^2/Q^2 = 0.32$  [104], which is used for the stated value. Note that in another thesis of the same experiment [105], again another definition is given for the ENF:  $F = \sqrt{1 + \sigma/Q}$ . However, a comparison of the stated value 1.15 to the reference in [104] reveals that probably the formula was reproduced incorrectly, and the same definition as in [104] is effectively used:  $1.15^2 = 1.32$ .

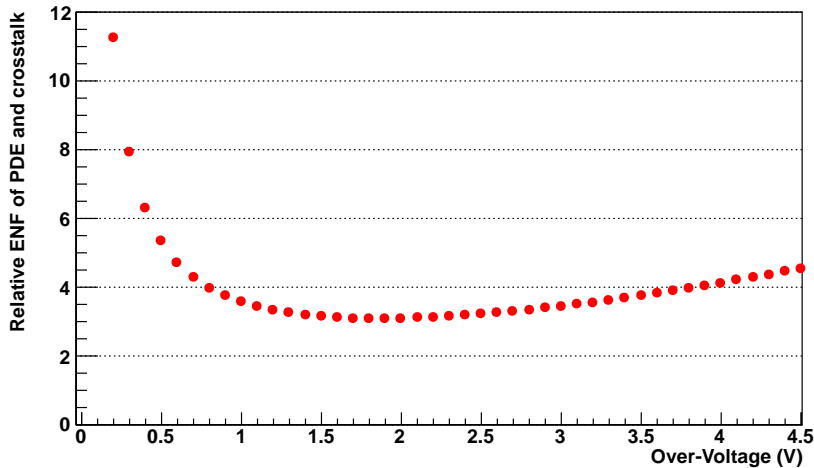


Figure 2.31.: Relative ENF in dependence of the over-voltage: in comparison with a photosensor with a PDE of 100 % and no crosstalk, the Hamamatsu devices with a cell spacing of  $50 \mu\text{m}$  (S10362-33-050C) have an ENF as plotted above in dependence of the over-voltage. For small voltages, the PDE is dominant, whereas for larger voltages the crosstalk leads to a worse ENF. The over-voltage around 1.1 as proposed by the manufacturer is at the lower edge of the flatter part of the distribution, which minimizes the device current and self-heating and is optimal considering the single photon resolution (see section 2.3.5).

### 2.5.5. ENF dependency on the over-voltage

The ENF depends mostly on parameters which change with the over-voltage of the G-APDs: the PDE, the crosstalk probability and avalanche fluctuations. Using the equations (2.53)-(2.55) as summarized in the previous section, it is possible to calculate the combined ENF in dependence of the over-voltage: the PDE transforms the Poisson distribution of the incoming photon number into another Poisson distribution (neglecting saturation), which is used as input distribution for the crosstalk. The avalanche fluctuations are neglected since they are relatively small. The total ENF in comparison to a perfect photosensor with a PDE of 100 % and no crosstalk is then

$$\text{ENF} = \frac{1 + p_{\text{ct}}}{\text{PDE}}. \quad (2.56)$$

According to the definition of the ENF in equation (2.42), the width of the signal distribution is

$$\frac{\Delta(S)}{S} = \sqrt{\frac{\text{ENF}}{N_\gamma}}. \quad (2.57)$$

Note that we have  $N_\gamma$  and not  $N_{\text{pe}}$  as in the original formula, since we include the PDE here.

Using the measured voltage dependencies from section 2.4.1, the voltage dependency of the ENF for the device can be plotted (see figure 2.31). For small voltages, the low PDE leads to a wide distribution and a large ENF. By increasing the voltage and thus the PDE, the signal precision is enhanced, until the crosstalk probability becomes dominating and widens the distribution. The best operation voltage in terms of signal precision is thus not found by maximizing the PDE, but by minimizing the ratio  $(1 + p_{\text{ct}})/\text{PDE}$ .

For the G-APD type in the plot<sup>(20)</sup>, the ENF varies only little between 1 V and 3 V. In

<sup>20</sup>Hamamatsu S10362-33-050C, which is the type later chosen for the FACT camera.

this range, other considerations can be used to determine the best operation voltage, e.g. the minimization of the currents to reduce the power consumption.

## 2.6. Choosing the right G-APD type for the camera

When the decision on the manufacturer and the specific type of G-APD was due in the beginning of 2009, two manufacturers were producing blue sensitive p-on-n type G-APDs in the necessary quantities: Zecotek and Hamamatsu. The devices by Hamamatsu were found to suit our requirements due to their higher PDE. They were available in in the sizes  $1 \times 1 \text{ mm}^2$  and  $3 \times 3 \text{ mm}^2$ , the smaller ones being too small for our application. The cell size could be chosen from  $25 \mu\text{m}$ ,  $50 \mu\text{m}$  and  $100 \mu\text{m}$ .

Table 2.2 shows some basic properties of the devices.

Cell spacing	$25 \mu\text{m}$	$50 \mu\text{m}$	$100 \mu\text{m}$
Gain [64]	$2.75 \times 10^5$	$7.5 \times 10^5$	$2.4 \times 10^6$
Cell number	14400	3600	900
Geometric fill factor [64]	30.8 %	61.5 %	78.5 %
Full recovery time [106]	20 ns	50 ns	100 ns

Table 2.2.: Comparison of the different types of G-APDs with sensitive area  $3 \times 3 \text{ mm}^2$  of one manufacturer (Hamamatsu): three different cell sizes are available. The gain is the number of electron-hole pairs produced per breakdown. The cell number is an important property for the statistics of the signal saturation. The geometric fill factor is proportional to the PDE, and the “full” recovery time is the time a cell needs after a Geiger discharge until a next trigger has the same amplitude.

The main differences in the three device types are their gain, cell number and PDE, which is proportional to the fill factor. Smaller cells with a larger cell number per area are an advantage due to smaller influence of saturation. Further the single cells have a smaller capacity, and thus a smaller gain and recovery time (in combination with the over-voltage and the quenching resistor, respectively).

The larger cells have mainly the advantage of the higher fill factor and thus the better PDE. This value is doubled for the  $50 \mu\text{m}$ -devices compared to the  $25 \mu\text{m}$  devices, which ruled out the latter. The difference to the  $100 \mu\text{m}$ -devices is smaller, but still notable.

However, we have to consider the other properties of the devices, especially under the conditions of an IACT: even in observations during darkest night, the rate of background photons is in the order of some MHz, and rises up to some GHz when the moon is visible (see section 3.2.1). This creates two problems for larger cell sizes:

- The background light causes some level of cells of the device to be insensitive or in recovery (see 2.2.6). This number of cells is higher for the devices with larger cells due to the higher PDE and recovery time. A signal photon from an air shower hitting one of these cells has a smaller (during the recovery phase) or non-existing (during the dead time) probability to be detected. This probability is proportional to

$$p_{\text{lost}} \propto \frac{R_{\text{NSB}} \cdot \text{PDE} \cdot T_{\text{recovery}}}{N_{\text{cells}}}. \quad (2.58)$$

In the case of the high background flux, this probability can be 10 % to 20 % of photons which are lost for the  $100 \mu\text{m}$ -devices, but a factor 8 smaller for the  $50 \mu\text{m}$

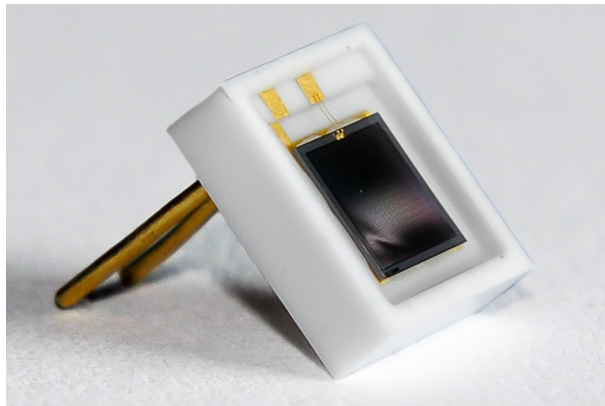


Figure 2.32.: G-APD type selected for FACT: Hamamatsu MPPC S10362-33-050C have a sensitive area of  $3 \times 3 \text{ mm}^2$  comprising 3600 cells. The semiconductor (black) is embedded in a ceramics package and covered with an epoxy resin.

devices (ratio of recovery times and cell numbers). This background light level is difficult to calibrate, which is a strong argument for the smaller cells<sup>(21)</sup>.

- The higher PDE and gain induce four times larger currents in the camera. This is a challenge for several reasons: first the bias voltage supply must be able to deliver the corresponding power. Second, the effect of any serial resistor to the G-APD in the circuit becomes larger due to Ohm's law  $\Delta V = R\Delta I$ : changes in the rate of the background photon flux lead to a larger change of the current, and thus to larger voltage variations. And finally, the larger current leads to more heat produced by the sensors, which has to be dissipated.

For all these reasons, it was decided to use the devices with a cell spacing of  $50 \mu\text{m}$ , or more precisely, the type S10362-33-050C by Hamamatsu (see figure 2.32).

---

<sup>21</sup>The baseline for the construction parameters was to keep effects on the signal chain from photons to digital signals within 5%.

# 3. Construction of the First G-APD Cherenkov Telescope (FACT) camera

This chapter describes the design decisions taken during the construction and the technical properties of the prototype module M0 and the First G-APD Cherenkov Telescope (FACT) camera. For a short introduction to the cameras and their schedule please refer to section 1.5 on page 12.

## 3.1. The prototype module M0

The prototype module M0 was initially aimed at being the first component of a full camera consisting of several identical modules. However, already during its design phase it became clear that a two-step solution with a new design for the full camera would be the better approach for mechanics, electronics and optics of the camera. Dropping the requirement of a modular design facilitates both the mechanics and the electronics of the camera. The development of the electronics could be focused on those parts closest to the G-APDs, the pre-amplifier and the bias voltage system, whereas the digitization for the full camera would be developed later. Further the development of solid light-collecting cones required more time than was available in the schedule for M0. The aim of M0 was thus to gain experience with the operation of G-APDs under outdoor conditions and test the first part of the electronics for its suitability to record air showers. The G-APDs would be of the same type as the final camera, and the pre-amplifier and bias voltage system as close to the final design as possible, if no necessary changes were found.

The G-APDs with a sensitive area of  $3 \times 3 \text{ mm}^2$  were to be equipped with a light concentrator of folded reflective foil to increase the sensitive area. The concentration ratio of the input to the output area of such folded cones is limited (see section 3.3), which results in small pixels and a large number of readout channels. The complexity and cost of a camera scales approximately with the number of readout channels, and a too small angular resolution has no advantage (see section 1.2.7). Using open cones would thus only be reasonable if multiple sensors and cones are grouped into one pixel. One of the first designs (originally proposed by I. Braun) was to form groups of three hexagonal cones, whose sensor signals would be summed and share one readout channel (see figure 3.1[a]). One module would consist of 37 pixels, and it would even be possible to stack multiple modules to a full camera.

The design was soon discarded since the folding of cones with a hexagonal entrance area and a square exit window would be rather difficult, and for the prototype no additional insights are expected by using a hexagonal geometry compared to a square one. The next design was thus based on square pixels, where four G-APDs would be summed to form one pixel (see figure 3.1[b]). The size of a cone entrance window was set to  $7.2 \times 7.2 \text{ mm}^2$ , 0.65 mm larger than the size of the G-APD package (see section 2.3.1).

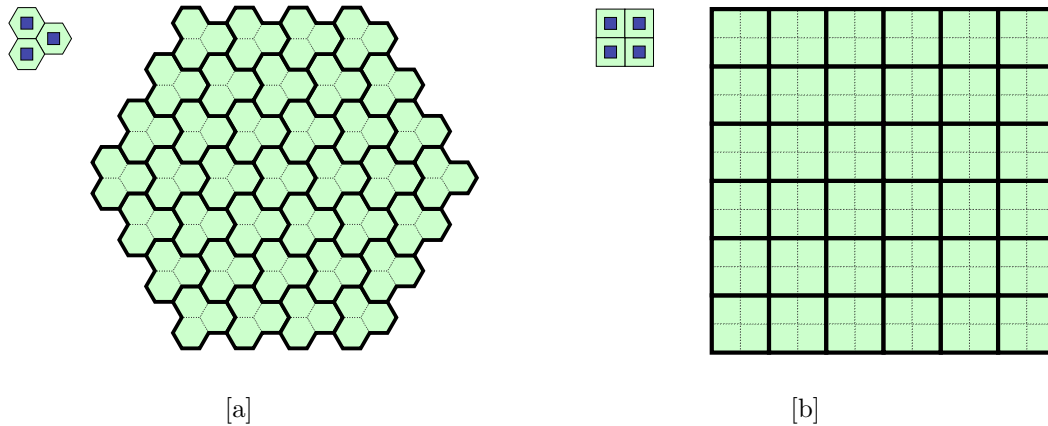


Figure 3.1.: Pixel layouts for the prototype module M0: [a] Discarded prototype design of M0 using groups of three hexagonal sensor/cone-pairs as pixels. 37 pixels would form one module, requiring 111 G-APDs. The design requires open, reflective cones with hexagonal entrance and square exit window, which are difficult to produce since they cannot be folded. [b] The module M0 finally used square pixels, each a group of four sensors and cones. The 144 G-APDs then form 36 pixels.

The prototype module M0 would contain 36 pixels, using a total of 144 G-APDs. Each pixel is equipped with a set of four light guides which concentrate the light onto the sensitive area of the G-APDs. Those are mounted directly on electronics boards which provide the bias voltage and pre-amplifiers for 12 pixels each, and which also sum up the signals of the four G-APDs per pixel (see figure 3.2).

In front of the reflective cones, a Plexiglas window was installed to protect the photosensors and electronics from dust and humidity. LEDs installed at the edge of this window allow to test the camera even when the shutter is closed and to provide a reference pulse when the observation conditions change. A water-cooled copper plate between the sensors and the boards isolate the G-APDs thermally from the electronics. Since there was no tight space limit for the housing of this prototype, enough space was left to allow easy access to the electronics and a facilitated cabling (see figure 3.3).

### 3.1.1. Hollow light guides

The light guides for the prototype module follow a simple square design with flat sides. Each cone concentrates the light of an area of  $7.2 \times 7.2 \text{ mm}^2$  onto the sensitive area of a G-APD ( $3 \times 3 \text{ mm}^2$ ). The exit area is  $2.8 \times 2.8 \text{ mm}^2$ , slightly smaller than the G-APD to avoid light loss at the edges. A light cone consists of a folded reflective foil with a very high reflectivity  $> 98\%$  (3M Vikuiti Enhanced Specular Reflector [107]).

The foil was cut by a manufacturer of high-precision knife cutting machines<sup>(1)</sup>, who also made folding aids (“scratches”). The reflective foil was inserted in groups of four into an aluminum frame which provided stability and the relative alignment of the cones. A custom-made tool was used for the assembly (see figure 3.4). The foil was fixed in the frame with a specialized glue for synthetics-metal combinations<sup>(2)</sup>. A total of 160 cones were assembled by J.-P. Stucki (ETH Zurich), which took around 5 working days. The precision is  $\sim 0.1 \text{ mm}$ . Figure 3.5 shows a completely assembled block of four cones for one

<sup>1</sup>Zünd Systemtechnik AG, Altstätten, Switzerland.

<sup>2</sup>ergo 5889 by Kisling AG, Wetzikon, Switzerland.



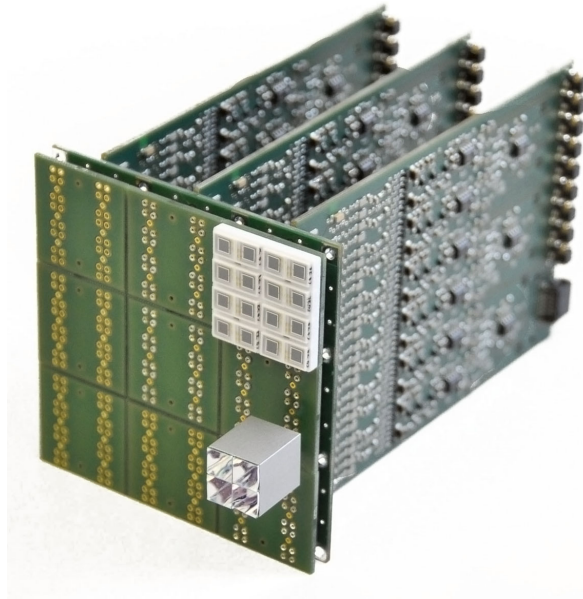


Figure 3.2.: Photo of the sensors and electronics of the prototype module M0: 4 G-APDs form one pixel, which is equipped with a set of light concentrators made of folded reflective foil (gray block). Groups of 4 pixels (16 G-APDs) are mounted on small carrier boards (white square). Each of the three electronics boards is connected to three groups and provides the amplifiers for the 12 pixels.

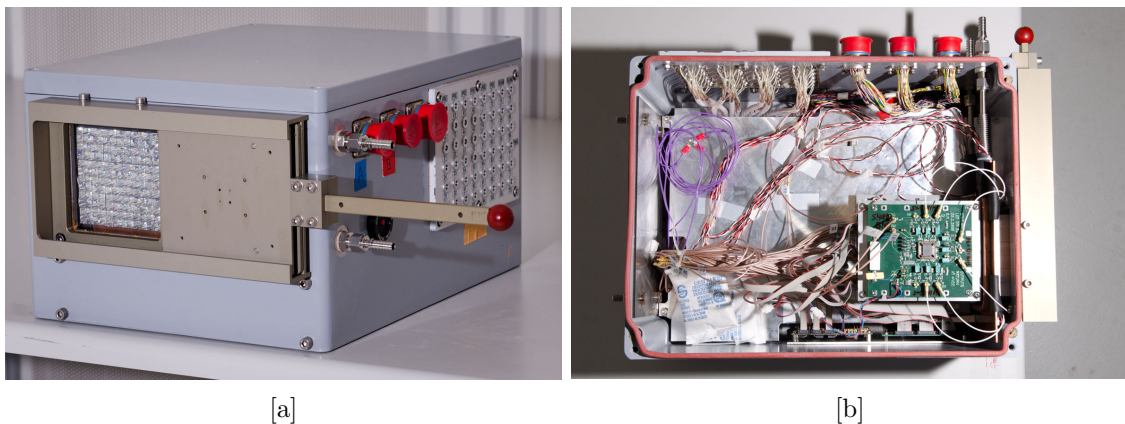


Figure 3.3.: Photos of the finished prototype module: [a] The photosensors of the camera covered a sensitive area of  $86.4 \times 86.4 \text{ mm}^2$ . To allow measurements during daylight a light-tight shutter was installed, which was also weather-sealed to provide protection from humidity and UV radiation. [b] Top view on the opened camera: the connectors on the upper side are for the output signals, bias voltage supply and water cooling, respectively.

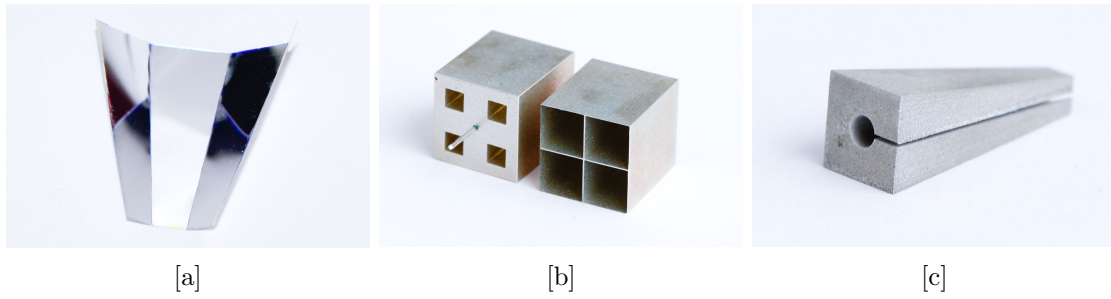


Figure 3.4.: Components for the light-concentrating cones: [a] The reflective foil was cut and scratched to facilitate the folding. [b] An aluminum frame provides stability for the thin reflective foil. The metal spike attaches the cones to the boards carrying the G-APDs. [c] A custom-made tool was used to hold the cones during the assembly.



Figure 3.5.: Assembled cone for the prototype module M0: the light is concentrated by reflections on the flat sides of the cone onto the sensitive area of the photosensor. 4 cone-photosensor pairs form one pixel of the module.

pixel.

The most important basic properties of such cones are the light collection efficiency and its angle dependency. Those properties were measured by U. Röser and S. Stark-Schneebeli (both ETH Zurich). I assisted in the setup of the measurements to ensure the correct use of the photosensors and the interpretation of the results by comparing the measurement with the simulation by I. Braun. The measurements were consistent within the margin of error after the introduction of surface roughness in the simulation. The simulation and early results were presented at the ICRC 2009 conference (see proceedings [108]).

### 3.1.2. Sensor unit mechanics

The G-APDs were placed in a tight grid which was produced in a 3D printing process (see figure 3.6). Below the grid were the carrier boards which provided the electronic contacts, to which the G-APDs were soldered. A metal spike on the aluminum frame of the cones

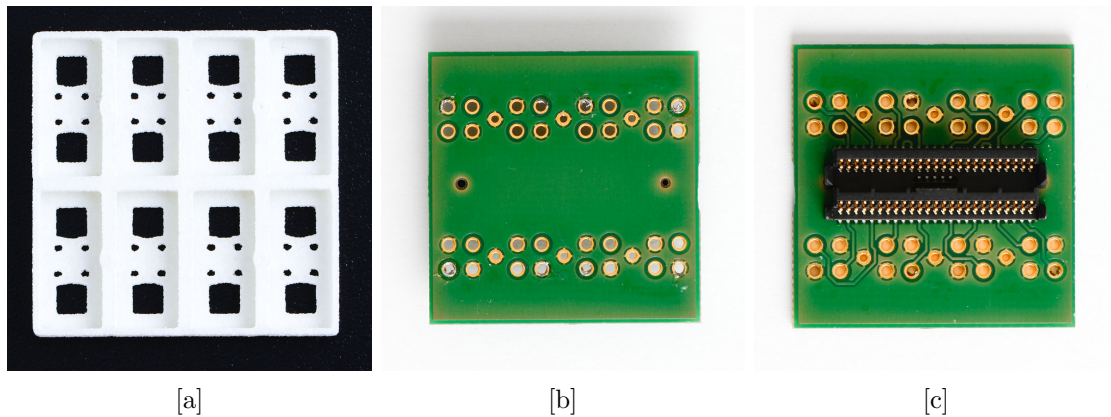


Figure 3.6.: [a] The G-APDs are placed in a tight grid which was produced using a 3D printing technique. [b] Front and [c] rear of the carrier boards which provide the electrical contacts for four pixels each.

fixed each block to the carrier boards and aligned the cones to the G-APDs<sup>(3)</sup>.

### 3.1.3. Electronics

The carrier boards were directly connected to the electronics boards, each of them providing the connections to 12 pixels (48 G-APDs). On these boards the signals of the 4 sensors of one pixel were summed up and shaped by an analog clipping circuit to limit the pulse decay time to  $<10$  ns). A transimpedance amplifier with an amplification ratio of  $4\text{ k}\Omega$  converted the current signals produced by the G-APDs into voltage pulses.

The next signal processing steps are the readout trigger and the digitization. Those were not performed in the M0 camera, but in a counting room, to which the signals were routed using coaxial cables of 20 m length. In the counting room, the signals were split in linear fan-out modules, which were developed in the electronics workshop of our institute<sup>(4)</sup>. One positive output was led to a ring buffer for the data digitization. For the inner 16 pixels, an inverted signal was led to a commercial CAEN<sup>(5)</sup> V812 module, which is based on the VME standard<sup>(6)</sup>. The module evaluates a majority coincidence: each signal is discriminated with an individually adjustable threshold, and the discriminated signals summed. The data acquisition electronics was triggered if  $N$  out of the 16 pixels were above their respective threshold, with  $N$  adjustable from 1 to 16.

### Data acquisition

The data was digitized using commercial boards equipped with the Domino Ring Sampling chip DRS2 [109]<sup>(7)</sup>. The signal is continuously stored in a capacitive ring buffer consisting of 1024 sampling cells each. When a trigger is issued, the writing is stopped and the cells read out and digitized in an Analog-digital converter (ADC). Compared to the direct,

<sup>3</sup>Note that with this mechanics the cones are positioned relative to the package of the G-APD and not the sensor chip, which leads to a partial light loss due to variations in the chip position (see section 2.3.1). This problem was solved for the final FACT camera (see section 3.4.1).

<sup>4</sup>The modules were developed by M. Morf and U. Röser (ETH Zurich) following the NIM standard.

<sup>5</sup>Costruzioni Apparecchiature Elettroniche Nucleari S.p.A., Italy, <http://www.caentechnologies.com>

<sup>6</sup>The VERSA module Eurocard (VME) standard defines a computer bus used for the communication of a wide range of electronics modules. Compared to the NIM standard, the VME standard is more modern and allows a faster communication between modules.

<sup>7</sup><http://drs.web.psi.ch>

continuous digitization in the ADC, this procedure has some advantages. A digitization process has three basic quantifiers, which are antagonistic: the sampling frequency, the resolution, and the power consumption. A power-saving approach requires a balance between high resolution and high sampling frequency, and it is not possible to optimize both parameters to the level desired for our project. The solution lies in the decoupling of the two steps: the analog sampling and temporary storing in the ring buffer allows to sample the signal with high frequency, and digitize later with a (comparably) low-speed ADC with high precision. In the case of the DRS2 chip, the sampling rate is between 0.5 GHz and 4.5 GHz, and the readout and digitization is at 40 MHz [109]. Each chip provides up to eight channels.

The 36 signals from the camera were fed into two commercial VME boards, which were equipped with four DRS2 chips on two custom-made mezzanine boards each<sup>(8)</sup>. The chips were run at 2 GHz, resulting in a pipeline length of 0.5  $\mu$ s. A VME single-board computer with an external hard disk was running the control software and saved the data for the later analysis.

#### 3.1.4. Front window and internal LED pulser

In front of the light-collecting cones, a front window from a UV-transparent PMMA was installed. The front window served two purposes: on the one hand, the window protected the light-collecting cones and the electronics from dust and humidity, and on the other hand it allowed to integrate a light-pulsing system into the camera. Fast LEDs were integrated into the sides of the window, and small holes drilled into the surface of the Plexiglas acted as scattering centers (see figure 3.7).

Using the LED system, the complete signal chain could be tested whether the camera shutter is open or closed, allowing system tests during daytime. The main purpose of the system was to provide a reference pulse, which could be used to monitor the G-APDs: the response of a G-APD depends strongly on the temperature (see section 2.2.1), which must be corrected for in the operation of the camera. For module M0, the approach was to use reference pulses, whose amplitude is kept constant by adapting the bias voltage (see also section 3.1.7).

#### 3.1.5. First air shower measurements

The construction of the module M0 was finished in early summer 2009. In order to prove the camera's ability to record air showers in a self-triggering mode, the camera was mounted on top of a small mirror on the roof of our institute at ETH Zurich (see figure 3.8). Both the camera and the mirror installation were fixed and did not allow to track a specific sky location. The mirror with a diameter of 90 cm and a focal length of 80 cm was looking in zenith direction. The camera was installed in focal distance of the mirror, with a FOV of 1.03° per pixel (see equation (1.3)).

In the night of July 2nd, 2009, the installed module M0 was for the first time opened and powered<sup>(9)</sup>. Using a majority coincidence of  $N = 4$  out of the 16 pixels and individual pixel thresholds of 40 mV (corresponding to roughly 5.7 photons), the very first air showers were recorded (see figure 3.9). To verify the air shower character of the recorded events, a comparison to simulated air showers was made. The simulated events were similar to

---

<sup>8</sup>The mezzanine boards were designed at the PSI Villigen.

<sup>9</sup>Unfortunately, I could not attend the first recording of air showers on site, since I was attending the PD09 conference in Matsumoto, Japan, where I presented my results on the characterization of G-APDs.



Figure 3.7.: The PMMA front window is equipped with LEDs at the side to provide a reference light pulse. Small holes were drilled into the surface of the window to act as light scattering center. Photo courtesy of Q. Weitzel.

the recorded ones both in shape and timing of the shower images, which confirmed the identity of the events.

The construction and first measurements with the module M0 were reported at the ICRC 2009 conference. Since its proceedings [110] had to be submitted before the conference, the measurements were not yet included there. A detailed description of the camera and the first measurements were published in H. Anderhub *et al.* [65].

### 3.1.6. Rate scans

Besides the observed air shower images and their similarity to simulated events, another important measurement confirmed the functionality of the prototype module: threshold rate scans. For this measurement, the threshold of the individual pixels was gradually increased, while the majority logic ( $N$  out of 16) was kept constant. Such rate scans show two distinctive branches: for low thresholds, the shape is dominated by random triggers induced by night sky background (NSB) photons, whereas for large thresholds correlated photon arrival times are necessary, which is the case for Cherenkov air shower photons.

The measurement I carried out in the night of September 23rd, 2009, together with P. Vogler. A majority coincidence of  $N = 3$  out of 16 was chosen<sup>(10)</sup>. The measurement was very successful (see figure 3.10), and confirmed that the previously recorded images correspond to Cherenkov air showers. The measurement was originally published in P. Vogler's Master thesis [111], more details on the measurement can be found there.

<sup>10</sup> $N = 4$  results in very low trigger rates, increasing the measurement time dramatically.



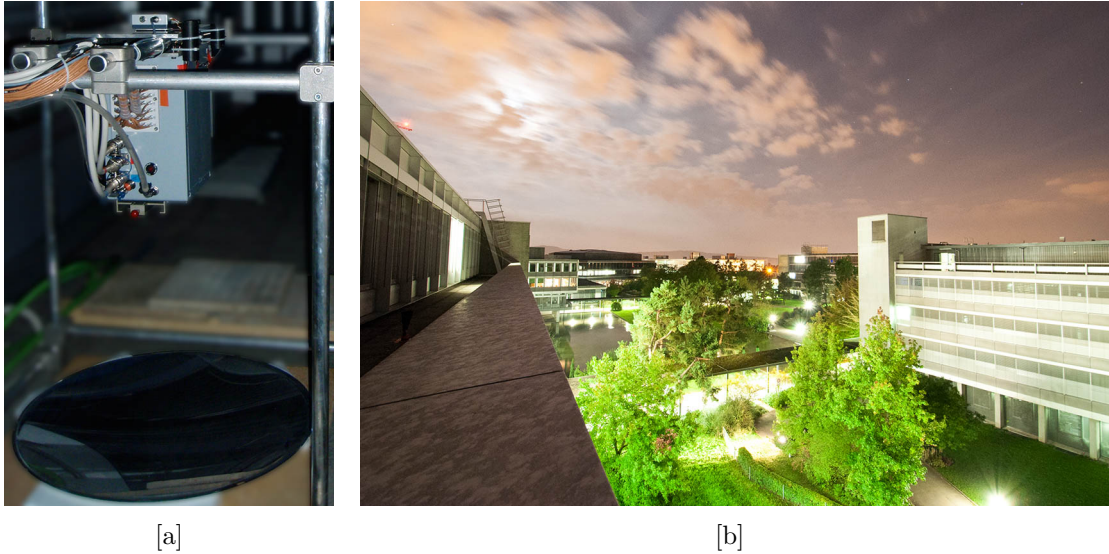


Figure 3.8.: Setup of the module M0 on the roof of our institute at ETH Zurich: [a] The module (gray box) was mounted on top of a mirror (dark ellipse) using a metal frame. Picture courtesy of Q. Weitzel. [b] A night-time picture of the immediate surroundings of the setup shows the high level of background light at this location.

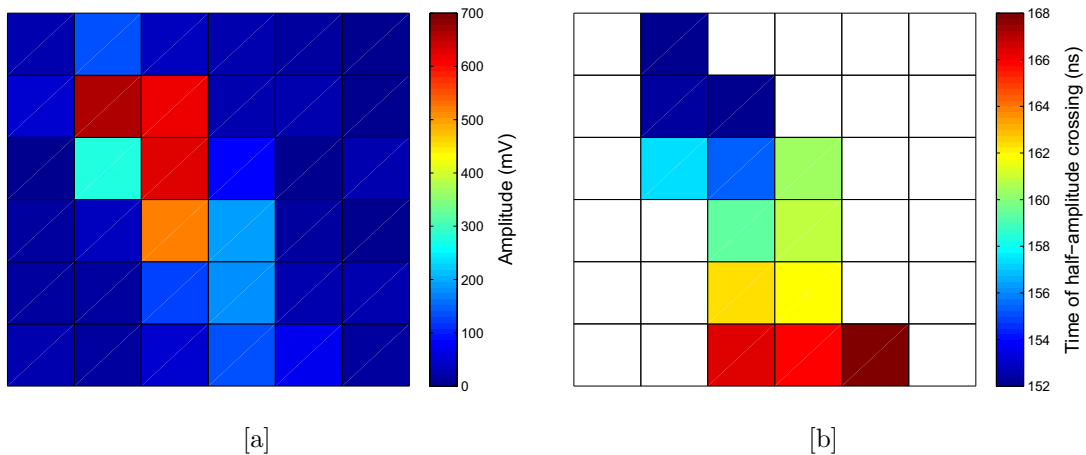


Figure 3.9.: Example of a shower recorded with M0: [a] Amplitude and [b] arrival time of the shower in the camera. The shower moves from the top left to the bottom within  $\sim 15$  ns and extends over more than  $6^\circ$ , indicating a very large energy of the primary particle above several TeV and a large angle of the shower direction to the mirror's pointing direction. Plots from [65].

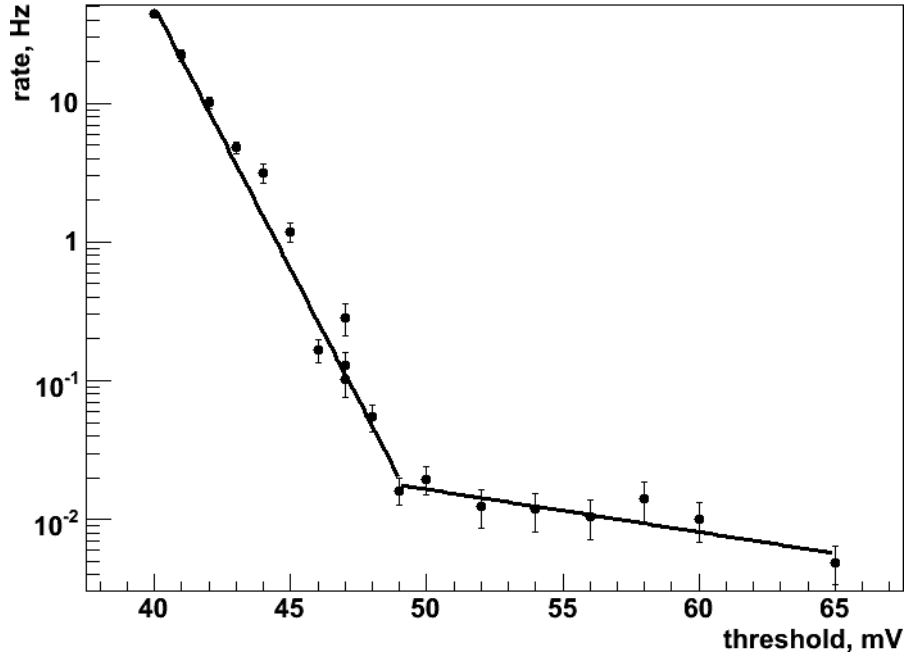


Figure 3.10.: Rate vs. threshold scan with the prototype module M0: for low thresholds, accidental coincidences of NSB photons dominate, which vanish for larger thresholds. The remaining events are based on correlated photon arrival times on the sensors, as they are produced by Cherenkov air showers. Plot from [111].

### 3.1.7. Temperature stabilization

The strong temperature dependence of the G-APD’s over-voltage and thus the device response is considered one of the basic challenges in the use of G-APDs in IACT cameras. When the temperature changes are small<sup>(11)</sup>, the correction can in principle be made in the data analysis if the temperature is known, however on the cost of non-optimal device performance. For large temperature changes, the bias voltage must be adapted according to the temperature changes.

The temperature correction is in principle possible using a passive circuit incorporating thermistors. However, the required linear behavior with high precision in a large temperature range is difficult to achieve, in particular for a large number of channels. The approach we chose is thus to use a bias voltage supply which has the ability to change the voltage during operation. A control software would calculate the required voltage and send it to the bias voltage supply.

For the prototype module M0, the available parameters for this control software were the temperature sensors in the camera and the pulses provided by the LED system: those pulses are periodically generated and recorded in the same way as external Cherenkov flashes. An on-line software analyzed the magnitude of the pulses and compared them to reference values which were defined under controlled and known conditions. If a systematic difference between the on-line and reference value is found, a voltage correction is sent to the bias voltage crate and the pulse magnitude checked for the desired effect.

The software controlling the bias voltages for M0 was referenced as “feedback”-software and was written by O. Grimm (ETH Zurich), who also performed a test of the algorithm

<sup>11</sup>This assessment must be based on the temperature coefficient (around 55 mV/K), the over-voltage (around 1.1 V) and the dependence of the device parameters on the over-voltage. See chapter 2 for details on the operation of G-APDs.

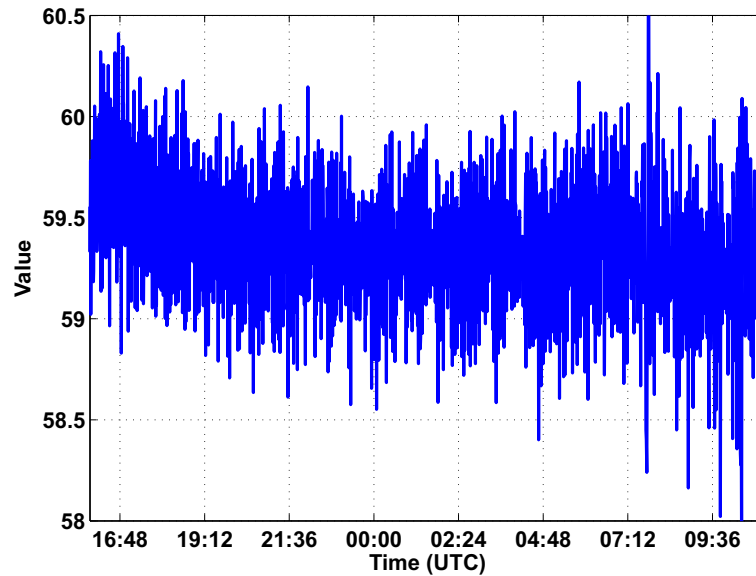


Figure 3.11.: Stability of the light pulses during the second half of the extended run of M0: even though the ambient temperature changed by almost 8 °C, the G-APD response to a reference light pulse is kept constant to 0.5 % with a feedback software, which monitored the pulses and adapted the bias voltage if necessary. Figure by O. Grimm [112].

with a long run of M0 over more than 40 hours. During the first half the feedback system was disabled and the change of the LED pulses with the temperature monitored. The observed temperature increase of 10 °C caused a drop of the pulse amplitude by almost a factor of four, even though the over-voltage is only approximately divided in half and the linear dependence of the G-APD gain on the over-voltage (see section 2.2.4). However, I could explain the drastic amplitude drop with the full analysis of the voltage dependence of the G-APD response including the PDE and the crosstalk probability (as presented in section 2.4.1).

For the second half of the run, the feedback software was active and regulated the bias voltage. In this time the pulses (and thus the G-APD response) could be kept stable to 0.5%, during an ambient temperature decrease around 8 °C (see figure 3.11). The measurement represented an important step to confirm the applicability of G-APDs under outdoor conditions and was published in 2011 [112].

## 3.2. The FACT camera: overview

Already during the construction of the prototype module M0 it became clear that a full camera would better follow a different design than the prototype module. The major redesign was based on new simulations on the light-concentrating cones: solid cones allow larger concentration ratios of the input to output area, thus allowing the use of a single G-APD per pixel. The saved cost in the number of G-APDs could be put to electronics channels, thus providing the possibility to go to nearly optimal specifications for a single telescope: pixels with a FOV of 0.11° and a camera diameter of 4.5° (see section 1.2.7).

Going from folded reflective foil to solid cones also allowed more complex forms of light-concentrators, so the entrance window could be made hexagonal instead of square. The corresponding hexagonal pixel arrangement has additional symmetries and well-defined next neighbors, which are advantageous in the data analysis. Further it would require less



modifications to use the MARS analysis package [113, 114], which was originally developed for the MAGIC telescopes.

### **Integrated digitization**

Based on the experience gained with the prototype module M0, also the readout for the full camera should be based on a Domino Ring Sampling chip, but in the updated version DRS4<sup>(12)</sup>. In the prototype module, the signals were amplified inside the camera box, and led to a counting room via long cables ( $\sim 20$  m) for the digitization. This approach was put up for debate, the alternative being the digitization inside the camera.

One major advantage of the M0 approach was that existing, commercial electronics boards could be used. However, it would have been impossible to obtain enough boards equipped with the DRS2 chip to read out a full camera, and commercial boards with the DRS4 chip were only just being developed. A quote from one manufacturer was a similar price per readout channel as our estimates for an in-house development of new boards, which would be tailored to our other electronics. Furthermore the manufacturer's schedule for the board production was barely within our own schedule.

When the electronics is tailored for our project, it opens up a new possibility: the digitization of the data stream inside the camera. This has the advantage that the G-APD signals are digitized without being transferred via long cables and the resulting quality loss. Since the investigation of the G-APD properties is one of the key goals of the project and relies heavily on the single-p.e. resolution of the devices, the signal quality is one of the crucial characteristics of the planned camera.

A potential drawback of the integrated digitization is the additional weight of the electronics in the camera. However, if the signals of every single pixel in the camera must be transmitted in high quality, the required cables would also be of a significant weight. Only the confined space and the resulting heat problem would be challenges in the integrated solution.

After a careful examination of both options, the collaboration finally decided to favor the internal digitization due to the focus on signal quality.

### **Mechanics**

The integration of the readout electronics into the camera required a detailed planning of the available space. The existing telescope structure of the CT3 telescope on the Roque de los Muchachos on La Palma provides a fixation ring in focal distance of the mirror dish. The size of this ring is sufficient for the sensor area, but too narrow to fit the full electronics. The camera diameter is thus larger behind the fixation ring.

Since the tests with the prototype module M0 showed that the stable operation of G-APDs is possible during ambient temperature changes, no temperature stabilization is included in the sensor compartment of the camera. To protect the G-APDs from the heat of the electronics, the sensor compartment is thermally decoupled from the rest of the camera with an isolating baffle plate.

Four electronics crates are fixed to a central aluminum plate and contain the amplification and readout electronics. The aluminum plate is water-cooled and absorbs the heat of the electronics. The connectors for the electronics and water cooling are integrated in the backplane of the camera. Figure 3.12 shows an overview on the camera mechanics.

---

<sup>12</sup><http://drs.web.psi.ch>

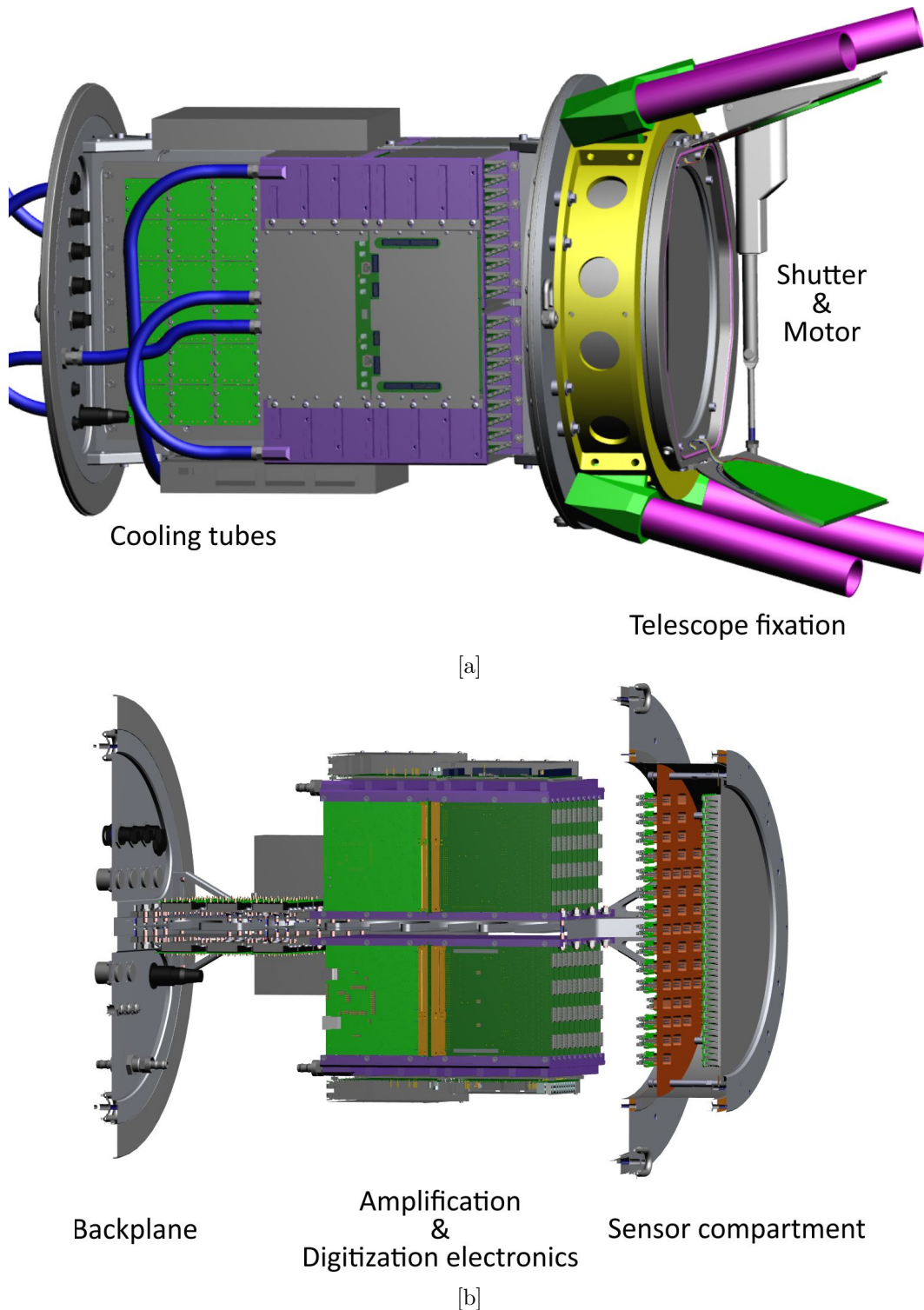


Figure 3.12.: Illustrations of the FACT camera (cover removed): [a] The camera is fixed at its front end to a fixation ring (yellow) of the telescope structure. An automatic shutter protects the front window from the harsh outdoor conditions with wind, rain or even sand. [b] Cross section with horizontal cooling plate: photons coming from the right are translated into electrical signals in the sensor compartment. An insulation plate protects the light sensors from the heat of the electronics. The signals are amplified and digitized in the central part of the camera. The space between the electronics and the backplane is occupied by DC-DC converters (not shown). Network switches reduce the number of cables which are guided to the counting house. Illustrations based on a 3D CAD model by A. Gendotti (ETH Zurich).

### 3.2.1. Photon rate estimates

The design of the camera electronics, in particular the bias voltage supply, requires an estimate of the currents in the camera. These currents are dominated by background light, be it from stars, airglow, or the second-brightest object in the sky, the moon<sup>(13)</sup> (see section 1.2.5 for an introduction). Based on estimates of the background photon rates, the approximate currents can be predicted. The estimated background rates are also a necessary input for the telescope simulation, in particular the trigger studies.

In addition, using a new type of photosensor inevitably raises the question, how the sensitivity of the sensor is competing with the existing technology. I thus compared the G-APDs used in FACT (Hamamatsu S10362-33-050C) with the PMTs used in the MAGIC-II telescope, which were optimized for this particular application. Three spectra were used in the comparison, an averaged Cherenkov spectrum (our “signal”) and the background spectra from moonlight and NSB light<sup>(14)</sup>.

#### Rate estimate using a hand-held light meter and a literature reference

During my shift at the MAGIC telescope in March 2009, I took several measurements of the sky brightness using a hand-held light meter (Unihedron “Sky Quality Meter” SQM-L<sup>(15)</sup>). The unit measures the apparent brightness of the sky in a cone with an opening angle around 10° in magnitudes per squared second of arc (mag/arcsec<sup>2</sup>). According to its instruction sheet [115], the conversion to candela per square meter is as follows:

$$[\text{cd/m}^2] = 10.8 \cdot 10^4 \cdot 10^{-0.4[\text{mag/arcsec}^2]} \quad (3.1)$$

Since a candela is defined as 1/683 watt/steradian of monochromatic light with a frequency of 540 THz, the corresponding photon rate is

$$[\text{photons/m}^2/\text{steradian/s}] = \frac{1}{683} \underbrace{\frac{1}{h\nu}}_{\text{photon energy}} \cdot 10.8 \cdot 10^4 \cdot 10^{-0.4[\text{mag/arcsec}^2]} \quad (3.2)$$

$$= 4.092 \cdot 10^{15} \cdot 10.8 \cdot 10^4 \cdot 10^{-0.4[\text{mag/arcsec}^2]} \quad (3.3)$$

using  $\nu = 540$  THz and Planck’s constant  $6.626 \times 10^{-34}$  Js. The pixels for FACT have an area of 78 mm<sup>2</sup> and an opening angle around 20°, i.e. 0.38 steradian<sup>(16)</sup>. Using these values, the corresponding photon rates for SQM readings can be calculated (see table 3.1).

A total of 20 measurements was made during various conditions, from darkest night to twilight or when the full moon was in the sky and MAGIC was not operating. The resulting readings during darkest night were at  $>21$  mag/arcsec<sup>2</sup>, corresponding to  $<50$  MHz of photons in a FACT pixel.

As a reference value the standard publication for NSB light on La Palma is consulted, where  $2.6 \times 10^{12}$  photons sr<sup>-1</sup> s<sup>-1</sup> m<sup>-2</sup> in the range from 300 nm to 650 nm are stated [20]. Using the FACT-specific pixel area and opening angle, the resulting 77 MHz are comparable to a reading of the SQM of 20.5. This is slightly higher than the measurements during darkest night, which is most probably explained by the sensitivity curve of the hand-held

<sup>13</sup>Observations with the brightest object above horizon are not yet possible with IACTs, independent of the technology.

<sup>14</sup>The term NSB comprises all other sources of light of the night sky besides moonlight and the brightest stars.

<sup>15</sup>Unihedron, Canada, <http://www.unihedron.com>

<sup>16</sup>The unit sphere surface in steradian is calculated as  $A = 2\pi(1 - \cos(\alpha))$ .

SQM reading [mag/arcsec <sup>2</sup> ]	Photon rate [MHz]
22.0	21
21.5	33
21.0	52
20.5	83
20.0	131
19.5	207
19.0	329
18.5	521
18.0	826
17.5	1309
17.0	2074
16.5	3288
16.0	5211

Table 3.1.: Corresponding photon rates in a FACT pixel for SQM readings: the measurements during darkest night ( $> 21$ ) correspond to pixel rates  $< 50$  MHz in the FACT pixels. For brighter values, rates in the GHz range can be expected.

device (the SI unit candela for other light frequencies than  $540 \times 10^{12}$  Hz are normalized according to the sensitivity of the human eye)<sup>(17)</sup>.

### Current prediction

Using these values, an estimate for the current per pixel can be made. The current is the product of the approximate single cell rates  $R_{\text{cell}}$  multiplied by the gain  $G$  and the electron charge  $e$ . The single cell rates are estimated by including estimated values for afterpulses ( $\mu_{\text{ap}}$ ), crosstalk ( $\mu_{\text{ct}}$ ) and dark counts ( $R_{\text{dc}}$ ):

$$I = R_{\text{cell}} \cdot G \cdot e \quad (3.4)$$

$$= (R_{\text{bg}} \cdot (1 + \mu_{\text{ap}}) + R_{\text{dc}}) (1 + \mu_{\text{ct}}) \cdot G \cdot e \quad (3.5)$$

$$I_{\text{d}} = 5.7 \mu\text{A} \quad (\text{dark night, } R_{\text{bg}} = 30 \text{ MHz}) \quad (3.6)$$

$$I_{\text{m}} = 0.33 \text{ mA} \quad (\text{twilight/moon observation, } R_{\text{bg}} = 2 \text{ GHz}) \quad (3.7)$$

The used values are  $\mu_{\text{ap}} = 0.15$  [67],  $\mu_{\text{ct}} = 0.2$  (see section 2.3.2),  $R_{\text{dc}} = 5 \text{ MHz}$  [64] and  $G = 7.5 \times 10^5$  (see table 2.2).

### Comparison PMT-G-APD

A more detailed estimate was made using spectra of Cherenkov light, the night sky background during dark nights and moon light. The spectra were multiplied by the sensitivity spectra and integrated for PMTs and G-APDs to get a relative comparison of the rates.

The main work for this comparison was to get reliable data and its conversion to photon rates. The following sources were used:

---

<sup>17</sup>Though it is also possible to explain the difference with higher background light during the measurements in C. Benn and S. Ellison [20], it appears rather unlikely due to the described method.

**Cherenkov spectrum:** The rate of emitted Cherenkov light from air showers is proportional to the inverse square of the wavelength  $1/\lambda^2$ , but is reduced due to atmospheric absorption in particular for small wavelengths (see sections 1.2.3 and 1.2.4). The used spectrum is based on a simulation by T. Bretz of electromagnetic air showers with energies from 100 GeV to 50 TeV with a spectral index of -2.7, measured at an altitude of 2000 m above sea level.

**NSB spectrum:** The spectral intensity of the night sky background light in moonless nights on La Palma was measured by C. Benn and S. Ellison [20], a measurement which is widely used as reference. However, the intensity was measured in Jansky per squared second of arc and plotted versus the wavelength of the light. Unfortunately, the Jansky is defined as  $10^{-26} \text{ W/m}^2\text{Hz}$  (i.e. the differential intensity versus the *frequency*), such that the area under the curve does neither correspond to an intensity nor a rate. If we want to integrate the data, a transformation is necessary (see below).

**Moon spectrum:** The spectrum of moonlight on earth is variable and depends both on its phase and the observation angle. Most of the spectra found in literature were measured above the atmosphere for satellite experiments, and would thus require precise data of the spectral atmospheric absorption. The more precise approach is thus to use the direct solar spectrum on earth surface multiplied with a spatially averaged lunar spectral albedo. The latter was found in S. Miller and R. Turner [23], and for the sun the reference spectrum by ASTM International [116] was used. The reference spectrum exists in two versions, once with a hemispherical integration and once for a field of view of  $5.8^\circ$  centered on the sun. The hemispherical spectrum contains more scattered light, so the difference between the two spectra is most distinct for small wavelengths<sup>(18)</sup>. Since I wanted to get an upper limit on the ratio between PMT and G-APD, the direct spectrum was used. The reference spectra are provided in  $\text{W/m}^2\text{nm}$ , so again a transformation is necessary.

The derivations of the transformations can be found in appendix A.5. The solar spectrum needs to be multiplied by the photon wavelength  $\lambda$  to get a rate, and the NSB spectrum needs a division by  $\lambda$ .

In addition to the spectra, the sensitivities of PMT and G-APD are necessary for the rate comparison. The PMT sensitivity is taken from a publication of the MAGIC-II telescope [84]. The G-APD values are taken from the manufacturer’s datasheet [64]. The measurement “includes effects of crosstalk and afterpulses” [64], which needs to be corrected. Since this overestimation is linear in the PDE (at least if the dark current is subtracted), the curve can be scaled according to an own measurement [67] (see also section 2.2.2). Furthermore, the published spectrum only goes up to 900 nm, missing a significant part of moonlight and NSB photons. The spectrum was thus extended with a polynomial fit to 1000 nm where the fit becomes zero. The final spectra and sensitivities are shown in figure 3.13.

For the comparison of the light captured by PMT and G-APD, the spectra are multiplied by the respective sensitivities, integrated and the ratios calculated. For Cherenkov light, moonlight and NSB light the ratios are 1.17, 3.2 and 4.2, respectively. As expected, G-APDs collect more Cherenkov light (17%), and significantly more background light<sup>(19)</sup>. The normalized spectral integrals can be found in figure 3.14.

<sup>18</sup>The dominating process is Rayleigh scattering, which occurs proportional to  $\sim 1/\lambda^4$ .

<sup>19</sup>Note that for PMT an additional factor around 0.8 – 0.9 would be necessary, since not all electrons from the cathode are collected in the first dynode. This factor is called collection efficiency (CE). Including a factor of 0.85 the ratios are 1.37, 3.8 and 4.9 for Cherenkov light, moonlight and NSB light.

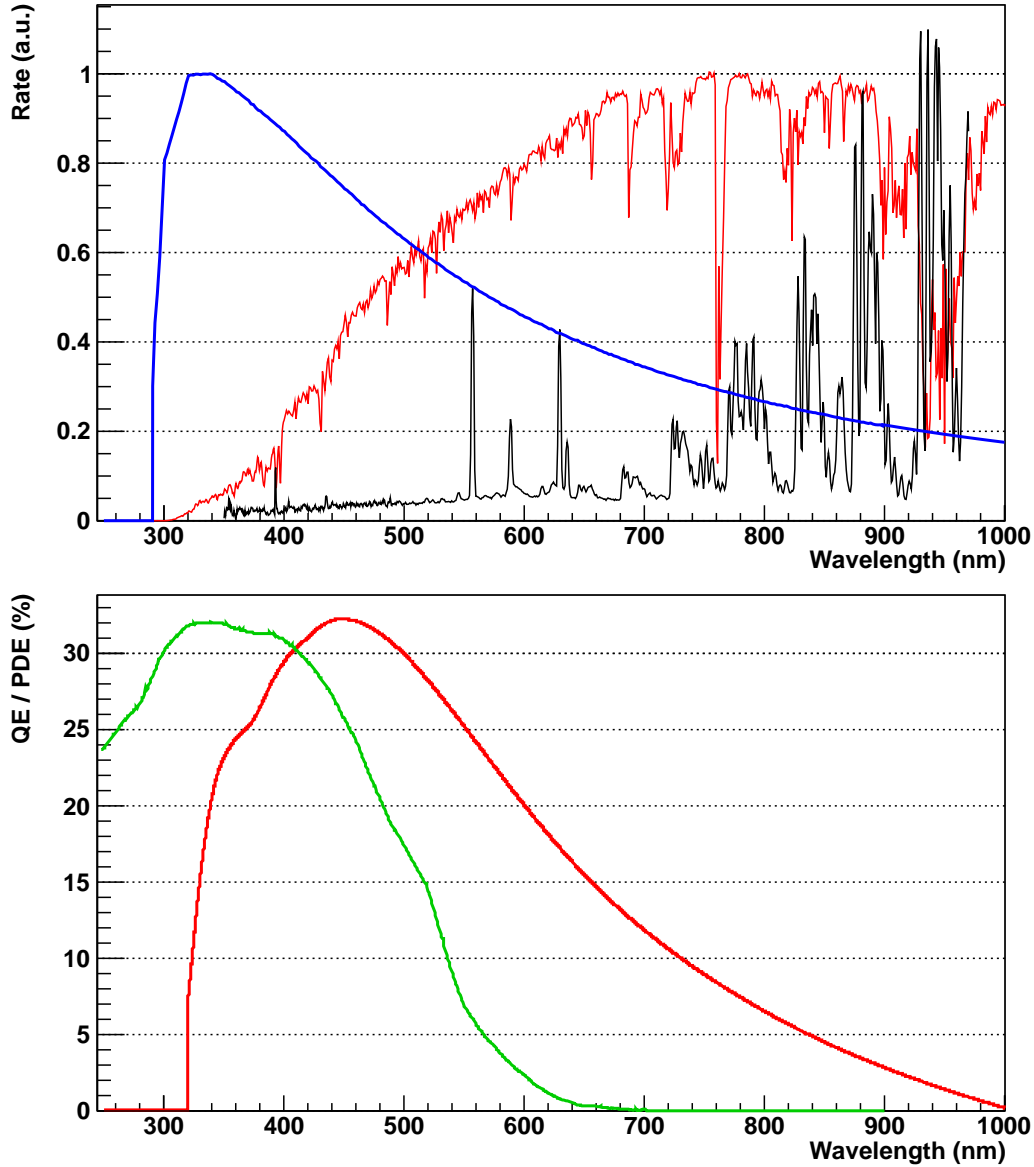


Figure 3.13.: **Top:** Spectra of Cherenkov light (blue, from simulation), moonlight (red) [23, 116] and other sources of background light (NSB, black) [20]. The moonlight and the NSB spectrum were weighted with  $\lambda$  and  $1/\lambda$ , respectively, to convert the original intensities to rates (see text). While the Cherenkov spectrum peaks around 330 nm, the intensity of background light is very low in this region. **Bottom:** QE of the MAGIC-II PMTs (green) [84] and PDE of the G-APDs used in FACT (red) [64, 67]. Due to the tail towards large wavelengths, the G-APDs collect some additional Cherenkov light, but significantly more background light.

The potential problems from the higher background rates must be evaluated under consideration of the other device properties: most PMT-based telescopes are not operating under strong moon conditions to protect the sensors, G-APDs have a much higher tolerance in this regard. Even when the background rates are larger, the telescope operation is possible even though its performance will be reduced.

For nights with low background rates (dark nights), it must be considered that Cherenkov photons are time-coincident whereas the background photons are random. Triggering the readout of a telescope is based on the recognition of photon coincidences, which of course worsens with higher background rates, but far less than the often used  $1/\sqrt{N}$  (see appendix A.4). In order to judge the full effect on a telescope's trigger threshold, a full simulation including e.g. PMT afterpulses and G-APD crosstalk is necessary.

In summary, G-APDs collect much more background light than PMTs. While this would be a problem for PMTs due to the device degradation, it is no concern for G-APDs. Concerning the readout triggering, the lack of PMT afterpulses are an important plus for G-APDs, which needs a careful weighting up against the higher background rate and the effect of crosstalk. Finally, G-APDs have a better pulse resolution and ENF (see section 2.5.4), which are important for the signal size reconstruction independent of the background rate.

### 3.3. Solid light-collecting cones

#### 3.3.1. Concept

The light-collecting cones have to serve a variety of functions. The most basic one is to eliminate dead space between the photosensors: PMTs are typically round and cannot be packed neither hexagonally nor in a square arrangement without losing sensitive area (9.3% and 21.5%, respectively). The G-APDs available at the time of the design of the FACT camera were integrated in a packaging significantly larger than the sensitive area of the chip (see section 2.3.1 for our devices). The cones thus also had the function to increase the sensitive area. Additionally, the G-APD market prices were around 10 US\$/mm<sup>2</sup>, so rather high to cover the full camera area.

The problem with the dead area can be minimized if the photosensor is delivered without packaging (e.g. Surface Mount Device (SMD) G-APDs). Together with the dramatically decreasing market prices of the devices, it would today be possible (but still expensive) to cover the full camera area with photosensors. However, there is an important reason to use cones anyway: the reduction of background light. As seen from the camera, the signal photons from the direction of the mirror dish arrive at small incidence angles, whereas every photon with larger incidence angle belongs to the background. The efficiency of the cones is thus optimized to guide photons below a cutoff angle onto the sensitive area, and reject photons from directions above this angle.

For the optimization of the cone geometry, computer Monte Carlo (MC) simulations are used. For their input parameters and verification of a correct implementation, real-world measurements are necessary. The cone simulation was programmed by I. Braun, the measurements were set up and operated by me. One of the first and most basic measurements was the angle dependence of the PDE of the G-APDs (see 2.3.6).

#### 3.3.2. Simulation: basic designs

The design of a light-collecting optics for a photosensor usually starts with the research by R. Winston [117]. His standard design ("Winston cone") uses tilted parabolic curves,

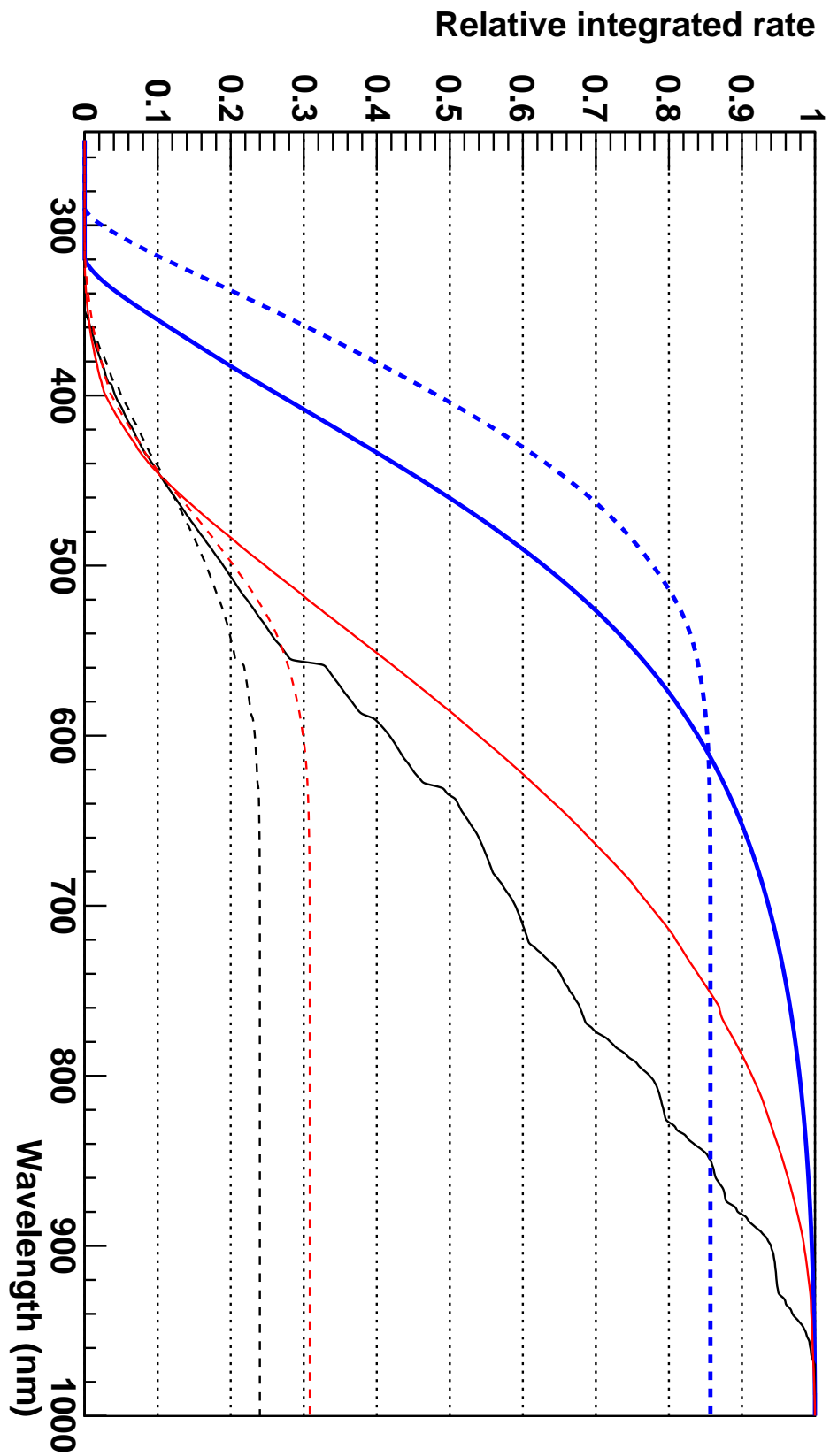


Figure 3.14.: Additive spectra of Cherenkov light (blue), moonlight (red) and NSB light (black) as measured with G-APDs (solid lines) and PMTs (dashed lines). PMTs collect about 85% of the Cherenkov light compared to G-APDs, but only 30% and 25% of the moonlight and NSB light, respectively. Below 400 nm, almost only Cherenkov light is collected, whereas above 750 nm, G-APDs collect mostly background light.



which reflect light arriving at the entrance area with an angle below a cutoff  $\Theta_{\max}$  onto the exit area within one reflection, whereas light arriving at a larger angle is reflected onto the opposite side and leaves the cone in the entrance direction. For an axisymmetric Winston design the maximal concentration ratio  $R_{\max}$  between the entrance area and exit area is defined by the cutoff angle  $\Theta_{\max}$ :

$$R_{\max} = \left( \frac{1}{\sin(\Theta_{\max})} \right)^2 \quad (3.8)$$

All calculations assume a perfect efficiency of the reflections. If the light concentrator has a refractive index  $n$  not equal to 1 (i.e. the cone is not open with reflective sides but made from a refractive material), the efficiency is higher by a factor of  $n^2$ : the incident light with an angle  $\Theta'_{\max}$  is refracted at the entrance of the cone to an angle  $\Theta_{\max}$  in the cone according to Snell's law ( $\sin(\Theta'_{\max}) = n \cdot \sin(\Theta_{\max})$ ). The maximal concentration ratio is thus

$$R_{\max} = \left( \frac{1}{\sin(\Theta'_{\max})/n} \right)^2 = \left( \frac{n}{\sin(\Theta'_{\max})} \right)^2 \quad (3.9)$$

for solid, axisymmetric Winston cones. The cutoff angle  $\Theta_{\max}$  is defined by the telescope geometry, specifically the focal length  $f$  and the mirror diameter  $D$  of the telescope:

$$\Theta_{\max} = \tan^{-1} \left( \frac{D}{2f} \right) \quad (3.10)$$

However, Winston's calculations were two-dimensional, and were then extrapolated to three-dimensional geometries. While there is a sharp cutoff angle in the two-dimensional case, the three-dimensional efficiency is "smeared out" (see figure 3.15). For geometries with hexagonal entrance and exit windows, Bézier curves were found to produce a sharper cutoff than the original Winston design [118].

The geometry of the entrance window of the FACT pixels was discussed to be either hexagonal, rectangular, or square, and the pixels would be arranged in a grid with the same geometry as the respective entrance window. Though it is possible to use rectangular cones in a hexagonal array (proposed by D. Hildebrand), this design has the disadvantage that a photon is not necessarily detected by the pixel whose center is closest to its impact location (see figure 3.16).

The mechanics for the sensor compartment (in particular for the electronics boards) is in general less complex in a rectangular or square arrangement. However, the existing telescope mount is too narrow at the focal plane to contain the planned readout electronics, requiring the use of cables between photosensors and electronics. Those cables allow the reorganization of the hexagonal pixel array to a simpler, rectangular arrangement of the readout electronics channels.

The hexagonal array has some advantages in the analysis of the data, starting from the extended symmetry (especially considering the well-defined next neighbors of each pixel) to the possibility to use existing algorithms from other Cherenkov telescopes. This would also facilitate the comparison of the FACT camera performance to existing camera designs.

For geometries with hexagonal entrance and square exit windows (matching the photosensor), various wall shapes were tested and compared, from flat sides to parabolic to tilted parabolas as in the Winston design.

### 3.3.3. Simulation: setup

Besides the geometry of the cones, a variety of settings could be adjusted:

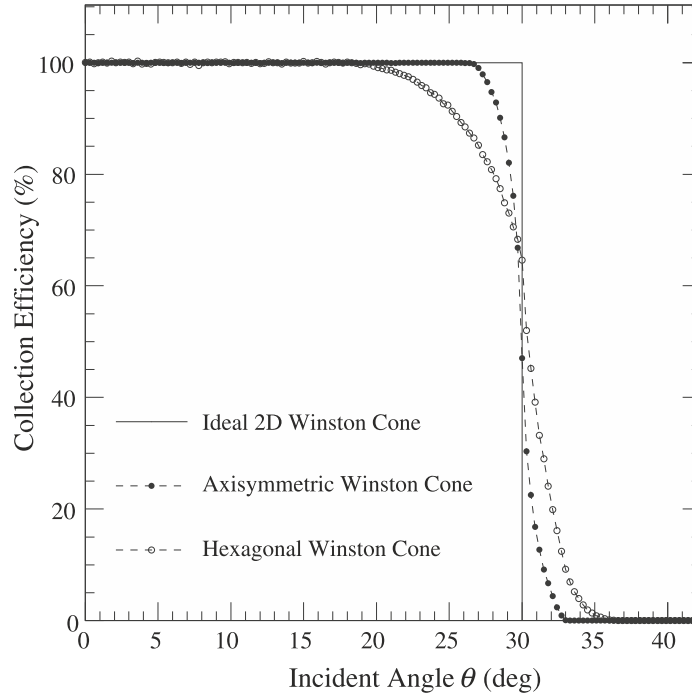


Figure 3.15.: Efficiency of the light-collecting cones as a function of the light's incidence angle: the ideal cone has a sharp cutoff at a predefined angle  $\Theta_{\max}$  (in this plot  $\Theta_{\max} = 30^\circ$ ). For three-dimensional geometries the sharp cutoff is smeared out. Figure from [118].

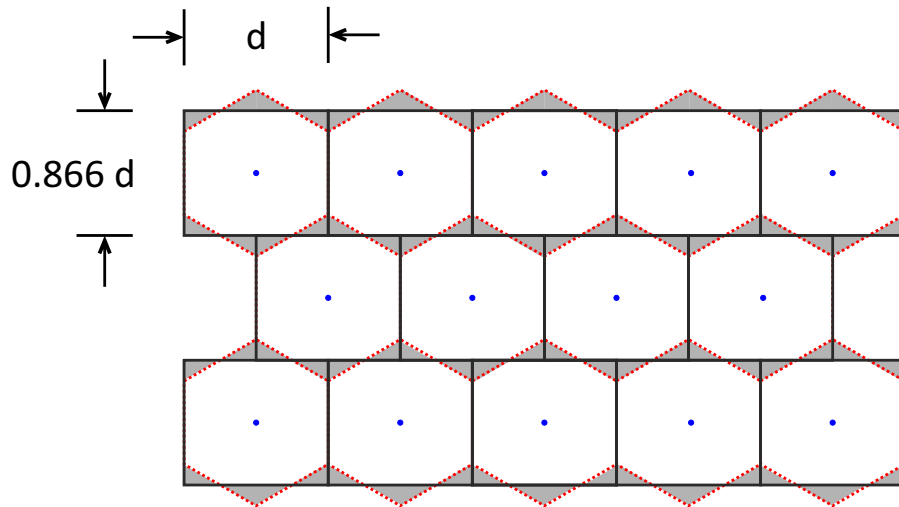


Figure 3.16.: Arrangement of rectangular pixels in a hexagonal array: using an aspect ratio of  $\sqrt{3}/2 : 1 = 0.866 : 1$ , it is possible to arrange rectangles in a hexagonal array. The problem with this design is that photons arriving at a gray area are not assigned to the pixel with the closest center (blue dots). The fraction of wrongly assigned photons is  $1/12 = 8.3\%$ .



Figure 3.17.: Geometry of the final cones for FACT: the hexagonal entrance area is concentrated by a factor of ten onto the square exit area. Four of the six corners of the entrance area are connected via an edge to the corners of the exit window, whereas the other two edges vanish into opposite sides of the square.

- The refractive index of the cone material.
- The spectral absorption properties of the cone.
- The geometry, layers, and angular acceptance of the photosensor.
- The spectrum and angular distribution of the input photons.
- The reflection properties (efficiency and surface roughness).

The output distribution is then simulated according to the geometric propagation of the photons (including Fresnel reflection and refraction at boundaries), reflection losses (negligible for solid cones with total internal reflection) and wavelength dependent absorption.

As input spectrum, an averaged Cherenkov spectrum is used. The angle distribution of the incoming photons  $\frac{dN}{d\Theta}$  is proportional to  $\sin(\Theta)^2$  if  $\Theta$  is the angle from the photon direction to the telescope main axis: the mirror area per angle rises with the square of the radius from the mirror center.

### 3.3.4. Simulation: final cone geometry

Based on the simulation, the final cones have parabolic sides. Those cones show a slightly higher transmission than the tilted parabolas of the Winston design. While the Winston design guides more photons onto the exit area and has a sharper angular cutoff, the photons arrive at larger angles which leads to losses at the chip surface due to Fresnel losses [119, 120].

The cones have a hexagonal entrance area with an inner diameter of 9.5 mm, which is also the step-size of the hexagonal pixel grid. The exit area is square with side lengths of 2.8 mm. The ratio from the input area ( $78.16 \text{ mm}^2$ ) to the output area ( $7.84 \text{ mm}^2$ ) is 9.97. The area ratio compared to a bare G-APD chip with 3 mm side length is 8.68.

The outer diameter of the cones is a factor of  $2/\sqrt{3} = 1.15$  larger than the inner diameter and is thus 10.97 mm. The sides of the hexagon have half this length, i.e. 5.48 mm.

### 3.3.5. Light-absorbing grid

The simulation also revealed another possible issue: optical inter-pixel crosstalk. Photons arriving in one cone might leave the cone and be detected in a neighboring pixel. For photons arriving at a small incidence angle, this is rarely the case, as they are mostly reflected onto the sensitive surface of the photosensor. Photons with large incidence angle (i.e. above the cutoff) are partly reflected backwards towards the entrance area of the cone, and partly leave the cone on its side.

As the signal photons arrive from the mirror dish and thus at a small angle, the problem is centered around NSB photons, which would be increased by almost 30 % according to the simulation. Using a 12 mm high hexagonal grid between the cones would absorb 88 % of these photons. It would have been placed after the optical part of the sensor compartment was finished<sup>(20)</sup>.

Two grids were evaluated: a commercial honeycomb for light-weight structures and a self-made paper grid. The commercial honeycomb (see figure 3.18) consists of a cardboard which is coated with an epoxy resin, making the grid rigid. The step size of the hexagonal cells is 10 mm, slightly larger than the desired 9.5 mm. There were several problems with this grid: one concern voiced by the electronics department was that the epoxy resin could accumulate electrical charge on its surface and distort the G-APD signals. The more difficult concern was the installation of the grid: the G-APDs are only slightly smaller than the grid. Since the grid geometry is not very precise, it would be difficult to place the grid over multiple pixels simultaneously. Additionally it would have to be cut every three to four pixels to correct the shift in the cell step size.

Due to the difficulties with the epoxy grid I decided to build a flexible grid from paper: a black paper was prepared with scratches to facilitate the folding and cut into strips, which were glued together to form a hexagonal grid (see figure 3.19). The grid was flexible enough to be placed over multiple pixels at once. In order to withstand a possible increased humidity, the paper would need to be treated with a water-repellent. The disadvantages of this grid are its unknown long-term behavior and the tedious construction. As with the epoxy grid, its electrical properties are unclear.

Due to the difficulties with both grids, it was decided not to install a grid in the FACT camera and accept the possible higher NSB photon rate.

### 3.3.6. Cone prototypes

The cones were manufactured by the company IMOS<sup>(21)</sup> by injection molding. The molten cone material<sup>(22)</sup> was injected into a molding form at one of the sides around 2.5 mm from the entrance window. The very first prototypes were delivered end of July 2010 and immediately thoroughly examined. Besides tests on the spectral transmission (see section 3.3.7), the focus was on the surface quality. Based on our feedback, the company gradually adapted and improved the production process and provided us with samples of each new generation.

#### **Cone prototypes: ripples and bulge**

In the first generation of cones, the surface showed ripples (see figure 3.20). Since most of the light is reflected at the sides of the cone before being detected by the photosensor,

---

<sup>20</sup>Pictures of this state are found in figure 3.53 and 3.60.

<sup>21</sup>IMOS Gubela GmbH, Germany, <http://www.imos-gubela.de>

<sup>22</sup>Evonik Industries "PLEXIGLAS 7N".

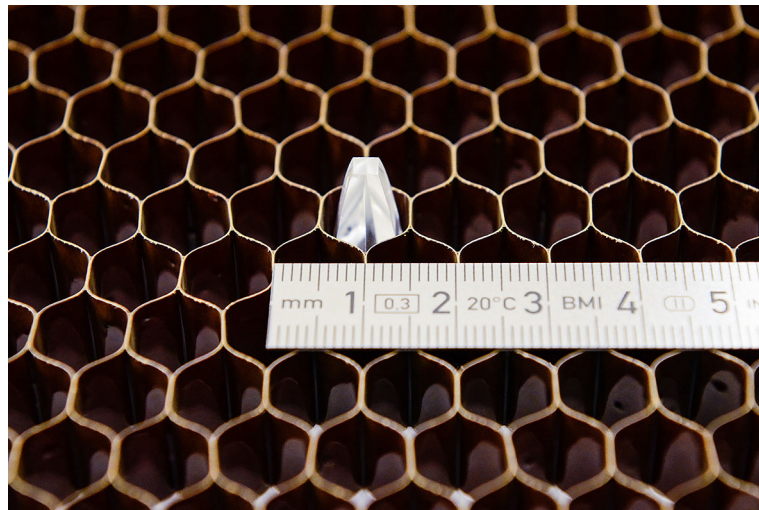


Figure 3.18.: The first light-absorbing grid to absorb light between the PMMA cones was a commercial, epoxy-coated cardboard grid. However, placing the grid on the pixels would be very difficult, since it is rigid and the precision not sufficient.



Figure 3.19.: The second grid was a handmade light-weight structure from black paper. Since it is flexible, it would have been easy to place over the final pixel structure. Its main disadvantage was its unknown long-term behavior.

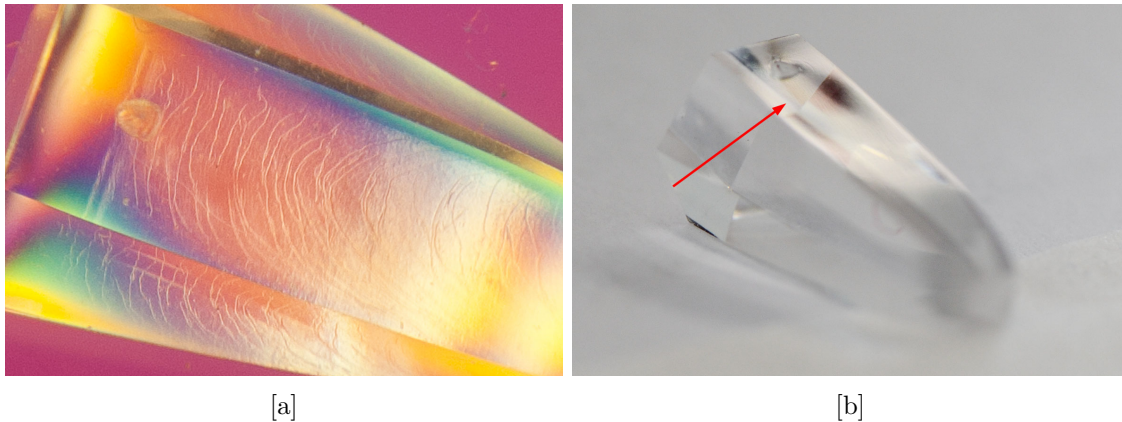


Figure 3.20.: Surface problems with cone prototypes: [a] In the first two generations, the flat side of the cone showed ripples. [b] The next generation had a bulge at the injection hole. Both problems could be solved by the manufacturer and were not present in later generations.

these ripples were suspected of significantly reducing the efficiency of our cones. The ripples were reported to the manufacturer and were not in later prototype generations due to adjustments in the production process (e.g. an enlargement of the injection hole).

The third generation of cones showed a different problem around the injection hole: a bulge at the injection hole. Also this problem was not present in later generations of cones.

### Cone prototypes: rim

Another problem turned out to be more persistent: some cones showed a rim at the square side of the cone (see figure 3.21). This rim causes two problems: first it prevented the cone from having direct contact with the epoxy of the G-APD. Simulations showed that this distance is crucial and already small additional distance lead to light loss on the percent level. The second problem was that these rims were quite fragile and partly fell off when touched. This was a problem since the crumbs could get trapped in the glue and scatter light.

The problem could with the given production process only be minimized with a new expensive mould or by mechanical lapping of each single cone. This was an extremely time-consuming process, but solved the problem for most cones. During the assembly of the G-APDs, cones with a rim were sorted out before the gluing.

### Cone prototypes: surface contaminations

For the lapping of the cones, the manufacturer used a diamond lapping compound. Many of these compounds contain silicon, which would be very difficult to remove when cleaning the cones, and which would impair the stability of the gluing of the cone to the G-APD. To investigate whether there are leftovers from the lapping process, one cone with and one without lapping were analyzed with an electron spectrometer<sup>(23)</sup>.

The analysis of the two spectra showed no difference between the cones. In particular, no trace of silicon was found, which assured us that the lapping would not lead to unwanted side effects in the gluing.

<sup>23</sup>Many thanks to Peter Wägli, ETH Zurich, for helping us with this measurement.



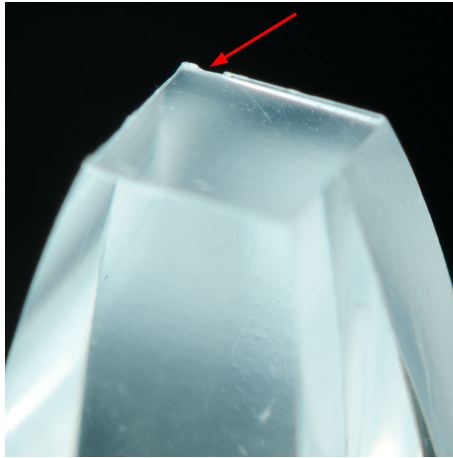


Figure 3.21.: Some cones showed a rim at the edge of the square exit window. This rim was quite fragile and fell off at some parts when touched (red arrow).

### 3.3.7. Transmission measurements

#### Measurement at 380 nm with a pulsed LED

To measure the efficiency in the area concentration of the cones, I tested a cone of the first generation in comparison to a single G-APD. A light pulser at a wavelength of  $(380 \pm 10)$  nm illuminated the area of the G-APD homogeneously. As in the measurement of the angle dependence of the G-APDs (section 2.3.6), the LED pulser triggered the read-out, creating a Poisson spectrum in the histogram of the pulse heights of the signals. When calculating the average number of detected photons using the properties of the Poisson distribution ( $\mu = -\ln(N_0/N_{\text{tot}})$ , again as for the angle dependence), the measurement is free of saturation and crosstalk effects.

The measured ratio of the number of detected photons was around three. The ratio of the entrance area to the sensor area of the G-APD is 8.7 (see section 3.3.4). With an efficiency around 90% for perpendicular light, we expected a much higher value. Part of the difference can be explained by the non-optimal optical coupling between cone and G-APD using optical grease, and the usage of an aperture in front of the cone which shaded around 10% of the entrance area. Still almost a factor of two was missing.

Due to the discrepancy with the simulation, this measurement triggered several other measurements on the efficiency of cones. The focus was on the spectral transmission and the surface quality. I designed and conducted several of these tests, the measurement of the overall cone efficiency was handed over to B. Huber as part of his thesis [121].

#### Spectrometer measurements

The spectral transmission of the cones was measured at CERN by F. Nessi-Tedaldi and W. Lustermann using a Perkin-Elmer Lambda 650 spectrophotometer. The apparatus measures the transmission from 200 nm to 900 nm. It was found that the devices by IMOS start to cut off light below 400 nm (see figure 3.22).

The spectrometer data can explain the bad efficiency described in the previous section: the transmission at 380 nm is considerably lower than the data sheet values, and is quite steep in this area. The transmission at 370 nm (the wavelength of the measurement was at  $(380 \pm 10)$  nm) is about a factor of two lower than the data sheet, which agrees with the measurement.

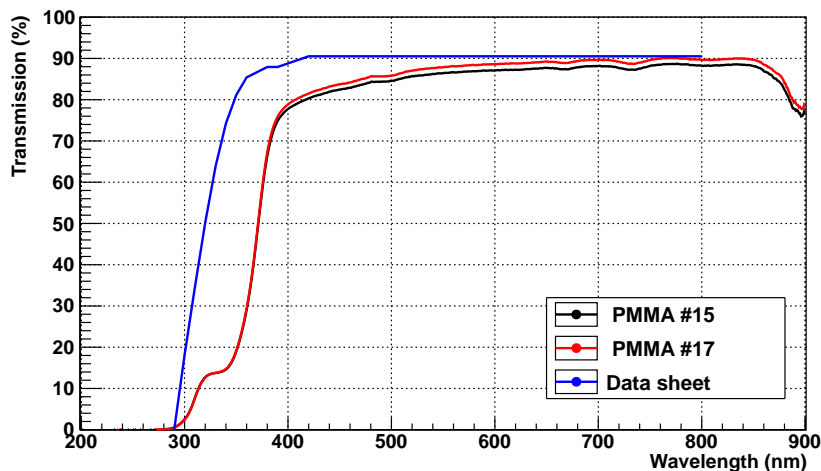


Figure 3.22.: Transmission of two cones of the very first prototype generation as measured with a spectrophotometer: the transmission below 400 nm is significantly lower than the data sheet values (blue) of the cone material [122]. This measurement was provided to the manufacturer of the cone who thereupon reviewed the production process. The quality could be improved, but was never stable such that every cone for the camera was tested (see section 3.3.9). Plot based on measurements by F. Nessi-Tedaldi and W. Lustermann.

The results from the spectrometer measurement were passed on to the manufacturer, who reviewed the production process and adapted the procedure (details were not provided to us). The spectrometer measurements were repeated with each following generation of prototype cones, and showed that the transmission could be improved, but was never stable (see section 3.3.9 for the results on the batch spectrometer measurements).

### 3.3.8. Cone prototype evaluation: laser measurements

To have an independent measurement of the absorption at fixed wavelengths, I set up an additional measurement at ETH Zurich.

A monochromatic laser beam was attenuated and collimated. The laser beam ended at a screen consisting of a sheet of paper. A digital photograph of this screen showed the location and extent of the laser beam spot. Most measurements were made with a laser with wavelength 683 nm (red), except for one test series at 405 nm (blue).

Between the attenuator and the screen, a cone could be installed. The cone could be rotated in all directions and its location moved in the plane perpendicular to the beam direction (see figure 3.23). This setup allowed two types of measurement: first to compare the intensity of the laser beam spot with and without cone, and second to analyze the light distribution when the laser beam does not pass through the center of the cone but is reflected at the side of the cone (see figure 3.24). If the laser beam hits an edge of the cone, the beam is split and two spots appear on the screen.

#### Cone alignment

The cones had to be aligned with high precision in the setup. The following steps were made:

1. A fraction of the laser light is reflected at the cone entrance window (around 4%) due to Fresnel reflections. The spot of this light was moved by tilting the cone until



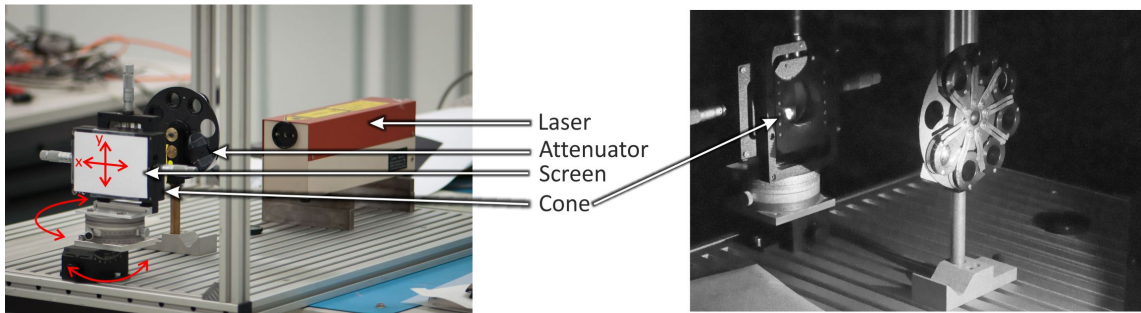


Figure 3.23.: Setup for the laser measurements of the cones: the laser beam is attenuated and collimated at the filter wheel, and ends at the screen. A cone can be installed in the beam line, allowing absorption and surface quality measurements (see also figure 3.24). The red arrows indicate the alignment directions of the cone in the setup: the cone can be moved in the plane perpendicular to the beam, and the angular direction can be adjusted in two axes. Additionally the cone could be rotated around its main axis.

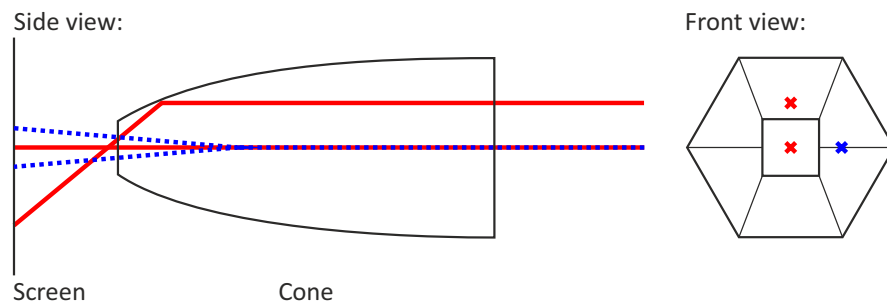


Figure 3.24.: Illustration of the laser measurements: a laser beam was shot perpendicular to the entrance window of the cone. Depending on the entrance point on the cone, the beam passes straight through the cone or is reflected at the sides of the cone. If the laser beam is directed at an edge of the cone (blue dotted line), the beam is split and two spots appear on the screen. The direct passing beam can be used to measure the absorption of the cone material, whereas the reflected beams allow conclusions on the surface and edge quality.

the reflected spot and the spot of the direct laser light coincide. This method allows to align the entrance window perpendicular to the laser beam with a high precision around  $0.2^\circ$ <sup>(24)</sup>.

2. The second alignment position of the cone in y-direction (vertical). For this the laser beam was guided onto one of the central edges (see figure 3.24), and then the y-position adjusted until the intensities of the two spots on the screen match.
3. Next the rotation along the main axis of the cone was adapted. For this purpose, the beam was directed onto the edge opposite of the one in the previous step and then the intensities compared. If the intensities were not identical, the axis rotation was adapted and step 1-3 repeated.
4. The last step is the alignment in x-direction, for which the beam was directed onto the corner of this edge and the square. The coordinates on the x/y table were noted and the mean value used.

### Transmission measurement: method

The pictures were taken using a Nikon D90 camera with a 105 mm Nikkor macro lens. The laser was kept running for at least 30 minutes before the measurements to avoid warm-up effects, for the dark frames the laser was closed with a shutter.

After the initial measurements where warm-up and stability issues were investigated, three measurement series were taken. Each measurement series contains dark frames which were subtracted from the data. The measurements without cone were interleaved with the measurements with cone to investigate the stability of the setup. For each setting, five pictures were taken to reduce the effect of shutter speed variations, and the focus of the lens was untouched during the measurements.

The camera exposure was chosen such that the maximal pixel value was in the range 15000 to 55000 for measurements without cone, i.e. in the highest two bits of the camera's linear range<sup>(25)</sup>. The camera raw data was analyzed linearly (see appendix B), and then opened in Matlab. For each image it was checked that the pixel with the highest exposure is not saturated. The central square of  $500 \times 500 \text{ px}^2$  (around  $3 \times 3 \text{ mm}^2$ ) was selected (see figure 3.25) and integrated. For the calculation of the transmission of a cone, the mean value of this integral over all five pictures was divided by the average value of all integrals of pictures without cone of this measurement series. See table 3.2 for the results of the three measurement series.

### Transmission results

The measurements were an important independent confirmation of spectrometer measurements. The measurements were made with a precision around 0.5%. The transmissions were significantly lower than the data sheet values [122] both for red and blue light, with a larger difference for blue wavelengths. Additionally the transmission was found to differ significantly more between the different cones than expected from the measurement precision.

The cones from the third generation seemed to look better with values, but still the cones differed a lot. This was another reason for the conclusion to measure every single cone in the spectrometer at CERN.

---

<sup>24</sup>Angular precision =  $\arctan\left(\frac{\text{Spot alignment precision}}{\text{Distance cone-collimator}}\right) = \arctan(0.5 \text{ mm}/150 \text{ mm})$

<sup>25</sup>The linear range of the camera is around 25-55000 (11.1 bit). See appendix B.

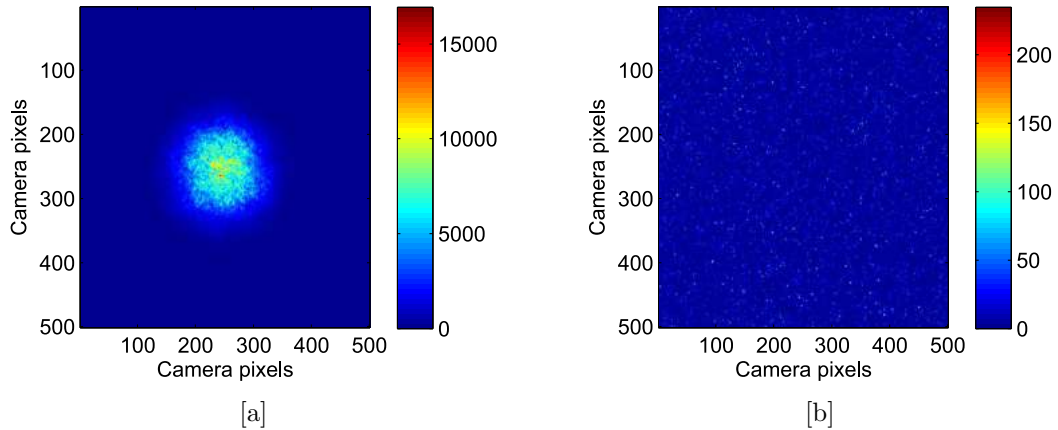


Figure 3.25.: Analysis of the laser measurements: [a] The integral over an area of  $500 \times 500 \text{ px}^2$  containing the laser spot was taken. [b] Dark frames were made and subtracted from the data.

Measurement	Cone	Wavelength [nm]	Cone [ $\times 10^8$ ]	Reference [ $\times 10^8$ ]	Transmission [%]
A1	2g-1	683	1.0668	1.2039	88.6
A2	1g-1	683	1.0309	1.2039	85.6
B1	2g-1	405	1.0096	1.1954	84.5
B2	2g-1	405	1.0070	1.1954	84.2
B3	1g-1	405	0.9421	1.1954	78.8
B4	1g-1	405	0.9404	1.1954	78.7
C1	2g-2	683	0.9989	1.1616	86.0
C2	3g-2	683	1.0519	1.1616	90.6
C3	3g-1	683	1.0587	1.1616	91.1
C4	3gl-2	683	1.0265	1.1616	88.4
C5	2g-2	683	1.0035	1.1616	86.4

Table 3.2.: Cone transmission measurements: three sets of measurements were made. Between each sub-measurement in series “A” and “B”, dark frames and reference pictures without cone were taken, then the cone reinstalled. In the measurement series “C”, dark frames and reference pictures were only taken after every second sub-measurement (see figure 3.26). The comparison of measurements with the same cone shows that the method is stable within  $\sim 0.5\%$  (B1-B2, B3-B4, C1-C5). The transmission at 405 nm is significantly lower, which confirmed the spectrometer measurements at CERN and was a hint that a wrong cone material was used which is not transparent in the UV wavelength range. *Cone identification:* The number before the “g” denotes the cone generation as delivered by the manufacturer, the number at the end identifies single cones. The letter “l” in the 3rd generation denotes a cone where the edges of the exit window were smoothed by lapping.

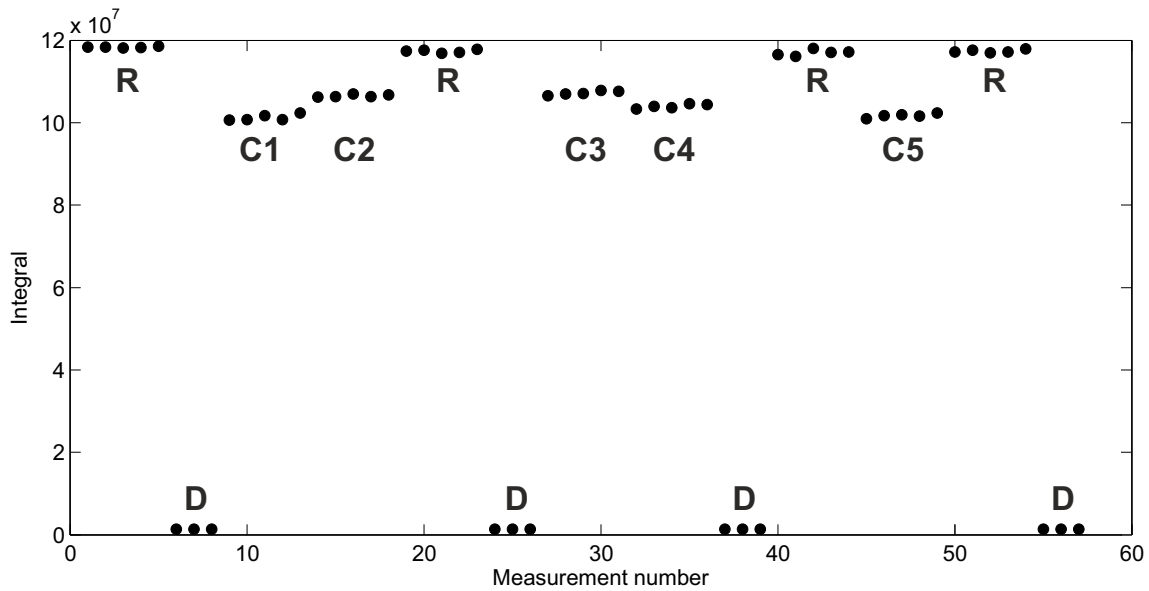


Figure 3.26.: Overview on the measurement series “C”: five cone measurements were made (C1-C5), with interleaved dark frames (D) and reference pictures without cone (R). For each measurement five pictures were taken, the dark frames were taken in groups of three.



Figure 3.27.: Processing of the reflection images: the original images from the photo camera (left) were converted to grayscale and inverted (right) for the comparison with the simulation.

### Reflection measurements

For the other type of measurements with the same setup, the reflection measurements, the images were taken in the same way as for the transmission measurements. These measurements were an important input for the surface parameters of the cone simulation: depending on the surface roughness and edge quality the spot on the screen changes its shape. A conventional non-linear image processing was used since only qualitative comparisons with the simulation were planned. The images were converted to grayscale and the brightness of the images inverted such that the laser spot appears dark against a bright background (see figure 3.27).

The reflection measurements were made for three cones: one cone of the first two generations each of injection molded cones by IMOS, and one cone which was produced by milling from the mechanical workshop at the University of Zurich. Starting from the center of the cone, the laser spot was moved in steps of 1 mm in horizontal and vertical direction (see figure 3.28) and a picture taken at each position. The distance between the exit window of the cone and the screen was around 315 mm.

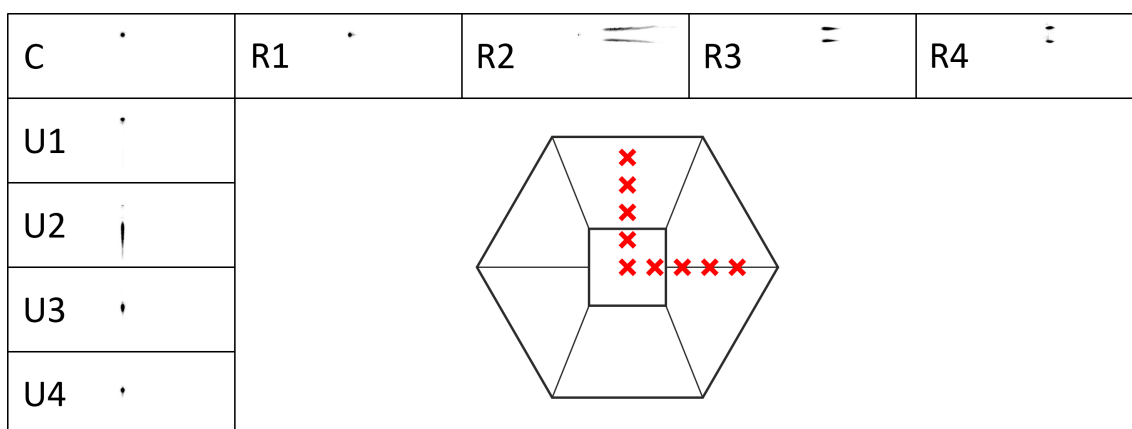


Figure 3.28.: Overview on the reflection measurements of one cone: the laser is moved from the center in steps of 1 mm in horizontal (R1-R4) and vertical (U1-U4) direction. If the laser spot is aimed at an edge of the cone, two spots appear on the screen (R2-R4). The spots from reflections close to the central square (R2, U2) are elongated since the angle from laser direction to the cone surface is largest at the bottom end of the cone.

### Reflection measurement results

Figure 3.29 shows the overlay of the measurements in steps of two millimeters for all three cones. The reflections of the milled cones are the worst as expected, due to the grooves from the milling which could not be fully removed by polishing. The reflections from the injection molded cones are thinner and more regular.

The reflection measurements were also used to fine-tune the simulation, in particular the surface roughness.

### 3.3.9. Cone batch tests

#### Simple transmission test

The spectrometer measurements at CERN and my laser tests at ETH Zurich showed the need to evaluate each cone before using it in the assembly of the sensor compartment. However, the spectrometer measurements are time-consuming with high manpower requirements.

To sort out at least part of the cones with a bad transmission before they are sent to CERN, I developed a simple test for the UV transmission. As a source of UV light I used a Philips “Blacklight blue” fluorescent tube<sup>(26)</sup>, which emits light from around 350 nm to 400 nm, peaking at 365 nm [123]. Since UV light is (per definition) invisible to the human eye, a wavelength shifting material is necessary. Fortunately enough, white paper is usually treated with fluorescent substances to make it appear whiter and thus a suitable candidate. The setup was as shown in figure 3.30: the light from the UV tube is collected by the cone and concentrated onto the white paper. The fluorescent chemicals shift the wavelength of the light into the visible range, and emit it (approximately) isotropically. This light is again collected by the cones (this time at the smaller square end) and distributed over the full hexagonal area, where it exits. As seen from the direction of the UV tube, the cone appears bright if it is transparent to UV light.

<sup>26</sup>Philips TLD 36W/08

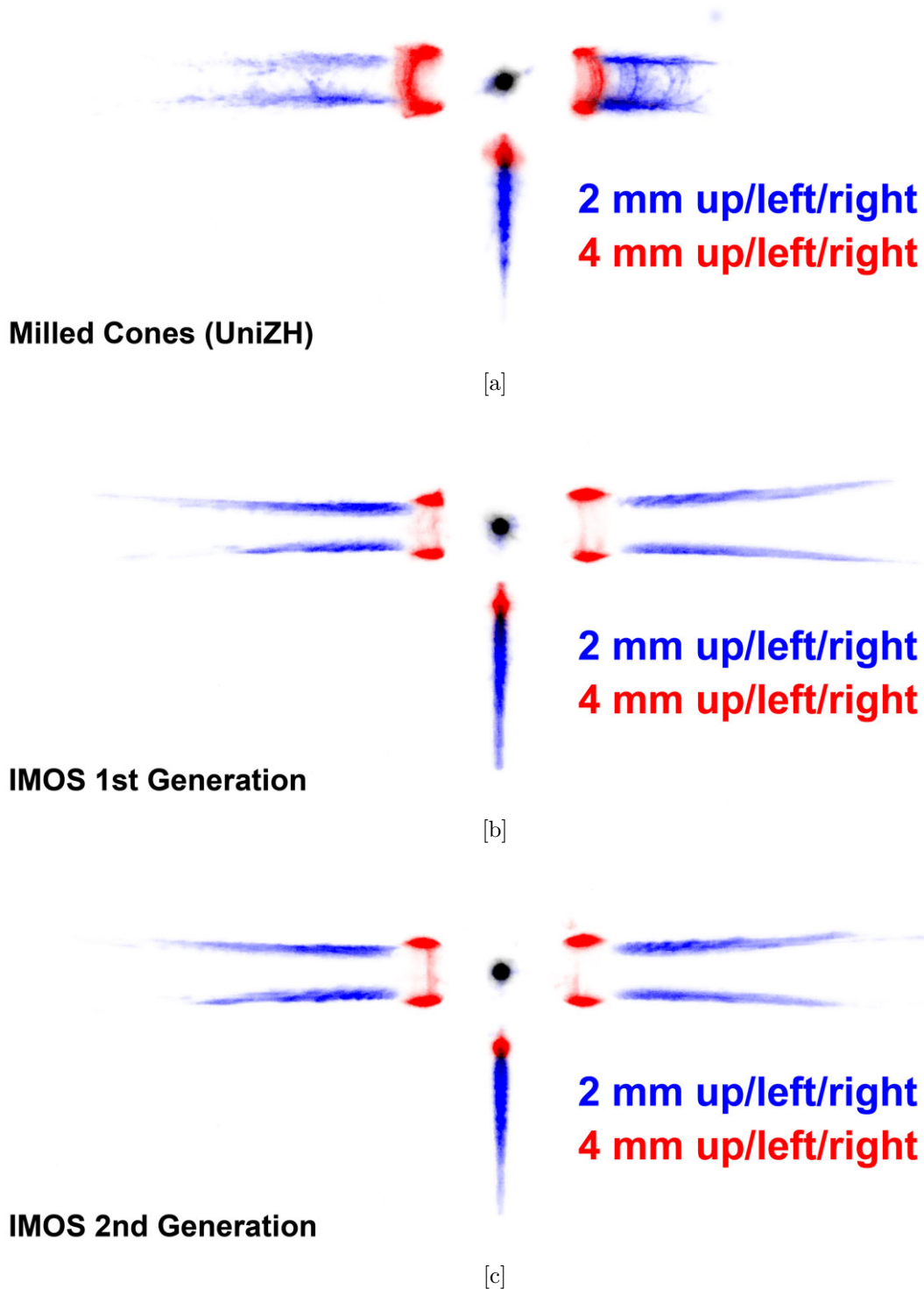


Figure 3.29.: Comparison of the reflection spots of three prototype cones, with the laser moved in steps of 2 mm from the center (black): blue are the reflections from 2 mm away, the reflections from 4 mm are in red. Note that if the spot is further from the center, the reflection moves closer due to the parabolic shape of the cone sides.

The reflections of the milled cones are most irregular as expected, due to the grooves from the milling which could not be fully removed by polishing. The reflections from the injection molded cones are thinner and more regular. The reflections from 4 mm in horizontal direction allow to compare the edge quality: for sharp edges, two well distinguishable points are visible (red, left and right of the central spot). The edges of the milled cones are less sharp, which smears out the two spots.

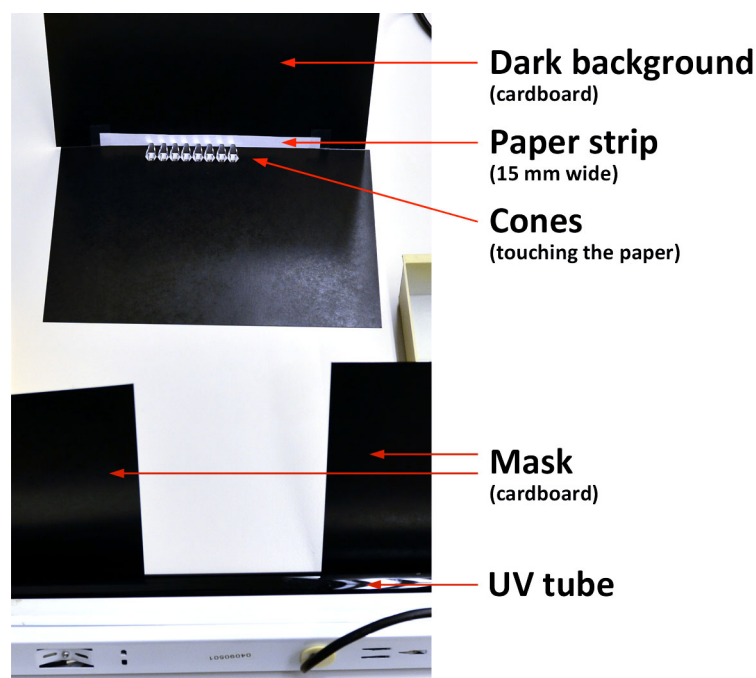


Figure 3.30.: Setup for the batch UV transmission measurement: The light from the UV tube passes the cones, is shifted to visible light in the paper strip and pass the cones a second time. As seen from the direction of the UV tube, cones which are nontransparent to UV light appear dark (see figure 3.31). This fast measurement was used to find and sort out bad cones before they are time-consumingly tested in the spectrometer.

The differences in the UV transmission are better visible in digital images than by eye. An example is shown in figure 3.31. The setup allowed the fast testing of cones, and was used to test  $> 500$  cones, of which around 30 % were rejected. The other cones were sent to CERN for a more precise (and time-consuming) evaluation in the spectrometer.

### Batch spectrometer measurements

The quality of the cones was improved in the first four generations by adaptations in the production process. The changes which were communicated by the company were an enlarged injection hole into the molding form and non-specified changes in the temperatures during the material injection and the subsequent cooling.

Of the fifth generation, 25 out of 230 cones were tested in the spectrometer at CERN and found to have a transmission curve close enough to the data sheet values of the cone material. However, the results from the next delivery of cones contained again cones with worse transmissions. It was thus decided to test every single cone which will be used in the camera, and to sort out cones with a lower transmission.

The cutoff was defined based on the cones of the fifth generation: the transmission of the worst cone of this generation was the reference, and the cutoff was 3 % less than this reference curve. Figure 3.32 shows the transmission curve of all cones which were tested at CERN.

There seem to be two populations of cones with lower transmission: in one population, the transmission is reduced over the full wavelength range, whereas the second population only has a reduced transmission below 400 nm. The latter transmissions have similarities to conventional PMMA which is not UV transparent, however, a possible contamination



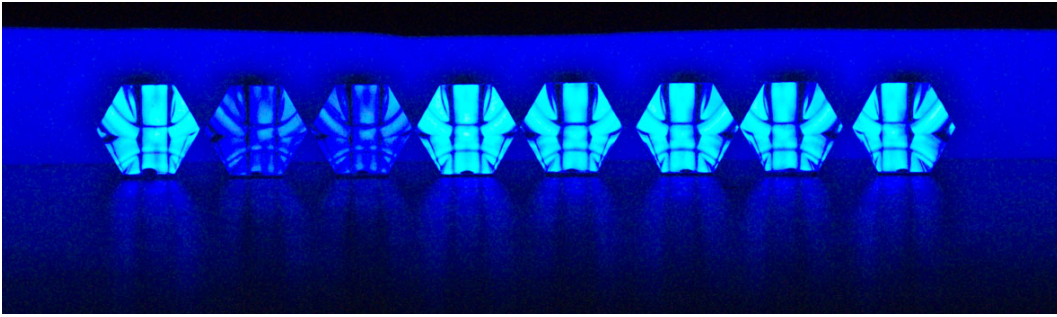


Figure 3.31.: Example of cones in the batch UV transmission setup: two cones show a clearly lowered UV transmission and can be sorted out even without a full spectrometer measurement.

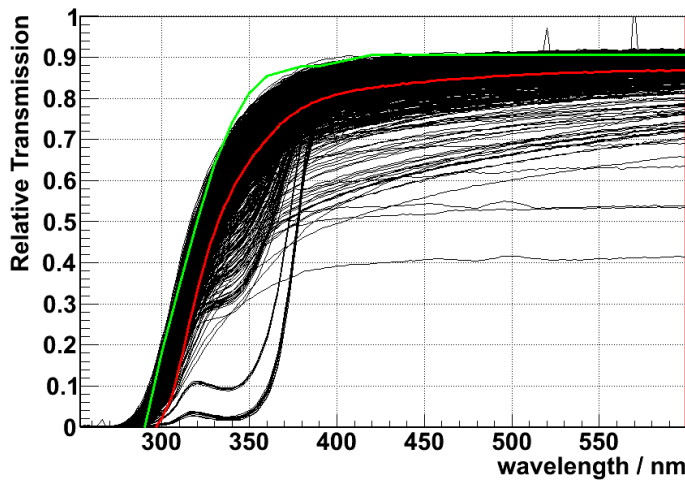


Figure 3.32.: Spectral transmission of all 2344 cones which were measured at CERN: the green curve is the reference curve as provided by the material producer [122], the red curve the cutoff we applied. Around 750 cones were below the threshold and sorted out. The cones with a bad transmission seem to have two different problems: the first causes the transmission over the full wavelength range to be reduced, the second only below 400 nm. Figure based on a plot by I. Braun.

with other material was never confirmed. The first type of reduced transmission might be due to scattering in the cone due to bubbles (see section 3.3.10). Such impurities may occur when too high temperatures are used in the injection process.

Nonetheless, when all cones of the fifth generation were tested, the next step in the construction of the camera was started: the gluing of cones to G-APDs. The spectrometer tests were going on in parallel to the gluing of the cones.

### 3.3.10. Laser transmission: bubbles

One issue which lowered the transmission of light I identified when looking at the scattered light when a laser beam passes the cone: the laser is well visible inside the cone, which is only possible if light is scattered inside the cone. Even though a quantitative measurement of the scattered light is quite sophisticated, it is easy to show differences between cones with a laser pointer. A green laser pointer (532 nm) was used. One cone with a reduced transmission over the full spectrum was compared to a cone within the specification (see



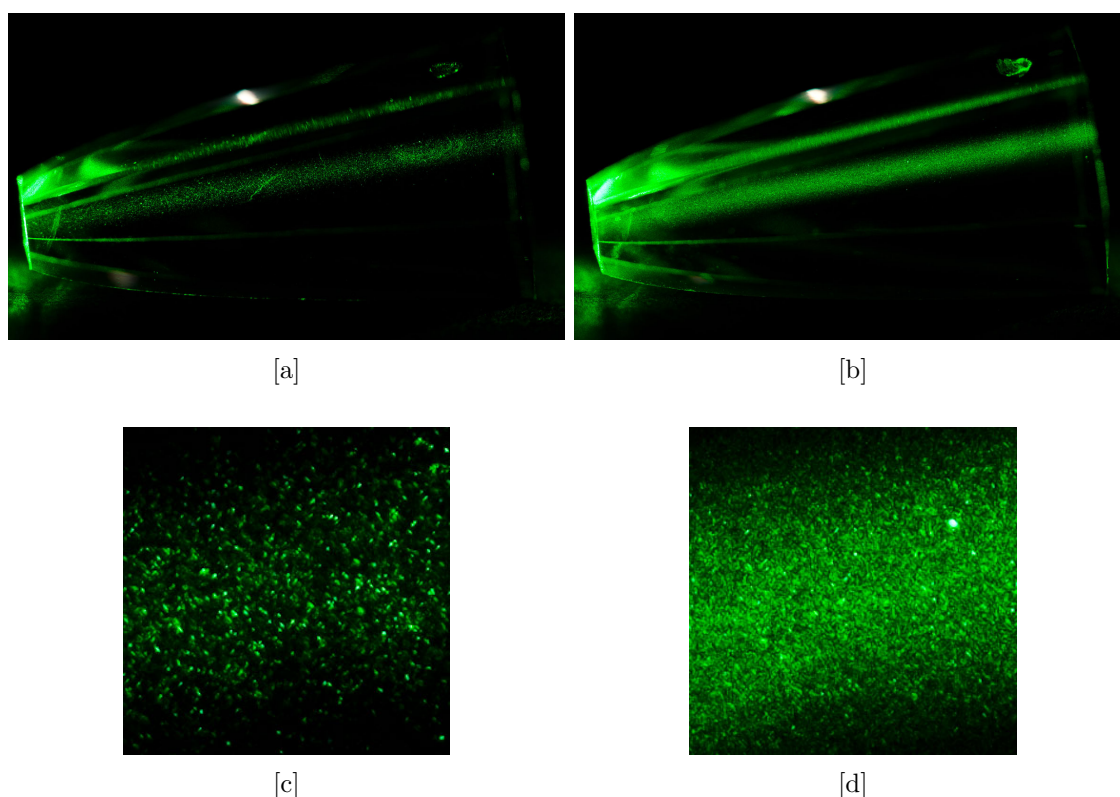


Figure 3.33.: Comparison of the scattered light of a laser pointer: [a] For cones with standard transmission, the laser beam is barely visible. [b] For cones with a reduced transmission over the full spectrum, a lot more light is scattered (the exposure of the two images is identical). [c] and [d] show zooms of the first two images: it seems as if the light is scattered at small, distinct targets in the cone material.

figure 3.33). The cone with the lowered transmission scatters significantly more light, and the scattering seems to be restricted to small scattering centers.

### 3.4. The sensor compartment

The section from the front window to the baffle plate is denoted the sensor compartment (see figure 3.34). Since the tests with M0 showed that the response of the G-APDs can be kept stable when the temperature changes by adapting the bias voltage, the sensor compartment is not temperature regulated. The purpose of the baffle plate is to isolate the G-APDs from the heat of the electronics, in particular from fast temperature changes and inhomogeneous temperatures across the sensor plane. It consists of two 1 mm aluminum plates with 23 mm Styrofoam in between.

Other than for M0, there is a cable between the G-APDs and the pre-amplifier. Cables for the non-amplified signals are problematic since the signal quality gets lost and noise signals can get picked up. The cable was necessary for two reasons: geometry and insulation. The diameter of the sensor compartment is limited by the ring mount of the CT3 telescope. The adaptation of the electronics to this confined space would have complicated its design. And the thermal insulation of the sensor compartment from the heat of the electronics with the baffle plate also required the use of cables.

The optical part of the sensor compartment starts with the front window, a 4 mm UV-

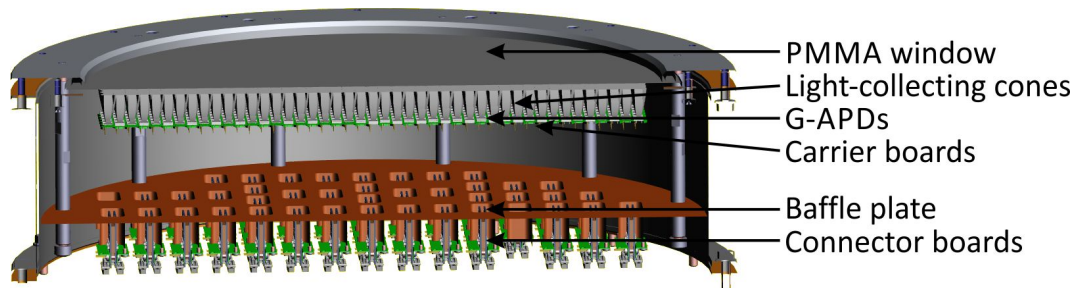


Figure 3.34.: Illustration of the sensor compartment of the FACT camera: it consists of a UV transparent PMMA front window, onto which the light-collecting cones are glued. The G-APDs are glued onto their exit windows and soldered to carrier boards. Cables (not shown in the figure) connect the sensors to the connector boards, where the bias voltage is provided. The baffle plate isolates the sensors from the heat of the electronics. Illustration based on a 3D CAD model by A. Gendotti (ETH Zurich).

transparent PMMA plate<sup>(27)</sup>. The light-collecting cones are glued onto this window, and a second gluing connects the cones to the photosensors. This part of the construction was the responsibility of J.-P. Stucki and me. Together we made and evaluated gluing tests, devised the cleaning of G-APDs and cones and finally assembled the sensor compartment with the help of several other persons.

### 3.4.1. Gluing of G-APDs to cones

In the prototype module M0, the light-collecting cones are fixed and aligned on the G-APD by a mechanical spike on the aluminum frame of the cones (see section 3.1.2). This approach was also discussed for the final camera. However, this would require some contact of the cones to this fixation structure, which would result in light losses at the contact points and damage to the surface of the cones during the construction (scratches). Further, the alignment of the cones would be fixed to the package of the photosensors, and not to the sensitive area itself. Furthermore, the alignment would be difficult to maintain during the vibrations and mechanical stress in the operation of the camera (e.g. when changing the zenith angle of the observation).

It was thus decided to glue the cones directly onto the G-APDs (see figure 3.35). With this approach, the cone only has mechanical contact at the input and exit apertures, and the gluing would ensure both a fixed and a precise alignment.

There are several challenges for such a gluing: first, the glue must not form additional interfaces for Fresnel refractions. For this, the refractive index of the glue must match either the cone material or the protective coating of the G-APD. Second it must be transparent to UV light (obviously), and third it must be strong enough to resist the forces on the gluing as they appear during the construction and operation.

The optimal glue for this purpose was found by asking the G-APD manufacturer Hamamatsu what material was used for the protective layer on top of the G-APD: EPO-TEK 301 by Epoxy Technology<sup>(28)</sup>. Using this two-component glue ensures that there is no change in the refractive index between the glue and the photosensor. According to its data sheet [124], the glue has a spectral transmission  $> 99\%$  above 380 nm, but the glue manufacturer provided us with (internal) measurements which show a transmission  $> 94\%$

<sup>27</sup>Evonik Industries, “GS 2458 SunActive”.

<sup>28</sup><http://www.epotek.com>

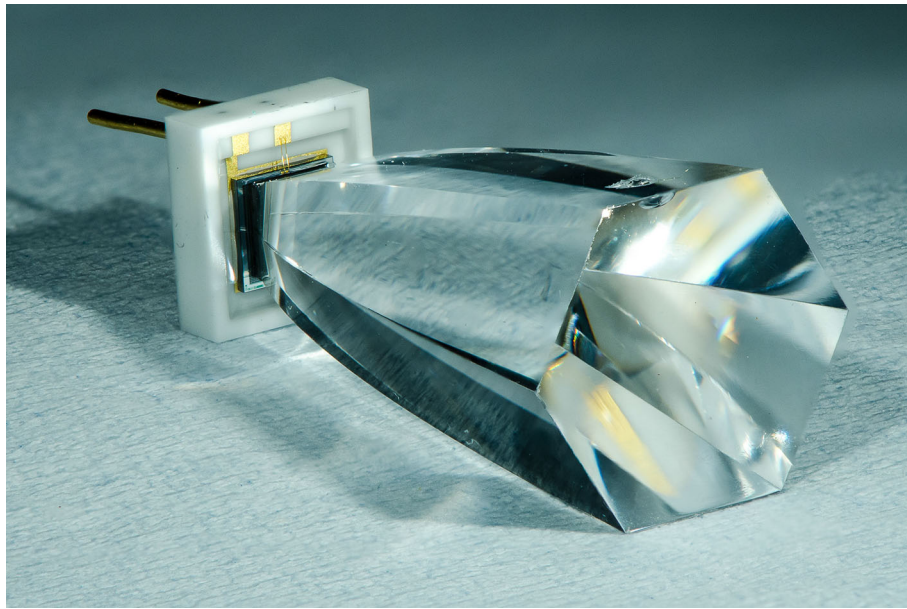


Figure 3.35.: The light-collecting cones are glued directly onto the G-APDs. This approach ensures that the alignment of the cones on the sensitive surface (black) remains unchanged during construction and operation of the camera.

down to 300 nm<sup>(29)</sup>.

### Tools and methods

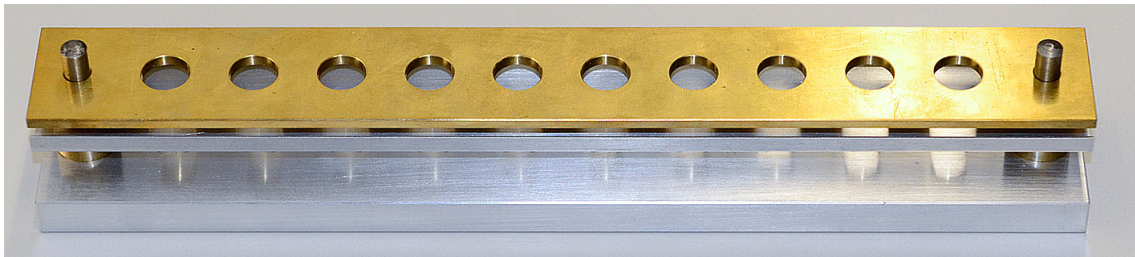
The cones are glued in batches of 40 pieces onto the G-APDs, for each batch a new quantity of glue is mixed (see next section). For the mechanical stability during the gluing a customized tool was used, which can hold up to 10 pixels (see figure 3.36). The G-APDs are cleaned and placed in the cut-out of the tool. To avoid dust on the cleaned surface of the photosensor, the gluing was done in a clean room, and all involved persons wore gloves, masks, hoods and dust-free clean room coats. In the next step the cones are cleaned one by one and checked for impurities. Each cone is closely examined for a rim (see section 3.3.6) and scratches or ripples on the square side of the cone. Then the glue is applied with a high-precision dispenser (Fishman LDS9000<sup>(30)</sup>) and distributed evenly across the surface. For the placing on the G-APD, the cones are held with a suction cup and carefully lowered onto the photosensor. If the amount of glue is not sufficient for a cone, the cone is removed and half of the standard amount added (see section 3.4.1).

The alignment of each cone on the photosensor is checked by looking from the hexagonal side of the cone onto the gluing: if the cone is not well-centered, the sides of the G-APD chip are visible, and the cone is then carefully moved. In the same step, the distribution of the glue is checked.

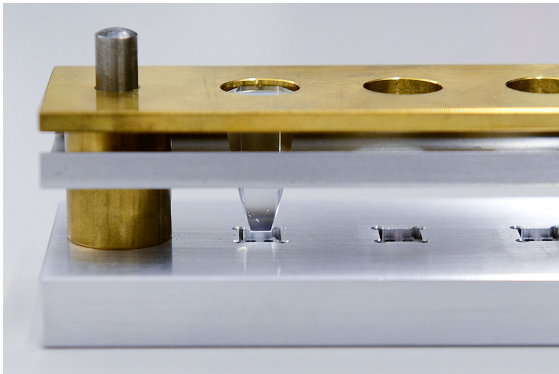
For each pixel, the unique G-APD and cone identification number as well as the tool number and the position therein are documented.

<sup>29</sup>The transmission is similar to the glue EPO-TEK 301-2, but the two glues differ in several other properties.

<sup>30</sup>Fishman LDS9000 AirFree Dispensing System, <http://www.fishmancorp.com>.



[a]



[b]



[c]

Figure 3.36.: Tool for the gluing of the cones to the G-APD: [a] Each tool can hold up to 10 pixels. [b] The cones are fixed on two levels, of which the lower level also fixes the rotation around their main axis. [c] The G-APDs were cleaned and placed in cut-outs in the tool, which were slightly larger than the ceramics package. The position of the G-APDs within the cut-outs was fixed by small pieces of metal.



### Amount of glue

A first estimate was based on the surface profile measurements of the G-APDs (see section 2.3.1): the volume is approximated as a pyramid of height  $h = 0.4$  mm with square base area  $s^2 = 2.8 \times 2.8$  mm<sup>2</sup>, where the top  $d = 0.1$  mm are missing:

$$V = \frac{1}{3}s^2h - \frac{1}{3}\left(\frac{d}{h}s\right)^2 d \quad (3.11)$$

$$= \frac{1}{3}s^2\left(h - \frac{d^3}{h^2}\right) \quad (3.12)$$

$$= 1.03 \text{ mm}^3 = 0.00103 \text{ cc} \quad (3.13)$$

This estimate was used to choose the glue dispenser (Fishman LDS9000) and the syringe (volume 5 cc). The step size of the dispenser is 0.39 mm<sup>3</sup>, and the first gluing tests showed that the step below the estimate (0.78 mm<sup>3</sup>, 24 % less) is sufficient for most cones.

### Gluing tests and bubble reduction

Besides establishing a procedure for the mass gluing of pixels, the first gluing tests also served the investigation of the stability and quality of the gluing. A simple problem was the systematic offset of the first glued pixels: most cones were systematically off the center of the G-APD by about 0.2 mm. This was corrected by enlarging the cut-outs in the gluing tool and placing space-holders to fix the G-APDs (see figure 3.36[c]).

Another problem of the first glued pixels was their stability: some pixels fell off even when handled carefully. Two explanations seemed possible: either some contamination of the surface of cone or G-APD, or a problem in the mixing of the (two-component) epoxy glue. The third and most prominent problem were bubbles in the glue layer: in many pixels, such bubbles were easily visible by eye when looking from the hexagonal side of the cone onto the gluing (see figure 3.37). These bubbles were later found to be air which is trapped between the glue and the G-APD.

Another type of bubbles was more difficult to see: when the illumination of the pixel was set up in exactly the correct angle, additional bubbles became visible (see figure 3.38). The origin of these bubbles could not be conclusively identified, the assumptions were either remaining liquid from the cleaning or inhomogeneities in the glue.

To reduce the number of bubbles and improve the stability of the gluing, a variety of measures was evaluated. Two of the evaluated ideas did not work out: to draw out bubbles, the pixels were placed in a vacuum chamber during the hardening of the glue. This test was successful in the sense that the bubbles were drawn out, unfortunately not without taking along the glue which was spilled upward along the sides of the cone. Those joints broke at the slightest touch. A reduction of the vacuum strength did not improve the result, either the bubbles stayed or the glue was also sucked out. Further it was evaluated whether a surface treatment of the G-APDs with oxygen plasma would lower the surface tensions and thus reduce the bubbles. Since no significant difference was found between treated and untreated pixels and the effect on the cone surface was not clear, the idea was dropped.

A significant improvement in the number of bubbles of type 1 and an almost complete avoidance of type 2 bubbles was achieved by improving the quality of the glue and by a careful cleaning of both cone and G-APD (see the next two subsections).

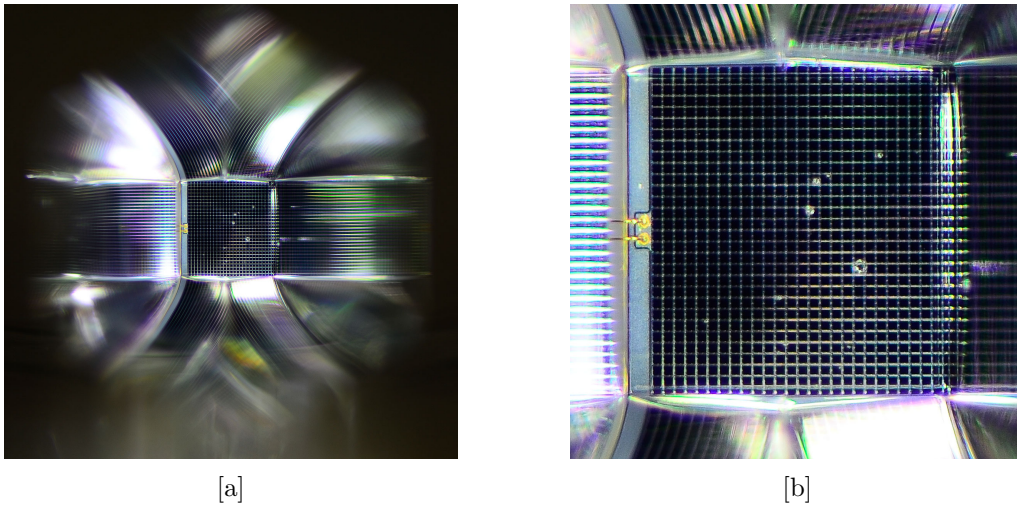


Figure 3.37.: View from the hexagonal entrance window of the cone: [a] Full area and [b] zoom onto the gluing joint. The offset of the cone to the sensor area is clearly visible (left side of the central square, note the golden bonding wires), as well as small bubbles in the glue. The systematic offset was corrected with a change in the tool, and the alignment checked for every single pixel during the batch gluing. The bubbles were reduced by various steps, most notably the careful cleaning of cone and G-APD before the glue is applied.

### Glue preparation

The glue EPO-TEK 301 is a two-component epoxy glue with a mixing ratio of 4:1. The two components were weighted and mixed by hand until the glue was homogeneous (checked with a strong light at varying light incidence directions). After filling the glue into the syringe for the dispenser, it was put into a centrifuge at 500 rpm/min for four minutes (see figure 3.39) to get rid of small bubbles in the glue volume which appeared during the mixing or pouring of the glue. It was also tested whether removing the bubbles by placing the glue in a vacuum chamber was more efficient, but no difference was found and the centrifuge was the more practical solution.

### Cone and G-APD cleaning

Most of the reduction in the amount of bubbles and improving the stability of the gluing can be assigned to the cleaning of the contact surfaces of the cone and the G-APD. The surface of the G-APD is an epoxy layer, which is relatively resistive against most chemicals compared to the PMMA cones. Since the surface of the cones was more exposed to potential contaminations than the one of the G-APDs (from the lapping at the manufacturer to the spectrometer transmission tests at CERN), the effort in the cleaning tests was put on the cones. The G-APDs were usually cleaned in the same way as the current status of the cone cleaning.

For the cleaning of the cones, a variety of soaps and other chemicals were in discussion. More than fifteen soaps were evaluated but discarded due to aggressive or unnecessary ingredients (often strong fragrances, colorants and/or dyes). Low-boiling petroleum ether was rejected due to its aggressive characteristics and its unhealthy vapors (in particular a problem in the poorly ventilated clean room). The final evaluation round consisted of isopropanol and several mild soaps: a conventional mild dish washing soap (“Handy”), an alcohol and fragrance-free outdoor soap (“MSR Packsoap”) and a mild organic soap in

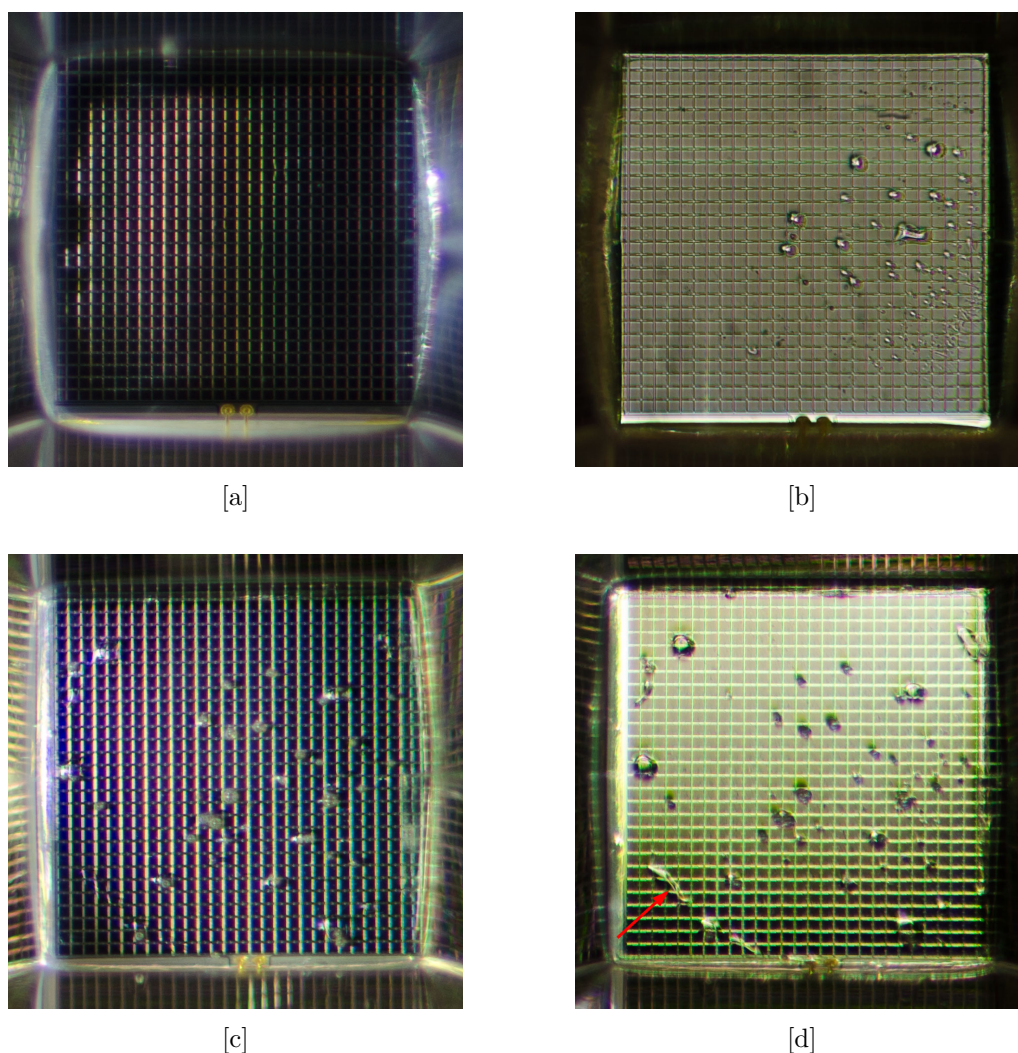


Figure 3.38.: Illustration of bubble types: [a] and [c] show two pixels without and with bubbles from trapped air (bubble type 1), respectively. [b] and [d] show the same pixels, but with carefully adjusted illumination: additional bubbles become visible, whose origin is not clear (bubble type 2).



Figure 3.39.: Preparation of the glue: [a] The two components of the glue were weighted and mixed carefully. [b] To get bubbles out of the glue, the syringe was put into a centrifuge at 500 rpm/min for four minutes.



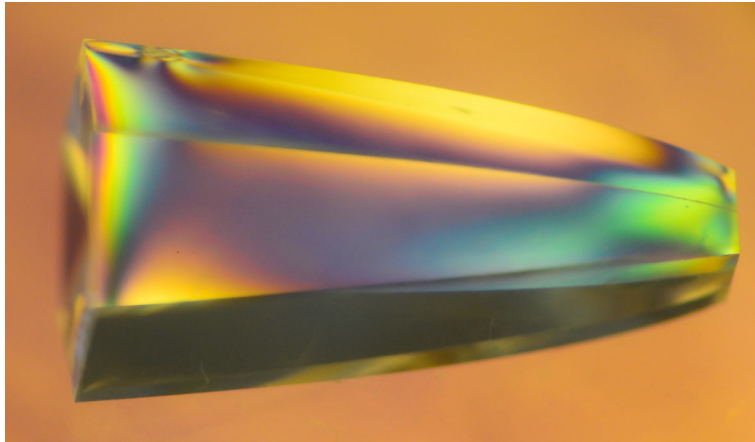


Figure 3.40.: Tensions within the cone can be made visible using polarized light: tension-free Plexiglas would appear homogeneous in color. The strongest tensions are visible around the injection hole and at the light entrance and exit windows. Even though no quantitative statement was possible, we ruled out isopropanol for the cleaning of the cones since it is not suited for material with internal tension.

block form.

Using isopropanol for the cleaning was dropped due to a note from the manufacturer of the cone material, Evonik Industries, that this solvent might lead to micro-cracks in the cone surface if there are tensions in the cone material. Using polarized light (see figure 3.40) we found strong tensions inside the cone, so we ruled isopropanol out to be on the safe side.

The organic soap in block form was ruled out due to the impracticality of its solid form. The last two remaining soaps were evaluated in several gluing tests, and both showed a similar improvement in the reduction of bubbles. The decision in favor of the dish-washing soap instead of the outdoor soap was taken due to its common use for Plexiglas scintillators in particle physics applications of our institute.

Another question was the one for an appropriate tissue for the cleaning, which must be lint-free and consist of soft fibers, in order to not impair the surface of the cone while cleaning. The finally used tissue was “TIFFEN Lens Cleaning Paper”<sup>(31)</sup>.

After the cleaning with water and soap, the cones were rinsed with distilled water and carefully dried using a new piece of tissue and compressed air.

### Stability test of the gluing

The mechanical stability of gluing of the cones to the G-APDs was tested for three cones using a simple setup: the G-APD was fixated in a bench vise. A metallic weight was placed on the outer end of the cone around 18 mm from the gluing, creating a leverage force on the gluing (see figure 3.41). If the gluing held the weight for at least 10 seconds, the procedure was repeated with a heavier weight.

Since the peak of the force onto the gluing occurs when the weight is placed on the cone, this has to be done very carefully. The force peak during the placement of the weight can exceed the gravitational force of the weight by a factor of two or more (estimated using a fast weighing scale). The test was made with three pixels from the 6th (one pixel) and 7th (two pixel) gluing test batch, for which the final cleaning and gluing procedure was used.

<sup>31</sup>According to its product description, it is “a soft, lintless paper specially prepared for cleaning lenses, filters and other highly polished glass surfaces. Safe for coated lenses too.”



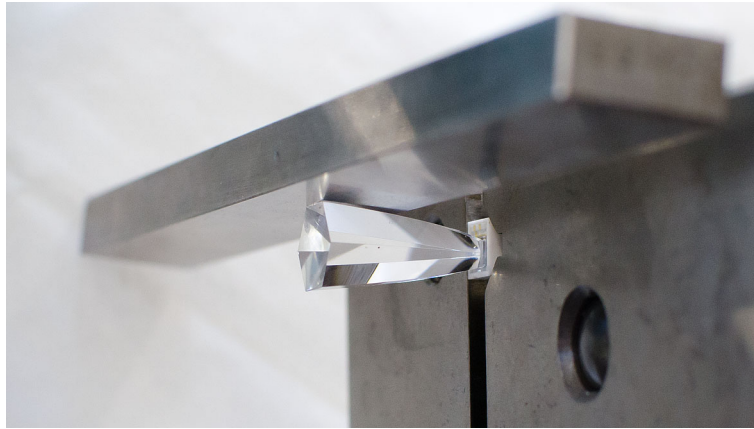


Figure 3.41.: Setup for the load tests of the gluing joints: the G-APD is fixed in a bench vise. Metal weights are placed carefully on the outer end of the cone, touching it at a distance around 18 mm from the gluing. If the gluing held the weight for more than ten seconds, a larger weight was placed.

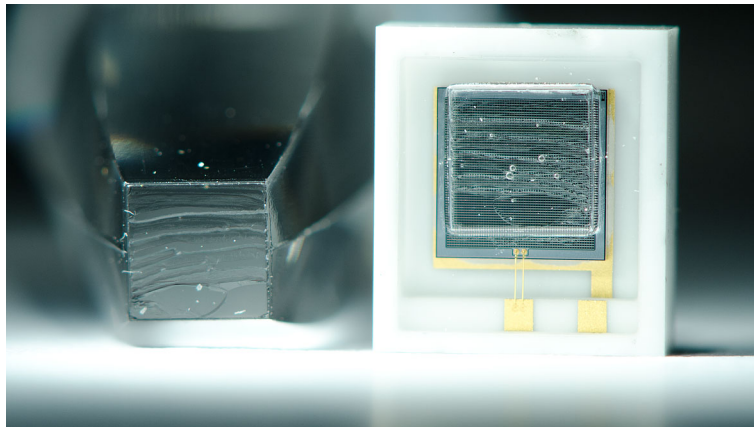


Figure 3.42.: Example of a broken gluing joint: the connection does not break between glue and cone or G-APD, but is torn apart, showing the excellent adhesion of the glue to both cone and G-APD surface. The broken gluing joint also allowed to determine the location of type 1 bubbles: they are clearly visible between the glue and the surface of the G-APD.

The first pixel held the weight up to 720 g, but fell off some seconds after an additional weight was placed to 998 g. The second pixel resisted only 300 g, but fell off while the next weight of 120 g was being placed. It is assumed that the placing was not careful enough, producing a peak in the effective force on the gluing. The third pixel resisted 570 g and broke after some seconds at 675 g.

The gluing joints from the first gluing tests usually broke between the glue and the cone, which was addressed by the cleaning of the cone surface prior to the gluing. The load tests also showed that the weakness of the gluing joint is now no longer the adhesion of the glue to the cone or the G-APD, but the glue itself (see figure 3.42). This result was a confirmation that the gluing of the cones to the G-APD could not be improved further concerning its stability, and that the cleaning procedure for the cones was successful.

### Gluing batch tests

A total of 1535 pixels were glued during 25 days in March to May 2011. Every single pixel was tested in order to ensure that only qualitatively good pixels are used in the final camera. Since I made the previous tests of the G-APDs and gluings, I developed the test setups and defined the quality criteria, but the batch testing was done by visiting diploma and PhD students from the collaboration.

The first and simplest test was the load test: in the same way as the stability tests described above, every gluing was tested with a weight of 210 g. Of all 1529 tested pixels<sup>(32)</sup>, only two did not pass the load test, both during the force peak when loading the weight onto the cone.

The other test was a function test of the G-APD: most of the G-APDs (1430) were directly glued as delivered from the manufacturer. The other 105 G-APDs were previously used in the prototype module M0 and were functional, but could have suffered during the disassembly and desoldering of M0. Based on our experience and the knowledge of other experiments<sup>(33)</sup>, we decided to test only whether a pixel works and not its specific properties<sup>(34)</sup>. For this, the most simple G-APD readout as it is described in the manufacturer's data sheet [64] was used. The G-APDs were operated at their nominal voltage, and a pulsed LED used to produce signals in the photosensors, which were visualized in an oscilloscope. The pulses were large enough such that no amplification was necessary. A pixel passed the function test when light pulses were visible in the oscilloscope, which was the case for *all* 1535 tested pixels.

### Test patches

Already during the gluing of the pixels, our electronics engineers wished to have test patches to test the electronics and readout chain of the camera. For this purpose, 18 pixels of average gluing quality were selected. The 18 pixels were glued onto a  $10 \times 10 \text{ cm}^2$  square Plexiglas window of the same type as the front window for the camera (see figure 3.43). The first placed pixel was a single cone without a G-APD to test the placing accuracy on the window. The carrier boards and cables were soldered as for the final focal plane (see next sections).

The bias voltages of the G-APDs within one bias voltage group are identical (see figure 3.44). The voltages between the bias groups within the patches are similar such that they can be operated at the same voltage. If *all* pixels are operated at the same bias voltage, the error in the over-voltage (and thus the gain) of the single G-APDs is around 2%.

### 3.4.2. Focal plane layout and pixel ordering

The focal plane of the FACT camera consists of 1440 hexagonal pixels with a pixel spacing of 9.5 mm. The pixels are grouped into “patches” consisting of 9 pixels. Those nine pixels form one trigger patch and are supplied by two bias voltage channels, one for 4 and one for 5 pixels (for more details on the electronics please refer to section 3.5). Of course the pixels in one bias voltage group must share a similar operation voltage of the G-APDs. Having

---

<sup>32</sup>Six pixels were directly used for electronics and optical tests.

<sup>33</sup>We relied in particular on the experience from the T2K experiment (<http://t2k-experiment.org/>), which tested more than 40000 G-APDs from Hamamatsu: pixels were either working as specified, or did not respond at all (e.g. due to broken bonding wires) [125].

<sup>34</sup>This would on one hand take a lot of time and is further much easier after the camera is assembled and every pixel attached to its own readout channel.

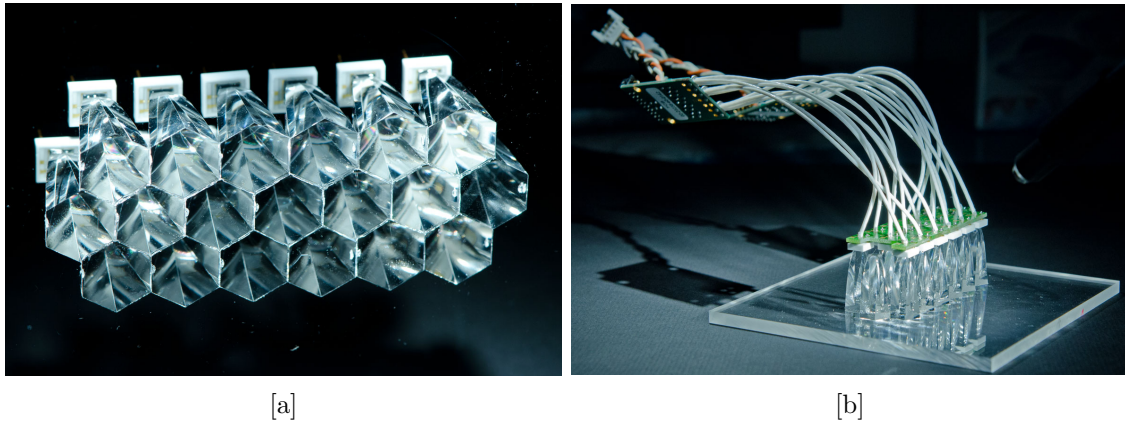
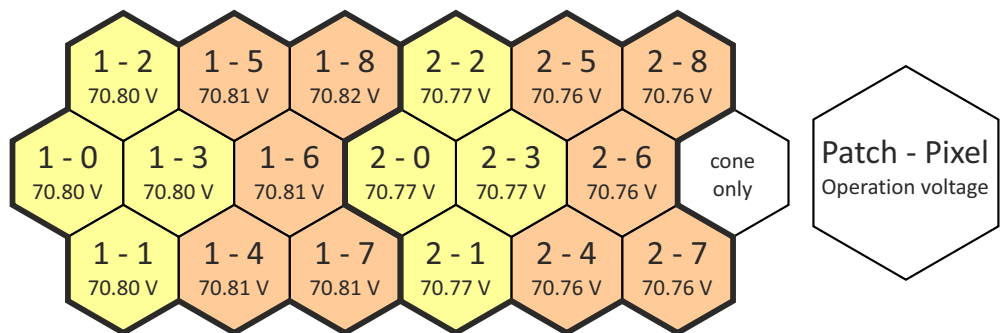


Figure 3.43.: 18 pixels were used to build two test patches for electronics tests. [a] Front view onto the 18 pixels. The 19th (rightmost) pixel only consists of a cone without a G-APD. [b] Side view onto the test patches including the coaxial cables connecting the G-APDs.



Rear view (as seen from the electronics)

Figure 3.44.: Bias voltages of the two test patches: the two bias voltage groups per patch can be connected and the full patch operated at the same voltage. If both patches are connected and operated at the same voltage (70.79 V), the error in the gain of the G-APDs is around 2%.

<b>Glued pixels</b>	<b>1535</b>
Test patches	-18
Optical / electronics tests	-13
Failed load test	-2
<b>Available pixels</b>	<b>1502</b>
Required pixels	1440
Spare pixels	62 (4.3 %)

Table 3.3.: Overview on the pixels for the final focal plane: of 1535 glued pixels, 33 were not available for the final focal plane since they were used for tests. Most of those pixels were used for two test patches, which were used to test electronics boards and the trigger.

more glued pixels than necessary allowed to select only the best pixels for our camera, and optimize the bias voltage groups for small voltage spreads. Of the originally 1535 glued pixels, 1502 were available for the focal plane (see table 3.3), 1440 are necessary.

### Bubble types

The main characteristics for the sorting of the pixels was the quality of the gluing. For the categorization, a high-resolution picture of the gluing was made, with the illumination optimized for the visibility of bubbles in the gluing. Each pixel was examined for both bubble types (see the section 3.4.1 and figure 3.38) and classified according to the extent of those bubbles into categories a/b/c for both bubble types. For type 1 bubbles, the category “a” was divided into subcategories a/a+/a++, allowing a few small type 1 bubbles within the category “a”. If any hint of type 2 bubbles was present, it was categorized as “b” (see figure 3.45).

The worse of those two categories determined the bubble class A/B/C of a pixel: if a pixel had a categorization of c for one bubble type, it belonged to class C and was disqualified for the use in the camera. 61 pixels were in this bubble class. Of the remaining 1441 pixels, 1224 belonged to the top quality class A, and 217 pixels to the class B. The outermost ring of the camera consists of 38 patches, i.e. 342 pixels. This allowed to use only class A pixels for the inner part, and pixels of class A and B for the less important outer ring.

This approach in the handling of bubbles was very conservative, as can be seen when examining the effect of type 1 bubbles on the light transmission by estimating the covered area. Even though the bubbles are very prominent when looking at the gluing joint, they usually cover less than 50 G-APD cells, i.e. 1.5 % of all cells. Even the largest bubble (shown in figure 3.45[e]) only covers less than 1/30 of the area. Even when assuming that every photon hitting a bubble would be lost, the light loss would only be a few percent. On the other hand, the relative size of the bubbles becomes larger for photons with a small angle to the sensitive surface. The net effect was estimated by introducing a large bubble in the simulation, confirming <5 % light loss even for the largest bubbles and a negligible loss for smaller ones.

### G-APD operation voltage distribution

The bias voltage groups were chosen within the bubble class. Bubble class A consists of 1224 pixels, i.e. 136 groups of 4 and 5 pixels each. Bubble class B consists of 217 pixels,



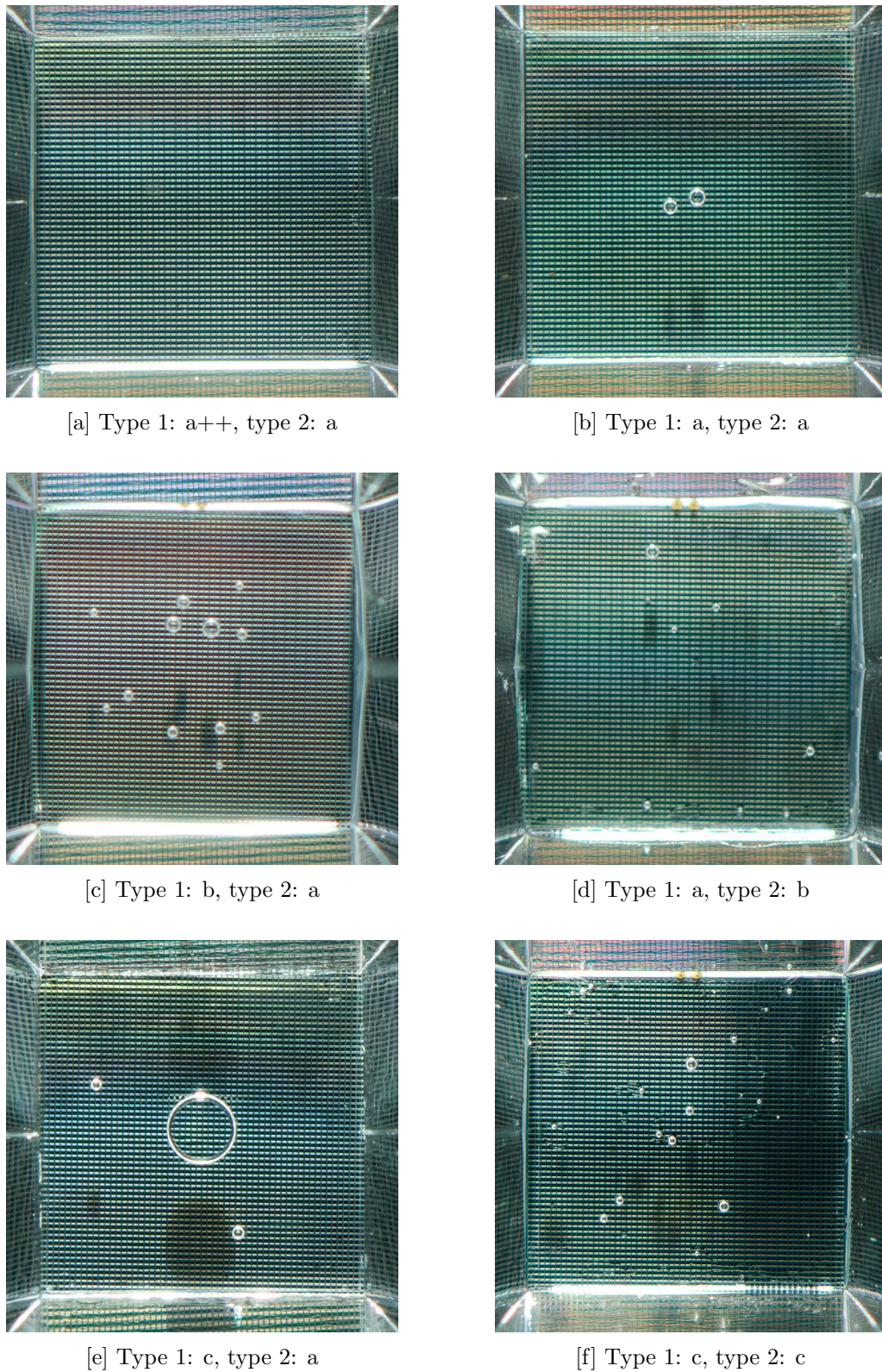


Figure 3.45.: Categorization of the pixels according to the amount of bubbles in the gluing of the cone to the G-APD: type 1 bubbles consist of trapped air and are well visible. Type 2 bubbles form less visible structures and are of unknown origin. The worse categorization determined the bubble class: [a][b] class A is the top class of pixels, for which only few small bubbles of type 1 were allowed. [c][d] Pixels of class B are only used in the outermost ring of the camera. [e][f] class C pixels are not used in the camera.

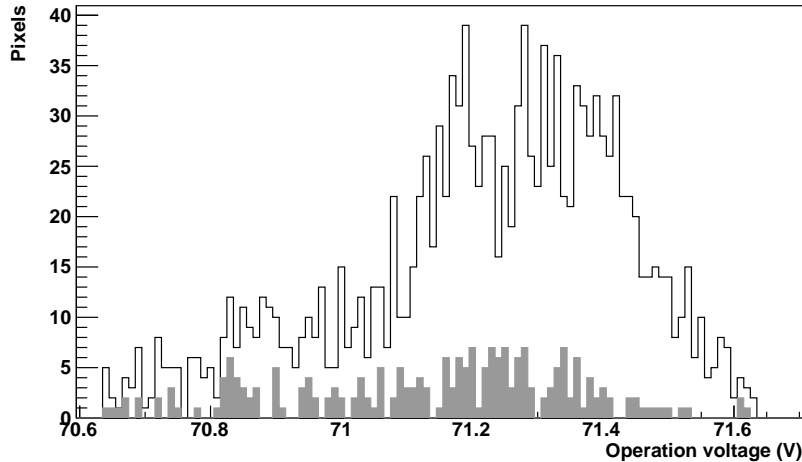


Figure 3.46.: Operation voltage distribution of the 1441 pixels of the gluing classes A (1224 pixels) and B (217 pixels, gray). One pixel from class B with an operation voltage of 70.64 V was not used in order to optimize the voltage spread within the bias groups.

resulting in 24 groups each with one spare pixel. The operation voltage distributions are shown in figure 3.46. The voltage groups were optimized to minimize the spread within the 320 groups for as many pixels as possible. This minimization was done by hand.

For 312 groups, the spread of the operation voltage is below 0.02 V, thus setting the bias voltage to the mean value would result in a deviation of the bias voltage below 0.01 V for those pixels. Of the other 8 groups, 7 have a spread below 0.05 V and one of 0.09 V. Figure 3.47 shows the average operation voltages per group and the histogram of the voltage spreads per group.

### 3.4.3. Gluing of the pixels to the front window

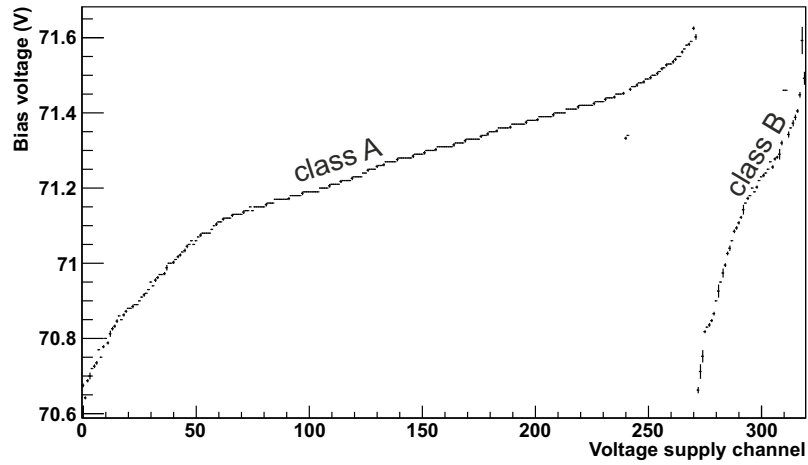
The gluing of the pixels to the front window started with extensive tests of the gluing procedure and the evaluation of the gluing quality. It was discussed to use the same glue (EPO-TEK 301) also for this gluing joint, but the idea was discarded mainly for two reasons: the pixels are glued row by row. If there was spill-over from the glue beside a cone, it would be very difficult to remove, and potentially interfere with the placing of neighboring pixels. Further it would be very difficult to avoid trapped air over the large gluing area.

The pixels were thus placed and aligned on the front window without glue. Then a low-viscosity glue is supplied to the edge of the pixel with a syringe: due to capillary action, the glue is drawn into the gap between the pixel and the front window. The glue was manufactured by the same company that produced the front window and the cone material, Evonik Industries<sup>(35)</sup>: ACRIFIX 1R 9019 Solar, a glue optimized for this gluing process.

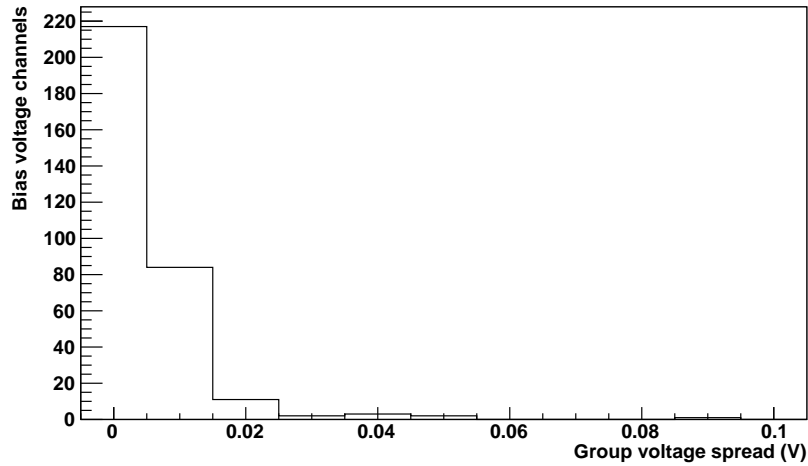
Obviously, the success of the procedure depends largely on the capillary action and thus on the homogeneity and cleanliness of the surfaces. A variety of soaps and cleaning techniques were evaluated, and the composition of the glue optimized in cooperation with the manufacturer.

The gluing procedure was as follows: the hexagonal sides of the cone and the window were carefully cleaned. Then the pixel was placed on the front window, touching the previously

<sup>35</sup>Evonik Industries, Germany, <http://www.evonik.com>.



[a]



[b]

Figure 3.47.: Visualization of the operation voltage groups for the FACT camera: [a] The operation voltages of the 320 channels are distributed from 70.6 V to 71.6 V. The first 272 groups are from class A pixels, the 48 upper groups consist of class B pixels. [b] The spreads of the single G-APDs operation voltages within one group could be kept small for most patches. This was important since most operation parameters depend on the over-voltage, which is around 1.1 V for our devices. The gain is linear in the over-voltage, such that the gain variations within one patch are below 1% with these bias voltage groups.

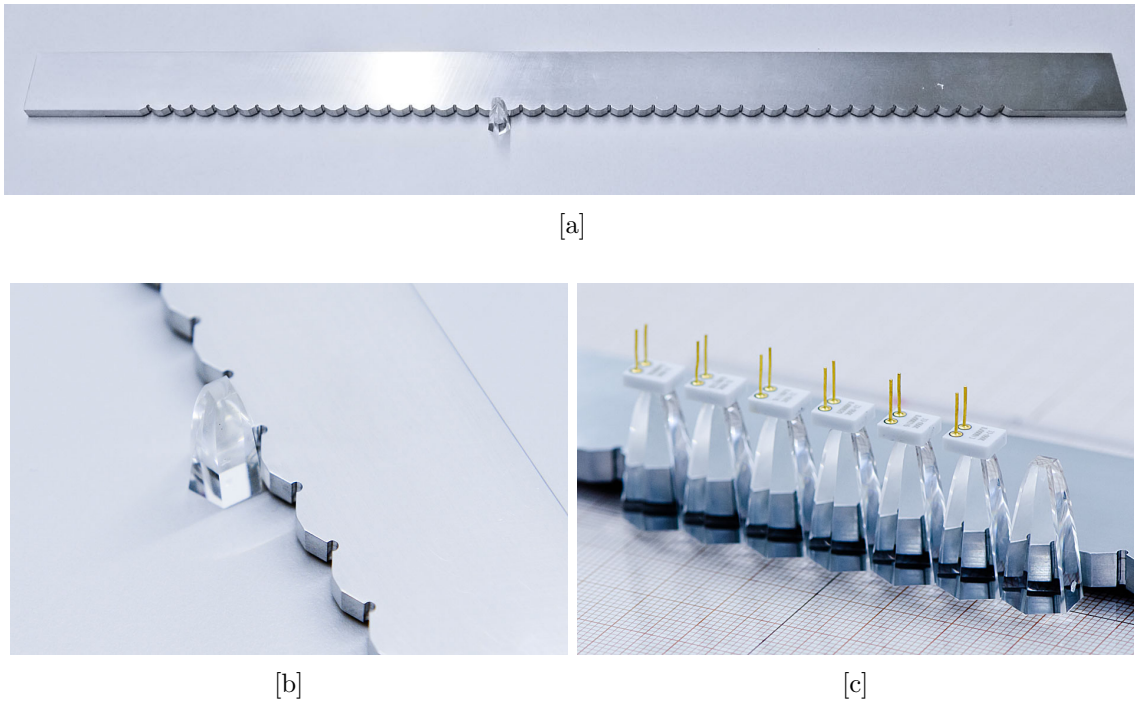


Figure 3.48.: [a] For the alignment of the first row of pixels, a custom-made ruler was used. [b] Zoom to one pixel. [c] Gluing of the test patches: the first pixel without G-APD was placed to test the alignment of the cones to the ruler. The six complete pixels form the middle row of the test patches.

glued pixels. After the check of the position and alignment of the cone, the glue was applied, and the next pixel cleaned. When a full row of pixels was placed, the glue was hardened for 40 minutes with a strong Philips UV lamp<sup>(36)</sup>, and the next row started<sup>(37)</sup>. For the alignment of the first row, a custom-made ruler was used (see figure 3.48).

### Glue optimization

The glue Acrifix 9019 was developed for the connection of flat, cast Plexiglas. Such materials have a better surface quality than what can be achieved in an extrusion process as in the production of our cones. This led to the problem that often the glue would flow around small volumes while being drawn in, producing bubbles of enclosed air.

On May 26th, 2011, J.-P. Stucki and I visited the research laboratory of the glue manufacturer Evonik in Darmstadt, Germany. After explaining the purpose of the gluing and the problem with the bubbles, we went to their laboratory and tested various cleaning methods of the front window and the pixels on unused cones.

However, the cleaning method developed by J.-P. Stucki and me turned out to be as successful as their propositions, and the bubbles could not completely be avoided. The breakthrough came when we realized that the bubbles appeared when the glue was flowing around a region too fast. The solution was to *increase* the viscosity of the glue slightly: the same glue existed also in a higher-viscosity version (ACRIFIX 1R 9016 Solar), of which we added some percent.

<sup>36</sup>Philips HPLR E40 250 W

<sup>37</sup>A possible degradation of the cone quality from the UV light was excluded by measuring the transmission of a sample cone before and after an illumination with a UV lamp for more than 500 h, where no difference was found.



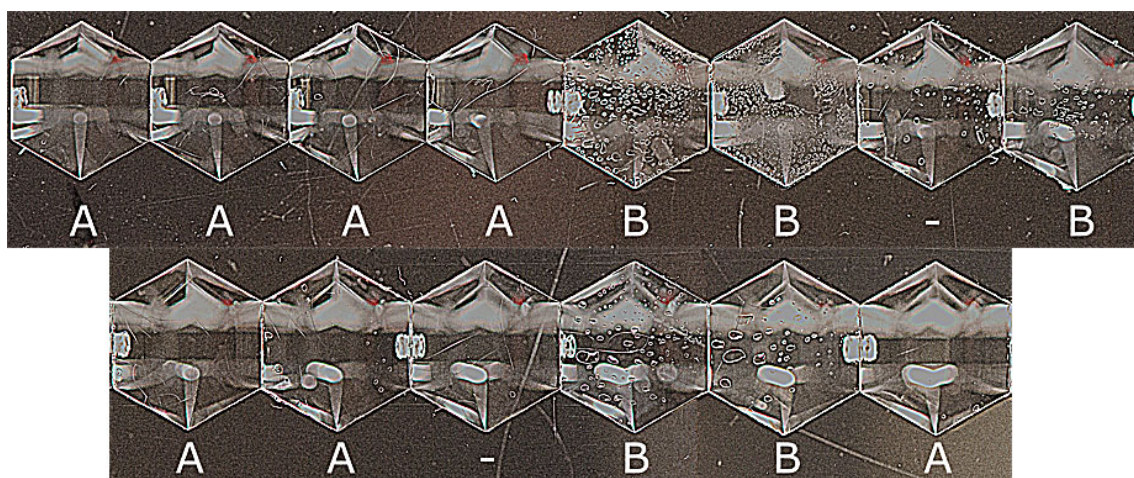


Figure 3.49.: Comparison of two cleaning methods: in “A”, the cones are being cleaned pressed to the thumb, whereas in “B” the cones were cleaned pressed to the palm of the person (gluings denoted with “-” were cleaned using a mixture of the two methods). The first method was completely bubble free, whereas the second method showed much worse results. The significance of the difference was rather surprising, but the gluing procedure could easily be adapted once the problem was found.

In further tests back at ETH Zurich with various amounts of Acrifix 9016, we determined the optimal percentage at 5%. Together with the optimized cleaning, bubbles could be completely avoided.

### Cleaning tests

Compared to the cleaning of the cones or G-APDs, the cleaning of the front window had an additional problem: new pixels are glued adjacent to existing pixels. This makes it difficult to use soap water and rinse with distilled water afterwards, since the soap water would also be distributed between the already glued pixels. Fortunately, one of the cleaning detergents which was ruled out for the cones is no problem for the front window: since the front window has no internal tensions, the use of isopropanol is not a problem. Isopropanol also evaporates completely without any trace, so no rinsing with distilled water was necessary. The “cleaning power” was found to be even slightly better than soap water.

The hexagonal side of the cone was cleaned with soap water in the same way as for the cone-G-APD gluing. It turned out that the “cleaning technique” is crucial: figure 3.49 shows a row of test gluings, where the cones were cleaned by two persons (A/B). Person A cleaned the cones with circular motions when pressing the cone to the thumb and subsequent linear movements from the center to the edge, whereas person B cleaned the cones with similar motions while pressing the cone to the palm of his hand. Surprisingly, only this difference resulted in a significant difference in the amount of bubbles. Our only explanation was that using the thumb produces a higher and more homogeneous pressure on the cone surface. The method was then successfully transferred to person B.

### Load tests

The stability of the gluing was tested in the same way as the first gluing: the window was fixed in a bench wise. A screw is drilled into the square side of the cone and a cord

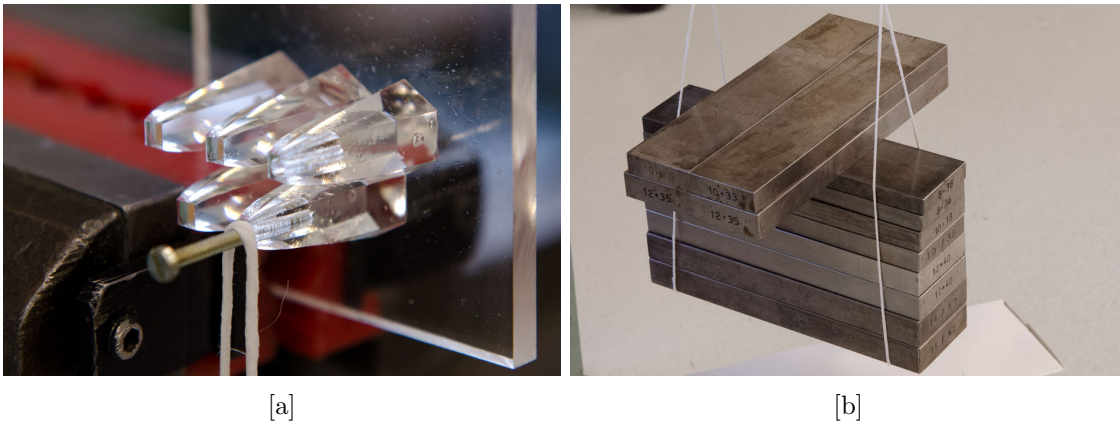


Figure 3.50.: Setup for the stability measurement of the window gluing: [a] A screw is drilled in a hole in the square side of the cone. [b] A force was applied to the end of the cone via a cord, which was loaded with metal weights. The gluings were extremely stable, requiring more than 7 kg of weights until they broke.

fixated, which was loaded with metal weights (see figure 3.50). The force was gradually increased until the gluing broke. As in the gluing of the cones to the G-APDs, the weak point in the gluing is not the contact between glue and one of the surfaces. As can be seen in figure 3.51, the gluing was so strong that a part of the cone remained on the window, i.e. the cone was ripped apart.

Two gluings were tested: both held a weight of 6880 g, and broke when the next weight was added (330 g and 245 g, respectively). Such large forces would never be reached in the sensor compartment, and anyway the other gluing would break first, so the stability of this gluing was not an issue.

### Capillary effect between the cones

The low viscosity of the glue also had unwanted consequences: the glue was also drawn up between the cones (see figure 3.52). This allows optical crosstalk between the pixels, and light can get lost since the angle between photon direction and glue surface is too small for total internal reflection.

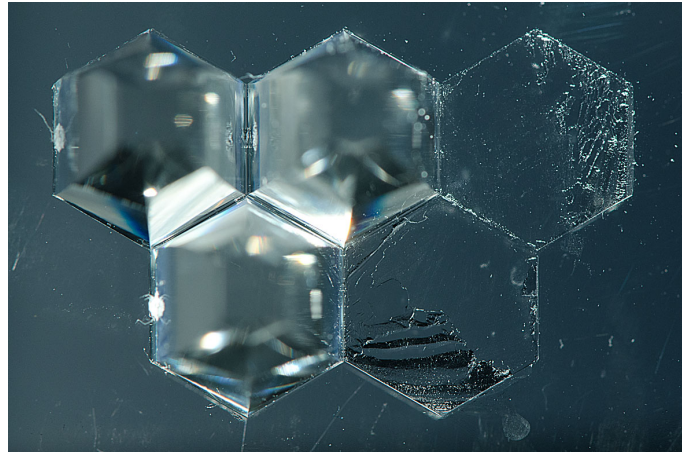
The extent of the effect was measured using a macro photography and the measuring tools in Adobe Photoshop<sup>(38)</sup>. The glue was drawn up between 0.3 mm to 0.65 mm depending on the amount of glue. For the final front window assembly, surplus glue was retracted into the syringe.

### Gluing administration

The final gluing of the pixels onto the front window was a delicate task: since there is no chance to remove or replace a pixel once it is glued, no mistake in the administration of the cones was allowed. Since the position of a pixel on the front window defines its bias voltage group members, gluing a pixel to a wrong location could make a full voltage group inoperative depending on the operation voltage of the pixel and the other group members<sup>(39)</sup>.

<sup>38</sup>Adobe Photoshop CS5 Extended, <http://www.adobe.com/products/photoshopextended.html>.

<sup>39</sup>It would in principle have been possible to correct such a mistake by adapting the cabling of the front window, but only with difficulty and large administrative efforts.



[a]



[b]



[c]

Figure 3.51.: Result of the load test: Two gluings were tested, both broke not at the contact between glue and cone or window. [a] Remnants of the cones are still attached to the front window. [b][c] The two cones were ripped apart during the load test.

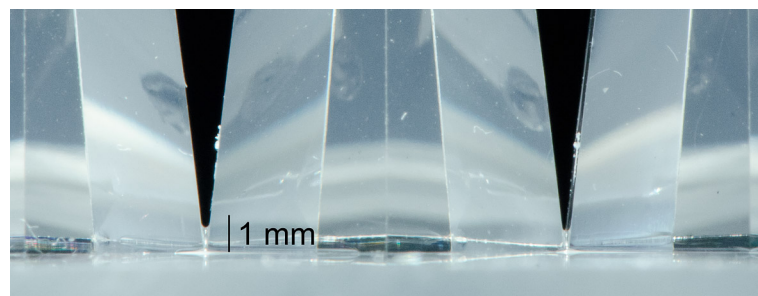


Figure 3.52.: Due to the low viscosity of the glue used for the gluing of the pixels to the front window, it is being drawn up between the cones. For the final camera, the effect was minimized by retracting surplus glue back into the syringe.

One measure to limit the effect of a potential wrong gluing was to arrange the bias voltage groups in ascending order in a spiral from the center of the camera: if two neighboring pixels swap their position, the bias voltage group in the new position would only be off by maximally the step between the spiral arms. The exceptions are the pixels in the outermost ring, where large steps are possible.

To facilitate the administration of the pixels during the gluing, the pixels were sorted into the rows as they are positioned on the front window. From there they could be taken one by one and placed on the front window, making a mistake in the gluing difficult. The challenge was thus shifted to the selection of the right pixel out of 1540 and the sorting into the correct row. Since this job was quite demanding and time-consuming, J.-P. Stucki and I decided that the gluing would be done with the help of another PhD student (B. Huber from university of Zurich), so I could focus on the administration.

The system with the sorted rows proofed to be very successful. Not a single mistake happened in the administration of the 1440 pixels<sup>(40)</sup>. Figure 3.53 shows some impressions of the finished front window.

#### 3.4.4. Cable soldering and baffle plate installation

For the connection to the electronics, small circuit boards are soldered to the G-APDs. For the inner, regular patches each board connects to 9 pixels, adding stability to the setup. The outer, irregular patches are connected individually. The boards were soldered by L. Djambazov and H. von Gunten (see figure 3.54).

The groups of cables are led to the baffle plate, which isolates the sensor compartment from the heating of the electronics. The cables are tied to strings which are lead through the respective holes in the baffle plate. Afterwards the baffle plate is carefully lowered into its final position (see figure 3.55).

#### 3.4.5. Pixel repairs

Even though every single pixel built into the FACT camera passed the load test of the cone-G-APD gluing, for some pixels the mechanical stress during the soldering of the pixels or in particular the installation of the baffle plate was too large such that they broke. Five of these pixels were in the outermost ring of the camera, where the pixels are connected to single boards, but also one complete patch and seven of the inner pixels were affected (see figure 3.57 and table 3.4).

The pixels at the edge and the broken patch were repaired using the same glue as used before (EPO-TEK 301). The pixels were carefully cleaned of easily removable glue parts and new glue applied on both cone and G-APD, with special care on filling the irregular surface of the old glue. The front window was placed between two tables, such that I could check the alignment of the G-APD through the front window after placing it on the cone. Small weights were placed on the G-APDs to stabilize the gluing during the following 24 hours (see figure 3.56).

The inner pixels could not be accessed after the cables were soldered and the baffle plate installed. For the seven broken inner pixels, a different approach was necessary. The sensor compartment was turned upside down such that the G-APDs were below the cones (note that also for the broken pixels the G-APDs remained at their location since they

---

<sup>40</sup>However, one mistake happened in the gluing: the two first pixels of a new row were glued one position off, and exactly over the edge from the outermost bias voltage ring to the inner range. I could correct this error by reshuffling most of the pixels in the outer ring, which led to the bias groups presented above.



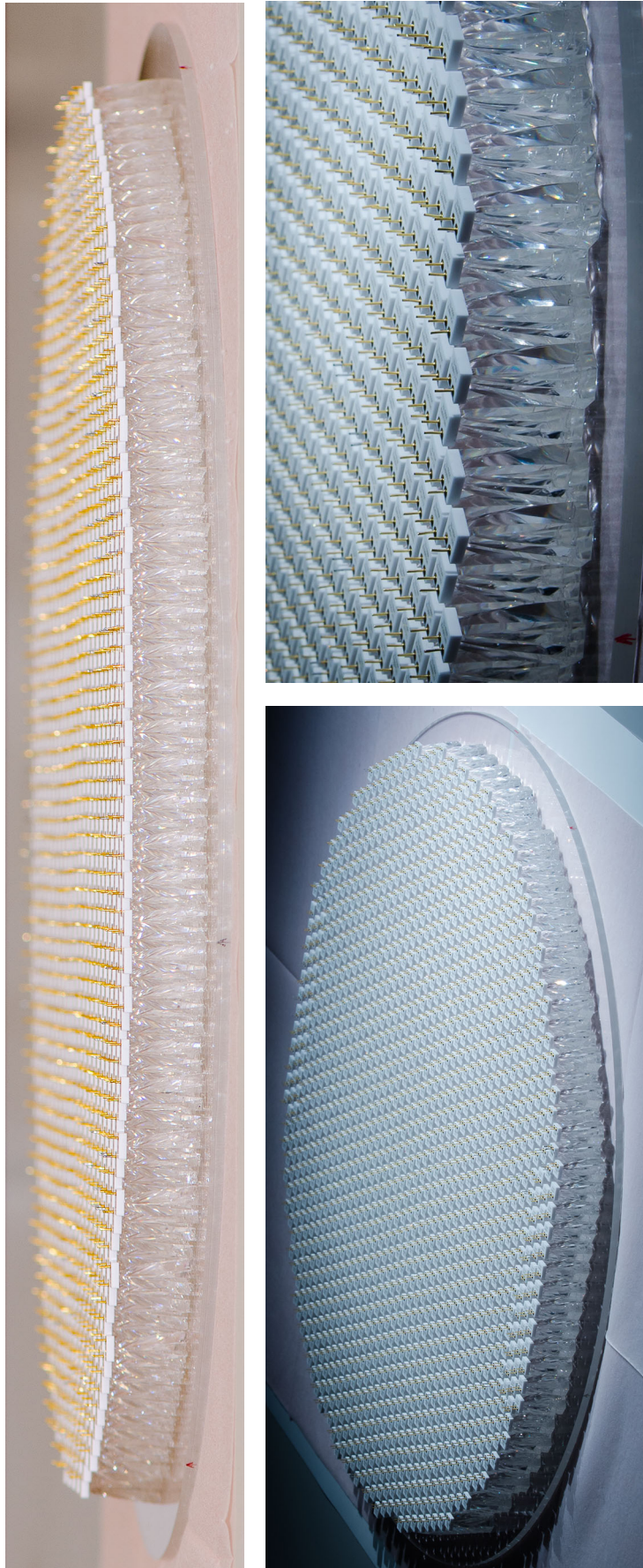


Figure 3.53.: Impressions of the front window after the assembly of the optical part was finished.



Figure 3.54.: Soldering of the cables to the G-APDs: [a] The G-APDs are soldered to small circuit boards, which are connected to the coaxial signal cables. Each board is for one patch (9 pixels). The 18 pins must be exactly parallel in order to fit the boards. [b] The cables were soldered from the center of the camera towards the outer ring, since the cable density made it difficult to access pixels after their neighbors were connected.

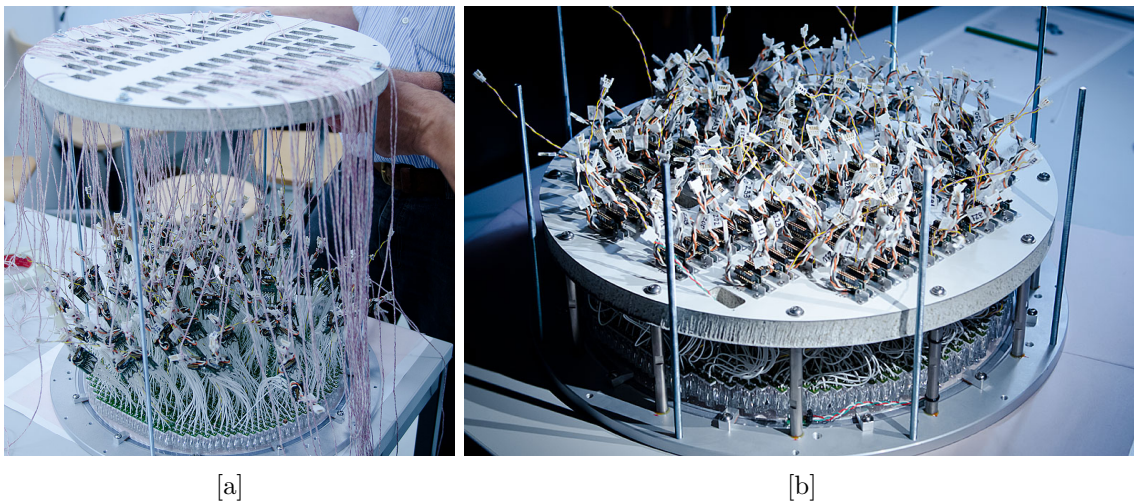


Figure 3.55.: Installation of the baffle plate: [a] The cables are attached to strings, which are lead through the holes in the baffle plate. [b] Afterwards the baffle plate is lowered and fixed firmly to the front window. The image shows the final sensor compartment of the FACT camera.



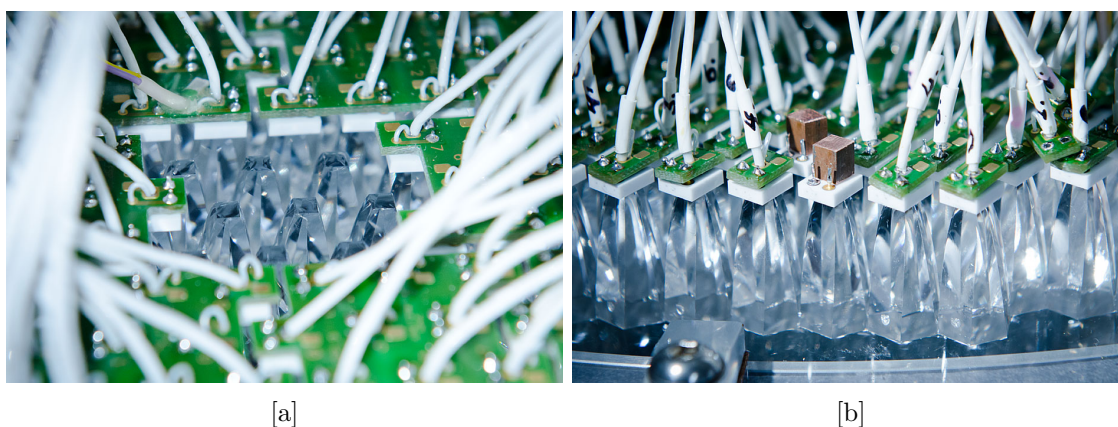


Figure 3.56.: [a] One full patch was torn off during the installation of the baffle plate. [b] The G-APDs were stabilized using small weights.

were soldered to the small carrier boards). The only way to access the gluing joint was by using a syringe with a long needle (see figure 3.58). Since the epoxy glue would be too viscous to flow into the gap between G-APD and cone, the low-viscosity glue Acrifix 9019 (which was used for the gluing of the pixels to the front window) was chosen. The method was first tested with an unused broken pixel (see figure 3.59).

The positioning of the needle in the labyrinth of pixels was a challenge. The needle could only be inserted along the rows of the camera. Markings on the needle showed the length of the inserted part in the sensor compartment. The position of the needle tip could only be determined using those markings and by feeling the contact of the needle with the cones. When the needle was placed, the gap was filled with glue, and surplus glue retracted into the syringe. This repair method required three persons, one for the positioning of the needle, a second one to operate the syringe and a third one checking the gluing joint through the front window.

Using these two methods, all G-APDs could be reattached to their cones. The inner pixels could only be partially repaired, since it was not possible to control the application of the glue precisely. The only alternative would have been to remove the baffle plate and unsolder the respective patches, but this idea was dropped due to the resulting risk to other pixels. For the pixels which could be accessed from the edge of the camera and were glued with the original epoxy glue, no difference to the other pixels could be detected after the gluing. A front view of the camera after the repairs is shown in figure 3.61.

### 3.4.6. Final front window

Of both sides of the front window, a high-resolution image was taken. The rear view (see figure 3.60) allowed to read the serial numbers on the back of each G-APD, which was used to recheck the position of each pixel on the focal plane.

The high-resolution image from the other side (see figure 3.61) was taken after the front window was installed in the camera. The illumination was chosen such that the pixels are well visible. The image was used to measure the deviation from the camera center as defined by the pixels to the camera center defined by the aluminum ring. The deviation is below 0.5 mm, which is by far accurate enough.

Category	SoftID	G-APD	Glue
<i>Edge pixels</i>	1373	256	Epoxy
	1376	277	
	1400	1128	
	1435	283	
	1438	1985	
<i>Broken patch</i>	909	47	Epoxy
	910	1707	
	911	516	
	1017	1834	
	1018	406	
	1019	478	
	1130	253	
	1131	1826	
1132	323		
<i>Inner pixels</i>	241	649	Acifix
	760	591	
	847	1928	
	853	1781	
	923	626	
	952	219	
	955	520	

Table 3.4.: List of pixels with broken cone-G-APD gluing: most pixels were ripped off by tension on the cables during the installation of the baffle plate. All gluings were remade, the ones at the edge and the patch with the same glue as before (EPO-TEK 301), the other ones with the low-viscosity glue from the window gluing (Acifix 9019).



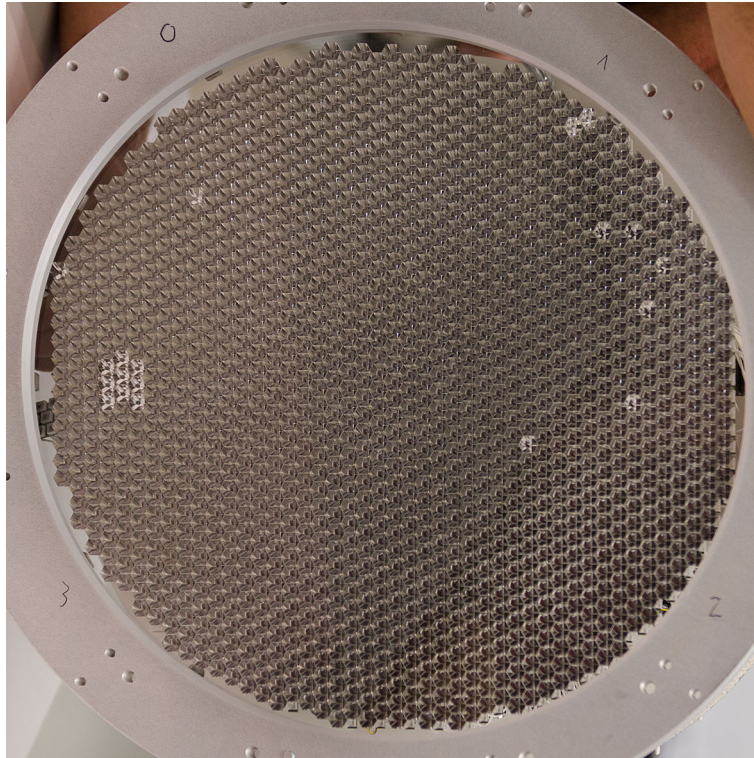


Figure 3.57.: The broken pixels are clearly visible when looking on the front window of the FACT camera: if the gluing joint is intact, the dark G-APD sensor is reflected at the sides of the cone, such that the full hexagonal area appears dark. Picture 3.61 shows the final front window after the repairs.

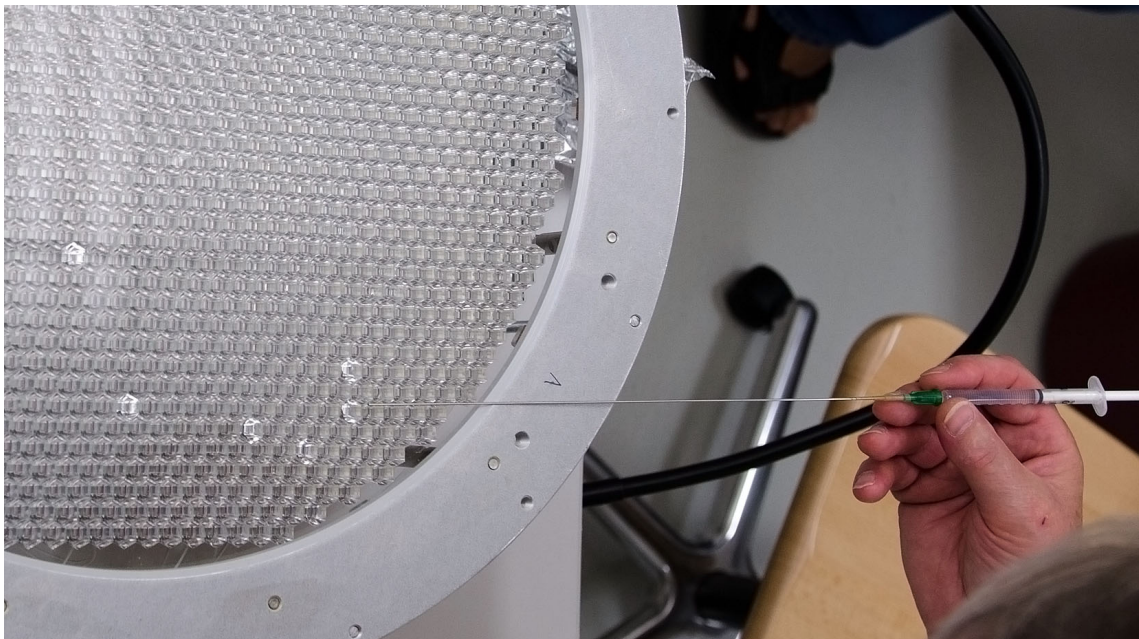


Figure 3.58.: A syringe with a long needle was necessary to access the inner pixels. The needle could only be inserted along the rows of the pixels, and the position of the tip of the needle could only be determined by feeling the contact between the needle and the cones.

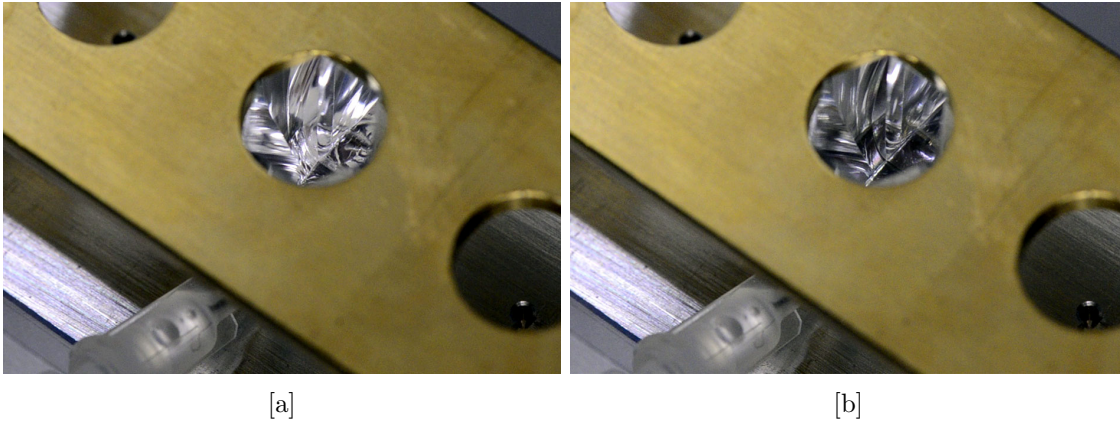


Figure 3.59.: The repair of broken inner pixels using the low-viscosity glue Acrifix 9019 was first tested with an unused broken pixel. The success of the repair can be estimated by the brightness of the hexagonal entrance area, since only with intact gluing joints the dark G-APD chip is projected to the full hexagonal entrance area. The pictures show the entrance area [a] before and [b] after the glue is applied.

### 3.5. Electronics

The electronics for the final FACT camera features two important concepts which were not used for the prototype module M0: the integrated digitization and the sum trigger. The trigger for M0 consisted of a majority logic on the discriminated signals from the single pixel signals using analog thresholds. The new trigger for FACT first sums the analog signals of nine pixels, onto which the threshold is applied. This approach has several advantages, among other an improved signal-to-noise ratio<sup>(41)</sup> and the contribution to the trigger of signals which are smaller than the single pixel threshold. A similar design was also implemented in the camera of the MAGIC-I telescope [58]. The best patch size for the FACT camera was determined with a simulation (T. Bretz, D. Hildebrand).

While the signals of the prototype module M0 were guided to external digitization electronics via long cables, an integrated digitization was targeted for the FACT camera. In order to achieve a fast digitization rate with low power consumption (see also section 3.1.3), the Domino Ring Sampling chip DRS4 is used. The signals from the digitization boards are sent via an Ethernet switch to a computer, where the events are assembled and stored on hard disks.

In the following, the part of the electronics which is of particular importance for the operation of the G-APDs is described. A full overview on the design of the electronics and the interplay of the electronics boards is given in the design paper of the FACT project [126].

#### 3.5.1. Pixel organization

The electronics of the FACT camera is organized in 160 patches of nine pixels. The signals of these nine pixels are summed up for the readout trigger of the camera, they are thus also called “trigger patches”. Furthermore, these nine pixels share a connector at the baffle plate and are processed on the same amplifier and digitization board. Each trigger patch is supplied by two bias voltage channels. The grouping of the pixels was made based on

<sup>41</sup>For a Gaussian noise, the improvement would be a factor of  $9/\sqrt{9} = 3$ . As can be seen in appendix A.4, the improvement is even larger for low rates of background photons, i.e. during dark nights.



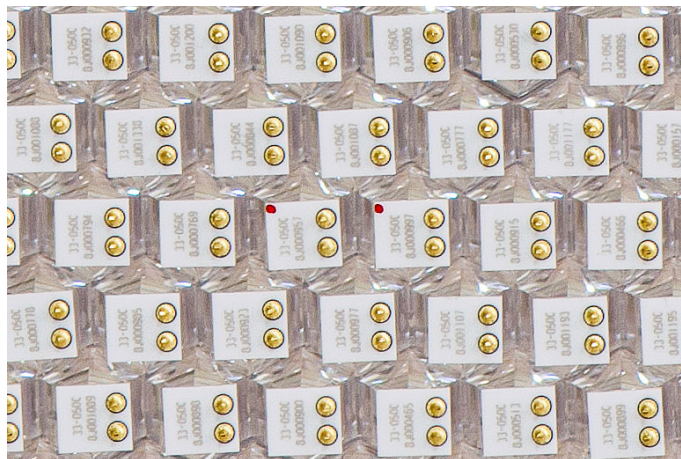
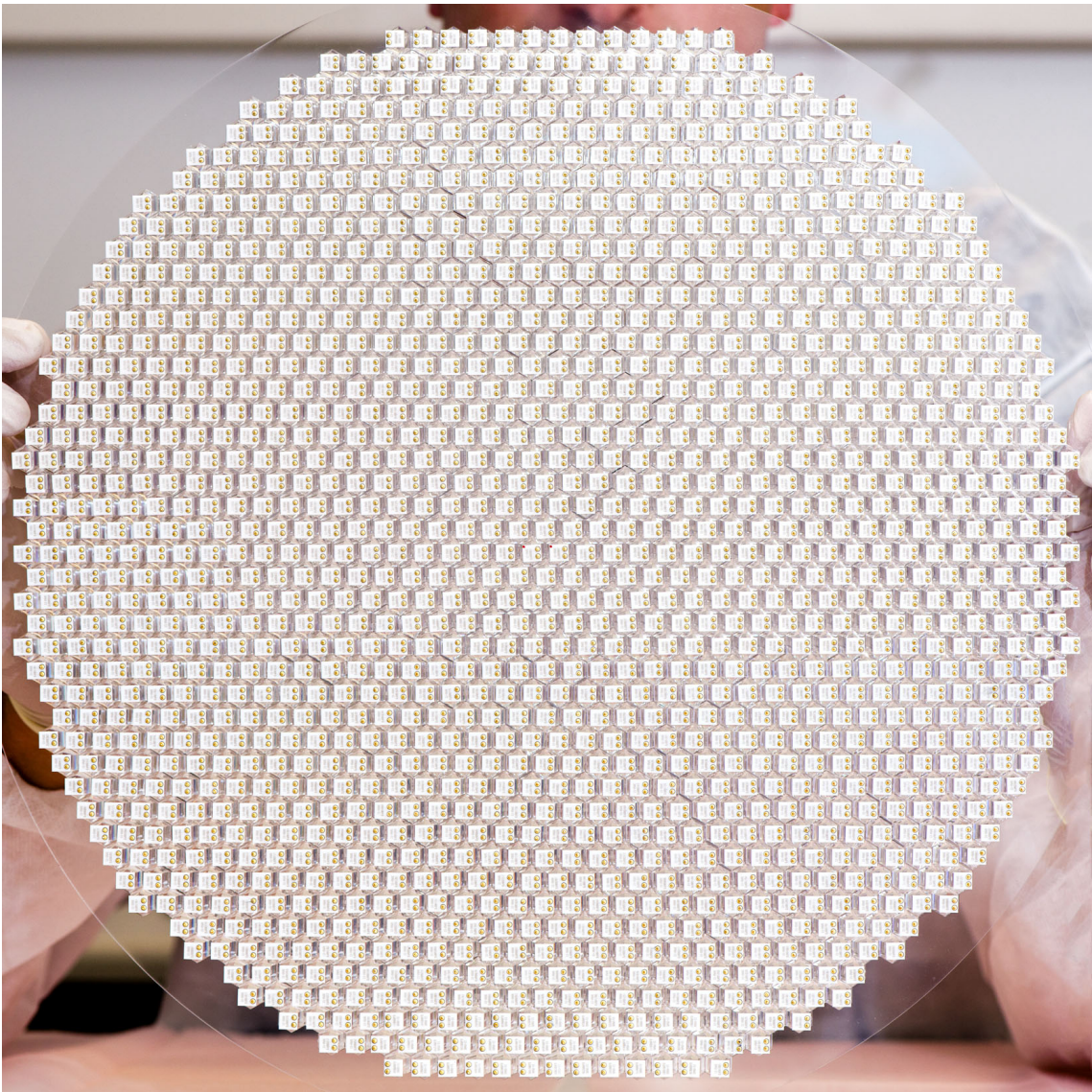


Figure 3.60.: High resolution image of the front window: the serial numbers on the back of the G-APDs allowed to check the position of every single pixel. The red dots mark the two pixels adjacent to the center of the camera.



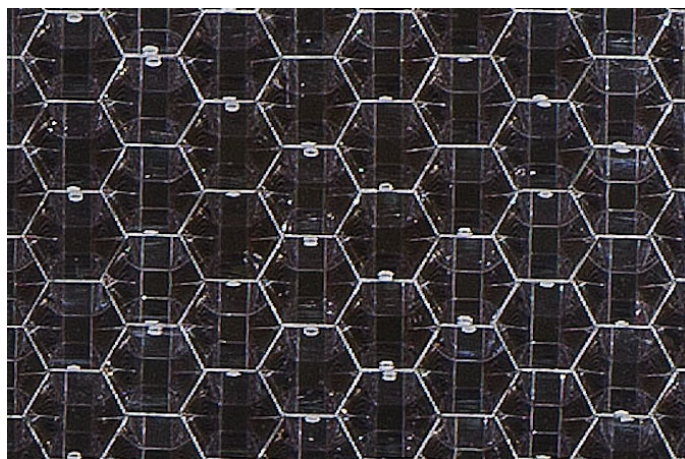
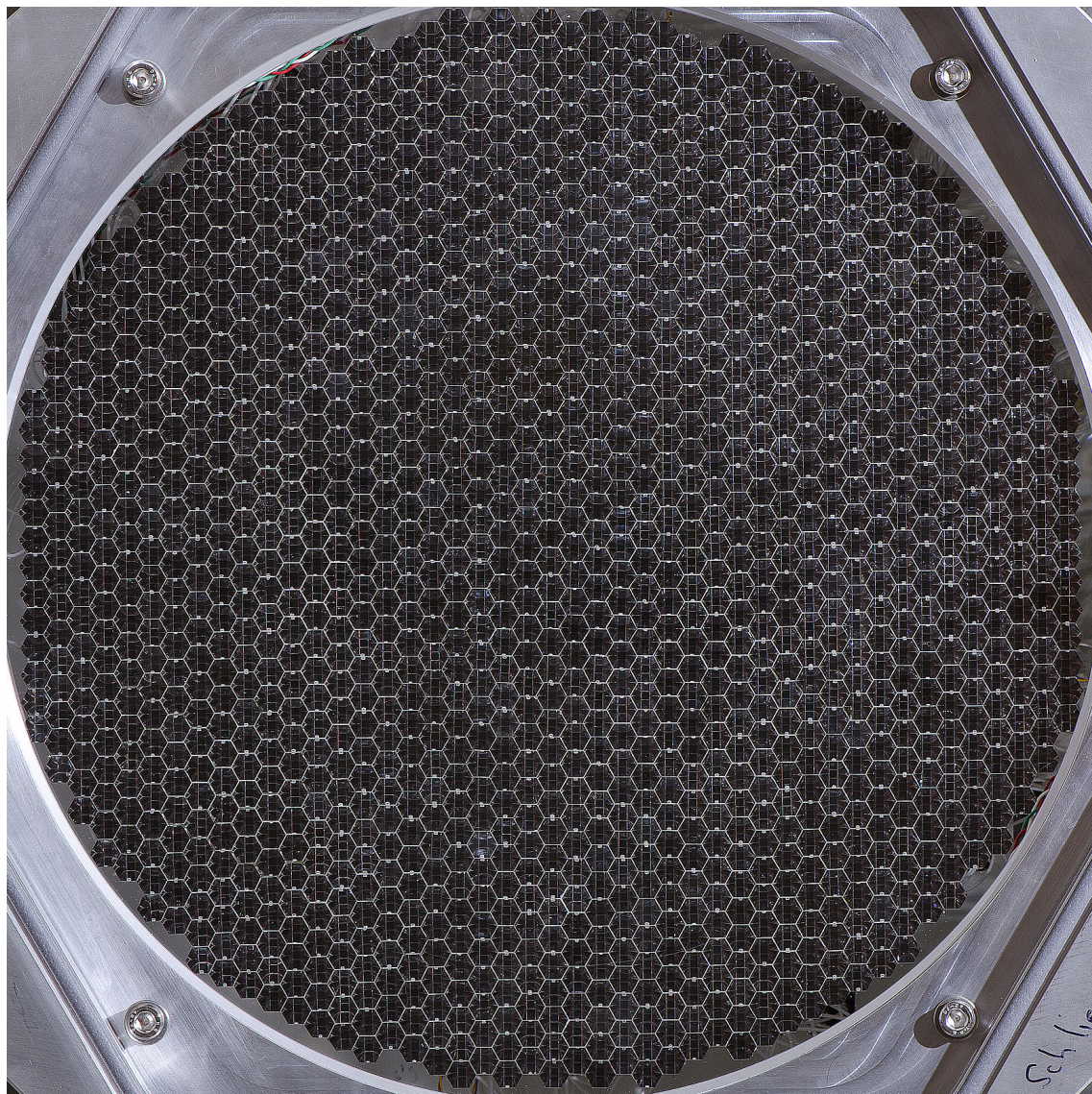


Figure 3.61.: High resolution image of the front window (diameter 396 mm): this image was taken after the assembly of the full camera. The pixels appear dark since the black G-APD sensor is reflected onto the full hexagonal entrance area of the cones.



two criteria: for the inner pixels, the groups should be as compact as possible, and for the outermost ring of pixels the aim was to minimize the cable length between the pixels and the connectors of the baffle plate (optimization by A. Biland). See figure 3.62 for an illustration of the trigger patches.

### 3.5.2. Electronics: front-end layout

Each G-APD of the FACT camera is amplified and read out individually. The signals are AC-coupled to the pre-amplifier boards, which have an input impedance around  $25\ \Omega$ . The nine G-APDs of one patch are divided into two groups, which share one bias voltage channel each. The connection of the G-APDs for the bias supply leads to electronic cross-talk within the bias voltage groups. To reduce this effect, the channels are decoupled with a resistor of  $3.9\ \text{k}\Omega$ . This resistor has a very important consequence for the operation of the telescope: since it is in series with the G-APD, the current flowing through the sensor induces a voltage drop, which in turn reduces the effective bias voltage which is applied to the G-APDs. In case of high ambient light, this voltage drop is large enough to make it necessary to be corrected by adapting the bias crate voltage.

Figure 3.63 shows a schematic drawing of the FACT electronics up to the first transistor of the pre-amplifier board.

### 3.5.3. Pre-amplifier and trigger system

The photosensors produce a well-defined charge per photon around  $7.5 \times 10^5$  electron charges (see table 2.2). The stream of these pulses from dark count, background photons and signal photons is converted into voltage pulses with an current-to-voltage amplifier whose bandwidth is around 200 MHz (see H. Anderhub *et al.* [126] for more details). The input impedance of the circuit is around 25 Ohm.

The signal is then split, one line going to the connectors to the readout boards, the other being destined for the trigger logic. The trigger signals of all nine pixels are summed up analogously. Every pixel can be left out of the analog sum for test purposes, or, during normal operation, if a pixel is noisy due to a bright star or being broken. To make the trigger signals short, its reflection at the end of a short-circuited coaxial cable is added, which reduces the signal length to about 10 ns.

On one electronics board, the signals of four patches (36 pixels) are processed. The trigger signals are put to a comparator with an adjustable threshold up to  $\sim 270$  single photon signals. The resulting (digital) signals are summed and fed into a discriminator, which allows in principle to apply an *N out of 4* logic. This design was originally foreseen for more complicated trigger layouts, but abandoned after tests with the prototype module M0 and simulations. Except for tests, the configuration during normal operation is always 1 out of 4. The discriminator still serves a purpose: since the input signals need a minimal time above the threshold ( $\sim 1$  ns) to trigger the discriminator, noise signals which are larger than the comparator threshold usually do not trigger the discriminator due to being too short, which effectively filters noise spikes.

The forty discriminated signals are called trigger primitives and collected by a central trigger master board. Another coincidence logic (now *N out of 40*) with an adjustable time window from 8 ns to 68 ns creates the final trigger signal. Again, the coincidence is operated as 1 out of 40 during normal operation.

Besides those so-called “physics triggers”, the trigger master board creates random triggers for pedestal events and manages the two light pulser systems. When a start signal is sent to the internal light pulser in the closed camera lid, the readout signal for the

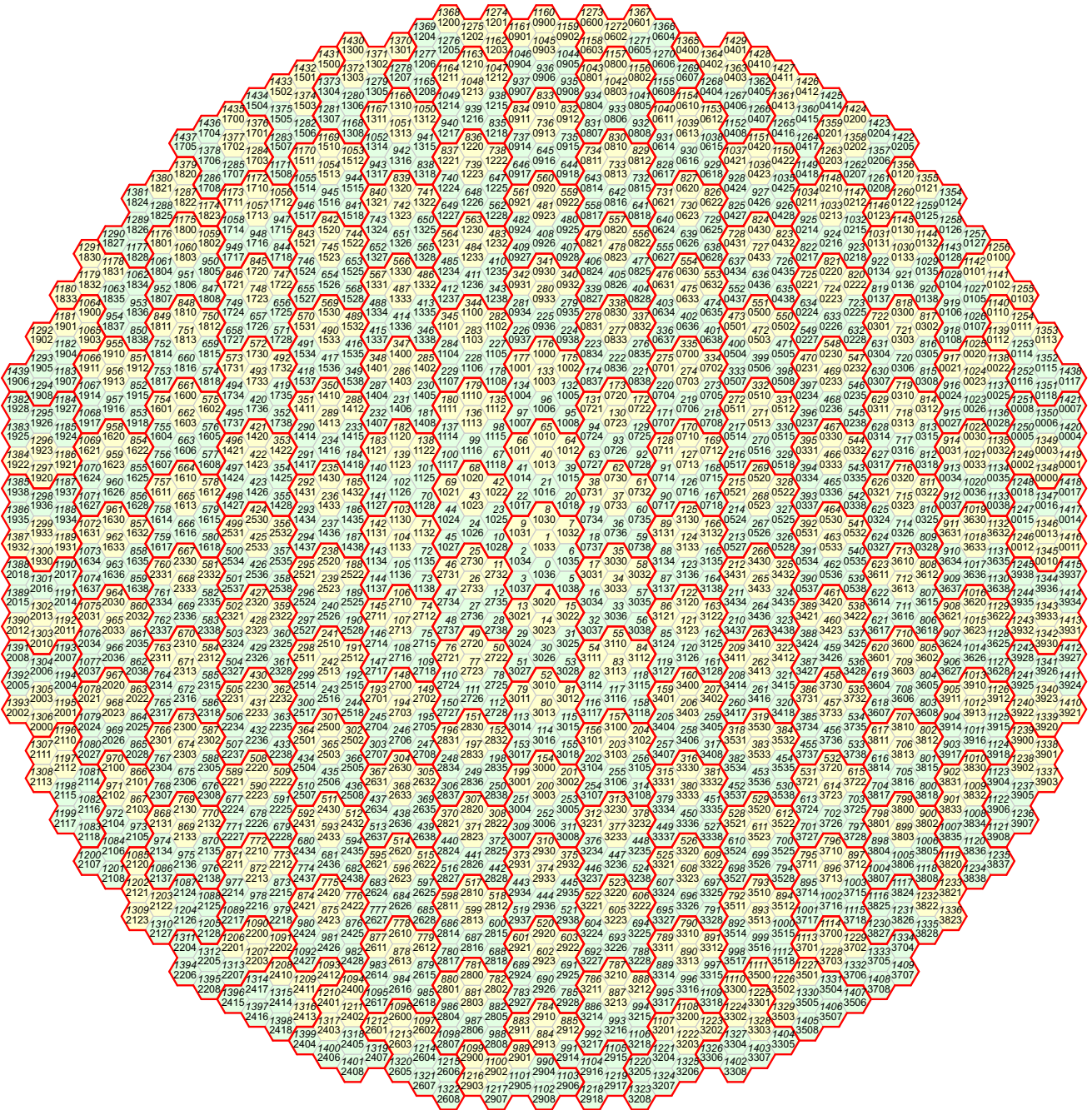


Figure 3.62.: Grouping of the pixels into patches (red lines): the inner patches all have the same compact layout. The outermost ring of patches was optimized for short cable lengths from the pixels to the baffle plate. The two numbers are the identification numbers of the pixels. The upper, italic number denotes the “SoftID” of a pixel. It is fixed to a geometric position and runs in a spiral from the center of the camera. The lower number denotes the hardware number (“HardID”) of the pixel, which is fixed to the readout channel of a pixel. It follows the scheme CBPX: crate number (0-3), board number (0-9), patch number (0-3) and position within the patch (0-8). The positions 0-3 (yellow) and 4-8 (green) share a bias voltage channel each. The view of the sensor plane is from the side of the electronics (“back view”). Figure based on illustrations by A. Biland.

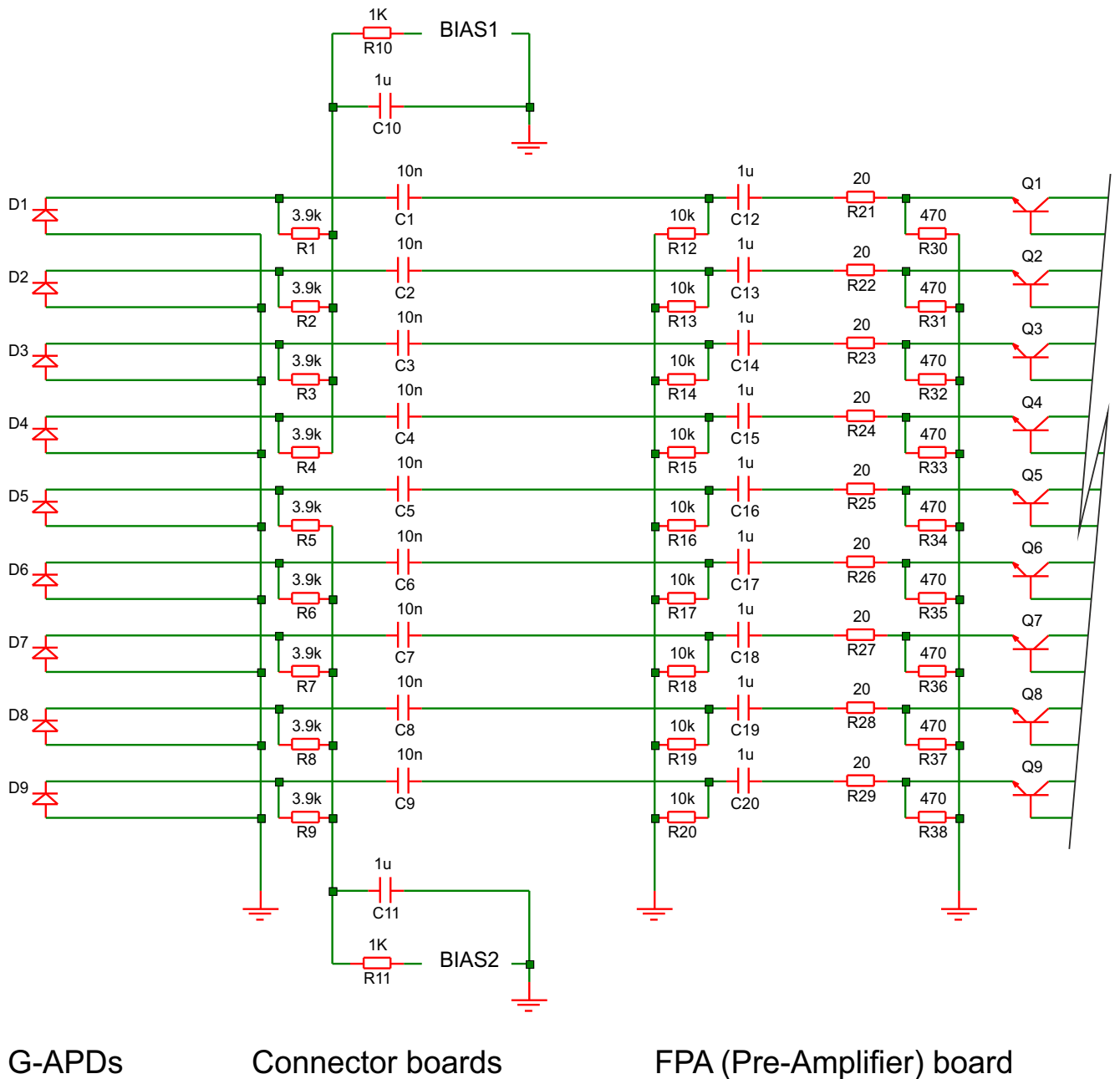


Figure 3.63.: Schematic drawing of the front-end layout up to the first transistor of the pre-amplifier: the nine G-APDs of one patch are connected to the bias crate via an individual  $3.9\text{ k}\Omega$  resistor and a common  $1\text{ k}\Omega$  resistor. The first four G-APDs share a bias voltage channel, the other five a second one. These resistors are on the connector boards, together with a  $10\text{ nF}$  capacitance on the signal line. Another capacitance is at the entrance of the pre-amplifier board. The serial  $20\ \Omega$  resistors define the input impedance of the amplifiers, together with the (approximate) input resistor of the transistor around  $5\ \Omega$ . Coaxial cables connect the G-APDs to the connector boards and those to the pre-amplifier.

digitization electronics is automatically sent with an adjustable delay. The external light pulser does not create an automatic readout signal, but its light flash is detected by the G-APDs and processed by the standard trigger chain identical to a physics trigger, which allows its testing. When the trigger master logic decides on the readout of an event, the corresponding commands are sent to the 40 readout boards.

The trigger master board is a central part of the upcoming thesis by P. Vogler (ETH Zurich), more information on the functionality and design of the board will be found there.

### 3.5.4. Digitization

The readout boards are organized the same way as the preamplifier boards: each of the 40 boards processes four groups of nine channels. The Domino Ring Sampling chip DRS4 [127, 128]<sup>(42)</sup> is used, which is the renewed version of the chip used for the readout of the prototype module M0, DRS2<sup>(43)</sup>. The main differences are not only the improved performance parameters (sampling rate 0.7 to 5 Giga-samples per second (GSPS), bandwidth 850 MHz, bit-depth 11.5 bits), but also the enhanced temperature stability and the reduced power consumption. The electronic crosstalk between the channels on the same chip was greatly reduced. Each chip can sample nine channels: the signal is continuously stored in a ring buffer consisting of 1024 capacitors. When the readout signal by the trigger master board is issued, the writing is stopped and the capacitor charge read out by an ADC with lower frequency.

The DRS4 chip has another important advantage over the previous versions: it is possible to read the buffer chain partially, decreasing the readout time and thus the dead time of the system. This Region of Interest (ROI) readout also reduces the amount of data which has to be processed and saved to disk.

The boards for the FACT camera were developed within the FACT project, in close collaboration with S. Ritt (PSI Villigen), the main developer behind the DRS4 chip. The data streams are sampled with a rate of 2 GHz, and read out at 20 MHz with a 12-bit Analog-to-digital converter (ADC). The standard readout of FACT uses a ROI of 300 samples. More detailed information about the digitization boards will be found in the upcoming thesis by D. Neise (University of Dortmund).

### 3.5.5. Bias voltage supply

Also the voltage supply was developed specifically for the FACT project. The main challenges are closely connected to G-APDs and this specific application:

- Almost all device parameters depend strongly on the over-voltage, which is around 1.1 V at a bias voltage of 70 V (see section 2.4.1). In order to keep the device parameters constant to 5 % (as specified within the collaboration), the voltage source needs to be stable within 50 mV, i.e. in the range of 0.1 %.
- The power supply must be able to deliver large currents due to the high background rate: only the rate of background photons can induce currents  $>0.3 \text{ mA}$ <sup>(44)</sup> per pixel, which is by far larger than typical other experiments with photosensors.
- Since the bias voltage must be adapted to changes in the ambient temperature, and, due to the serial resistors in the front-end electronics, to changes in the background

---

<sup>42</sup><http://drs.web.psi.ch>

<sup>43</sup>The intermediate version DRS3 was only used for prototype studies [129].

<sup>44</sup>This value is estimated by multiplying the expected NSB rate with the gain of the G-APDs (see section 3.2.1).



photon rate in order to keep the over-voltage constant, the voltage supply must support smooth changes of the output voltage during operation.

The device was designed and constructed by V. Commichau (ETH Zurich). It provides bias voltages up to 90 V with a step size of 20 mV<sup>(45)</sup>, and is controlled via a USB interface. The maximal current for each of the 320 channels is limited to 4 mA.

### 3.5.6. Light pulser

One of the main issues in the operation of a G-APD-based experiment is keeping the operation parameters constant. For a large part, this is equivalent to keeping the over-voltage of the devices constant (see section 2.4.1), for which purpose a feedback system using a light pulser was foreseen. Such a light pulser optimally fulfills the following conditions:

- Fast pulses: the flashes produced by Cherenkov air showers last a few nanoseconds. Ideally, the pulser emits light with a similar temporal structure, such that the same algorithms can be used for both types of events.
- Precise pulses: the pulses should be as constant as possible, i.e. have a small intrinsic intensity fluctuation.
- Accordingly the pulse intensity should be independent of ambient conditions such as the temperature.
- Adjustable intensity: it is useful for tests to adjust the intensity from few photons per pixel to saturation, i.e. over the full dynamic range of the camera.
- Homogeneous light distribution: the distribution of the light in the focal plane of the camera should be homogeneous within a few percent.

The most important property for FACT is the temperature independence due to the strong temperature dependence of the G-APDs. Various designs used by other telescopes were discussed (e.g. D. Hanna *et al.* [130]), but were either far too complex or not sufficiently addressing the ambient temperature independence. It was thus decided to develop an own design.

The main improvement of the new development is an internal intensity regulation: besides the Light Emitting Diodes (LEDs) pointing towards the camera, an additional LED of the same type is mounted directly in front of a PIN diode<sup>(46)</sup>, which have the advantage that their signal is independent of the operation temperature (see section 2.1.2). The output of the diode is used to regulate the intensity of all LEDs of the light pulser, such that a temperature-induced change in the light output of the control LED is corrected in a direct feedback loop.

The final light pulser contains 18 LEDs directed at the FACT camera, which are organized in three groups. Each group can be switched on and off separately. Due to the focus on the stability and temperature independence, the pulse duration was accepted to be slower than the Cherenkov pulses (see figure 3.64).

## 3.6. Calibration

The task of the camera of an IACT is to record the number and timing of photons arriving at its focal plane. In order to analyze this data, the recorded events are compared to events from a computer simulation.

---

<sup>45</sup>The resolution over the full range is 12 bit.

<sup>46</sup>The PIN diode is a “S5821 high-speed Silicon PIN photodiode” by Hamamatsu Photonics.

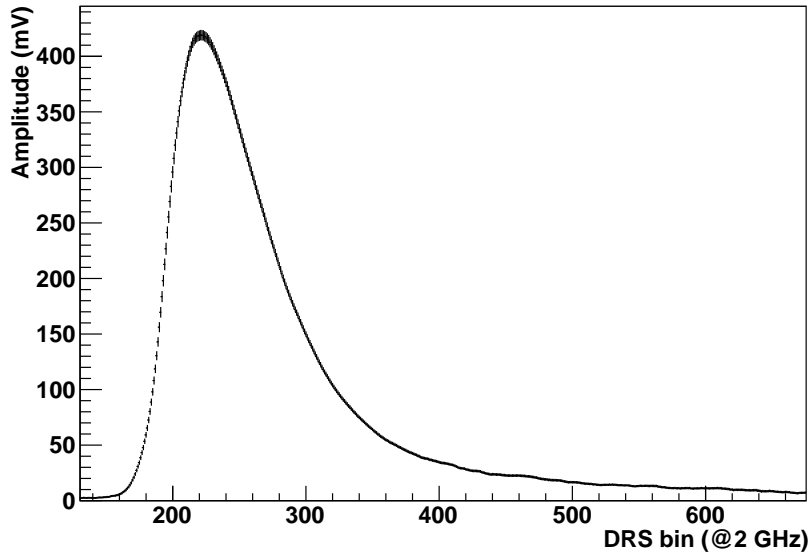


Figure 3.64.: Temporal structure of light pulser events: the signal in a single pixel was averaged over 300 light pulses. The rise time from 10 % to 90 % is 16 ns, the exponential decay constant around 30 ns (including the decay time of the G-APD).

This simple description already contains one of the main challenges in the operation of such a camera: its calibration. In general, this comprises the knowledge about the current state of the camera, in particular the conversion of photons into electrical signals. It can be divided in three sections:

1. Monitoring the camera state under all observation conditions.
2. Monitoring the long-term stability of the camera.
3. Obtaining knowledge about the values of the various parameters.

In principle, the third item includes the other two. However, it is easier to monitor the stability of a value than to determine its exact value, for which reason it is listed separately. The stability is further divided into variability within one observation night (e.g. various observation conditions) and long-term effects, such as the degradation of the sensor over time. The observation conditions include the ambient temperature and humidity of the telescope, the amount of background light (NSB rate) and the pointing position (zenith and azimuth angle) of the telescope. Some of the basic concepts for the calibration I presented at the ICRC 2011 conference in Beijing [131].

### 3.6.1. The case with PMTs

The standard photosensor in IACT cameras are PMTs. These devices are challenging from a stability point of view, and this for multiple reasons. One of the simplest is the dependency of the PMT gain from the orientation in the earth's magnetic field: the primary photo-electron as well as those emitted by the dynodes are influenced in their trajectories, which can lead both to an increase or decrease of the gain in the percent range [69, 70]. This makes the gain dependent on the pointing direction (both zenith and azimuth) of the telescope. Notably the dependence on the pointing direction is different for each PMT in

the camera, except if they are aligned along their main axis<sup>(47)</sup>.

The gain of a PMT also shows some percent change within hours, typically a small drop: “A major cause of this output variation is that the secondary electron multiplication factor of the dynodes (particularly at the latter stages) changes over time.” [70] In addition there are small temperature (in the percent range per 10 K) and photon rate dependencies.

In the long run, PMTs show a performance degradation over time, on one hand due to the worsening vacuum, and on the other hand due to the degrading of the anode depending on its total accumulated charge [61, 132–135].

These issues make it necessary to have a real-time monitoring of the PMT properties. In current IACTs, this is achieved by using a light source, which illuminates the camera with short pulses [135–137]. The intensity of a single light pulse is determined using calibrated PIN-diodes, blind pixels, and/or the excess noise factor of the PMTs. In particular the last method contains large systematic uncertainties of 20 % to 30 % [136], but in combination with the other methods, the MAGIC telescope states “a global absolute calibration uncertainty of about 13 %.” [104]

### 3.6.2. Advantages and disadvantages using G-APDs

Using G-APDs as photosensors in such a camera eliminates several of the problems, while others are more accentuated. A clear advantage is their insensitivity to magnetic fields (G-APDs were operated in fields up to 7 T [138]) and the absence of aging effects [74].

The major disadvantages are their stronger dependence on the bias voltage, background light level and ambient temperature. The former requires a very stable voltage supply, which is independent of all other operating parameters. The main issue here is the stability when the amount of background light changes, be it due to twilight or the moon rising above the horizon: the photons induce a current in the photosensors, which can vary by orders of magnitude and change within some tens of seconds. The bias voltage supply must deliver its output voltage independent of the current, and additionally the voltage drop due to the induced current in the serial resistors of the front-end electronics (see section 3.5.2) must be corrected, requiring precise and noise-free voltage changes.

The ambient light influences also another G-APD-specific parameter: the cell occupancy, i.e. the number of cells which are triggered by background photons and thus (during a short dead-time and the following recovery phase, see section 2.2.6) completely or partly insensitive to Cherenkov photons. The total signal of an air shower is thus lower when the background rate is high. The impact of this NSB dependence was contained in the construction of the camera when we decided to choose a photosensor with 3600 cells (see section 2.6).

The dependence of the G-APD parameters on the ambient temperature is quite strong, as it changes the breakdown voltage of the device with around 55 mV/K (see section 2.2.1). However, if the over-voltage is kept constant, all major device parameters such as gain (see section 2.2.4), photon detection efficiency (2.2.2) and crosstalk probability (2.2.7) show no (significant) further dependence on the temperature.

### 3.6.3. FACT-specific issues

The adaptation of the bias voltage to the temperature and ambient light requires a reliable method to control the voltage changes and monitor their effect. The development and investigation of different methods for this purpose was an important task of my thesis.

---

<sup>47</sup>PMTs are not axially symmetric along their main axis, since the first dynode is fixed to one side of the tube.

The basic decision to take was whether we want to keep the gain (and thus over-voltage) of the devices constant, or rather their response to a light pulse. The latter also includes the reduction of the signal due to cell occupancy. However, if we keep the response constant, the over-voltage is larger for high background photon rates, since the “lost” photons are compensated by a higher gain, PDE and crosstalk probability (see also section 2.4.1). During operation, the exact over-voltage would thus not be known, which becomes a problem for the data analysis: in order to estimate the energy of a recorded air shower, the shape of the shower image is compared to the total number of photons in the shower, which depends on the PDE. As a consequence the over-voltage must stay as constant as possible.

#### 3.6.4. Available real-time information and calibration concept

The FACT camera collects a variety of real-time information describing the environment and the operation conditions of the camera. In particular, the following information is collected:

- The external, temperature stabilized light pulser (see section 3.5.6) provides reference pulses which are recorded with the camera in the same processing chain as the air showers.
- A total of 31 temperature (and two humidity) sensors were installed in the sensor compartment, distributed over the full focal plane close to the G-APDs.
- The bias crate is equipped with a current measurement for each channel.
- Both the rates at the comparators (160 values) and the  $N$  out of 4-logic (40 values) can be read.

In the beginning it was not clear whether the current measurement reaches the required precision to regulate the bias voltage based on their readings. The operation mode I originally proposed was thus as follows: during dark night, the cell occupancy can be neglected<sup>(48)</sup>. Temperature and changes in the background light can thus be handled by keeping the signal of the reference pulses in the camera constant in a feedback loop. This was also the system which was implemented for the prototype module M0 (see section 3.1.7). The investigation of the current and temperature changes during operation and the comparison with the voltage changes from the feedback system would allow to develop the “backup operation”, where the voltage would be regulated based on the temperature and current readings. This mode was foreseen in particular for situations with high background photon rates.

As a cross-check to prove that the G-APDs run on the correct over-voltage, making a spectrum of the observed pulses allows to determine the gain of the devices. This analysis was deemed possible with closed camera shutter using dark counts, and during dark nights also with open camera using dark counts and background photon signals. This would even allow to check the gain during normal air shower observations, since most showers only affect a small fraction of all camera pixels: in the “off-shower” pixels, only dark counts and single background photons are visible.

An important result from those checks is the homogeneity of the sensor plane, from PDE and gain to the trigger rates of the individual patches. Further checks of this homogeneity

---

<sup>48</sup>For background rates below 200 MHz per pixel and a recovery time around 50 ns (see table 2.2), the average number of cells in recovery state is  $<10$ .

require a full software analysis of the shower images, where e.g. the homogeneity of the showers' center of gravity (COG) is investigated.

During the construction of the camera, additional calibration aids were discussed. One of them are so-called "blind pixels", which are used e.g. in the MAGIC telescopes. Such pixels are equipped with a filter which attenuates the light from the light pulser to a level where the average number of photons per pulse is very small ( $\mu_{p.e.} \ll 1$ ). A Poisson spectrum is fitted to the data<sup>(49)</sup>. From the resulting parameters, the average number of photons per pulse can be calculated for the other camera pixels, if the filter's attenuation factor, the averaged photon detection efficiency of the blind pixel and the pulser's light distribution is precisely known [104]. By comparing the expected photon number with the measured light pulser signal, the average charge per photon can be calculated for each pixel. For our camera, this technique is not applicable: a single attenuated pixel would run on a completely different over-voltage than the other pixels, since the voltage drop at the serial resistor would be smaller. The idea was thus discarded. Attenuating a full bias voltage patch would solve this problem, but make it impossible to regulate its voltages via the light pulser feedback system. And finally the good single photon resolution of G-APDs should make it possible to directly measure the gain during operation (at least during dark nights).

Another installation which is found in conventional, PMT-based Cherenkov telescopes, are PIN diodes to measure the intensity of the calibration light pulses. PIN diodes have the advantage that they are temperature independent, but since they have no internal signal amplification (see section 2.1.2), a light pulse needs to be very strong to be detectable. In consequence, the PIN diode is installed much closer to the light pulser than the telescope's camera. If the light pulser's emission is not point-like (as for our light pulser or the MAGIC system [104]), the distance must be large enough for the light field to be similar to the camera distance (i.e. PIN distance  $\gg$  pulser diameter). In the case of MAGIC, the PIN diode is at a distance of 1.14 m and the camera at 17 m from the light pulser, so the intensity is 220 times stronger at the PIN diode. For FACT, the installation of such a diode is not possible: first, the light pulser diodes are distributed over two circles with 11 cm and 13 cm radius, making it impossible to place the diode sufficiently far away to make the emission distribution negligible. Second, even with a point-like distribution, placing the diode in 1 m distance from the light pulser would only result in an approximately 25 times stronger intensity, making the pulses almost impossible to detect. And third, the light pulser has an internal intensity regulation which contains a PIN diode, so an additional monitoring would be redundant (see section 3.5.6).

Also installing a PIN diode was thus discarded. As previously noted, this poses no problem for FACT since the systems are used in other Cherenkov telescopes in order to monitor the gain of the photosensors, which should be observable during normal operation with G-APDs due to their high single photon resolution. However, besides the gain, other parameters need to be monitored, in particular the total light collection of the telescope. A degradation can occur at many stages, for example due to dust and scratches on the mirrors or the front window, degrading transmission of the light-collecting cones or troubles with one of the gluings. While problems with single pixels (e.g. a gluing) can be monitored by comparing the single pixel values to the other pixels, changes in the total transmission need a different cross-check. Such cross-checks and the monitoring of the long-term behavior are

---

<sup>49</sup>This requires the visibility of peaks in the spectrum corresponding to single photons, which is usually not possible with the PMTs used in Cherenkov telescopes. The blind pixels are thus operated with a higher gain. For G-APDs, the visibility of such peaks is possible at nominal gain, but can be difficult to find if the rate of background photons is high.

possible either by using the ring images produced by the Cherenkov light of muons [139–141], or by using the cosmic ray spectrum [142].

## 4. Operation and performance of the FACT camera

### 4.1. Camera tests at ETH Zurich

#### 4.1.1. DRS charge calibration and sample signals

The DRS ring buffer consists of small capacitors, which store the differential input signal as charge. When these charges are read out and digitized, the capacitance and a linear offset must be calibrated. Those two corrections correspond to the hardware properties of the sampling cells, and are thus specific to the “physical pipeline”.

The necessary information for this so-called charge calibration is collected in dedicated runs. The first run records pedestal events<sup>(1)</sup> with a ROI of 1024, i.e. the full DRS chain is read out. For each cell, the average value is calculated and stored. For the second run, a constant voltage is applied to the input channels of the DRS chip, and again events with the full ROI recorded. For each capacitor, the averaged values now correspond to a specific input voltage, and allow thus to correct the small variations in the capacitance (i.e. the “gain”) of the sampling cells.

A minor third correction is necessary, which is relative to the so-called “logical pipeline”. The trigger signal (which stops the writing to the cells) causes some crosstalk into the signal channels. A third run with the ROI of the desired length is taken, and the average for each position in the logical pipeline calculated, which is later subtracted from the data signals.

The charge calibration reduces the noise on the signals significantly from a RMS of  $\sim 15$  mV to around 2 mV. This allows to find and analyze signals corresponding to single G-APD cells (see figure 4.1), which have an amplitude of  $\sim 12$  mV. When browsing through pedestal events, pulses corresponding to one, two, three or more cells can be well distinguished (see figure 4.2).

The clear visibility of signals corresponding to single photons was a first proof for the successful design of the FACT electronics.

#### 4.1.2. First dark count spectrum

The success in seeing signals corresponding to single G-APD cells was the starting point for a more complex analysis: the amplitude spectrum of the dark count signals. If successful, the spectrum would allow to recognize distinct peaks for each number of G-APD cells. The single cell peak consists of dark counts of the device, whereas the upper peaks are created by singular or multiple crosstalk. Such spectra are one of the key selling points for G-APDs, and successfully creating a spectrum is a fundamental proof for their correct handling and readout.

---

<sup>1</sup>Pedestal events are triggered with a fixed frequency which is unrelated to (G-APD) noise or air showers. They thus represent the “baseline” behavior of the system.

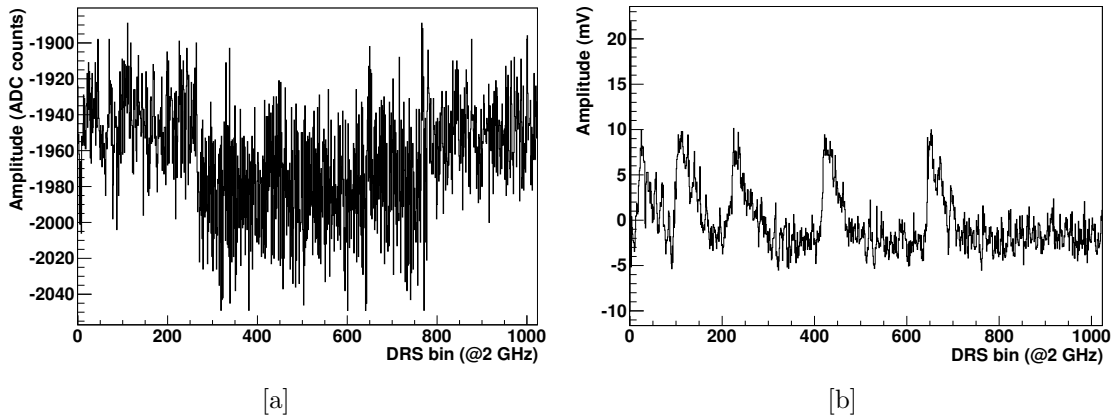


Figure 4.1.: DRS charge calibration: each slice of the recorded signal must be calibrated according to the time since the trigger and the position of the corresponding capacitance on the DRS chip. This allows to reduce the noise on the signal significantly, such that the signals from single G-APD cells become visible. [a] Uncalibrated signal. [b] Calibrated signal, with five signals from single G-APD cells visible.

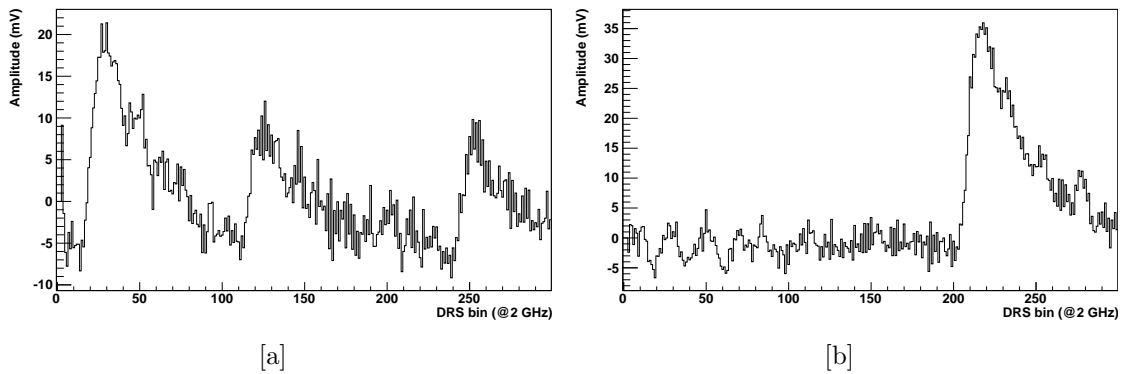


Figure 4.2.: G-APD sample signals: the signal from a single cell has an amplitude around 12 mV. [a] The initial pulse created by two simultaneously triggered G-APD cells (e.g. via crosstalk) is followed by two single cell signals. [b] The signals of multiple cells are linearly added up, in this case to an amplitude around 38 mV which corresponds to three cells.



The camera readout was finished shortly before the ICRC 2011 conference in Beijing, such that there was no time to finish a spectrum beforehand. Since it would be an impressive result for the overview talk by A. Biland on the first results of FACT, I worked on the spectrum in parallel to attending the conference.

For the analysis, an algorithm similar to the working principle of oscilloscopes was developed. A pedestal file with activated G-APD bias voltage was used, with a ROI of 1024 and 1000 events. In a first step the baseline was determined by averaging over all samples in the data. This approach is working since the G-APD pulses are rare in the data, thus most samples contain only electronics noise. The threshold was set to 2.5 mV, which corresponds roughly to the baseline value of  $-2.2 \text{ mV}^{(2)}$  plus one standard deviation. Next the data stream was scanned for signal crossings of the threshold in positive direction. For each crossing, the signal is integrated for 5 ns after a delay of 2.5 ns, and the integral added to a histogram. The same histogram is used for all 1440 pixels.

In the final histogram, peaks corresponding to one to four G-APD cells can be well distinguished (see figure 4.3). The spectrum could be fitted with Gaussian peaks under the assumption of an exponentially decreasing amount of background events. The visibility of so many peaks was a great success for the collaboration, since it proves the correct functioning of many parts of the camera:

- The same threshold was used for all pixels (and thus readout channels) and all events. In order for this to work, the electronic baseline of the signals must be very similar and stable.
- For this, also the bias voltage supply must be very precise and stable.
- The summed electronics noise of the full readout chain is very low.
- The G-APDs are working as expected.
- The histogram is the overlay of *all* pixels of the FACT camera, and all of them were handled identically. No correction to “flat-field” the pixels was made. The visibility of peaks corresponding to single cells show that the majority of the G-APDs are operated with an approximately identical gain.
- The interplay of the full camera is working as planned. Especially notable is the fact that the spectrum is from the camera directly after its assembly, without any fine-tuning of the camera parameters.

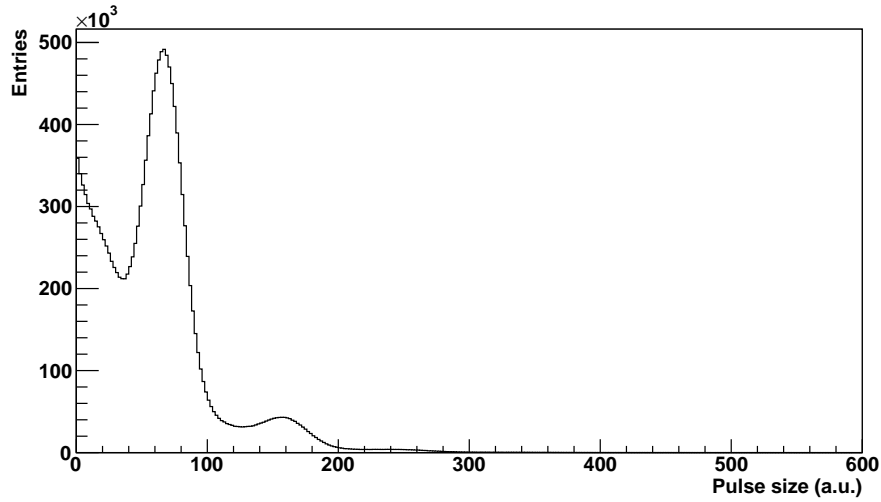
This great result was presented at the ICRC 2011 conference in Beijing [143].

### 4.1.3. Relative photon detection efficiency

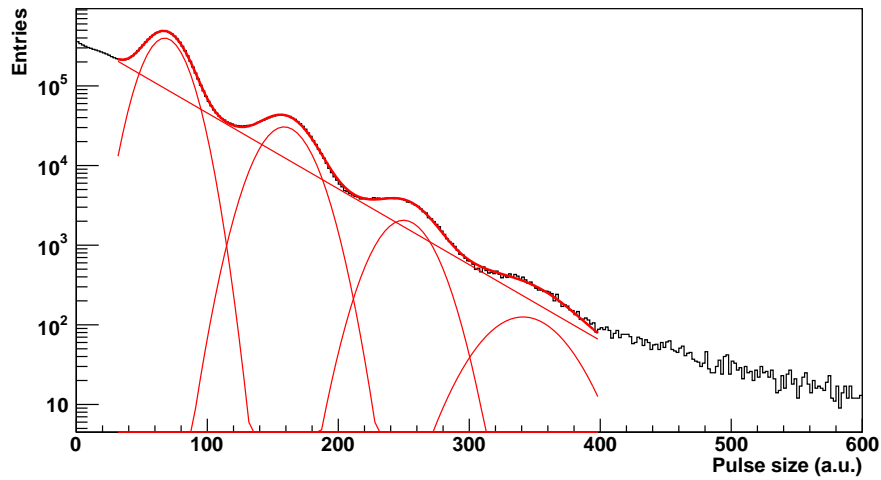
While it is possible to calibrate the average sensitivity of a camera using the ring images of muons [139–141], a calibrated sensitivity for single pixels is more difficult to obtain. Measuring this sensitivity requires knowledge about the light distribution and the size of single photon signals in the light sensors. In PMT-based telescope cameras, the size of the single photon signal is not easily obtained, and is usually deducted from the signal of a light pulser in combination with estimates of the light guide efficiency and front plane transmission for each pixel. Additional information is obtained using the excess noise factors of the PMTs (see sections 3.6.1 and 3.6.4 as well as the references therein). For those measurements it is difficult to disentangle the sensitivity of the sensors from their gain, or only with large error bars. An advantage of the G-APD-based approach is that

---

<sup>2</sup>Note that the baseline is shifted into the negative range due to the averaging of the AC coupling.



[a]



[b]

Figure 4.3.: First spectrum of the FACT G-APDs in [a] linear and [b] logarithmic view. The peaks for one to four triggered cells are clearly visible and can be fitted with Gaussian peaks with equal distance. An exponential underground of background events was empirically assumed in order to fit the data.

This spectrum is the overlay of all pixels in the FACT camera, which proves the excellent homogeneity of the gains of the G-APDs, the electronics baseline and many other components of the camera. No flat-fielding or other correction was applied, and an identical baseline was used for all readout channels.

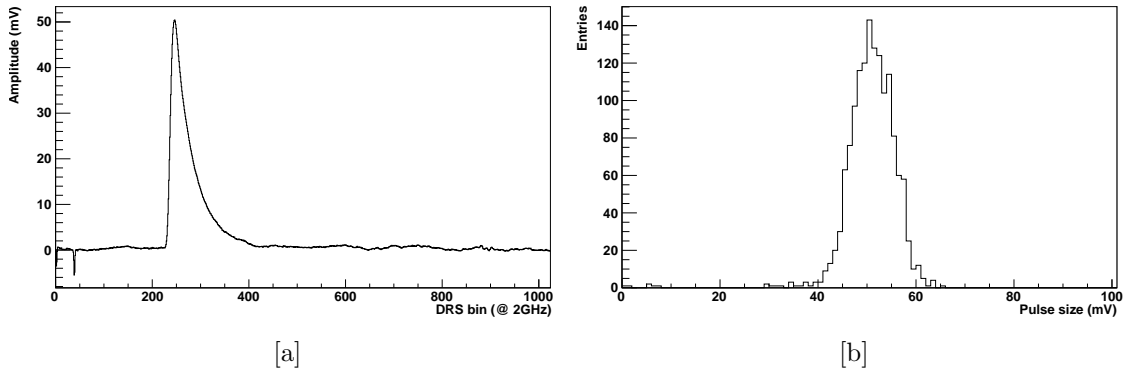


Figure 4.4.: Pulse size determination for the relative PDE measurement: [a] The events are averaged and its maximum determined. The mean value of the samples 80-180 defines the baseline for the pixel. Starting from sample 500, dark counts were searched for the determination of the gain. [b] The distribution of all 1440 pixels is approximately Gaussian with a standard deviation of 7.8%. The outliers at small pulse sizes correspond to the known broken pixels.

the size of single photons can be measured in parallel to light pulser signals. This was used to measure the relative sensitivity of each single pixel compared to the camera average.

## Setup

To deliver the light pulses, a commercial LED pulser with a wavelength of 380 nm by Picoquant was used<sup>(3)</sup>. This LED pulser allows to adjust frequency and intensity of the light flashes over a wide range. A small pulse size with a Poisson distributed average number of (detected) photons around five to ten per pixel was chosen, and the camera readout started using one of the connections for external trigger signals on the trigger master board (see section 3.5.3). The events were read with the full ROI of 1024 slices with a sampling frequency of 2 GHz. More than 200000 events were recorded, corresponding to a data file size >600 GB.

## Data analysis

The analysis of the recorded events was made using “numpy” routines in Python<sup>(4)</sup>. For each pixel, an average pulse size and the size of single cell signals was determined. The pulse size was determined by averaging the events (see figure 4.4) and taking its maximum. As the baseline, the mean of 100 slices before the light pulse was taken, which includes the contribution of dark counts to the total signal of this pixel.

The second half of the original pulses was used to determine the gain of each pixel by producing a spectrum of the dark counts as in section 4.1.2. The spectrum was fitted with the sum of three Gaussian functions with equal distance and coupled widths (see section 2.3.4). The distance between the peaks is proportional to the gain. Determining a value for the gain was not possible in all pixels: for 17 pixels, the fit function was unsuccessful. These contain the known 12 broken pixels (see section 4.3.2) and five additional

<sup>3</sup>Picoquant “PDL800-D Picosecond Pulsed Diode Laser Driver”, PLS 370 LED head, <http://www.picoquant.com>.

<sup>4</sup>“numpy” is the standard package for numerical data analysis with the Python programming language. See <http://www.numpy.org/> for more information.

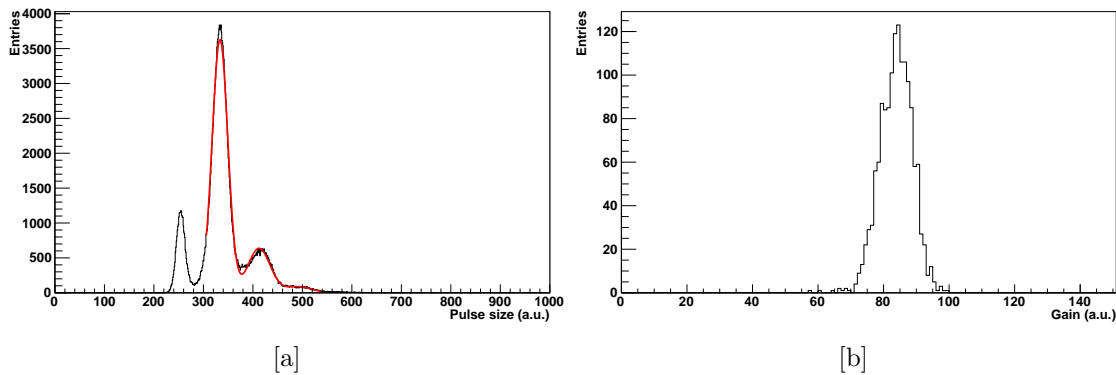


Figure 4.5.: Determination of the gain for the relative PDE measurement: [a] A spectrum of the dark counts was created for every pixel and fitted with the sum of three Gaussian functions. The distance between the peaks is proportional to the gain of this pixel. [b] The gain distribution of the 1423 pixels where the fit was successful has an RMS of 5.9%.

pixels where no singles spectrum could be extracted. The RMS of the other pixels is 5.9% (see figure 4.5).

The relative PDE is now calculated as the pulse size (maximum minus baseline) divided by the gain and normalizing the values of all pixels to an average of one. Since the pulse size is small, saturation effects are neglected.

## Results and discussion

The distribution of the relative PDE has an RMS of 6.83% (see figure 4.6). This value is an upper limit on the variations of the effective relative PDE, since it was measured with a non-optimized bias voltage supply<sup>(5)</sup> and contains several other components with variations. For example, also the crosstalk probability has small differences between the devices. Those are estimated at the same magnitude as the gain variations (i.e. 6%), but relative to the crosstalk probability which is around 10 percent. Their contribution is thus with  $\sim 0.6\%$  very small.

A significantly larger contribution comes from the light distribution of the light pulser. To get an estimate, the light distribution on a white sheet of paper on the camera entrance plane was photographed and the raw data processed into a linear 16-bit TIFF file (see appendix B). A pseudo-light distribution was created by integrating a circular area for each pixel position (see figure 4.7). This light distribution has a standard deviation of 4.2%. When this contribution is quadratically subtracted from the RMS of relative PDEs, a relative width of 5.4% remains.

## Summary

The relative PDE of the pixels in the FACT camera depends on many parameters: the transmission of the front window, the quality of the gluing of the cones to the front window, the spectral transmission of the cones, the gluing of the cones to the G-APDs, the PDE of the G-APDs and the exact over-voltage at which the G-APDs are operated. In a laboratory measurement, the relative PDE of 1423 of the 1440 pixels was measured.

<sup>5</sup>Some channels of the bias voltage supply were not yet calibrated and thus up to 0.3 V off their nominal value. Further only a global temperature correction was made, and no correction for the voltage drop at the serial resistors.

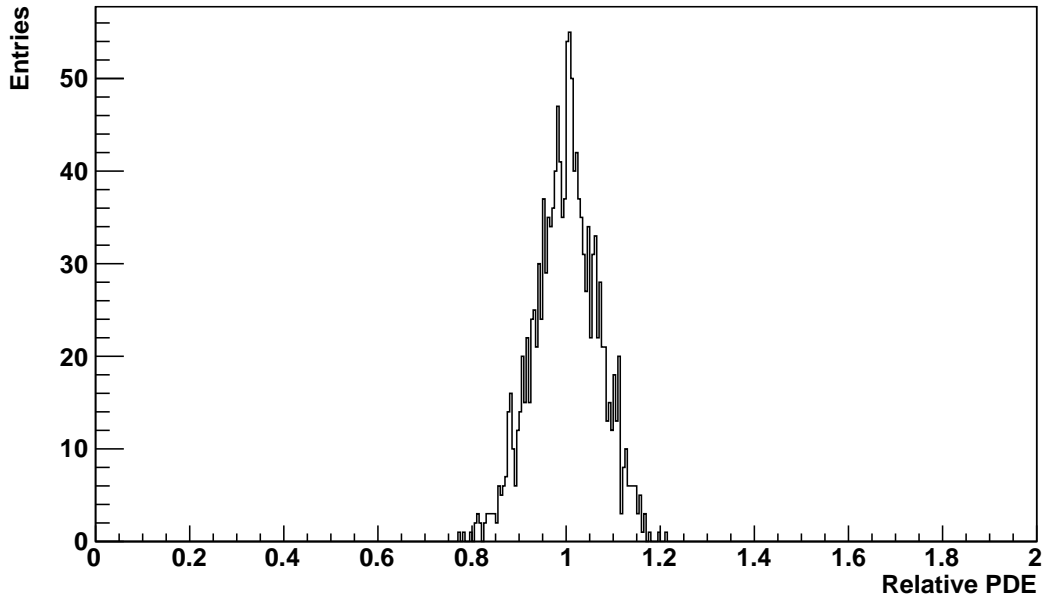


Figure 4.6.: The distribution of the relative PDEs of 1423 pixels of the FACT camera has an RMS of 6.83%, including the non-optimal light distribution (around 4.2%) and measured without bias voltage optimization (see text). The value is thus an upper limit and is estimated around 5% effectively.

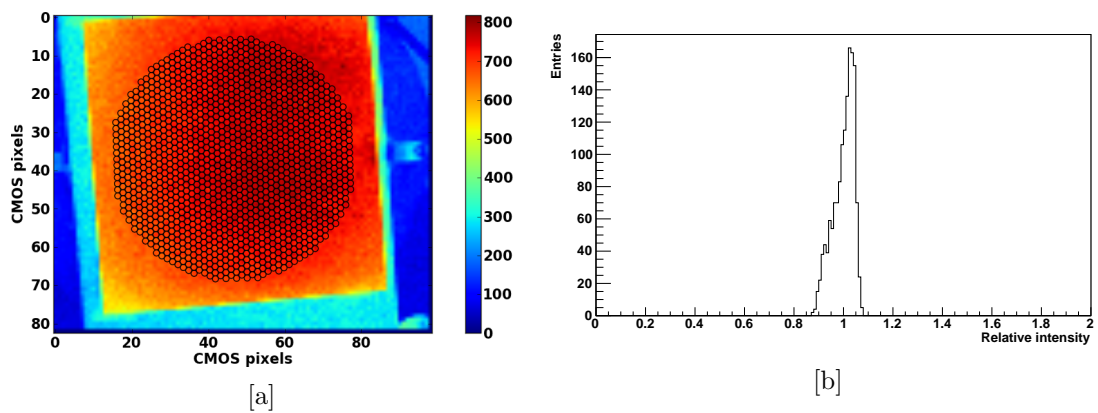


Figure 4.7.: [a] In order to estimate the contribution of the non-optimal light distribution to the variations of the measured PDE, a digital photography was linearly processed and analyzed by integrating a circular area at each pixel position. [b] The resulting distribution has an RMS of 4.2%, which contributes significantly to the variations of the measured relative PDEs.

The relative sensitivity of those 98.8% of all pixels of the FACT camera is significantly better than the expected 10% from the interplay of so many parameters: its RMS is 6.8%, and is reduced to 5.4% when the contribution of the light inhomogeneity during the measurement is subtracted.

## 4.2. Camera installation and first operation

The tests in the laboratory in Zurich were decided to end with the transport of the camera to its final location on the Roque de los Muchachos on La Palma, Spain. Before the camera transport, the telescope site needed to be prepared: the camera was to be installed in a mount used for the HEGRA experiment, which ended in 2002. Since then, the mount of the Cherenkov Telescope 3 (CT3) was unused except as a exhibit object for visitors. The telescope mount was revised and repainted and new motors installed. The original round mirrors were replaced by 30 hexagonal mirrors with a total area of 9.5 m<sup>2</sup>. For the computers and electronics outside the camera, an office container was placed beside the telescope.

The camera was installed end of September 2011, followed by the installation of the cables for the bias voltage supply, low voltage for the electronics, network access and the pipes for the cooling unit (see figure 4.8). The computer system consisting of the control and DAQ computers was set up in the office container to allow the local operation of the telescope. I joined the crew on La Palma towards the end of the installation period on October 9th for the startup of the camera and its first outdoor operation.

### 4.2.1. First operation

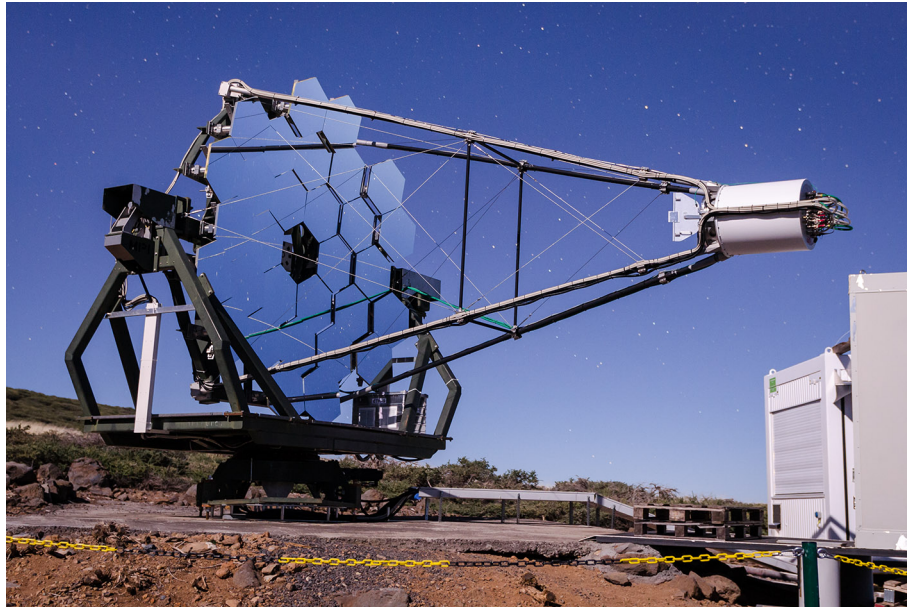
The last cables were installed on October 11, 2011. After checks of the connections to all electronics boards, the operation of the camera was checked by ramping the bias voltage to the operation voltage and observing G-APD dark counts, still with closed camera shutter.

When those tests were successful, I saw no hindrance to open the camera, though the level of background light was exceptionally high due to the full moon shining onto the telescope. Before the camera was opened, the bias voltage was switched off and the camera temperature noted. The bias voltage was ramped step-wise, while in parallel observing the bias currents and the temperature in the sensor compartment. The bias voltage was ramped up to an average currents of 1.4 mA per bias patch, i.e. 350  $\mu$ A per pixel.

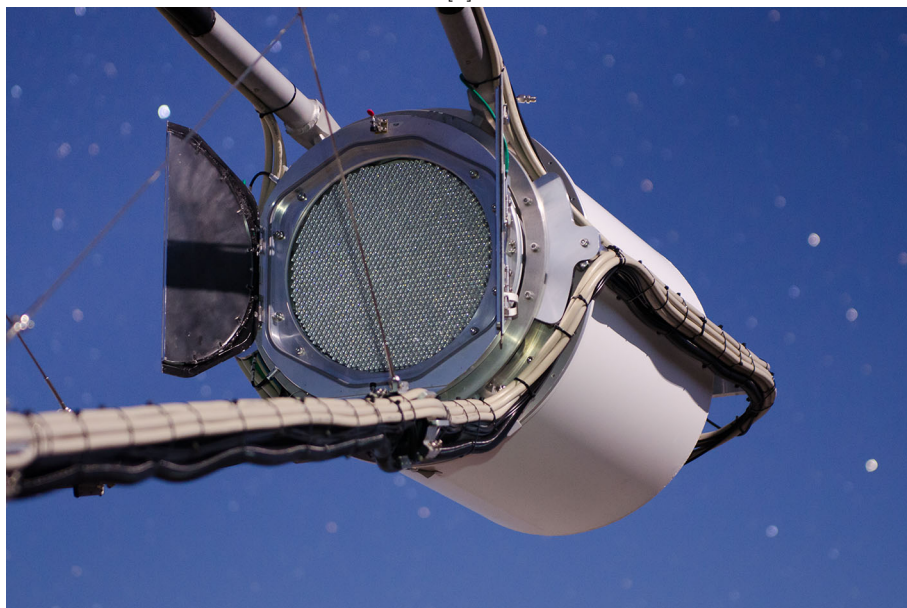
As a first test, the trigger of the camera was tested with the external light pulser. The readout for the external light pulser events are triggered in the same way as the air showers, except that the number of boards with a trigger in the *N out of 40*-logic is set to a value larger than one (typically >20). In order to observe air showers, a different trigger setting was used: the *N out of 40*-logic was set back to 1. The telescope was moved to point to a direction around 40° from the moon (see figure 4.9). Since even setting high single patch thresholds did not filter the background events sufficiently, the *N out of 4*-logic was set to two, which requires that two adjacent patches (more precisely: patches on the same electronics board) trigger simultaneously. Using these settings,

**we recorded the very first air showers with the FACT camera,  
in a full moon night and only hours after the installation of the last cables.**

Some example showers from the first night can be seen in figure 4.10. The successful start of operations was communicated to the IACT community by our spokesperson A. Biland, and was even published in the “CERN Courier” [144].



[a]



[b]

Figure 4.8.: [a] The FACT camera was installed in the refurbished HEGRA CT3 mount. The hexagonal mirrors are newly coated mirrors from another HEGRA telescope (CT1). Cables and pipes are guided along the poles of the telescope to the cooling unit and the container with the computer system (right side). [b] View onto the opened camera: the sensor plane with its 1440 optical light guides makes for an impressive sight.





Figure 4.9.: The FACT camera was observing its first air showers in the full moon night from October 11-12, 2011.

#### 4.2.2. Rate scans

Besides observing and recording the very first air showers with the FACT camera, rate scans with various settings were measured. The principle behind those measurements is simple: the trigger is set to a certain threshold, and its rate noted. By changing one parameter at a time, the dependence of the trigger rate on this parameter is recorded. Despite the simplicity of the measurement, its application possibilities are powerful: from the standard measurement (see below) to optimize the trigger threshold or commissioning of the camera electronics, rate scans offer information about almost every part of the system.

During my stays on La Palma for FACT<sup>(6)</sup>, I measured several types of rate scans. The classical rate scan is made under the same conditions as air shower observations: the telescope points to a location in the sky, the camera is open and the bias voltage on nominal level. The standard trigger for those operations sets a certain threshold on the summed signals of nine pixels, and if any of these patches triggers, the readout of the full camera is started (see section 3.5.3). For the standard rate scan, the patch threshold is gradually increased and the trigger rates of the camera recorded.

An example from one of my measurements can be found in figure 4.11. The curve has a characteristic shape, with a steep part for low thresholds and a flatter upper part. By looking at example events in the online display, the origin of the two branches is confirmed: the lower part consists of events triggered by background photons, whereas the upper branch is dominated by air showers. The gradient is dominated by photon statistics in the lower branch and the air shower spectrum and corresponding trigger sensitivity in

---

<sup>6</sup>I traveled three times to La Palma for FACT, each time for two weeks (October 2011, December 2011 and January 2012).

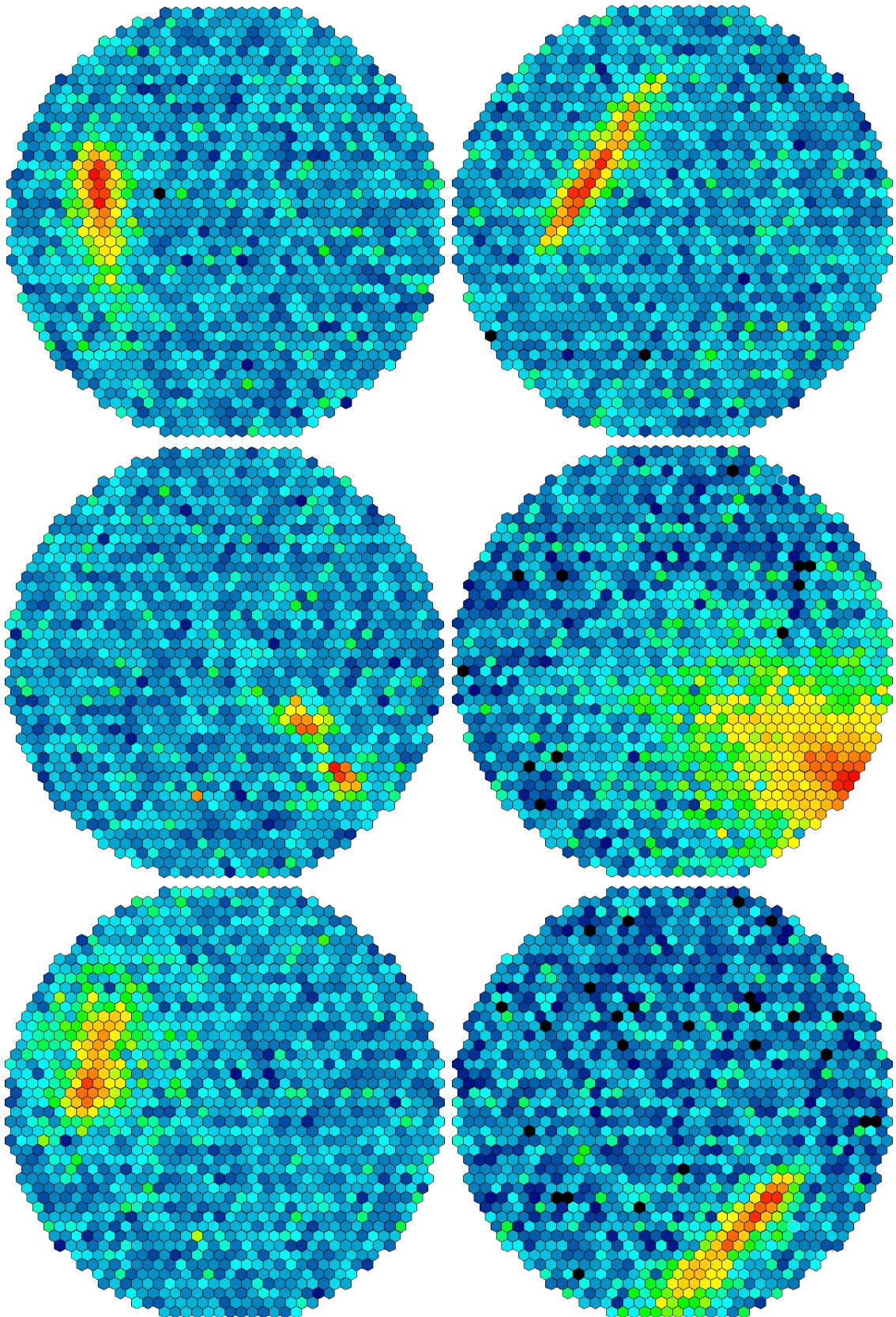


Figure 4.10.: Example showers from the first observation night: these air showers were observed during full moon in the night from October 11-12, 2011, within minutes after the first attempt was made.



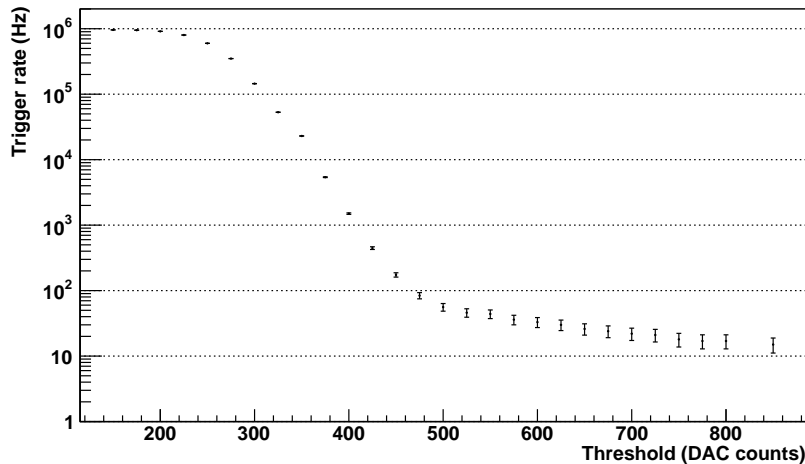


Figure 4.11.: Standard rate scan of background light and air showers: when the telescope is in the same mode as for air shower observations (pointing to the sky, camera open, bias on, standard trigger settings), varying the patch thresholds leads to this characteristic curve. For low thresholds, mostly random background events triggered by NSB and moonlight photons are recorded, which saturate the counter at very small thresholds. When the threshold is increased, those events are cut away and the smaller but flatter component of air showers becomes visible. The trigger thresholds for regular observations is usually at the bend (here: around 450 DAC counts) to record as many air showers as possible without saturating the readout with background events.

the upper area<sup>(7)</sup>.

When the bias voltage is switched off, rate scans allow to find noise sources which influence the trigger (and thus in addition often the digitized data). An example is shown in figure 4.12. For very low thresholds the rate is dominated by the falling edge of the standard electronics noise. The deviations from this behavior for larger thresholds must come from other noise sources, which can be identified by an investigation of digitized events in this domain. In the shown example, the events showed some sort of “ringing”. It was found that the communication with the electronics boards for the readout of the trigger rates can produce noise spikes, which are detected by the trigger electronics. The problem was reduced by adapting the communication protocol between the boards and a reduction of the readout frequency.

In the course of doing various types of rate scans, I had the idea for another measurement, which can be used for the characterization of the trigger electronics and threshold. For the measurement the camera is kept closed, and the bias voltage of the G-APDs is on. Only a single patch is active in the trigger, and all but one pixel taken out of the analog sum: the rate scan now measures the noise of a single G-APD, which is dominated by dark counts and additional cells triggered by crosstalk. In the rates, this is visible as a step-like structure. The analysis of these steps provides valuable information about the trigger system: since the signals are processed differently after the splitting into readout and trigger branch (in particular, the trigger signals are shaped and have an additional amplification step, the rate scan allows to evaluate the precise size of a single cell at the trigger level. And since this measurement can be repeated anytime without having to

<sup>7</sup>The gradient in the air shower branch depends amongst other things on the air shower spectrum, the energy dependence of the Cherenkov photon density, the area illuminated by the Cherenkov light, the size of the trigger patches (in case of a sum trigger), and the size of single photons at the electronic discriminator.

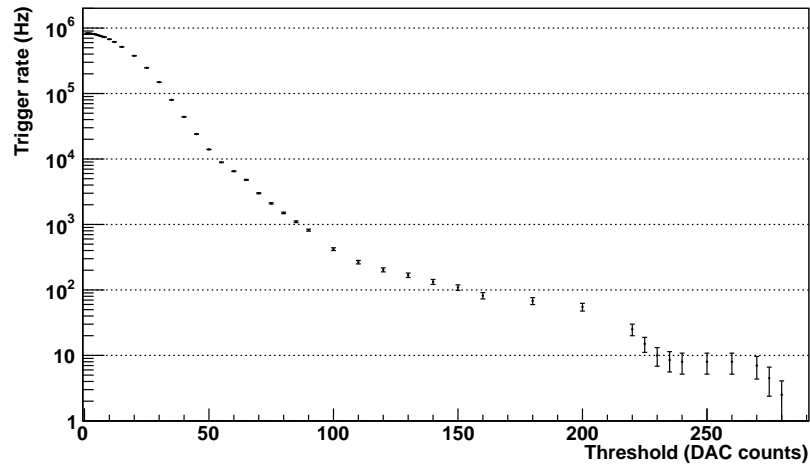


Figure 4.12.: When a rate scan is made with closed camera and deactivated pixels, the noise of the electronics becomes visible. The resulting curve has a similar shape as the standard rate scan, but at much lower thresholds. The tail around 8 Hz at high thresholds was found to correspond to internal communication between boards, which was also visible as a “ringing” in the digitized data (see figure 4.13). By adapting the transfer protocol and reduce the amount of internal communication, the problem was almost completely solved.

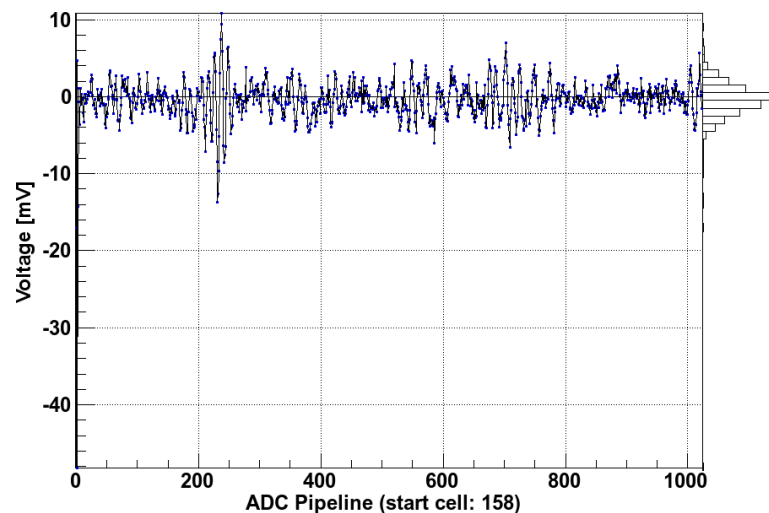


Figure 4.13.: Screenshot of the online display of an event found via an electronics rate scan: a characteristic noise with a frequency around 200 MHz is visible. The noise was found to correspond to internal communications between the electronics boards, and could be reduced by adapting the transfer protocol.

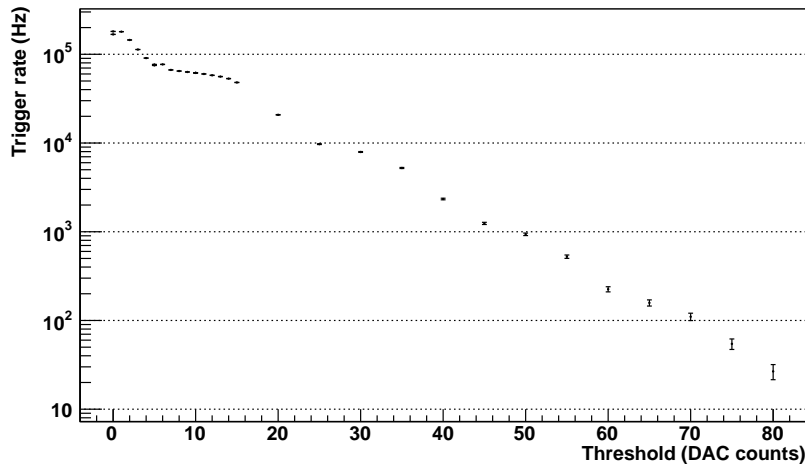


Figure 4.14.: This single pixel rate scan demonstrates the excellent electronics of the FACT camera in combination with the single-cell resolution of G-APDs: every  $\sim 18$  DAC counts, a step in the rate is visible. The steps correspond to single cells of the G-APD and allow to calibrate the trigger for each single pixel of the camera. While this rate scan served as a demonstration of the idea for the collaboration and was made by hand, later scans were automatized, providing a higher resolution of the second and upper steps.

access the electronics boards, the trigger properties can be monitored in an simplicity and precision which is unprecedented in IACTs. The first rate scan which proved the excellent electronics and the new possibilities of G-APDs is shown in figure 4.14.

### 4.2.3. Crab occultation observation

Two months after the first operation of FACT, the chance for an interesting observation came up: the standard candle of IACTs, the Crab nebula, was going to pass behind the full moon. For about 40 minutes, its gamma rays would be blocked. Two interesting measurements are then possible: on the physics side, the two transitions at the moon's edge in principle allow conclusions about the morphology of the gamma ray emission in the Crab nebula in a higher resolution than currently possible with IACTs. However, this requires a significant counting rate of gamma rays on the minute scale, which would even be difficult with the large telescopes, and out of reach for FACT<sup>(8)</sup>. The second reason which makes the occultation interesting is the proof of concept: if FACT would be able to observe the expected drop in the photon rate, it would be a verification of the analysis chain, and further demonstrate the possibility to operate FACT close to the moon. The operation would result in high currents in the camera, posing a potential risk to the photosensors and the gluing of the light-collecting cones to the G-APDs. It was thus decided that I should be on-site for the measurement, together with Susanne Tobler, a master student from ETH Zurich.

The observation itself could be carried out in two ways: either the telescope would be tracking the Crab nebula, and the moon would pass through the camera, or the other way around. The former allows (ideally) to observe a stable rate of photons and to use a rather standard analysis, while the latter facilitates the handling of the high brightness of the

<sup>8</sup>The counting rate of photons from the Crab nebula is around 3.4 gamma/min above 300 GeV for the MAGIC telescopes under good conditions [145]. A later analysis of FACT data showed a preliminary rate of 21 counts per hour [66], far too little to observe the transitions.

moon in the camera. The safety of the camera was the deciding argument to keep the moon centered: the very high photon rate of the direct image of the moon in the camera requires to lower the bias voltage of the affected patches. The operation software was at the time not prepared for moving objects, while a fixed bright object could be easily implemented. A stationary moon would also facilitate the surveillance of the critical camera parameters (in particular the patch currents and sensor compartment temperatures). Figure 4.15 shows a photo of the camera with the direct image of the moon in its center.

The bias voltage settings for the observation were found by tracking the moon and slowly increasing the bias voltage by hand. Already at a bias voltage below 10 V the currents in the central three bias patches (corresponding to the direct image of the moon) were significantly above the camera median current<sup>(9)</sup>. For the affected patches, I set the operation voltage to 30 V below the original target value in a configuration file<sup>(10)</sup>. When ramping the voltage closer to the operation voltage, we found it was necessary to reduce the voltage in a second ring around the moon by 20 V due to scattered moonlight. In total, 51 pixels were deactivated. A screenshot of the online display with the final bias voltage settings can be found in figure 4.16.

With the reduced voltages in the center it was possible to operate the external light pulser. Due to the high currents, the over-voltage of the G-APDs was not at their nominal value, but the operation of the light pulser proved that it is possible to trigger bright flashes (and thus large air showers) while having the moon in the center of the camera<sup>(11)</sup>. However, it was not possible to get the camera into a stable observation condition and observe air showers: moving clouds would often scatter a lot of the moonlight into active patches, which forced us to ramp down the bias voltage. The high currents (around 1 mA per patch) even led to a significant increase of the sensor compartment temperature by several degrees.

When the night of the occultation finally came, the atmospheric conditions did not allow the operation of the camera: moving clouds and high air humidity were scattering light and made it impossible to operate the camera. It was nonetheless a successful measurement attempt since it was shown that the light pulser can trigger the camera readout while the moon is in the center of the camera, making it reasonable to observe air showers under the same conditions or very close to the moon.

### 4.3. Camera performance

While the first indications of the potential of the FACT camera were soon visible after its installation or already in laboratory tests before (see previous sections 4.1 and 4.2), it was yet to be seen whether the promising first results could be transferred to the real-world observations of gamma ray sources.

In this section the camera performance related to the photosensors is discussed. Though the electronics and analysis software performance are equally important, information on those topics can be found in other sources<sup>(12)</sup>.

---

<sup>9</sup>The G-APDs are already sensitive to light below the breakdown voltage, they are simply operating in a linear APD mode (see section 2.1.2).

<sup>10</sup>The pixels were not completely deactivated, since the applied voltage changes the sensor capacitance, and the readout electronics was optimized for standard settings.

<sup>11</sup>Note that external light pulser events are triggered with the same processing chain as air showers, except with a higher setting in the *N out of 40*-logic.

<sup>12</sup>See e.g. the upcoming theses by D. Neise (University of Dortmund) and P. Vogler (ETH Zurich) as well as upcoming publications by the FACT collaboration.

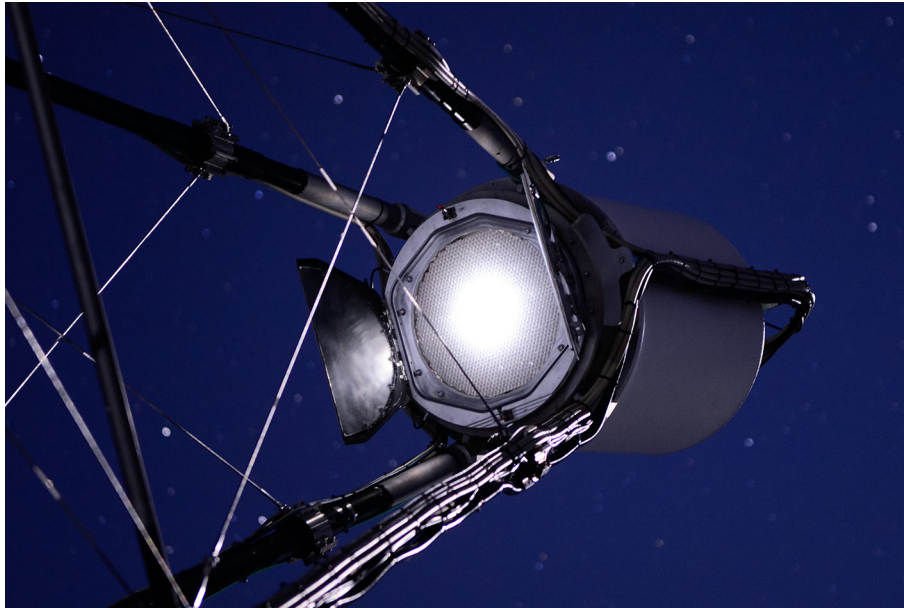


Figure 4.15.: Image of the full moon in the FACT camera: two months after its first operation, FACT attempted to observe the passing of the Crab nebula behind the full moon.

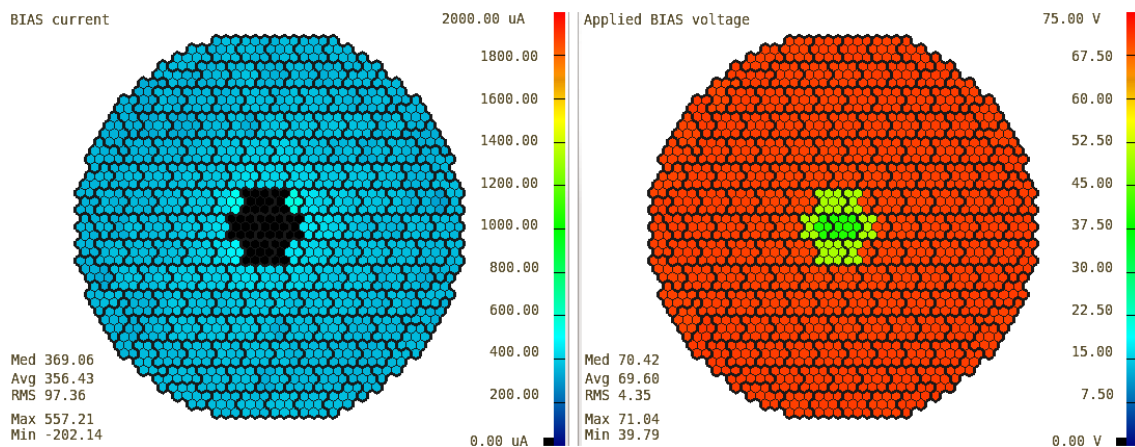


Figure 4.16.: Currents (left) and bias voltage settings (right) for the crab occultation measurement: for the innermost 51 pixels the bias voltage was lowered by around 25 V due to the very high rate of direct moonlight and scattered moonlight at small angles. The other patches were running at a reduced over-voltage, but still sensitive enough to detect light pulser events. For air shower observations and the observation of the Crab occultation, the atmospheric conditions were unfortunately not stable enough.



### 4.3.1. Gain homogeneity

While the initial analysis of the dark count spectra as in section 4.1.2 was made using independent hand-made scripts, a systematic analysis is easier to handle if it is embedded into the standard data analysis chain. This analysis chain is based on the MARS framework [113, 114].

This implementation was one of the major goals of an analysis software workshop in June 2012, which took place at the ISDC in Versoix. The original pulse finder algorithm with the “oscilloscope-style” search was improved with a sliding window averaging, a baseline correction for each pixel and an extended set of conditions to suppress noise<sup>(13)</sup>. The improved algorithm was then used to create a spectrum of the pulse size for each single pixel in the camera. By fitting these spectra with a sum of Gaussian functions, the gain of each G-APD is determined. Knowing the gain of each single pixel can now be used for a variety of investigations: from the homogeneity of the camera and the identification of anomalous pixels (see section 4.3.2) to the temporal stability and temperature dependencies.

The first two items were completed at the workshop. An example of a gain distribution over the camera is found in figure 4.17. The typical RMS of the gain distribution was below 4%, and below 5% for all investigated files. This small spread was a positive surprise since it is the sum of many different sources of variations:

- The operation voltages of the G-APDs within one bias voltage group have a spread below 20 mV, thus contributing around 1% to the total variations<sup>(14)</sup>.
- The step-size of the bias voltage supply is 20 mV (see section 3.5.5), contributing another 1% – 2%.
- The temperature correction of the bias voltage is regulated for the full sensor compartment as one. Since the measured temperature in the sensor compartment deviate from the average temperature by up to 1 °C (corresponding to an change in the over-voltage around 55 mV), this is one of the main contributions to the gain variations<sup>(15)</sup>.
- Additional contributions from the electronics (e.g. electronics noise and variations in the pre-amplifier gain) and the analysis algorithm of unknown size are also contained in the total variation.

The analysis and results from this homogeneity investigation I presented at the PhotoDet 2012 conference in Orsay, France [146].

An impressive demonstration of the G-APD possibilities was made by T. Bretz: the pulses found with the algorithm were divided by the previously determined gain of the pixel for the data file (i.e. normalized to single cells), and then added to a total spectrum of the full camera (see figure 4.18). In this normalized spectrum, peaks corresponding up to nine (!) single G-APD cells are easily recognized, and the full spectrum can be fitted with a plain sum of Gaussian functions.

An additional result concerning the stability of the gain with varying temperatures is obtained by looking at the normalization factors: the dark count runs were taken over a temperature range of more than 20 °C from <5 °C to >25 °C. The normalization factors

---

<sup>13</sup>The implementation of this analysis was done by Q. Weitzel (ETH Zurich), J. Buss (University of Dortmund) and me.

<sup>14</sup>This value is obtained by assuming 10 mV distance to the (ideal) applied voltage and dividing it by the over-voltage of 1.1 V.

<sup>15</sup>The implementation of a local temperature correction in the sensor compartment is in planning.

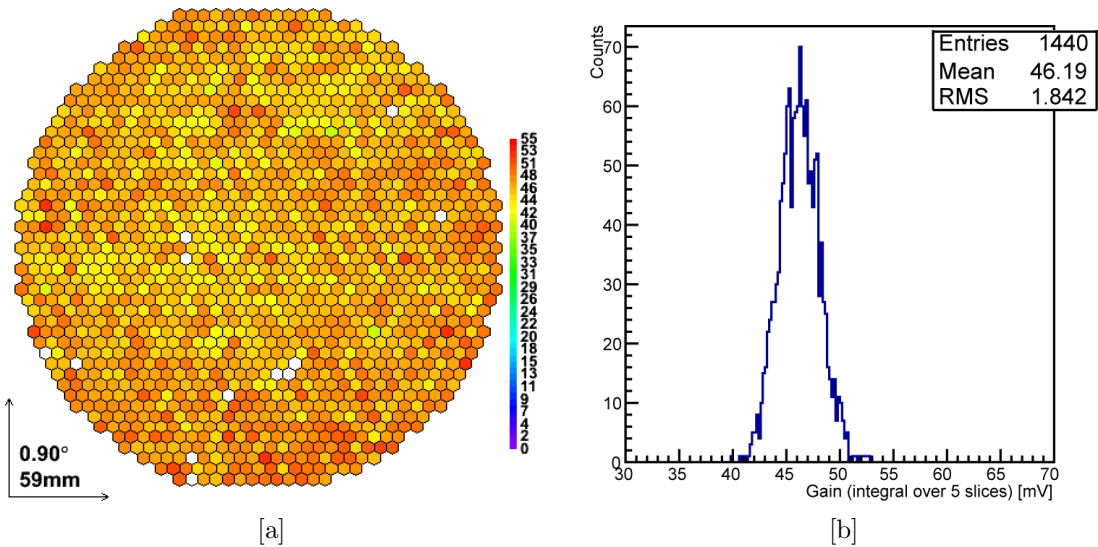


Figure 4.17.: Gain distribution: the improved extraction algorithm of dark counts allows to determine the gain for every single pixel in the camera. The RMS of the gains is  $<5\%$  in all investigated datasets. The above pictures show the gain distribution of one dataset [a] in the camera and [b] as a histogram with an RMS of 4%.

(which are linear to the gain) vary by less than 3.5%, proving that the G-APDs' temperature dependence can be well controlled. For details on the study, please refer to T. Bretz *et al.* [147].

### 4.3.2. Broken pixels

Already early in the operation of the camera, it became clear that three pixels were significantly different than the rest of the camera. They were first identified when the standard trigger was tested, since they appeared far noisier than standard pixels and dominated the triggered events. When looking at the signal stream of those pixels, their baseline was found to be unstable, and the pulses were far larger than normal. Due to their unstable behavior, they are called “*crazy pixels*” and are excluded from the standard trigger. One possibility that could explain their characteristics is that their individual serial resistor (figure 3.63) is only  $390\ \Omega$  instead of  $3.9\ \text{k}\Omega$ . This would also explain the higher currents in the affected bias voltage patches, but cannot be checked without detaching the sensor compartment from the camera. This is avoided due to the huge workload and the risk of damaging the pixels.

The second category of broken pixels are the three “*dead pixels*”, of which no signal from the G-APDs is received and only electronics noise is visible. Since their functionality was tested before being used in the camera, it is assumed that the cable connection from the sensors to the electronics is damaged.

The third and last category of anomalous pixels was found with the extended gain analysis (see section 4.3.1), the so-called “*twin pixels*”. Twin pixels always occur in pairs of the same electronics patch, and have the exactly same signal on their channels except for the digitization noise. Signals from the external light pulser are on their nominal height, but single cell signals are only half the usual size. This led to the conclusion that those channels are short-circuited, and both see the average signal of the two sensors.

An overview of all broken pixels can be found in table 4.1. The list was compared to the list of pixels where a gluing broke during the assembly (see table 3.4). Only one dead

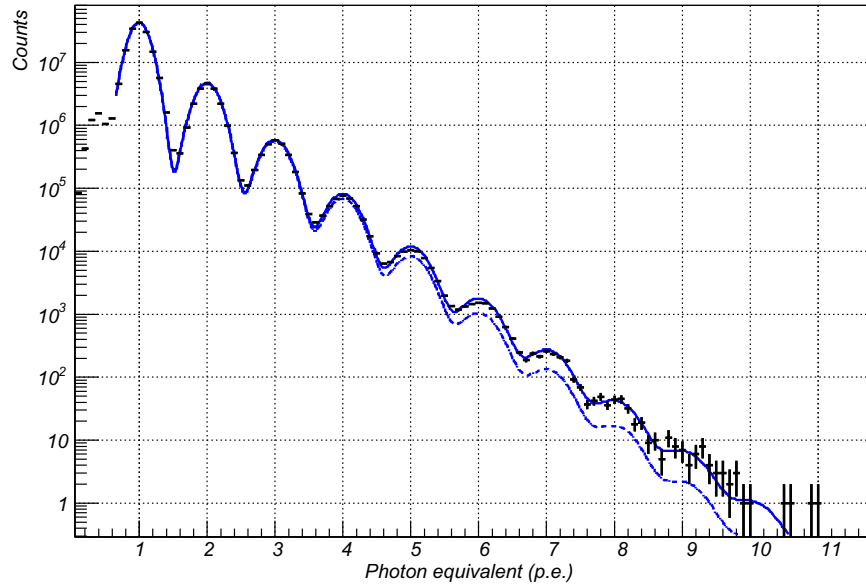


Figure 4.18.: Improved G-APD spectrum: by normalizing the signals in each pixel with their respective gain and adding the spectra of all pixels into one histogram, the statistics is sufficient to resolve peaks corresponding to up to nine cells. The data can be fitted with Gaussian peaks with equal distance and coupled widths (according to section 2.3.4). Plot by T. Bretz in [147].

pixel (SoftID 923) showed up in both tables.

It is important to note that none of these pixels broke during the operation of the camera. All pixels were already broken during the laboratory tests at ETH Zurich and were thus faulty to begin with (as assumed for the crazy and twin pixels) or damaged during the assembly (as assumed for the dead pixels). Not a single pixel was lost or changed its behavior significantly in the past two years of operation.

The status of the gluing joints of the repaired pixels was checked in detail in January 2012. In the three months where the camera was installed, the pixels were exposed to large temperature variations from direct sun exposure to sub-zero temperatures. No change was found for any gluing, in particular the status of the seven repaired inner pixels remained unchanged.

### 4.3.3. Extraction of calibration information from data runs

The extraction of single cell spectra as in the previous sections is based on algorithms which only work if the rate of single cell signals is low and a stable baseline is present. In consequence, all studies concerning the temperature dependence and its correction with the voltage regulation system were made with closed camera shutter, thus only using the dark counts of the G-APDs. Even though single cell peaks are visible in the signal stream during the observations, it was not yet possible to extract a spectrum to determine the gain. In summer 2013 I therefore developed an algorithm which works also with the higher single cell rate due to background photons with an open camera.

The approach to solve this problem is based on the fact that pulses of single cells can often be identified by eye, but not with the existing software algorithm (sliding window averaging with fixed threshold). By eye, the typical rising edge of a pulse can be recognized even when the signal is noisy. The solution to the problem is to combine two different

sliding window averages: a long one to determine the baseline, and a shorter one for the signal peaks. The time constants of the averaging were determined by evaluating typical pulses, and a short study on variations of those values. The baseline time constant was set to 8 slices (4 ns), the peak time constant to 4 slices (2 ns). The pulses are searched for by comparing the difference between the two averaged signals with a threshold value, with an offset between the two signals which corresponds to the typical rise time of pulses (10 slices, 5 ns)<sup>(16)</sup>.

Around this threshold crossing, the minimal baseline value and the maximal peak value are searched and the difference defined as pulse height, which is added to a separate histogram for each pixel. As with the regular algorithm, the spectrum is fitted with the sum of three Gaussian functions with equal distance, and the distance used as value for the gain of this pixel.

The pulse finding and extraction algorithm was tested with data from a standard observation during dark night (no twilight, no moon). It returned a gain value for *all* 1428 regular pixels, i.e. all but the 12 broken pixels (see previous section)<sup>(17)</sup>. The distribution of the gains has an RMS of 3.7% (see figure 4.19).

This demonstration proves for the first time that it is possible to extract the gain of each pixel from the observation data itself, and thus allows an in-situ calibration without any additional device such as a light pulser. For future telescopes, this can result not only in lower costs, but also in a reduced complexity of the full system, which in turn increases its reliability. The algorithm is currently being investigated within the FACT collaboration for extended stability studies and its potential implementation in the data analysis chain.

## 4.4. Telescope PSF measurement

One of the most important characteristics of the mirror dish is its Point Spread Function (PSF). It quantifies the light distribution in the focal plane for a point-like light source. For the FACT telescope, only an estimate from the group responsible for the mirror installation was available, based on the overlay of the single mirror PSFs and the mirror alignment in the telescope's parking position. Since this approach only allows a very approximate quantization, I decided on my third stay at the telescope in January 2012 to perform a more precise measurement.

### Measurement

As point-like sources, bright stars are a sufficient approximation<sup>(18)</sup>. The image of a star in the focal plane of telescope can thus be used to directly measure the PSF of the telescope. The drawback of this method is that IACTs are focused to air showers in the atmosphere, whereas stars are in infinite distance.

<sup>16</sup>This is equivalent to searching for threshold crossings of

$$\hat{s}_k = \frac{1}{n_{\text{peak}}} \sum_{i=n_{\text{bsl}}+n_{\text{offset}}}^{n_{\text{bsl}}+n_{\text{offset}}+n_{\text{peak}}-1} s_{k+i} - \frac{1}{n_{\text{bsl}}} \sum_{i=0}^{n_{\text{bsl}}-1} s_{k+i}, \quad (4.1)$$

where  $s_k$  is the original signal stream and  $n_i$  the time constants of the baseline averaging, peak averaging and offset.

<sup>17</sup>The algorithm also worked for the five pixels for which the PDE analysis failed (see section 4.1.3). The reason might be the calibration of the bias voltage supply.

<sup>18</sup>The angular size of a star is significantly smaller than the optical resolution of an IACT.

Category	SoftID	HardID	ContHardID
<i>Crazy</i>	583	2338	863
	830	810	297
	1399	2404	868
<i>Dead</i>	424	2530	927
	923	208	80
	1208	2410	873
<i>Twin</i>	113	3014	1093
	115	3015	1094
	354	1425	527
	423	1426	528
	1195	2001	721
	1393	2002	722

Table 4.1.: Of the 1440 pixels, twelve pixels show a irregular behavior which requires a special attention in the data analysis. While three pixels show no G-APD signal at all, others show baseline jumps and large signals and need to be excluded from the trigger. The three pairs of twin pixels are short-circuited and show the same signal.

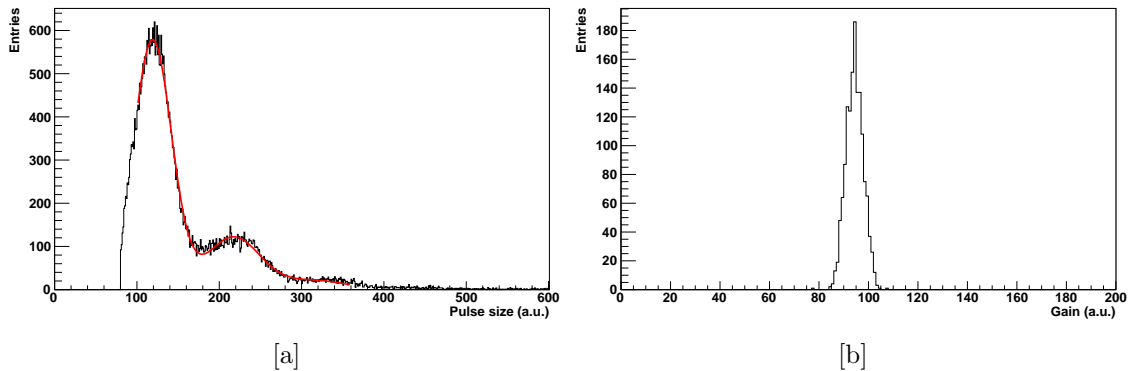


Figure 4.19.: Extracted calibration information from data runs: an algorithm was developed which allows the extraction of pulses corresponding to single cells even from standard observation data, which allows its independent calibration. [a] The extracted pulse sizes are filled into separate histograms for each pixel and fitted with the sum of three Gaussian functions with equal distance. [b] The distance between the peaks in the spectrum is proportional to the gain. The distribution of all 1428 regular pixels of the camera has an RMS of only 3.7%, which proves the excellent homogeneity of the camera during observations.

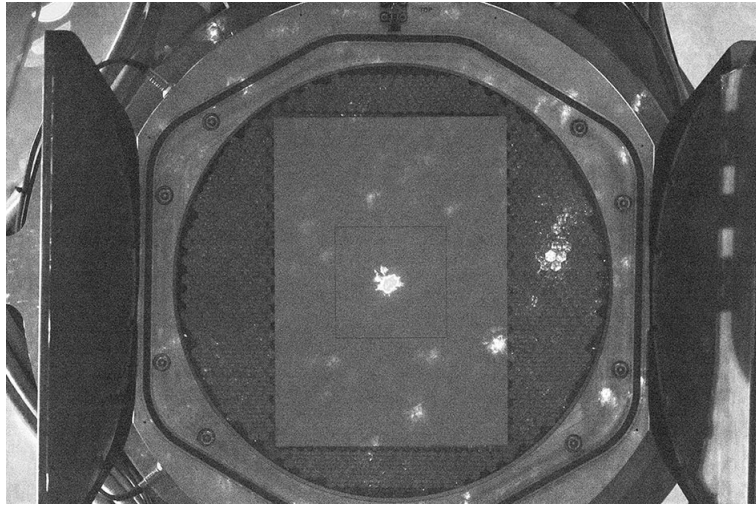


Figure 4.20.: Setup for the PSF measurement as seen from the photo-camera in the mirror dish: a white sheet of paper is fixed to the front window of the FACT camera. The faint black square is used to define a length scale in the picture. Besides the bright star in the center (Gamma Persei), spots from other stars in its vicinity are visible. Note that this picture was over-exposed in the post-processing to make the surroundings visible, hence saturating the image of the central star.

As in other measurements before, a digital Nikon photo-camera was used (see appendix B). The camera was equipped with a 180 mm macro lens by Sigma, and mounted in the center of the mirror dish. A radio remote control was used to trigger the camera. A white sheet of paper with a  $10 \times 10 \text{ cm}^2$  printed rectangle was fixed to the front window of the FACT camera (see figure 4.20). The white sheet acted as reflector for the stars, the printed rectangle was used as a length scale in the image analysis.

In the night of January 26th, 2012, the atmospheric conditions were sufficient for the measurement, with a humidity at the telescope site around 20 % and no wind. Several bright stars were tracked and images taken, interleaved with dark frames with the lens cap on for the noise subtraction. The exposure of the pictures was checked with the selective histogram of the photo-camera to avoid over-exposed pixels in the star region.

## Analysis

The images were converted into 16-bit TIFF-files using the previously established linear processing chain (see appendix B). As a first analysis step, the length scale of the sensor pixels was determined by opening a processed TIFF-file in an image editing software<sup>(19)</sup> and measuring the size of the black rectangle. The obtained scale is 723 px per 10 cm.

For the further processing, the files were read into Python “numpy” arrays. Star-free regions in the central part of the image were used for the background subtraction. The noise in the dark frames was negligible compared to the diffuse background light. The further analysis was restricted to the central area around the star. Starting from the center of gravity of the light distribution, the relative amount of light is calculated for circles with varying radius and the result plotted (see figure 4.21). Two values of the light distribution are of special interest: the amount of light in one pixel and the radius of the

<sup>19</sup>Note that the image must be processed in the same analysis chain, since different raw data converters have different algorithms for the assignment of sensor pixels to image pixels.

circle containing 68.3% of the light<sup>(20)</sup>, both of which can be read from the plot.

### Result and discussion

The full analysis was made for two stars, Betelgeuse at a zenith angle of 29° and Procyon at 46°. One pixel (approximated as circle with 4.8 mm radius) contains 51.9% and 52.3% of the total light, respectively, if it is perfectly centered onto the pixel. The circles containing 68.3% of the light have a diameter of 12.1 mm and 12.0 mm, respectively.

Using a star in infinite distance instead of the focal distance of 8 km contributes approximately 2.2 mm to the PSF<sup>(21)</sup>. The calculation is only approximative for tessellated mirrors, but is sufficient when averaging over the 30 mirrors in the FACT telescope. Subtracting this geometrical effect from the obtained PSF values, the PSF of our telescope was 10.3 mm.

This value was worse than expected from the single mirror properties, but in accordance with the expectation from the first data analysis. Since the effective PSF is a combination of the pointing position of each of the 30 mirrors and its single mirror PSF, it was assumed that the alignment of the mirrors was not sufficient. This result was supported by the shape of the light distribution: two spots on the upper left are almost disconnected from the main spot, which may be due to two strongly misaligned mirrors.

Since my measurement in January 2012, the PSF was not directly measured. For a repetition of the measurement, the following suggestions are made:

- The analysis of the images was complicated by edges of hard shadows close to the central spot. The origin of these shadows is unclear (the moon was just below horizon), but it may be possible that they were produced by clouds which were illuminated by the moon.
- It is strongly recommended to use a camera with a real-time preview of the picture<sup>(22)</sup> which can be zoomed, since probably manual focusing of is necessary.
- Similarly the availability of a function to create a histogram of a zoomed section of a captured image is recommended, since over-exposed pixels of the central star will not be visible in the histogram of the full picture.
- The measurement of the PSF should be made systematically for various Zenith angles, e.g. from 5° to 60°.
- The method allows also to measure the off-center PSF of the mirror dish. Note that for this measurement the photo-camera should be realigned (and refocused) to have the star spot in its center in order to minimize effects of lens vignetting and distortion.

---

<sup>20</sup>This can be denoted as “one standard deviation” in a 2-dimensional Gaussian distribution, which is different from the standard deviations of the one-dimensional projections. See appendix A.2 for the calculations.

<sup>21</sup>This value is derived by assuming a perfect PSF in 8 km distance, and then calculating the geometric shift in the camera over the mirror dish (diameter 3.9 m, focal length 4.89 m) for a source in infinite distance. See appendix A.3 for the calculation.

<sup>22</sup>This feature is present in most modern DSLRs and is called “Live view” in Nikon cameras.



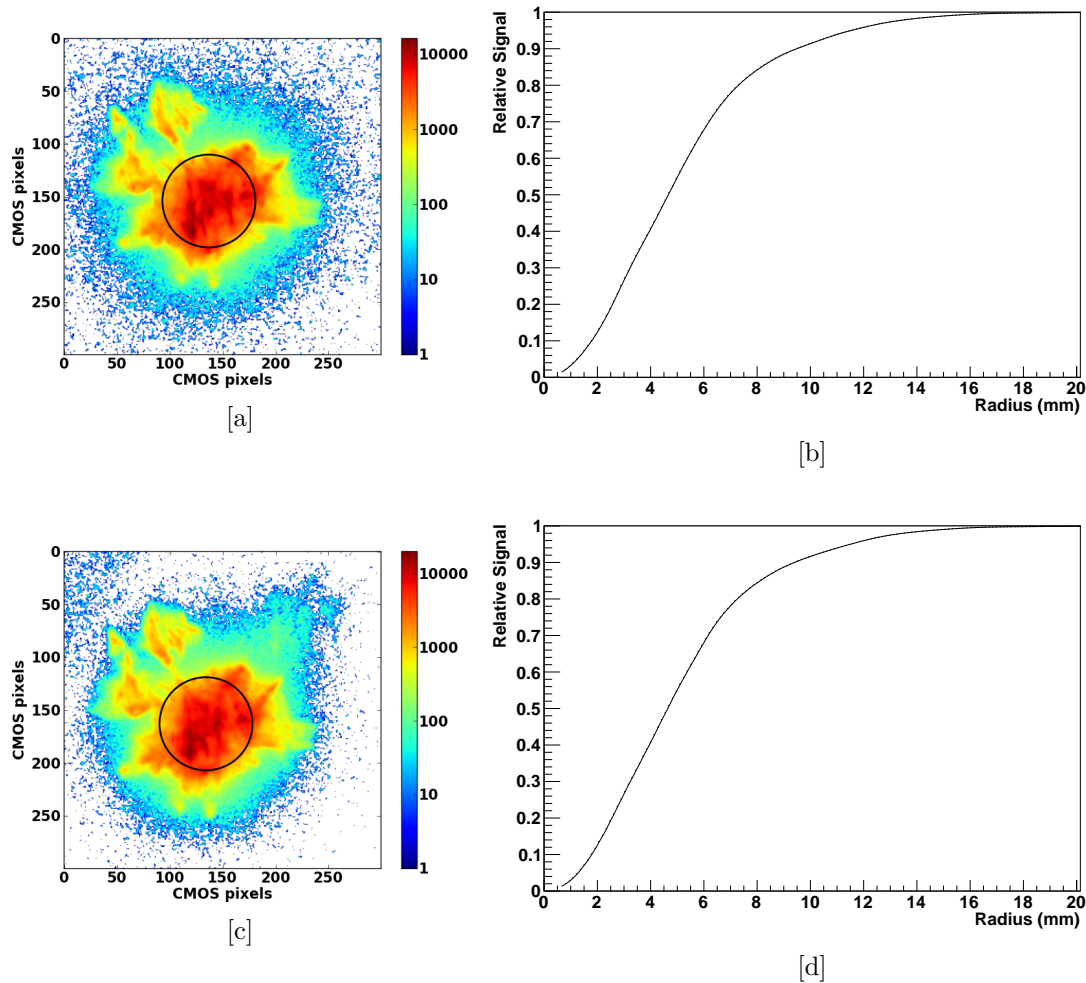


Figure 4.21.: Light distributions for the two PSF measurements at zenith angles of [a] 29° (Betelgeuse) and [c] 46° (Procyon). The plots on the right show the relative amount of light for circles around the center of gravity. The circle containing 68.3% of the light is indicated in the light distributions.

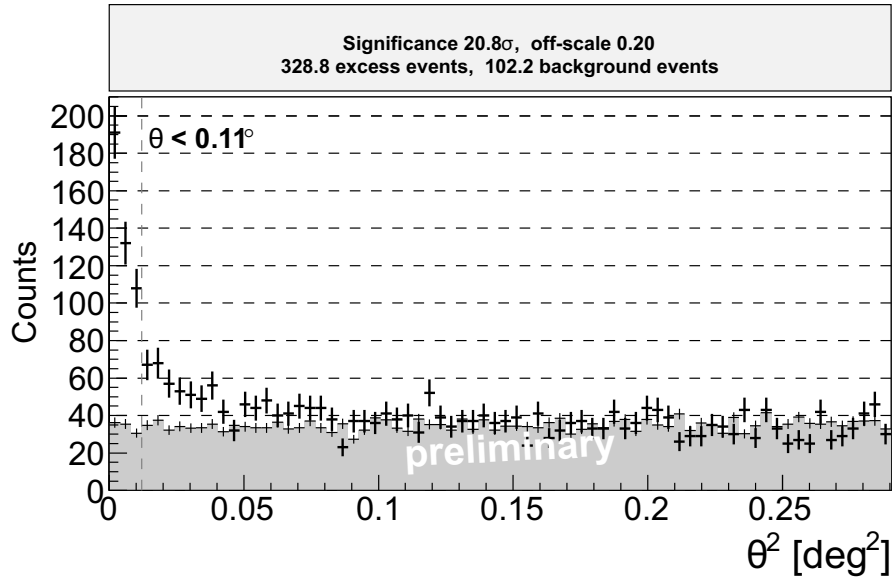


Figure 4.22.: Detection plot for the Crab nebula: in July 2012, the detection of the first three sources (Crab nebula, Mrk 501 and Mrk 421) with FACT was announced to the public at the Gamma2012 conference. The detection plots show an excellent agreement between the on- and off-data (source direction and background, respectively), an indication for the homogeneity of the telescope’s camera. Plot taken from [66].

## 4.5. Observations of sources

### 4.5.1. First detections of strong sources

Soon after the first air showers were recorded in October 2011, the observations of the Crab nebula were started. Even though the commissioning of the telescope and the camera were only in the beginning, the data was used to set up and test the software analysis chain. The choice of astronomical object to observe was based on the high-energy photon emission of the Crab nebula: even though other sources temporarily show higher fluxes, the Crab nebula is the strongest known steady source and is considered the “standard candle” of very high energy astronomy.

Already in February 2012, the first detection plots of high energetic photons from the Crab nebula with FACT were circulated within the collaboration. However, publishing the results was adjourned until the analysis and data taking routines are further established and tested. In July 2012, the detection of the first three sources with FACT was announced to the public and the astrophysics community in particular at the Gamma2012 conference in Heidelberg, Germany [66]. Besides the Crab nebula (see figure 4.22), two known variable sources were detected, Markarian 501 and Markarian 421. To be able to detect VHE gamma-ray sources with high quality within less than a year of operation is considered an important achievement of the FACT collaboration.

### 4.5.2. Monitoring of variable sources

Confirmation of known sources is an important proof for the correct operation of the camera and its performance for real-world astrophysical observations. However, the detection of known sources is of limited scientific interest, and “source-hunting”, the search for new sources, requires telescopes with a lower energy threshold and therefore higher sensitivity

which is closely tied to the available mirror area<sup>(23)</sup>. FACT has thus only a limited chance to contribute there scientifically. But there is another, very important task that FACT can take over: the observation and monitoring of bright variable sources. While this can also be done with the large telescopes, these usually spend little of their expensive observation time on those well-known sources and use their strengths (high sensitivity and low energy threshold) on more rewarding objects. This opens an opportunity where FACT can contribute: spending a lot of observation time on the same object allows to investigate a source's variability, and, in the case of extraordinary behavior, to alert the large telescopes for follow-up observations. The first of these alerts was sent on May 25, 2012, when the blazar Markarian 501 showed a flux several times stronger than the Crab nebula [148].

---

<sup>23</sup>The sensitivity of a telescope is defined as the weakest source strength which can be detected with the telescope within 50 h of observations (see also section 1.4). This depends mostly on the number of observed gamma showers, and thus on the energy threshold above which the telescope can distinguish air showers from background fluctuations. Though this depends also on the camera, the mirror area and the number of telescopes of an array are equally important.

# 5. Summary and future prospects of the FACT technology

## 5.1. Project summary

At the time of this writing, the FACT camera exists already more than two years. In all this time, there was absolutely no major problem with the camera, and even less anything directly related to the novel photosensors.

When the design phase of the project started, the basic operation of G-APDs under outdoor conditions has been tested with the prototype module M0. In many laboratory tests during my diploma thesis and the early phase of this PhD thesis I characterized the sensors and got a feeling for the main issues with the sensors. These were on one hand the unknown saturation level under high background conditions, and on the other hand the sensitivity of the devices towards temperature changes and the bias voltage stability. Further the electronics should allow to resolve single cell signals, ensuring that one of the main advantages of G-APD can be used in its full extent in the final camera.

Those concerns were addressed in the early project phase by the choice of the photosensors (section 2.6) with 3600 cells, which would keep the non-linearity effects in the photosensors at a small level. The bias voltage supply was developed in-house with a focus on the high resolution of the adjustable voltage and smooth transitions of voltages during operation, which would allow to keep the over-voltage of the G-APDs constant even under changing environmental conditions. Finally, the integration of the electronics in the camera allows short signal transmissions paths, reducing noise pickup and increasing the electronics signal resolution. The development of the full electronics of course meant a huge workload for the collaboration.

Another challenge was the development and production of the optical light-guides. Their design was optimized with a ray-tracing computer simulation, resulting in a three-dimensional model where every surface is optically active, either for total internal reflections or as entrance and exit area for the light. A special UV-transmitting PMMA was used for the injection molding, whose light transmission turned out to be extremely sensitive to production fluctuations. Before being selected for the use in the camera, each light-collecting cone was thus characterized in a spectrometer.

In summer 2011, the assembled camera was put to test in the laboratory at ETH Zurich and the first performance parameters measured. As expected, some minor “hiccups” in the electronics and software were found, as well as six pixels with no or unusable sensor signals (see section 4.3.2). Since no major issue with any component of the camera was found, it was decided to ship the camera to the telescope at La Palma for the first real-world operation in a telescope. The repair of the broken pixels was postponed to some months after the first observations, where the occurrence of further problems was expected. However, those first observations mainly showed that the general caution in the design of the camera as well as the experience from the prototype module M0 and other experiments paid off in a very stable and predictable operation. The benefit of repairing the broken

pixels and some minor electronics changes would be marginal compared to the required manpower and finances for the transport and repair work.

The absence of any significant problem in the operation of FACT came as a surprise even to the collaboration itself. Except for (not unexpected) electronics and software communication issues, taking the camera into operation both in the laboratory and in the telescope was immediately possible, without the need of any hardware or configuration work<sup>(1)</sup>.

In the operation of the camera, the main advantages of the camera can be summarized with the categories homogeneity, calibration, stability and predictability. The homogeneity of the PDE was measured to vary less than 7% (RMS), and the single photon signals by less than 5% over the full camera without any fine-tuning. This is reflected in very homogeneous trigger distributions and good agreement of source and background data. The single photon resolution of the G-APDs and the readout electronics allows to measure the gain for each single pixel, both in the digitized data and for the trigger, making an external calibration device (as a light pulser) superfluous [149]. The performance parameters of the camera were measured in various environmental conditions with changing temperatures and amount of background light and found to be very stable using the live regulation of the bias voltages [147]. The stability of the camera also allows to predict the currents and thresholds [150], which reduces the amount of configuration steps in the operation of the telescope.

The stability and predictability in the telescope operation allow the routine remote operation since early summer 2012, and a full robotic operation is currently in planning [151].

## 5.2. G-APD summary

Besides the careful planning and high quality of the electronics, also the photosensors themselves play an important role in the successful operation of the camera. The main disadvantages of G-APDs compared to PMTs could be well handled by the design and operation mode of the camera. The temperature dependency is regulated via a voltage correction system, which also handles the current dependency of the bias voltage supply due to serial resistors. The comparably slow pulses are shaped for the trigger system, but pose no further problem in the data analysis. Another problem might be the division of the sensitive area into cells with a binary light detection, but our choice of a sensor with 3600 cells, of which usually only a few dozen are occupied (see section 2.6), prevents any major effect of this pixelisation.

On the plus side, the application of G-APDs in the camera of IACTs allows to use many of their advantages to their full extent. Most notable are the precise signals of single cells, their homogeneity, stability and reliability which are directly impacting the behavior of the camera (see previous section). The single cell resolution allows the precise calibration of data and trigger, and the absence of aging and magnetic field dependence as well as the homogeneity of the sensor parameters over the full camera ensure a stable and predictable operation. On the design side, the low weight, lack of high-voltage parts and general robustness facilitates not only the design of the camera electronics, but also the camera and telescope mechanics. Not to forget is the lack of PMT-like afterpulses, which facilitates the trigger design<sup>(2)</sup>.

---

<sup>1</sup>The installation of the camera was called a “Plug and play” experience by collaboration members.

<sup>2</sup>Note that afterpulses in a G-APD are not comparable to PMT afterpulses. Since they are triggering only one cell (except for others by crosstalk), the signals are identical to those of dark counts or background photons.

The generation of G-APDs that were used in FACT, the MPPC S10362-33-050C by Hamamatsu from 2009, are in terms of PDE only comparable to specialized PMTs (see section 3.2.1), and the price per area was very high. Both parameters are by now changing fast, for a large part due to the increased number of manufacturers of the devices. But already now, the many other advantages make it very difficult for competing technologies to be selected for IACT cameras or similar applications.

### 5.3. Desired improvements of G-APDs for IACT cameras

While current G-APDs already show major advantages to the conventionally used PMTs, there is of course still a lot of room for improvement. The important question is then the priority of the development: which parameters are central, and which are less relevant?

Possibly the most important parameter is the PDE of the sensors. It defines together with the crosstalk probability<sup>(3)</sup> to a large part the precision, with which the number of incoming photons can be determined (see section 2.5.4). The optimization of the sensitivity towards Cherenkov photons and the reduction of the crosstalk probability are central.

Reducing the amount of detected background photons is of course also interesting, but far less important (see section 3.2.1). Even less important is the reduction of dark counts of the sensors, since they are in general very low compared to the NSB, and in very dark conditions the rate is not an extremely sensitive parameter both for the trigger (see appendix A.4) and for the signal reconstruction.

However, the reduction of the background photon rate is interesting from a different point of view: the high currents. Due to the high gain of G-APDs compared to PMTs, the currents which must be supplied are far higher. Solutions are the reduction of the background rate as well as a reduction of the device gain, where the single cell resolution should be maintained.

Further improvements can be made in the facilitation to keep the device properties constant. Since most parameters depend strongly on the over-voltage (see section 2.4.1), its stabilization is a key issue in the device operation. An enlarged over-voltage would facilitate the bias voltage supply and reduce the effect of temperature variations. The latter can also be achieved by a reduction of the temperature coefficient of the breakdown voltage.

Most of these issues are being intensely researched, both from the manufacturers as well as in academic research.

### 5.4. Improvements of the FACT technology

As with the G-APDs, also the FACT camera has optimization potential. But since the camera is operating surprisingly well, most of these optimizations will only bring small improvements in the actual performance.

Concerning the sensor compartment of the camera, in particular two improvements are in discussion. While the use of the newest generation of G-APDs is obvious, the other one needs a closer look: using a filter to block light above a certain wavelength would allow to reduce the background photon rate of NSB photons significantly, while only little of the Cherenkov light is lost (see figure 3.14). The benefit of such a filter for the trigger and data reduction still needs a close examination, as losing signal photons is often far worse than the improvement obtained by reducing the background rate, especially at low rates

---

<sup>3</sup>Please note that throughout this thesis, only time-coincident triggering of other cells is called crosstalk.

(again, see appendix A.4). Large background rates usually occur due to moonlight, where the optimization potential is small due to the large overlap of Cherenkov and moonlight spectra (see figure 3.13).

In another category, the ideas can already be implemented with FACT: the operation and analysis software. The optimization of the analysis chain could lead to substantial improvements in the sensitivity of a telescope (see e.g. Y. Becherini *et al.* [37]). Room for an extended analysis exists also when showers saturate the dynamic range of the readout: a waveform analysis would allow to reconstruct such rare events, potentially increasing the observable energy range of the telescope towards larger energies. For small energies, operating the telescope at a lower trigger threshold and making a low-level software analysis to throw away background events (software trigger) is an option already being discussed in the collaboration.

## 5.5. Future of the FACT project

Since the announcement of the first successful observations of known sources to the community, FACT has continued its observations on the three objects and a few other known bright, variable sources of VHE photons. Besides optimization of analysis parameters to improve the sensitivity, the telescope is being prepared for its robotic operation. The manual camera lid was replaced by an automatic, remote controllable version. Other hardware modifications in particular for a “safety shutdown” are in planning [151]. The operation software is continuously extended to handle common errors during observations independently, alert a backup supervisor at irregular incidents and initiate the safety shutdown if necessary. The end of the preparations and the start of regular robotic operation are planned in the near future.

### Technology and knowledge transfer to CTA

The good results concerning the stability of FACT, its reliability and ease-of-use are regularly communicated to the astrophysics community through conferences and informal connections. In the field of astroparticle physics, the next large step for the community is the Cherenkov Telescope Array (CTA) project, aiming at operating over a hundred Cherenkov telescopes in parallel. For such a large number of telescopes, their reliability is of particular importance to maximize the observation time of the full system. Even though its design report from 2011 [28] specifically mentions G-APDs as alternative photosensor, they are only planned for a potential upgrade of the initial PMT-based cameras.

With FACT operating, most of the arguments against G-APDs from two years ago like “However, silicon sensors typically require cooling to reduce the dark count to a manageable level and also suffer from optical cross-talk and are not as well matched to the Cherenkov light spectrum as PMTs.” [28] can now be considered obsolete. As repeatedly discussed in this and previous chapters, dark counts only play a small role compared to photons of the night sky background. Optimizing the spectrum to cut off photons above some threshold will reduce the amount of NSB photons (relevant during dark nights) and a bit less the amount of moon light, but only on the cost of losing Cherenkov light. As the total Cherenkov photon detection efficiency is one of the key parameters for the precision of the reconstructed signals, a loss of signal photons must be carefully weighted against



the potential benefit from a reduced background photon rate<sup>(4)</sup>. The argument of optical crosstalk is still valid concerning the fact that it is besides the photon detection efficiency the key parameter for the signal reconstruction precision (see section 2.5.4). However, it is important to differentiate between two types of crosstalk which have nothing in common except for the name: the G-APD-specific device-internal crosstalk and potential crosstalk between the pixels of the camera. While the former is in the order of 10 % in the FACT camera, the latter is largely independent of the photosensor in the geometric arrangement of a camera.

The many advantages of using G-APDs for Cherenkov telescope cameras as demonstrated with FACT are slowly leading to a change in the intention of using PMTs in the first generation of cameras for CTA. Several groups world-wide are currently investigating the use of G-APDs for CTA cameras.

### **Closing words**

As the discussions for the best design of future experiments are ongoing, FACT continues to observe the night sky. The target objects of observations other than the three “standard” sources (Crab, Mrk 501, Mrk 421) are currently being discussed within the collaboration. After contributing to the field of astrophysics by successfully introducing a new technology, I am sure that FACT will soon present its first astrophysical results based on its unique capabilities of stable long-term monitoring.

---

<sup>4</sup>In particular it is difficult to argue with “signal over noise” for random events in time with low rate, since a doubling of the background rate does *not* increase the detection threshold by a factor of  $\sqrt{2}$  as often assumed (please see appendix A.4).



# Acknowledgements

A project with the extent of FACT can only be realized with the contribution of many people, which were either directly working on the project or supporting us in the background. All of them were an important part of my thesis, and I am deeply grateful to them. In the following I would like to name a few who played a particularly important role during my thesis.

First of all I would like to thank Prof. Felicitas Pauss who gave me the possibility to work on this great project. During the project I could always rely on her support and trust. Prof. Adrian Biland was the head of the IACT group in Zurich and was usually the first to read, review and comment the finished parts of this thesis, for which I am very grateful.

During the construction of the FACT camera, I was working with a great lot of people. Werner Lustermann was the technical coordinator, and we had many interesting and fruitful discussions. Working with Urs Horisberger from the mechanics workshop was always a pleasure, as it was with Fabian Mächler and Bruno Zehr. Ulf Röser was the head of the electronics group, whose frank German humor was an irreplaceable contribution to all measurements in the electronics laboratory. Furthermore I want to thank Hanspeter von Gunten and all the other people working in the electronics workshop. Gert Viertel and Volker Commichau were asking uncomfortable but important questions on the design and concepts, and supported the project with their experience in experimental physics. In the same way I want to thank Eckart Lorenz, who is a long-term member of the astroparticle community and fundamentally contributed to the initiation and realization of the FACT project.

With Jean-Pierre Stucki I spent countless hours evaluating the best procedures to assemble the sensor compartment, and shared the tenuous experience of the pixel gluing in the clean room. His exactness and patience which were necessary for this assembly made working with him a pleasant experience.

During all stages of my work I discussed every-day questions with my office partners and other group members, from programming errors to potential future applications of the FACT technology. I very much enjoyed the company of Isabel Braun, Michael Rissi, Dorothee Hildebrand, Andrea Boller, Oliver Grimm and Patrick Vogler. I am particularly grateful to Quirin Weitzel with whom I worked during the most vital stages of the project. Max Knötig is the newest member of our group and will continue with a similar main focus as I had, for which I wish him all the best and to maintain his enthusiasm and bright character.

A very special thanks goes to Dieter Renker, who supported me in all stages of my scientific career, from my first contacts to modern physics at the PSI in 2001 to invaluable feedback on various chapters of my thesis. From him I learned the setup and analysis of laboratory measurements, but also about the realities of being a physicist. I very much appreciate his guidance, support and friendship, which goes beyond the confinements of a laboratory.

Last but not least I would like to thank my family and friends. During the time of this

CHAPTER 5. SUMMARY AND FUTURE PROSPECTS OF THE FACT  
TECHNOLOGY

---

thesis I could not only rely on their support, but they enriched my time in a way that makes me never want to miss them. Thank you all!

# A. Calculations

## A.1. On the statistics of Cherenkov photon counting

The number of photons produced in a Cherenkov shower of a high energy photon with energy  $E$  is a typical process where the total number of produced photons  $N_S$  is approximately Poisson distributed<sup>(1)</sup>. If the average number of photons is  $\mu(E)$ , the probability to get exactly  $n = N_S$  photons is

$$P(n; \mu(E)) = \frac{e^{-\mu} \cdot \mu^n}{n!} \quad (\text{A.1})$$

Of these photons, only a fraction  $k$  arrives at a single pixel, depending on the shower parameters, the atmospheric absorption and the telescope geometry. For a single shower, the number of photons arriving at this pixel  $N_p$  is a fraction of all photons, each having a probability  $k$  to arrive at this pixel. This is a binomial process, i.e. the probability to get exactly  $m = N_p$  at a pixel is

$$B(m; n, k) = \frac{n!}{m!(n-m)!} k^m (1-k)^{n-m} \quad (\text{A.2})$$

If we look at the distribution of the number of photons at the pixel for a certain shower energy, we have to include the probability distribution of the number of shower photons  $N_S$ :

$$p(m; u(E), k) = \sum_{n=m}^{\infty} B(m; n, k) \cdot P(n; \mu(E)) \quad (\text{A.3})$$

$$= \sum_{n=m}^{\infty} \frac{n!}{m!(n-m)!} k^m (1-k)^{n-m} \frac{e^{-\mu} \cdot \mu^n}{n!} \quad (\text{A.4})$$

$$= \frac{k^m e^{-\mu}}{m!} \sum_{n=m}^{\infty} \frac{\mu^n}{(n-m)!} (1-k)^{n-m} \quad (\text{A.5})$$

$$= \frac{(k\mu)^m e^{-\mu}}{m!} \sum_{n=m}^{\infty} \frac{[\mu(1-k)]^{n-m}}{(n-m)!} \quad (\text{A.6})$$

$$= \frac{(k\mu)^m e^{-\mu}}{m!} \underbrace{\sum_{n=0}^{\infty} \frac{[\mu(1-k)]^n}{n!}}_{e^{\mu(1-k)}} \quad (\text{A.7})$$

$$= \frac{(k\mu)^m e^{-k\mu}}{m!} \quad (\text{A.8})$$

$$= P(m; k\mu(E)) \quad (\text{A.9})$$

<sup>1</sup>A further approximation would be a Gaussian distribution with width  $\sqrt{N_S}$ , but only for large photon numbers.

As we see, the combined distribution is again a Poisson distribution, where the mean value was multiplied by the probability factor  $k$  of the binomial distribution. **A process of binomial type applied to a Poisson distribution results in a Poisson distribution, even if the number of trials (or in our case, photons) is small.**

The same calculation applies for the number of photons which arrive on the surface of our detector after absorption processes at a front window or in a light guide: the number of photons on the detector surface is Poisson distributed. Of those photons, only a fraction would trigger an avalanche, and again we end up with a Poisson distribution, even though the process of detecting a certain number of photons of those which arrive on the surface is a Binomial process.

## A.2. Two-dimensional PSF

Assume for the photon flux a two-dimensional distribution  $\phi(x, y)$  of Gaussian shape:

$$\phi(x, y) = \frac{\Phi_{\text{tot}}}{2\pi\sigma_x\sigma_y} e^{-\frac{x^2}{2\sigma_x^2} - \frac{y^2}{2\sigma_y^2}} \quad (\text{A.10})$$

The integrated flux over the full plane is  $\Phi_{\text{tot}}$ . The parameters  $\sigma_x$  and  $\sigma_y$  are the standard deviations of the projected distributions, e.g. for the projection in  $y$  we get a one-dimensional Gaussian distribution in  $x$  with standard deviation  $\sigma_x$ :

$$\phi_x(x) = \int_{-\infty}^{\infty} \phi(x, y) dy = \frac{\Phi_{\text{tot}}}{2\pi\sigma_x\sigma_y} \sqrt{2\pi}\sigma_y e^{-\frac{x^2}{2\sigma_x^2}} \quad (\text{A.11})$$

$$= \frac{\Phi_{\text{tot}}}{\sqrt{2\pi}\sigma_x} e^{-\frac{x^2}{2\sigma_x^2}} \quad (\text{A.12})$$

We assume a symmetrical distribution, i.e.  $\sigma_x = \sigma_y = \sigma$ , and calculate the amount of light  $\Phi_C(R)$  we get within a circle with radius  $R$ :

$$\Phi_C(R) = \int_C \phi(x, y) dx dy = \int_0^R \int_0^{2\pi} \phi(x, y) r dr d\theta \quad (\text{A.13})$$

$$= \frac{\Phi_{\text{tot}}}{2\pi\sigma^2} 2\pi \int_0^R r e^{-\frac{r^2}{2\sigma^2}} dr = \frac{\Phi_{\text{tot}}}{2\pi\sigma^2} 2\pi\sigma^2 (1 - e^{-\frac{R^2}{2\sigma^2}}) \quad (\text{A.14})$$

$$= \Phi_{\text{tot}} (1 - e^{-\frac{R^2}{2\sigma^2}}) \quad (\text{A.15})$$

This means, that if we look at a circle with radius  $R = \sigma$  we only have  $\Phi_C(\sigma) = 39\%$  of the light inside this circle. The question is now, which radius is necessary to get a fraction of  $k$  of the total light:

$$\Phi_C(R) = k \cdot \Phi_{\text{tot}} \quad (\text{A.16})$$

$$\Leftrightarrow R(k) = \sigma \sqrt{-2 \ln(1 - k)} \quad (\text{A.17})$$

So in order to get  $k = 68.27\%$  of the light into one pixel, the pixel needs a diameter of  $2 \cdot R(0.6827) = 3.03\sigma$ .

### A.3. PSF widening for light sources in infinite distance

The mirror dish of an IACT is approximately focused to 8 km, which is the distance to the shower maximum of typical air showers for a telescope on 2000 m above sea level. If a star is used to measure the PSF, its image is expanded to a circle even for a perfect mirror due to its (in good approximation) infinite distance. In this section, the diameter of this circle is calculated. The parameters for the calculation are the mirror diameter  $D = 2R$ , its focal length  $f$  and the focusing distance  $L$ . The radius of the spot is denoted  $x$ .

First the angle  $\alpha$  between the star and the focusing direction at the edge of the mirror is calculated:

$$\sin(\alpha) = \frac{D/2}{L} = \frac{R}{L} \ll 1 \quad (\text{A.18})$$

A light ray impinging on the edge of the mirror from the focusing direction is reflected with an angle  $\delta$  onto the center of the camera. The angle between the star direction and the camera center is thus  $\delta + \alpha$ , which is given geometrically as

$$\sin(\delta + \alpha) = \frac{R}{f}, \quad (\text{A.19})$$

when approximating the distance between mirror and camera center as  $f$  over the full mirror.

Light coming from the star however is not reflected onto the camera center (angle  $\delta + \alpha$ ), but with a larger angle  $\delta + 2\alpha$ . The radius of the light spot can now easily be calculated:

$$\frac{R+x}{f} = \sin(\delta + 2\alpha) = \sin(\delta + \alpha) \cos(\alpha) + \cos(\delta + \alpha) \sin(\alpha) \quad (\text{A.20})$$

$$= \frac{R}{f} \cdot 1 + \sqrt{1 - \frac{R^2}{f^2}} \cdot \frac{R}{L} \quad (\text{A.21})$$

$$x = \frac{R}{L} \sqrt{f^2 - R^2} \quad (\text{A.22})$$

For the FACT telescope ( $D = 2R = 3.9$  m,  $f = 4.89$  m,  $L = 8$  km), the spot diameter is  $2x = 2.2$  mm.

### A.4. Noise characteristic of random background events

When an experiment such as the FACT camera is designed, one of the main questions is what the minimal size of signals is which can be distinguished from random noise events. In many cases, the effect of noise is said to “increase with the square root”, i.e. for four times as much noise the smallest signals have to be twice as large. A standard example for such a behavior is electronics noise: when  $n$  channels with (Gaussian) noise are added, the standard deviation of the summed noise is  $\sqrt{n}$  larger than a single channel.

However, the main noise source in IACT cameras are background photons, which show a different behavior. It is often assumed that this noise has a similar behavior as electronics noise, i.e. if we have twice the background rate, our signals must be  $\sqrt{2}$  larger. As we will see, this is not correct for low photon rates.

We assume that our signal photons arrive with a smaller spread than the time window our trigger electronics  $\Delta T$ . The background photons arrive with a rate  $R_B$ , and we get an accidental trigger if  $n$  or more photons arrive within  $\Delta T$ . The rate of accidental triggers



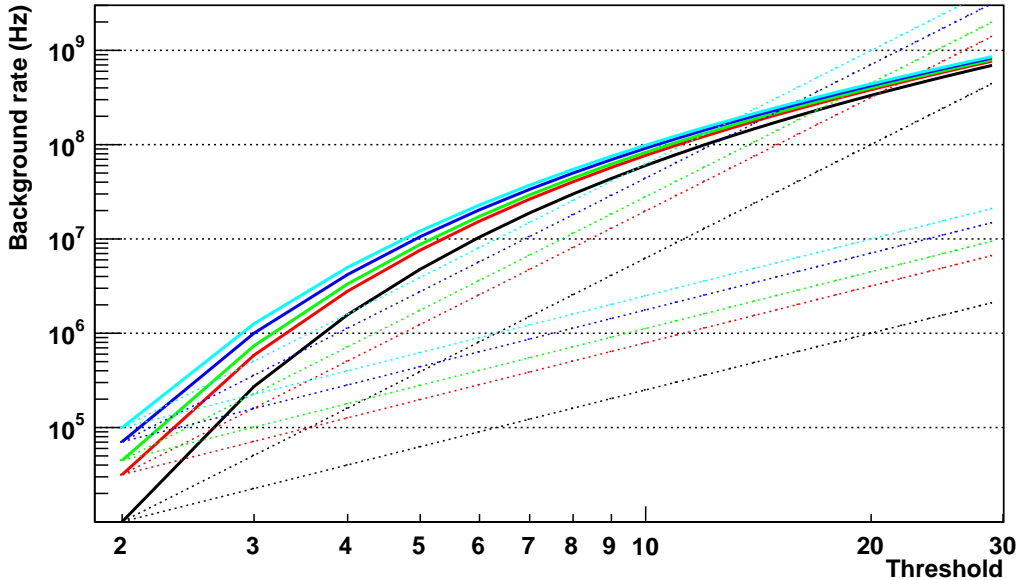


Figure A.1.: Background rate vs. threshold for constant accidental rates: for accidental rates of 1, 10, 20, 50 and 100 Hz the required background rate in dependence of the threshold is calculated. The coincidence time is 10 ns. The dotted lines show quadratic (lower lines) and quartic (upper lines) dependencies on the threshold. For low rates, the behavior is far from the expected quadratic behavior. For larger rates, the noise behavior is approximately quadratic (i.e. it has a derivative around two).

$R_A$  is calculated based on Poisson statistics: the average number of photons within  $\Delta T$  is  $R_B \Delta T$ . The probability to have exactly  $n$  photons is

$$p(n, R_B \Delta T) = \frac{e^{-R_B \Delta T} (R_B \Delta T)^n}{n!}. \quad (\text{A.23})$$

When can put the start of this time window on the arrival time of any background photon, and the rate of accidental triggers is thus

$$R_A = R_B \sum_{k=n-1}^{\infty} \frac{e^{-R_B \Delta T} (R_B \Delta T)^k}{k!} \quad (\text{A.24})$$

$$= R_B \left( 1 - \sum_{k=0}^{n-2} \frac{e^{-R_B \Delta T} (R_B \Delta T)^k}{k!} \right) \quad (\text{A.25})$$

Note that only  $n - 1$  photons are necessary within the time window, since there is an additional photon at the very start of the time window and we defined our threshold as  $n$  or more photons.

Based on this formula we can for each threshold  $n$  determine the background rate for a specific accidental rate<sup>(2)</sup>. If the behavior was quadratic, we get a straight line with a derivative of two in the double logarithmic plot. As we can see in figure A.1, the derivative is larger than four for small background rates, thus disproving the quadratic assumption. The consequence is that for low background noise rates, additional light is less problematic than it would be if the behavior was quadratic.

<sup>2</sup>This calculation was made iteratively with a precision of 1%.

## A.5. Unit transformations to photon rates

The transformation of the units is based on the integration, i.e. after integrating between two wavelengths we want a flux (rate per area) or angular flux (rate per area per solid angle). As symbols, we use  $\phi$  for flux and angular flux,  $I$  for intensity (energy flux),  $\Omega$  for solid angles, and  $E$ ,  $\lambda$  and  $\nu$  for the photon energy, wavelength and frequency.  $h$  is Planck's constant,  $c$  the vacuum speed of light. The following relations are used:

$$dI = \frac{d\phi}{d\lambda} d\lambda \cdot E(\lambda) \quad (\text{A.26})$$

$$E = h\nu = \frac{hc}{\lambda} \quad (\text{A.27})$$

$$c = \lambda\nu \quad (\text{A.28})$$

The solar reference spectra [116] are provided as differential intensities  $\frac{dI}{d\lambda}$  with the units  $\text{W}/\text{m}^2\text{nm}$  as a function of the wavelength in nm. The area under the curve is thus an intensity, and a transformation is necessary to get a flux:

$$\phi = \int_{\lambda_1}^{\lambda_2} \frac{dR}{d\lambda} d\lambda = \int_{\lambda_1}^{\lambda_2} \frac{1}{E} \frac{dI}{d\lambda} d\lambda \quad (\text{A.29})$$

$$= \int_{\lambda_1}^{\lambda_2} \frac{\lambda}{hc} \frac{dI}{d\lambda} d\lambda \quad (\text{A.30})$$

The provided values must thus be multiplied by the wavelength in order for the area under the curve being proportional to photon flux.

For the NSB measurement by C. Benn and S. Ellison [20], the situation is more complicated. The data is provided as  $\mu\text{Jy}/\text{arcsec}^2$  plotted against the wavelength  $\lambda$ . What we have is a differential intensity  $\frac{d^2I}{d\nu d\Omega}$  as a function of the wavelength. We first use the relation from above and then use the chain rule to substitute the differentiation with respect to  $\lambda$  by  $\nu$ :

$$\phi = \int_{\lambda_1}^{\lambda_2} \frac{\lambda}{hc} \frac{d^2I}{d\Omega d\lambda} d\lambda = \int_{\lambda_1}^{\lambda_2} \frac{\lambda}{hc} \frac{d^2I}{d\Omega d\nu} \underbrace{\left| \frac{d\nu}{d\lambda} \right|}_{c/\lambda^2} d\lambda \quad (\text{A.31})$$

$$= \int_{\lambda_1}^{\lambda_2} \frac{1}{h\lambda} \frac{d^2I}{d\Omega d\nu} d\lambda \quad (\text{A.32})$$

Note that  $\phi$  is an angular flux this time. The curve in C. Benn and S. Ellison [20] must thus be scaled with  $1/\lambda$ . This conversion is also confirmed in the appendix of the original publication as a technical note [152]:

$$1.24 \times 10^7 \cdot (\text{wavelength}/\text{m}) \cdot \mu\text{Jy}/\text{arcsec}^2 = 10^{10}/4\pi \text{ photons}/\text{s}/\text{m}^2/\text{sr}/\text{\AA} \quad (\text{A.33})$$

The conversion is also used in table 2 in C. Benn and S. Ellison [20]. It is identical to the division by  $h\lambda$  as in the calculation and transforming to SI units:

$$\frac{1}{1.24 \times 10^7 \cdot \lambda} \frac{10^{10}}{4\pi} \underbrace{10^{10}}_{\text{\AA}} = 6.418 \times 10^{11} \cdot \frac{1}{\lambda} \quad (\text{A.34})$$

$$\frac{1}{h\lambda} \underbrace{10^{-32}}_{\mu\text{Jy}} \underbrace{4.25 \times 10^{10}}_{\text{steradian}} = 6.414 \times 10^{11} \cdot \frac{1}{\lambda} \quad (\text{A.35})$$

As a second cross-check for both transformations we use the units:

$$\left[ \frac{\lambda}{hc} \frac{dI}{d\lambda} d\lambda \right] = \frac{m}{J_s \cdot m/s} \frac{J}{m^2 s \cdot m} m = \frac{1}{m^2 s} \quad (\text{A.36})$$

$$\left[ \frac{1}{h\lambda} \frac{d^2 I}{d\Omega d\nu} d\lambda \right] = \frac{1}{J_s \cdot m} \frac{J}{m^2 s \cdot sr \cdot Hz} m = \frac{1}{sr \cdot m^2 s} \quad (\text{A.37})$$

## A.6. Generalized mean value and variance for combined distributions

We start with a discrete distribution  $p_k$  with norm 1, average  $\mu_D$  and variance  $\sigma_D^2$ :

$$\text{Norm:} \quad \sum_{k=0}^{\infty} p_k = 1 \quad (\text{A.38})$$

$$\text{Average:} \quad \sum_{k=0}^{\infty} k \cdot p_k = \mu_D \quad (\text{A.39})$$

$$\text{Variance:} \quad \sum_{k=0}^{\infty} (k - \mu_D)^2 \cdot p_k = \sigma_D^2 \quad (\text{A.40})$$

For every value of  $k$  we assume a continuous distribution  $f_k(x)$ . We require that the average  $S_k$  is the linear superposition of the average for  $k = 1$ , and that the total variance is parameterized by three variables:

$$\text{Norm:} \quad \int_{-\infty}^{\infty} f_k(x) dx = 1 \quad (\text{A.41})$$

$$\text{Average:} \quad \int_{-\infty}^{\infty} x \cdot f_k(x) dx = S_k = k \cdot S_1 \quad (\text{A.42})$$

$$\text{Variance:} \quad \int_{-\infty}^{\infty} (x - S_k)^2 f_k(x) dx = \sigma_0^2 + k \cdot \sigma_{\text{lin}}^2 + k^2 \cdot \sigma_{\text{sq}}^2 \quad (\text{A.43})$$

First we calculate two expressions we need later:

$$\sigma_D^2 = \sum_{k=0}^{\infty} (k - \mu_D)^2 \cdot p_k = \sum_{k=0}^{\infty} (k^2 + \mu_D^2 - 2\mu_D k) \cdot p_k \quad (\text{A.44})$$

$$= \sum_{k=0}^{\infty} k^2 \cdot p_k + \mu_D^2 \sum_{k=0}^{\infty} p_k - 2\mu_D \sum_{k=0}^{\infty} k \cdot p_k \quad (\text{A.45})$$

$$= \sum_{k=0}^{\infty} k^2 \cdot p_k + \mu_D^2 - 2\mu_D^2 \quad (\text{A.46})$$

$$\Leftrightarrow \sum_{k=0}^{\infty} k^2 \cdot p_k = \sigma_D^2 + \mu_D^2 \quad (\text{A.47})$$

using the equations (A.40), (A.38) and (A.39). Similarly we calculate

$$\sigma_0^2 + k \cdot \sigma_{\text{lin}}^2 + k^2 \cdot \sigma_{\text{sq}}^2 = \int_{-\infty}^{\infty} (x - S_k)^2 f_k(x) dx = \int_{-\infty}^{\infty} (x^2 + S_k^2 - 2S_k x) f_k(x) dx \quad (\text{A.48})$$

$$= \int_{-\infty}^{\infty} x^2 f_k(x) dx + S_k^2 \int_{-\infty}^{\infty} f_k(x) dx - 2S_k \int_{-\infty}^{\infty} x f_k(x) dx \quad (\text{A.49})$$

$$\Leftrightarrow \int_{-\infty}^{\infty} x^2 f_k(x) dx = \sigma_0^2 + k \cdot \sigma_{\text{lin}}^2 + k^2 \cdot \sigma_{\text{sq}}^2 + k^2 S_1^2 \quad (\text{A.50})$$

We can now calculate the norm, average, and variance of the combined distribution which is the weighted sum of the distributions  $f_k(x)$ :

$$\sum_{k=0}^{\infty} p_k f_k(x) \quad (\text{A.51})$$

**Norm**

$$\int_{-\infty}^{\infty} \sum_{k=0}^{\infty} p_k f_k(x) dx = \sum_{k=0}^{\infty} p_k \int_{-\infty}^{\infty} f_k(x) dx = \sum_{k=0}^{\infty} p_k = 1 \quad (\text{A.52})$$

**Average**

$$S = \int_{-\infty}^{\infty} x \cdot \sum_{k=0}^{\infty} p_k f_k(x) dx = \sum_{k=0}^{\infty} p_k \int_{-\infty}^{\infty} x \cdot f_k(x) dx \quad (\text{A.53})$$

$$= S_1 \sum_{k=0}^{\infty} k \cdot p_k \quad (\text{A.54})$$

$$= S_1 \cdot \mu_D \quad (\text{A.55})$$

**Variance**

$$\sigma_S^2 = \int_{-\infty}^{\infty} (x - \mu_D S_1)^2 \sum_{k=0}^{\infty} p_k f_k(x) dx \quad (\text{A.56})$$

$$= \sum_{k=0}^{\infty} p_k \int_{-\infty}^{\infty} (x^2 + \mu_D^2 S_1^2 - 2\mu_D S_1 x) f_k(x) dx \quad (\text{A.57})$$

$$= \sum_{k=0}^{\infty} p_k ([\sigma_0^2 + k\sigma_{\text{lin}}^2 + k^2\sigma_{\text{sq}}^2 + k^2 S_1^2] + \mu_D^2 S_1^2 - 2\mu_D S_1 k) \quad (\text{A.58})$$

$$= \sigma_0^2 + \mu_D \sigma_{\text{lin}}^2 + (\sigma_D^2 + \mu_D^2)(\sigma_{\text{sq}}^2 + S_1^2) + \mu_D^2 S_1^2 - 2\mu_D^2 S_1^2 \quad (\text{A.59})$$

$$= \sigma_0^2 + \mu_D \sigma_{\text{lin}}^2 + (\sigma_D^2 + \mu_D^2) \sigma_{\text{sq}}^2 + S_1^2 \sigma_D^2 \quad (\text{A.60})$$

## A.7. Equivalence of the ENF definitions

We have two definitions for the ENF, one based on the signals produced by incoming photons with a Poisson distribution:

$$\frac{\sigma_S}{S} = \sqrt{\frac{\text{ENF}}{N_{\text{pe}}}} \quad (\text{A.61})$$

$$\text{ENF} = \frac{\sigma_S^2}{S^2} N_{\text{pe}} \quad (\text{A.62})$$

$\sigma_S$  is the standard deviation of the distribution of measured signals,  $S$  the average signal.

The other one is based on the signal of single photons (e.g. [99, 153]):

$$\text{ENF} = 1 + \frac{\sigma_1^2}{S_1^2} \quad (\text{A.63})$$

where  $\sigma_1$  is the width,  $S_1$  the average amplitude of the single photon signals.

We can prove that those two definitions are equivalent for a distribution  $p_k$  of  $k$  triggered cells (or photons) with norm 1, average  $N_{\text{pe}}$  and variance  $N_{\text{pe}}$  (as it is the case for a Poisson distribution). In the definitions of the previous section A.6 we have  $\mu_D = \sigma_D^2 = N_{\text{pe}}$ .

For  $k$  photons we get a distribution  $f_k(x)$  of detector signals. The average signal  $S_k$  is the linear sum of  $k$  times the single signal  $S_1$ , for the variance we include all three components  $\sigma_0^2 + k \cdot \sigma_{\text{lin}}^2 + k^2 \cdot \sigma_{\text{sq}}^2$ .

We can now calculate the ENF by putting average (A.55) and variance (A.60) in the first definition of the ENF (A.62):

$$\text{ENF} = \frac{\sigma_S^2}{S^2} N_{\text{pe}} \quad (\text{A.64})$$

$$= \frac{\sigma_0^2 + N_{\text{pe}}\sigma_{\text{lin}}^2 + (N_{\text{pe}} + N_{\text{pe}}^2)\sigma_{\text{sq}}^2 + S_1^2 N_{\text{pe}}}{(S_1 \cdot N_{\text{pe}})^2} N_{\text{pe}} \quad (\text{A.65})$$

$$= 1 + \frac{\sigma_{\text{lin}}^2}{S_1^2} + \frac{\sigma_0^2}{S_1^2} \frac{1}{N_{\text{pe}}} + \frac{\sigma_{\text{sq}}^2}{S_1^2} (1 + N_{\text{pe}}) \quad (\text{A.66})$$

If we only look at effects which are independent for each photon, we have  $\sigma_0 = \sigma_{\text{sq}} = 0$ , i.e. no pedestal noise (see section 2.3.4) and no saturation (see section 2.30). In this case we get exactly the second definition (A.63).

## A.8. Explicit calculation of the ENF of a Poisson distribution with noise

### A.8.1. Definitions

We start with a Poisson distribution. The probability for a value  $k$  is  $p_k$ . To this distribution we add noise in the form of a Gaussian shape,  $\sigma_k^2 = \sigma_0^2 + k \cdot \sigma_{\text{av}}^2$ . The widths of the pedestal  $\sigma_{\text{ped}}$  and the contribution of one avalanche  $\sigma_{\text{av}}$  are relative to the peak difference (i.e. the signal size).

We want to know the sum, average, and variance.

### A.8.2. Only Poisson statistics

The distribution is given by

$$p_k = \frac{e^{-\mu} \mu^k}{k!}.$$

**Sum**

$$\sum_{k=0}^{\infty} p_k = \sum_{k=0}^{\infty} \frac{e^{-\mu} \mu^k}{k!} = e^{-\mu} \sum_{k=0}^{\infty} \frac{\mu^k}{k!} = e^{-\mu} e^{\mu} = 1 \quad (\text{A.67})$$

**Average**

$$\sum_{k=0}^{\infty} k \cdot p_k = \sum_{k=0}^{\infty} k \frac{e^{-\mu} \mu^k}{k!} = e^{-\mu} \sum_{k=1}^{\infty} k \frac{\mu^k}{k!} = e^{-\mu} \mu \sum_{k=1}^{\infty} \frac{\mu^{k-1}}{(k-1)!} \quad (\text{A.68})$$

$$= e^{-\mu} \mu e^{\mu} = \mu \quad (\text{A.69})$$

**Variance**

$$\sum_{k=0}^{\infty} (k - \mu)^2 \cdot p_k = \sum_{k=0}^{\infty} p_k (k^2 + \mu^2 - 2\mu k) = (\mu^2 + \mu) + \mu^2 - 2\mu^2 = \mu \quad (\text{A.70})$$

$$(\text{A.71})$$

Calculation of the  $k^2 \cdot p_k$  term:

$$\sum_{k=0}^{\infty} k^2 \cdot p_k = \sum_{k=0}^{\infty} k^2 \frac{e^{-\mu} \mu^k}{k!} = e^{-\mu} \mu \sum_{k=1}^{\infty} k \frac{\mu^{k-1}}{(k-1)!} = e^{-\mu} \mu \frac{d}{d\mu} \sum_{k=1}^{\infty} \frac{\mu^k}{(k-1)!} \quad (\text{A.72})$$

$$= e^{-\mu} \mu \frac{d}{d\mu} \mu \cdot e^{\mu} = e^{-\mu} \mu (e^{\mu} + \mu \cdot e^{\mu}) \quad (\text{A.73})$$

$$= \mu + \mu^2 \quad (\text{A.74})$$

**A.8.3. Including noise**

The distribution is given by

$$p(x) = \sum_{k=0}^{\infty} \frac{e^{-\mu} \mu^k}{k!} e^{-\frac{(x-x_k)^2}{2\sigma_k^2}} \frac{1}{\sigma_k \sqrt{2\pi}}.$$

$x_k$  is the position of the  $k$ -th peak, and since we normalize the signal size to 1 we have  $x_k = k$ .

**Integral**

$$\int_{-\infty}^{\infty} p(x) dx = \int_{-\infty}^{\infty} \sum_{k=0}^{\infty} \frac{e^{-\mu} \mu^k}{k!} e^{-\frac{(x-x_k)^2}{2\sigma_k^2}} \frac{1}{\sigma_k \sqrt{2\pi}} dx \quad (\text{A.75})$$

$$= \sum_{k=0}^{\infty} \frac{e^{-\mu} \mu^k}{k!} \int_{-\infty}^{\infty} e^{-\frac{(x-x_k)^2}{2\sigma_k^2}} \frac{1}{\sigma_k \sqrt{2\pi}} dx \quad (\text{A.76})$$

$$= \sum_{k=0}^{\infty} \frac{e^{-\mu} \mu^k}{k!} \cdot 1 \quad (\text{A.77})$$

$$= 1 \quad (\text{A.78})$$

**Average**

$$\int_{-\infty}^{\infty} x \cdot p(x) dx = \sum_{k=0}^{\infty} \frac{e^{-\mu} \mu^k}{k!} \underbrace{\int_{-\infty}^{\infty} x \cdot e^{-\frac{(x-x_k)^2}{2\sigma_k^2}} \frac{1}{\sigma_k \sqrt{2\pi}} dx}_{=x_k} \quad (\text{A.79})$$

$$= \sum_{k=0}^{\infty} \frac{e^{-\mu} \mu^k}{k!} k \quad (\text{A.80})$$

$$= \mu \quad (\text{A.81})$$

**Variance**

$$\int_{-\infty}^{\infty} (x - \mu)^2 \cdot p(x) dx = \sum_{k=0}^{\infty} \frac{e^{-\mu} \mu^k}{k!} \int_{-\infty}^{\infty} (x - \mu)^2 \cdot e^{-\frac{(x-x_k)^2}{2\sigma_k^2}} \frac{1}{\sigma_k \sqrt{2\pi}} dx \quad (\text{A.82})$$

$$= \sum_{k=0}^{\infty} \frac{e^{-\mu} \mu^k}{k!} \int_{-\infty}^{\infty} (y + (x_k - \mu))^2 \cdot e^{-\frac{y^2}{2\sigma_k^2}} \frac{1}{\sigma_k \sqrt{2\pi}} dy \quad \text{with } y = x - x_k \quad (\text{A.83})$$

$$= \sum_{k=0}^{\infty} \frac{e^{-\mu} \mu^k}{k!} \int_{-\infty}^{\infty} \underbrace{(y^2)}_{\sigma_k^2} + \underbrace{2y(x_k - \mu)}_0 + (x_k - \mu)^2 \cdot e^{-\frac{y^2}{2\sigma_k^2}} \frac{1}{\sigma_k \sqrt{2\pi}} dy \quad (\text{A.84})$$

$$= \sum_{k=0}^{\infty} \frac{e^{-\mu} \mu^k}{k!} \left( \sigma_k^2 + \underbrace{(k - \mu)^2}_{\mu} \right) \quad (\text{A.85})$$

$$= \mu + \sigma_0^2 + \sigma_{\text{av}}^2 \sum_{k=0}^{\infty} \frac{e^{-\mu} \mu^k}{k!} k \quad (\text{A.86})$$

$$= \sigma_0^2 + \mu(1 + \sigma_{\text{av}}^2) \quad (\text{A.87})$$

**Excess noise factor**

The ENF is given by the variance divided by the average, if the underlying distribution is a Poisson distribution. We thus have

$$\text{ENF} = 1 + \sigma_{\text{av}}^2 + \frac{\sigma_0^2}{\mu} \quad (\text{A.88})$$

This is expected, due to the equivalence of the two existing definitions: the width of the signal for a single incoming photon is  $\sigma_{\text{av}}^2 + \sigma_0^2$ .

This ENF is not independent of the number of detected photons  $\mu$ , which contradicts the definitions.  $\sigma_0$  is thus usually set to 0 for values of  $\mu > 1$  in ENF considerations.



## B. Linearity of digital photo camera measurements

Using digital photo camera for measurements of light distributions is very convenient due to the easy availability of these devices and their high resolution. However, there is an important caveat in using such data: most image data is saved in a logarithmic scale to have a smaller scale for low-light areas of the picture. This is in particular the case for the JPEG file in the sRGB color space.

On a lower level, there are further problems: the processing in the camera for the creation of output files includes many small optimizations, from noise reduction to brightening of dark areas to improve color and contrast. And last but not least, digital cameras are optimized for appealing pictures and not for scientific measurements, so the sensor and digitization linearity must be checked.

In order to avoid the non-linearities of many image formats, the data in many digital cameras can be saved in a raw image format, where (more or less) unprocessed sensor data is saved. Using special software, this data can be converted to linear TIFF files, which can then be imported and analyzed using standard software as Matlab<sup>(1)</sup> or the Python programming language<sup>(2)</sup>.

During this thesis, digital photographs were used in several measurements, from the cone surface measurements (section 3.3.8) to the Point Spread Function (PSF) of the telescope (section 4.4). Two Nikon cameras were used, a D90 and a D7000. The camera settings and image processing were made as described below.

### B.1. Camera settings

The general baseline for the camera settings is to switch off all camera-internal optimizations, and fixate settings which are usually auto-adjusted such as the white balance. For the Nikon cameras, the following settings were made:

- Manual mode: aperture and shutter speed are set manually.
- Fixed ISO speed.
- White balance fixated.
- Noise reduction for high ISO switched off: this procedure applies a software averaging on the sensor data if high ISO values are used.
- Noise reduction for long exposure times: this settings defines, whether at the end of a long exposure a dark frame should be taken, which is directly subtracted from the raw data.

---

<sup>1</sup>Matlab is a commercial analysis package for the processing of numerical data. <http://www.mathworks.com/products/matlab/>

<sup>2</sup>Of course other programming languages are suited as well, Python was chosen due to its fast program drafting capabilities. <http://www.python.org/>

- Active D-Lightning switched off: modern Nikon cameras have an operating mode where the exposure in various regions of the image is adapted during the integration time of the sensor. The purpose of this mode is to darken highlighted areas and brighten dark areas, and must be switched off.
- Picture Control setting neutral.
- Manual focus: this is important if several pictures should be compared, since the focus of a lens also changes its absolute light transmission. The focus must be unchanged during a series of measurements.
- Vibration reduction (VR) off: many lenses have an internal image stabilization which mechanically compensates for vibrations. When a tripod is used, this feature should be switched off since there is a certain probability for unnecessary “corrections”.
- Write uncompressed raw files with the maximal available bit-depth.

## B.2. Image processing

### B.2.1. Conversion of raw files to TIFF image files using dcraw

For the translation of the raw files from the Nikon camera (NEF format), the program `dcraw`<sup>(3)</sup> was used. The parameter switches were as follows:

```
dcraw.exe -v -r 1111 -H 0 -4 -T filename.NEF
```

The switches have the following effect (according to the program’s help text):

**-v** Print verbose messages

**-r 1111** Set custom white balance

**-H 0** Clip highlights

**-4** Create linear 16-bit output (no automatic brightening, gamma correction parameters 1/1)

**-T** Write TIFF as output file

### B.2.2. TIFF image processing in Matlab

These 16-bit files can be read in Matlab using the `imread` function, which returns a three-dimensional array with the pixels  $x$  and  $y$  coordinate as first two dimensions, and its RGB values for the third dimension.

### B.2.3. Python image processing

Python is a programming language which offers a lot of programming comfort by providing packages for many common programming tasks. However, the standard imaging library “Python Imaging Library (PIL)” does only support images with up to 32 bit per pixel (version 1.1.7), which is not sufficient for the 48 bit in a RGB file with 16 bit per channel. The library “pylibtiff 0.1”<sup>(4)</sup> was also tested, but was also not able to read the files.

---

<sup>3</sup><http://www.cybercom.net/~dcoffin/dcraw/>

<sup>4</sup><http://code.google.com/p/pylibtiff/>

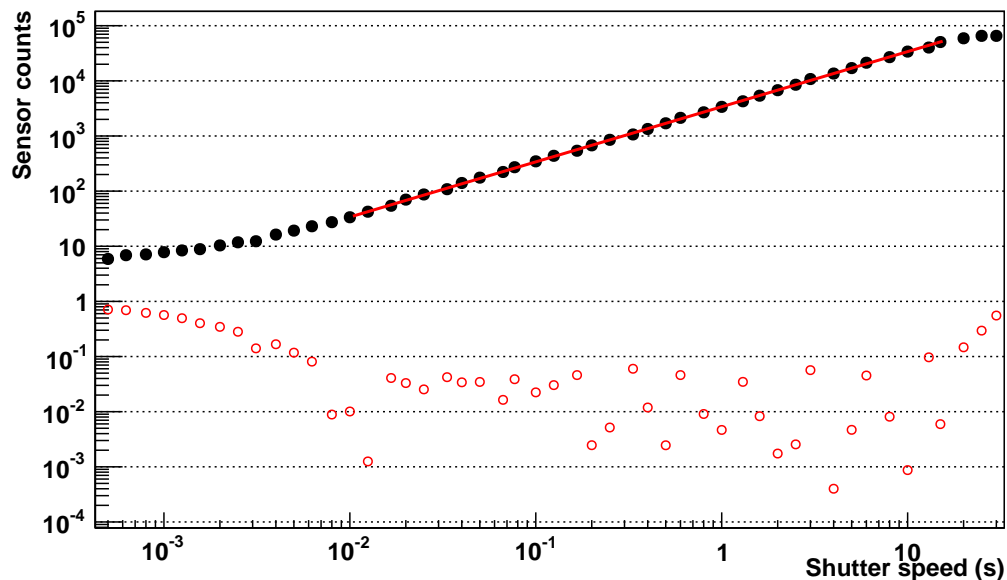


Figure B.1.: Calibration data for the Nikon D90 sensor: except for sensor noise at very low light levels and saturation towards  $2^{16}$ , the sensor response is proportional to the amount of input light from 25 to 55000 counts, i.e. over 11.1 bits. The red line is a fit of the function  $a \cdot x$  to the data, with  $a = 3391 \pm 42$ , the red circles are the absolute values of the relative residuals.

The files were finally read with the script `tifffile.py`<sup>(5)</sup> by Ch. Gohlke<sup>(6)</sup>. The script returns a numpy array containing the image data, which can then be processed using standard numpy routines.

### B.3. Result

The excellent linearity of the sensor is shown in figure B.1. Except for non-linearities at very small sensor readings (probably due to sensor and readout noise) and sensor saturation effects at the upper end of the scale, it is linear over a range of more than 11 bits.

<sup>5</sup><http://www.lfd.uci.edu/~gohlke/code/tifffile.py.html>

<sup>6</sup>Christoph Gohlke, Laboratory for Fluorescence Dynamics, University of California, Irvine. <http://www.lfd.uci.edu/~gohlke/>



# Glossary

- G-APD (Geiger-mode Avalanche Photodiode)** A semiconductor light-sensor with high sensitivity and simple usage.
- ADC (Analog-digital converter)** An electronics component which translates an analog signal into a digital quantity. Its two central properties are its resolution (in bits) and sampling frequency (typically in MHz).
- APD (Avalanche Photodiode)** A semiconductor light sensor similar to G-APDs which is operated below the breakdown voltage. In this operation mode, the released charge is proportional to the number of incident photons.
- CT3 (Cherenkov Telescope 3)** The third telescope of the HEGRA experiment on La Palma, Spain. It has a mirror diameter of 3.9 m and a focal length of 5 m.
- CTA (Cherenkov Telescope Array)** An international project planning to build and operate over a hundred Cherenkov telescopes in parallel. It is currently in its design phase [28].
- CU (Crab unit)** The standard unit for the flux of a source in the VHE gamma range. One CU is the flux necessary to observe a statistical significance identical to an observation of the Crab nebula under the same conditions for the same duration. The drawback of this unit is the fact that sources with a different energy spectrum might need more or fewer photons for the same significance, making the unit only an indirect indicator for the photon flux of a source.
- ENF (Excess Noise Factor)** A measure for the combined effect of multiple noise sources in a low-level light sensor. The ENF is by definition larger than 1, for a perfect (noise-free) detector it would be 1.
- FACT (First G-APD Cherenkov Telescope)** A project aiming to investigate the feasibility of using G-APDs in IACT telescopes. This thesis was written as part of the FACT project.
- FOV (field of view)** The size of the fraction of the sky that can be observed with the telescope. Since IACTs observe the atmosphere and not directly the firmament, there is often a differentiation between the camera FOV (the part of the atmosphere which can be observed by the telescope, mainly defined by the size of the camera and the geometry of the telescope) and an effective FOV (the size of the firmament where the showers can be assigned to in the analysis). The two are connected, but not identical.
- Geiger-mode multi pixel photon device** The most accurate term for G-APDs. It includes both of the most important properties of the devices: the pixelisation of the sensitive surface into single cells, each of which is operated in Geiger-mode.

**H.E.S.S. (High Energy Stereoscopic System)** The H.E.S.S. telescopes are a set of four telescopes with a diameter of 12 m each in Namibia. In July 2012, the four telescopes were complemented with a central telescope with a mirror diameter of 28 m, the largest Cherenkov telescope ever.

**HEGRA (High Energy Gamma-Ray Astronomy)** The HEGRA experiment was an array of six Cherenkov telescopes on La Palma, Spain, which started operation in 1992. In 2002, the experiment was replaced by the MAGIC telescope.

**IACT (Imaging Atmospheric Cherenkov Telescope)** is a telescope detecting and measuring the impact of high energy particles on the Earth's atmosphere. The same abbreviation is used to denote the technique of the measurements.

**IC (Inverse Compton)** Scattering of a photon and a highly relativistic electron, in which energy is transferred from the electron to the photon.

**jet** A stream of particles, which is emitted by an object in a constrained angular direction. Even for astronomical scales their length can be huge, as an example the jet of the galaxy M87, which is about 6000 light years long [45]. See e.g. E. M. de Gouveia Dal Pino [46] for more information on jets.

**LED (Light Emitting Diode)** .

**MAGIC (Major Atmospheric Gamma-Ray Imaging Cherenkov)** The MAGIC telescopes are two IACTs with 17 m diameter each on La Palma, Spain. MAGIC has currently the lowest energy threshold of all Cherenkov telescopes (around 30 GeV), and had until the inauguration of the H.E.S.S. II telescope in July 2012 the largest telescopes in operation.

**MC (Monte Carlo)** A type of (computer) simulation, where the outcome of single processes is only stochastically known. For the simulations a reliable random number generator is necessary.

**MPPC (Multi-Pixel Photon Counter)** Brand name of the G-APDs produced by Hamamatsu.

**NIM (Nuclear Instrumentation Module)** The NIM standard defines an interface for a wide range of electronics modules used for the processing of analog and digital signals.

**NSB (night sky background)** The abbreviation "NSB" is used to differentiate between photons from air showers, and photons coming from other light sources of the night sky, such as starlight, airglow, moon light, or artificial light.

**ORM (Observatorio del Roque de los Muchachos)** Observatory on the Roque de los Muchachos with more than 10 telescopes on the Canary Island of La Palma (Spain); location of both MAGIC and FACT.

**PDE (Photon Detection Efficiency)** The probability that a single photon impinging on a photosensor produces a signal.

**PMT (Photomultiplier Tube)** A light sensor working on the principle of a staged electron multiplication on multiple dynodes in an electrical field.

**PSF (Point Spread Function)** The PSF describes the light distribution of a pointlike light source after an optical system (e.g. a telescope mirror dish), i.e. how a small bright object is “smeared out”. Typically the standard deviations of one-dimensional projections are used as a quantification, or the radius of a circle containing 68% of the total light.

**PSI (Paul Scherrer Institute)** Research institute in Villigen, Switzerland.

**ROI (Region of Interest)** .

**SiPM (Silicon Photomultiplier)** Alternative name for G-APDs based on the similar applications of G-APDs and PMTs.

**SMD (Surface Mount Device)** Electronic component which can be mounted at the surface of the circuit boards. In the case of G-APDs, the chip is delivered without a packaging.

**SSC (Synchrotron Self-Compton)** A model for the production of high energy photons: highly relativistic leptons emit photons at low energies, which are then pushed to higher energies by Inverse Compton scattering.

**VERITAS (Very Energetic Radiation Imaging Telescope Array System)** VERITAS is an array of four Cherenkov telescopes in southern Arizona, USA.

**VHE (Very High Energy)** VHE photons have an energy above 30 GeV.



# List of Figures

1.1. Cross section of the interaction of photons with matter . . . . .	3
1.2. Comparison of air showers initiated by photons and hadrons . . . . .	4
1.3. Simulated Cherenkov spectrum on ground . . . . .	4
1.4. Illustration of pile-up . . . . .	7
1.5. Hubble image of the galaxy M87 . . . . .	10
1.6. Location of the major IACTs . . . . .	11
1.7. Early CAD drawings for the FACT project . . . . .	13
1.8. Comparison of pixels for the prototype module M0 and the final FACT camera	13
1.9. The FACT telescope during its first operation . . . . .	14
2.1. Schematic drawing of a PMT . . . . .	19
2.2. Avalanche development below and above the breakdown voltage . . . . .	20
2.3. Layer structure of a G-APD . . . . .	21
2.4. Plot PDE vs. over-voltage . . . . .	23
2.5. Quantum efficiency of a PMT and PDE of a G-APD . . . . .	23
2.6. Equivalent circuit of a G-APD . . . . .	25
2.7. Dead time and recovery time of a G-APD . . . . .	25
2.8. Measurement of G-APD afterpulses . . . . .	27
2.9. Geometry measurements . . . . .	28
2.10. Surface profiles . . . . .	29
2.11. Example dark counts spectrum . . . . .	30
2.12. Gain vs. over-voltage . . . . .	31
2.13. Crosstalk probability vs. over-voltage . . . . .	31
2.14. Average number of crosstalk cells vs. crosstalk probability . . . . .	32
2.15. Charge variations . . . . .	33
2.16. Dependence of charge variations on the over-voltage . . . . .	34
2.17. Setup for the angle dependence measurement . . . . .	35
2.18. Example Poisson spectrum . . . . .	36
2.19. Preparations for the angle dependence measurement . . . . .	37
2.20. Plot of the PDE angle dependence . . . . .	38
2.21. Plot of the angle dependence with geometric correction . . . . .	39
2.22. Notation used for the calculations . . . . .	40
2.23. Effect of saturation and different crosstalk probabilities . . . . .	41
2.24. Overview on the voltage dependencies . . . . .	42
2.25. Combined signal dependency on the over-voltage . . . . .	42
2.26. Variations due to statistical saturation . . . . .	45
2.27. Variations in the reconstructed number of photons due to statistical saturation	45
2.28. Comparison of the simulation to the measurement of crosstalk parameters .	49
2.29. Variations from the statistical saturation: simulation and calculation . . . .	49
2.30. ENF for different contributions of avalanche fluctuations and crosstalk prob- abilities . . . . .	50

2.31. ENF in dependence of the over-voltage . . . . .	52
2.32. G-APD type selected for FACT . . . . .	54
3.1. Pixel layouts for the prototype module M0 . . . . .	56
3.2. Photo of the sensors and electronics of the prototype module M0 . . . . .	57
3.3. Photos of the finished prototype module . . . . .	57
3.4. Components of the light-concentrating cones . . . . .	58
3.5. Assembled cone for M0 . . . . .	58
3.6. G-APD grid and carrier boards . . . . .	59
3.7. M0 PMMA front window . . . . .	61
3.8. Setup of the module M0 on the roof . . . . .	62
3.9. Example of a shower recorded with M0 . . . . .	62
3.10. Rate vs. threshold scan with the prototype module M0 . . . . .	63
3.11. Stability of the light pulses with feedback system . . . . .	64
3.12. Illustrations of the FACT camera . . . . .	66
3.13. Spectra and sensitivities . . . . .	70
3.14. Additive spectra of Cherenkov light, moonlight and NSB light . . . . .	72
3.15. Angle dependence of light collecting cones . . . . .	74
3.16. Arrangement of rectangular pixels in a hexagonal array . . . . .	74
3.17. Geometry of the final cones for FACT . . . . .	75
3.18. Light-absorbing grid: epoxy-coated cardboard . . . . .	77
3.19. Light-absorbing grid: paper . . . . .	77
3.20. Surface problems with cone prototypes . . . . .	78
3.21. Rim at the edge of the cone's exit window . . . . .	79
3.22. Transmission of two cone prototypes . . . . .	80
3.23. Setup for the laser measurements of the cones . . . . .	81
3.24. Illustration of the laser measurements . . . . .	81
3.25. Analysis of the laser measurements . . . . .	83
3.26. Overview on one measurement series . . . . .	84
3.27. Processing of the reflection images . . . . .	84
3.28. Overview on the reflection measurements of one cone . . . . .	85
3.29. Comparison of the reflection spots of three prototype cones . . . . .	86
3.30. Setup for the batch UV transmission measurement . . . . .	87
3.31. Example of cones in the batch UV transmission setup . . . . .	88
3.32. Spectral transmission of all measured cones . . . . .	88
3.33. Bubble visibility with scattered laser light . . . . .	89
3.34. Illustration of the sensor compartment . . . . .	90
3.35. G-APD with glued light-collecting cone . . . . .	91
3.36. Cone gluing tools . . . . .	92
3.37. Front view onto the gluing joint . . . . .	94
3.38. Bubble types . . . . .	95
3.39. Glue preparation . . . . .	95
3.40. Cones under polarized light . . . . .	96
3.41. Setup for the load tests . . . . .	97
3.42. Broken gluing joint . . . . .	97
3.43. Photos of the test patches . . . . .	99
3.44. Bias voltages of the test patches . . . . .	99
3.45. Pixel categorization . . . . .	101
3.46. G-APD operation voltages . . . . .	102

## List of Figures

---

3.47. Operation voltage groups . . . . .	103
3.48. Window gluing tools . . . . .	104
3.49. Cleaning method comparison . . . . .	105
3.50. Stability measurement of the window gluing . . . . .	106
3.51. Result of the window gluing stability test . . . . .	107
3.52. Capillary action between cones . . . . .	107
3.53. Finished front window . . . . .	109
3.54. Cable soldering . . . . .	110
3.55. Baffle plate installation . . . . .	110
3.56. Pixel repairs . . . . .	111
3.57. Front view before the repairs . . . . .	113
3.58. Pixel repairs: syringe . . . . .	113
3.59. Broken pixel before and after the repair . . . . .	114
3.60. High resolution image of the front window: rear view . . . . .	115
3.61. High resolution image of the front window: front view . . . . .	116
3.62. Grouping of the pixels into patches . . . . .	118
3.63. Electronics: front-end schematic . . . . .	119
3.64. Temporal structure of light pulser events . . . . .	122
4.1. DRS charge calibration . . . . .	128
4.2. G-APD sample signals . . . . .	128
4.3. First spectrum of the FACT G-APDs . . . . .	130
4.4. Relative PDE measurement: pulse size . . . . .	131
4.5. Relative PDE: gain distribution . . . . .	132
4.6. Distribution of the relative PDEs . . . . .	133
4.7. Estimate of the light distribution . . . . .	133
4.8. Installed FACT camera . . . . .	135
4.9. First operation of the FACT telescope . . . . .	136
4.10. Example showers from the first observation night . . . . .	137
4.11. Standard rate scan of air showers and background light . . . . .	138
4.12. Electronics rate scan . . . . .	139
4.13. Electronic ringing . . . . .	139
4.14. Single pixel rate scan . . . . .	140
4.15. Image of the moon in the FACT camera . . . . .	142
4.16. Currents and bias voltage settings for the crab occultation measurement . . . . .	142
4.17. Gain distribution over the camera . . . . .	144
4.18. Improved G-APD spectrum . . . . .	145
4.19. Extracted calibration information from data runs . . . . .	147
4.20. Setup for the PSF measurement . . . . .	148
4.21. PSF measurement results for Betelgeuse and Procyon . . . . .	150
4.22. Detection plot for the Crab nebula . . . . .	151
A.1. Background rate vs. threshold for constant accidental rates . . . . .	164
B.1. Calibration data for the Nikon D90 sensor . . . . .	173

# List of Tables

2.1.	PDE angle dependence measurement . . . . .	38
2.2.	Main parameters of Hamamatsu G-APDs . . . . .	53
3.1.	Corresponding photon rates for the SQM . . . . .	68
3.2.	Cone transmission measurements . . . . .	83
3.3.	Overview on the pixels . . . . .	100
3.4.	Pixels with broken cone-G-APD gluing . . . . .	112
4.1.	List of broken pixels . . . . .	147



## References

- [1] B. L. Waerden. *Science awakening II: The birth of astronomy*. Springer, 1974.
- [2] W. Herschel. Investigation of the Powers of the Prismatic Colours to Heat and Illuminate Objects; With Remarks, That Prove the Different Refrangibility of Radiant Heat. To Which is Added, an Inquiry into the Method of Viewing the Sun Advantageously, with Telescopes of Large Apertures and High Magnifying Powers. *Philosophical Transactions of the Royal Society of London*, 90:255–283, 1800. ISSN 02610523. URL <http://www.jstor.org/stable/107056>.
- [3] W. Herschel. Experiments on the Refrangibility of the Invisible Rays of the Sun. *Philosophical Transactions of the Royal Society of London*, 90:284–292, 1800. ISSN 02610523. URL <http://www.jstor.org/stable/107057>.
- [4] J. W. Ritter. Auszüge aus Briefen an den Herausgeber. *Ann. Phys.*, 7(4):527, 1801. ISSN 1521-3889. URL <http://dx.doi.org/10.1002/andp.18010070407>.
- [5] J. W. Ritter. Versuche über das Sonnenlicht. *Ann. Phys.*, 12(12):409–415, 1803. ISSN 1521-3889. URL <http://dx.doi.org/10.1002/andp.18030121205>.
- [6] K. Jansky. Directional Studies of Atmospherics at High Frequencies. *Proceedings of the Institute of Radio Engineers*, 20(12):1920–1932, December 1932. ISSN 0731-5996. doi: 10.1109/JRPROC.1932.227477.
- [7] K. Jansky. Electrical Disturbances Apparently of Extraterrestrial Origin. *Proceedings of the Institute of Radio Engineers*, 21(10):1387–1398, October 1933. ISSN 0731-5996. doi: 10.1109/JRPROC.1933.227458.
- [8] T. C. Weekes *et al.* Observation of TeV gamma rays from the Crab nebula using the atmospheric Cerenkov imaging technique. *Astrophysical Journal*, 342:379–395, July 1989. doi: 10.1086/167599.
- [9] B. Stappers *et al.* Observing pulsars and fast transients with LOFAR. *arXiv*, 1104.1577, 2011.
- [10] W. B. Atwood *et al.* The Large Area Telescope on the Fermi Gamma-Ray Space Telescope Mission. *The Astrophysical Journal*, 697(2):1071, 2009. URL <http://stacks.iop.org/0004-637X/697/i=2/a=1071>.
- [11] J. Beringer *et al.* Review of Particle Physics. *Phys. Rev. D*, 86:010001, July 2012. doi: 10.1103/PhysRevD.86.010001. URL <http://link.aps.org/doi/10.1103/PhysRevD.86.010001>.
- [12] M. Rao and B. Sreekantan. *Extensive air showers*. World Scientific Pub. Co. Inc., 1998.

- 
- [13] D. Heck. *CORSIKA: A Monte Carlo code to simulate extensive air showers*, volume 6019. FZKA, 1998.
- [14] F. Schmidt. CORSIKA Shower Images, June 2012. URL <http://www.ast.leeds.ac.uk/~fs/showerimages.html>.
- [15] P. A. Cherenkov. Visible emission of clean liquids by action of  $\gamma$  radiation. *Dokl. Akad. Nauk SSSR*, 2:451, 1934.
- [16] K. Bernlöhner. Impact of atmospheric parameters on the atmospheric Cherenkov technique. *Astroparticle Physics*, 12(4):255–268, 2000. ISSN 0927-6505. doi: 10.1016/S0927-6505(99)00093-6. URL <http://www.sciencedirect.com/science/article/pii/S0927650599000936>.
- [17] S. Preuss, G. Hermann, W. Hofmann and A. Kohnle. Study of the photon flux from the night sky at La Palma and Namibia, in the wavelength region relevant for imaging atmospheric Cherenkov telescopes. *Nuclear Instruments and Methods in Physics Research Section A*, 481(1-3):229–240, 2002. ISSN 0168-9002. doi: 10.1016/S0168-9002(01)01264-5. URL <http://www.sciencedirect.com/science/article/pii/S0168900201012645>.
- [18] B. Henke, E. Gullikson and J. Davis. X-Ray Interactions: Photoabsorption, Scattering, Transmission, and Reflection at  $E = 50\text{--}30,000$  eV,  $Z = 1\text{--}92$ . *Atomic Data and Nuclear Data Tables*, 54(2):181–342, 1993. ISSN 0092-640X. doi: 10.1006/adnd.1993.1013. URL <http://www.sciencedirect.com/science/article/pii/S0092640X83710132>.
- [19] A. Thompson *et al.* X-ray Data Booklet, Lawrence Berkley National Laboratory, University of California, Berkley, CA 94720, 2009.
- [20] C. Benn and S. Ellison. Brightness of the night sky over La Palma. *New Astronomy Reviews*, 42(6-8):503–507, 1998. ISSN 1387-6473. doi: 10.1016/S1387-6473(98)00062-1. URL <http://www.sciencedirect.com/science/article/pii/S1387647398000621>.
- [21] Ley 31/1988, de 31 de octubre, sobre Protección de la Calidad Astronómica de los Observatorios del Instituto de Astrofísica de Canarias. *Boletín Oficial del Estado*, 264:31451, November 1988. URL <http://www.boe.es/boe/dias/1988/11/03/pdfs/A31451-31451.pdf>.
- [22] W. R. Pendleton Jr., D. J. Baker, R. J. Reese and R. R. O’Neil. Decay of  $O_2(a^1\Delta_g)$  in the evening twilight airglow: Implications for the radiative lifetime. *Geophys. Res. Lett.*, 23(9):1013–1016, 1996. ISSN 0094-8276. URL <http://dx.doi.org/10.1029/96GL00946>.
- [23] S. Miller and R. Turner. A Dynamic Lunar Spectral Irradiance Data Set for NPOESS/VIIRS Day/Night Band Nighttime Environmental Applications. *IEEE Transactions on Geoscience and Remote Sensing*, 47(7):2316–2329, 2009. ISSN 0196-2892. doi: 10.1109/TGRS.2009.2012696.
- [24] S. J. Lawrence *et al.* A New Measurement of the Absolute Spectral Reflectance of the Moon. In S. Mackwell and E. Stansbery, editors, *Lunar and Planetary Institute Science Conference Abstracts*, volume 34 of *Lunar and Planetary Inst. Technical Report*, page 1269, March 2003.



- 
- [25] Y. Shkuratov *et al.* Optical measurements of the Moon as a tool to study its surface. *Planetary and Space Science*, 59(13):1326–1371, 2011. ISSN 0032-0633. doi: 10.1016/j.pss.2011.06.011. URL <http://www.sciencedirect.com/science/article/pii/S0032063311001954>.
- [26] A. Schliesser and R. Mirzoyan. Wide-field prime-focus imaging atmospheric Cherenkov telescopes: A systematic study. *Astroparticle Physics*, 24(4-5):382–390, 2005. ISSN 0927-6505. doi: 10.1016/j.astropartphys.2005.08.003. URL <http://www.sciencedirect.com/science/article/pii/S0927650505001209>.
- [27] J. M. Davies and E. S. Cotton. Design of the quartermaster solar furnace. *Solar Energy*, 1(2-3):16–22, 1957. ISSN 0038-092X. doi: 10.1016/0038-092X(57)90116-0. URL <http://www.sciencedirect.com/science/article/pii/0038092X57901160>.
- [28] M. Actis *et al.* Design concepts for the Cherenkov Telescope Array CTA: an advanced facility for ground-based high-energy gamma-ray astronomy. *Experimental Astronomy*, 32:193–316, December 2011. doi: 10.1007/s10686-011-9247-0.
- [29] D. Petry. Faster background determination—a method for gaining time coverage and flux measurement accuracy with Cherenkov telescopes. *Astroparticle Physics*, 20(1):45–52, 2003. ISSN 0927-6505. doi: 10.1016/S0927-6505(03)00139-7. URL <http://www.sciencedirect.com/science/article/pii/S0927650503001397>.
- [30] A. M. Hillas. Cherenkov light images of EAS produced by primary gamma. In F. C. Jones, editor, *International Cosmic Ray Conference*, volume 3 of *International Cosmic Ray Conference*, pages 445–448, August 1985.
- [31] R. Bock *et al.* Methods for multidimensional event classification: a case study using images from a Cherenkov gamma-ray telescope. *Nuclear Instruments and Methods in Physics Research Section A*, 516(2-3):511–528, 2004. ISSN 0168-9002. doi: 10.1016/j.nima.2003.08.157. URL <http://www.sciencedirect.com/science/article/pii/S0168900203025051>.
- [32] V. Dhar *et al.* ANN-based energy reconstruction procedure for TACTIC gamma-ray telescope and its comparison with other conventional methods. *Nuclear Instruments and Methods in Physics Research Section A*, 606(3):795–805, 2009. ISSN 0168-9002. doi: 10.1016/j.nima.2009.04.012. URL <http://www.sciencedirect.com/science/article/pii/S0168900209007906>.
- [33] J. Albert *et al.* Implementation of the Random Forest method for the Imaging Atmospheric Cherenkov Telescope MAGIC. *Nuclear Instruments and Methods in Physics Research Section A*, 588(3):424–432, April 2008. URL <http://www.sciencedirect.com/science/article/B6TJM-4RBYCX8-6/2/b7921b3c058159b58d58e569c6b6379e>.
- [34] T.-P. Li and Y.-Q. Ma. Analysis methods for results in gamma-ray astronomy. *The Astrophysical Journal*, 272:317–324, September 1983. doi: 10.1086/161295.
- [35] S. Klepser. A generalized likelihood ratio test statistic for Cherenkov telescope data. *Astroparticle Physics*, 36(1):64–76, 2012. ISSN 0927-6505. doi: 10.1016/j.astropartphys.2012.04.008. URL <http://www.sciencedirect.com/science/article/pii/S0927650512000916>.

- [36] J. Albert *et al.* VHE Gamma-Ray Observation of the Crab Nebula and its Pulsar with the MAGIC Telescope. *The Astrophysical Journal*, 674(2):1037, 2008. URL <http://stacks.iop.org/0004-637X/674/i=2/a=1037>.
- [37] Y. Becherini, A. Djannati-Atai, V. Marandon, M. Punch and S. Pita. A new analysis strategy for detection of faint gamma-ray sources with Imaging Atmospheric Cherenkov Telescopes. *Astroparticle Physics*, 34(12):858–870, 2011. ISSN 0927-6505. doi: 10.1016/j.astropartphys.2011.03.005. URL <http://www.sciencedirect.com/science/article/pii/S0927650511000673>.
- [38] F. Aharonian *et al.* An Exceptional Very High Energy Gamma-Ray Flare of PKS 2155-304. *The Astrophysical Journal Letters*, 664(2):L71, 2007. URL <http://stacks.iop.org/1538-4357/664/i=2/a=L71>.
- [39] J. Albert *et al.* Variable Very High Energy Gamma-Ray Emission from Markarian 501. *The Astrophysical Journal*, 669(2):862, 2007. URL <http://stacks.iop.org/0004-637X/669/i=2/a=862>.
- [40] F. Aharonian *et al.* Fast Variability of Tera-Electron Volt Gamma Rays from the Radio Galaxy M87. *Science*, 314(5804):1424–1427, 2006. doi: 10.1126/science.1134408. URL <http://www.sciencemag.org/content/314/5804/1424.abstract>.
- [41] J. Albert *et al.* Observations of Markarian 421 with the MAGIC Telescope. *The Astrophysical Journal*, 663(1):125, 2007. URL <http://stacks.iop.org/0004-637X/663/i=1/a=125>.
- [42] J. Albert *et al.* Periodic Very High Energy Gamma-Ray Emission from LS I +61°303 Observed with the MAGIC Telescope. *The Astrophysical Journal*, 693(1):303, 2009. URL <http://stacks.iop.org/0004-637X/693/i=1/a=303>.
- [43] J. Albert *et al.* Detection of Very High Energy Radiation from the BL Lacertae Object PG 1553+113 with the MAGIC Telescope. *The Astrophysical Journal Letters*, 654(2):L119, 2007. URL <http://stacks.iop.org/1538-4357/654/i=2/a=L119>.
- [44] C. Tadhunter. An introduction to active galactic nuclei: Classification and unification. *New Astronomy Reviews*, 52(6):227–239, 2008. ISSN 1387-6473. doi: 10.1016/j.newar.2008.06.004. URL <http://www.sciencedirect.com/science/article/pii/S1387647308001012>.
- [45] E. Perlman, J. Biretta, W. Sparks, F. Macchetto and J. Leahy. The synchrotron spectrum of the M87 jet. *New Astronomy Reviews*, 46(2-7):399–403, 2002. ISSN 1387-6473. doi: 10.1016/S1387-6473(02)00150-1. URL <http://www.sciencedirect.com/science/article/pii/S1387647302001501>.
- [46] E. M. de Gouveia Dal Pino. Astrophysical jets and outflows. *Advances in Space Research*, 35(5):908–924, 2005. ISSN 0273-1177. doi: 10.1016/j.asr.2005.03.145. URL <http://www.sciencedirect.com/science/article/pii/S0273117705004916>.
- [47] A. Djannati-Atai. Status of very high energy gamma-ray Astronomy as of early 2008. *Nuclear Instruments and Methods in Physics Research Section A*, 602(1):28–33, 2009. ISSN 0168-9002. doi: 10.1016/j.nima.2008.12.014. URL <http://www.sciencedirect.com/science/article/pii/S0168900208018202>.

- [48] J. Hinton. Ground-based gamma-ray astronomy with Cherenkov telescopes. *New Journal of Physics*, 11(5):055005, 2009. URL <http://stacks.iop.org/1367-2630/11/i=5/a=055005>.
- [49] *NASA and The Hubble Heritage Team (STScI/AURA)*, 2013. URL <http://hubblesite.org/gallery/album/pr2000020a>.
- [50] F. Tavecchio, L. Maraschi and G. Ghisellini. Constraints on the Physical Parameters of TeV Blazars. *The Astrophysical Journal*, 509(2):608, 1998. URL <http://stacks.iop.org/0004-637X/509/i=2/a=608>.
- [51] C. Urry. Multiwavelength properties of blazars. *Astroparticle Physics*, 11(1-2):159–167, 1999. ISSN 0927-6505. doi: 10.1016/S0927-6505(99)00043-2. URL <http://www.sciencedirect.com/science/article/pii/S0927650599000432>.
- [52] A. E. Wehrle. Multiwavelength observations of GeV blazars. *Astroparticle Physics*, 11(1-2):169–176, 1999. ISSN 0927-6505. doi: 10.1016/S0927-6505(99)00044-4. URL <http://www.sciencedirect.com/science/article/pii/S0927650599000444>.
- [53] A. A. Abdo *et al.* Gamma-Ray Flares from the Crab Nebula. *Science*, 331(6018):739–742, 2011. doi: 10.1126/science.1199705. URL <http://www.sciencemag.org/content/331/6018/739.abstract>.
- [54] T. C. Weekes. Very high energy gamma-ray astronomy. *Physics Reports*, 160(1-2):1–121, 1988. ISSN 0370-1573. doi: 10.1016/0370-1573(88)90177-9. URL <http://www.sciencedirect.com/science/article/pii/0370157388901779>.
- [55] M. Catanese and T. Weekes. Very High Energy Gamma-Ray Astronomy. *Publications of the Astronomical Society of the Pacific*, 111(764):pp. 1193–1222, 1999. ISSN 00046280. URL <http://www.jstor.org/stable/10.1086/316435>.
- [56] T. Weekes. *Very High Energy Gamma-Ray Astronomy*. Institute of Physics Pub., 2003.
- [57] R. A. Ong. Very high-energy gamma-ray astronomy. *Physics Reports*, 305(3-4):93–202, 1998. ISSN 0370-1573. doi: 10.1016/S0370-1573(98)00026-X. URL <http://www.sciencedirect.com/science/article/pii/S037015739800026X>.
- [58] M. Rissi. Detection of pulsed very high energy Gamma-rays from the Crab Pulsar with the MAGIC telescope using an analog sum trigger. *PhD thesis*, 2009. doi: 10.3929/ethz-a-005901896.
- [59] World map based on: *The World Factbook: Reference Maps*. Washington, DC: Central Intelligence Agency, 2013. URL <https://www.cia.gov/library/publications/the-world-factbook/docs/refmaps.html>.  
VERITAS: *UCLA Department of Physics and Astronomy* webpage, 2005. URL <http://www.physics.ucla.edu/astroparticle/img/veritasCrop.jpg>.  
H.E.S.S. II telescope: *H.E.S.S. Collaboration, Stefan Schwarzburg*, 2012. URL [http://www.mpi-hd.mpg.de/hfm/HESS/pages/press/2012/HESS\\_II\\_first\\_light/](http://www.mpi-hd.mpg.de/hfm/HESS/pages/press/2012/HESS_II_first_light/).  
Other H.E.S.S. telescopes: *H.E.S.S. collaboration*, 2006. Found via *Institut national de physique nucléaire et de physique des particules*, France. URL [http://www.in2p3.fr/presentation/thematiques/astroparticules\\_neutrinos/media/hess\\_telescope\\_grand.jpg](http://www.in2p3.fr/presentation/thematiques/astroparticules_neutrinos/media/hess_telescope_grand.jpg).

- MAGIC telescopes: *T. Krähenbühl*, January 2011. FACT: *T. Krähenbühl*, October 2011.
- [60] K. Nakamura, Y. Hamana, Y. Ishigami and T. Matsui. Latest bialkali photocathode with ultra high sensitivity. *Nuclear Instruments and Methods in Physics Research Section A*, 623(1):276–278, 2010. ISSN 0168-9002. doi: 10.1016/j.nima.2010.02.220. URL <http://www.sciencedirect.com/science/article/pii/S016890021000505X>.
- [61] C. Hsu *et al.* PMT characterization for the MAGIC-II telescope. *Nuclear Instruments and Methods in Physics Research Section A*, 610(1):267–270, 2009. ISSN 0168-9002. doi: 10.1016/j.nima.2009.05.175. URL <http://www.sciencedirect.com/science/article/pii/S0168900209010961>.
- [62] D. Renker. New developments on photosensors for particle physics. *Nuclear Instruments and Methods in Physics Research Section A*, 598(1):207–212, 2009. ISSN 0168-9002. doi: DOI:10.1016/j.nima.2008.08.023. URL <http://www.sciencedirect.com/science/article/B6TJM-4T72WP2-J/2/953019d161f1767141ba7d53ed843979>.
- [63] A. Biland *et al.* First detection of air shower Cherenkov light by Geigermode-Avalanche Photodiodes. *Nuclear Instruments and Methods in Physics Research Section A*, 595(1):165–168, 2008. ISSN 0168-9002. doi: 10.1016/j.nima.2008.07.097. URL <http://www.sciencedirect.com/science/article/pii/S0168900208009662>.
- [64] *MPPC - Multi-Pixel Photon Counter (Product Specifications)*. Hamamatsu Photonics K.K., Japan, November 2009. URL [http://www.hamamatsu.com/resources/pdf/ssd/s10362-33\\_series\\_kapd1023e05.pdf](http://www.hamamatsu.com/resources/pdf/ssd/s10362-33_series_kapd1023e05.pdf).
- [65] H. Anderhub *et al.* A novel camera type for very high energy gamma-ray astronomy based on Geiger-mode avalanche photodiodes. *Journal of Instrumentation*, 4(10):P10010, 2009. URL <http://stacks.iop.org/1748-0221/4/i=10/a=P10010>.
- [66] T. Bretz *et al.* FACT - The first G-APD Cherenkov telescope (first results). *AIP Conference Proceedings*, 1505(1):773–776, 2012. doi: 10.1063/1.4772374. URL <http://link.aip.org/link/?APC/1505/773/1>.
- [67] T. Krähenbühl. G-APD arrays and their use in axial PET modules. *Eidgenössische Technische Hochschule Zürich, Institute for Particle Physics*, 2008. doi: 10.3929/ethz-a-007636145. URL <http://e-collection.library.ethz.ch/view/eth:6706>.
- [68] A. Einstein. Über einen die Erzeugung und Verwandlung des Lichtes betreffenden heuristischen Gesichtspunkt. *Annalen der Physik*, 322:132–148, 1905. doi: 10.1002/andp.19053220607.
- [69] S.-O. Flyckt and C. Marmonier. *Photomultiplier tubes: Principles and applications*. Photonis, Brive, France, 2002.
- [70] T. Hakamata *et al.* *Photomultiplier Tubes—Basics and Applications*. Hamamatsu Photonics K.K. Electron Tube Division, 2006.

- 
- [71] D. E. Groom. Silicon photodiode detection of bismuth germanate scintillation light. *Nuclear Instruments and Methods in Physics Research*, 219(1):141–148, 1984. ISSN 0167-5087. doi: 10.1016/0167-5087(84)90146-7. URL <http://www.sciencedirect.com/science/article/pii/0167508784901467>.
- [72] J. C. Nirschl. Photodiode scintillation detector for radiac instrumentation. *Nuclear Instruments and Methods in Physics Research Section A*, 226(2-3):487–495, 1984. ISSN 0168-9002. doi: 10.1016/0168-9002(84)90069-X. URL <http://www.sciencedirect.com/science/article/pii/016890028490069X>.
- [73] K. Yamamoto, Y. Fujii, Y. Kotooka and T. Katayama. Highly stable silicon pin photodiode. *Nuclear Instruments and Methods in Physics Research Section A*, 253(3):542–547, 1987. ISSN 0168-9002. doi: 10.1016/0168-9002(87)90545-6. URL <http://www.sciencedirect.com/science/article/pii/0168900287905456>.
- [74] D. Renker and E. Lorenz. Advances in solid state photon detectors. *Journal of Instrumentation*, 4(04):P04004, 2009. URL <http://stacks.iop.org/1748-0221/4/i=04/a=P04004>.
- [75] W. Maes, K. D. Meyer and R. V. Overstraeten. Impact ionization in silicon: A review and update. *Solid-State Electronics*, 33(6):705–718, 1990. ISSN 0038-1101. doi: 10.1016/0038-1101(90)90183-F. URL <http://www.sciencedirect.com/science/article/pii/003811019090183F>.
- [76] R. McIntyre. A new look at impact ionization-Part I: A theory of gain, noise, breakdown probability, and frequency response. *IEEE Transactions on Electron Devices*, 46(8):1623–1631, August 1999. ISSN 0018-9383. doi: 10.1109/16.777150.
- [77] Z. Sadygov. Avalanche Detector. *Russian Agency for Patents and Trademarks*, Patent No. RU 2102820, 1998.
- [78] V. Golovin. Avalanche Photodetector. *Russian Agency for Patents and Trademarks*, Patent No. RU 2142175, 1998.
- [79] H. Oide, T. Murase, H. Otono and S. Yamashita. Studies on multiplication effect of noises of PPDs, and a proposal of a new structure to improve the performance. *Nuclear Instruments and Methods in Physics Research A*, 613:23–28, January 2010. doi: 10.1016/j.nima.2009.11.012.
- [80] M. A. Green and M. J. Keevers. Optical properties of intrinsic silicon at 300 K. *Progress in Photovoltaics: Research and Applications*, 3(3):189–192, 1995. ISSN 1099-159X. doi: 10.1002/pip.4670030303. URL <http://dx.doi.org/10.1002/pip.4670030303>.
- [81] R. McIntyre. On the avalanche initiation probability of avalanche diodes above the breakdown voltage. *IEEE Transactions on Electron Devices*, 20(7):637–641, July 1973. ISSN 0018-9383. doi: 10.1109/T-ED.1973.17715.
- [82] D. Orme, T. Nakaya, M. Yokoyama and A. Minamino. Measurement of PDE of MPPC with different wavelengths of light. *Proceedings of Science, PoS(PD09)019*, 2009.

- 
- [83] A. Vacheret *et al.* Characterization and simulation of the response of Multi-Pixel Photon Counters to low light levels. *Nuclear Instruments and Methods in Physics Research Section A*, 656(1):69–83, 2011. ISSN 0168-9002. doi: 10.1016/j.nima.2011.07.022. URL <http://www.sciencedirect.com/science/article/pii/S0168900211014513>.
- [84] D. Borla Tridon *et al.* Performance of the Camera of the MAGIC II Telescope. *arXiv*, 0906.5448, June 2009.
- [85] D. Renker. Private communication. 2008–2012.
- [86] H. Otono, H. Oide, S. Yamashita and T. Yoshioka. On the basic mechanism of Pixelized Photon Detectors. *Nuclear Instruments and Methods in Physics Research A*, 610:397–399, October 2009. doi: 10.1016/j.nima.2009.05.139.
- [87] F. Retière *et al.* Using MPPCs for T2K Fine Grain Detector. *Proceedings of PD07, PoS (PD07)*, 17, 2007.
- [88] H. Oide *et al.* Study of afterpulsing of MPPC with waveform analysis. *Proceedings of PD07, PoS (PD07)*, 8, 2007.
- [89] A. Lacaita, F. Zappa, S. Bigliardi and M. Manfredi. On the bremsstrahlung origin of hot-carrier-induced photons in silicon devices. *IEEE Transactions on Electron Devices*, 40(3):577–582, March 1993. ISSN 0018-9383. doi: 10.1109/16.199363.
- [90] A. N. Otte. On the efficiency of photon emission during electrical breakdown in silicon. *Nuclear Instruments and Methods in Physics Research Section A*, 610(1):105–109, 2009. ISSN 0168-9002. doi: 10.1016/j.nima.2009.05.085. URL <http://www.sciencedirect.com/science/article/pii/S0168900209010390>.
- [91] *WAVERUNNER Xi Series Oscilloscopes (Operator’s Manual)*. LeCroy Corporation, October 2008.
- [92] P. Beltrame *et al.* The AX-PET demonstrator - Design, construction and characterization. *Nuclear Instruments and Methods in Physics Research Section A*, 654(1):546–559, 2011. ISSN 0168-9002. doi: 10.1016/j.nima.2011.06.059. URL <http://www.sciencedirect.com/science/article/pii/S0168900211011831>.
- [93] M. Wojdyr. Fityk: a general-purpose peak fitting program. *Journal of Applied Crystallography*, 43:1126–1128, 2010. URL <http://fityk.nieto.pl/>.
- [94] P. Eckert, H.-C. Schultz-Coulon, W. Shen, R. Stamen and A. Tadday. Characterisation studies of silicon photomultipliers. *Nuclear Instruments and Methods in Physics Research Section A*, 620(2-3):217–226, 2010. ISSN 0168-9002. doi: 10.1016/j.nima.2010.03.169. URL <http://www.sciencedirect.com/science/article/pii/S0168900210008156>.
- [95] T. Krähenbühl *et al.* Geiger-mode avalanche photodiodes as photodetectors in Cherenkov astronomy. *Proceedings of Science, PoS(PD09)024*, 2009.
- [96] M. Metzger. Private communication. Hamamatsu Switzerland, June 2010.
- [97] A. Stoykov, Y. Musienko, A. Kuznetsov, S. Reucroft and J. Swain. On the limited amplitude resolution of multipixel Geiger-mode APDs. *Journal of Instrumentation*, 2(06):P06005, 2007. URL <http://stacks.iop.org/1748-0221/2/i=06/a=P06005>.

- 
- [98] A. Karar, Y. Musienko and J. Vanel. Characterization of avalanche photodiodes for calorimetry applications. *Nuclear Instruments and Methods in Physics Research Section A*, 428(2-3):413–431, 1999. ISSN 0168-9002. doi: 10.1016/S0168-9002(99)00177-1. URL <http://www.sciencedirect.com/science/article/pii/S0168900299001771>.
- [99] M. Teich, K. Matsuo and B. Saleh. Excess noise factors for conventional and superlattice avalanche photodiodes and photomultiplier tubes. *IEEE Journal of Quantum Electronics*, 22(8):1184–1193, August 1986. ISSN 0018-9197. doi: 10.1109/JQE.1986.1073137.
- [100] R. McIntyre. Multiplication noise in uniform avalanche diodes. *IEEE Transactions on Electron Devices*, 13(1):164–168, January 1966. ISSN 0018-9383. doi: 10.1109/T-ED.1966.15651.
- [101] K. Deiters *et al.* Investigation of the avalanche photodiodes for the CMS electromagnetic calorimeter operated at high gain. *Nuclear Instruments and Methods in Physics Research Section A*, 461(1-3):574–576, 2001. ISSN 0168-9002. doi: 10.1016/S0168-9002(00)01303-6. URL <http://www.sciencedirect.com/science/article/pii/S0168900200013036>.
- [102] M. Matsumoto and T. Nishimura. Mersenne twister: a 623-dimensionally equidistributed uniform pseudo-random number generator. *ACM Transactions on Modeling and Computer Simulation*, 8(1):3–30, January 1998. ISSN 1049-3301. doi: 10.1145/272991.272995. URL <http://doi.acm.org/10.1145/272991.272995>.
- [103] S. Vinogradov. Analytical models of probability distribution and excess noise factor of solid state photomultiplier signals with crosstalk. *Nuclear Instruments and Methods in Physics Research Section A*, 695(0):247–251, 2012. ISSN 0168-9002. doi: 10.1016/j.nima.2011.11.086. URL <http://www.sciencedirect.com/science/article/pii/S0168900211021565>.
- [104] M. Gaug. Calibration of the MAGIC Telescope and Observation of Gamma Ray Bursts. *PhD thesis*, 2006.
- [105] J. Flix. Observations of Gamma-rays from the Galactic Center with the MAGIC Telescope. *PhD thesis*, 2006.
- [106] *MPPC - Multi-Pixel Photon Counter (Technical Information)*. Hamamatsu Photonics K.K., Japan, May 2009. URL [http://www.hamamatsu.com/resources/pdf/ssd/mppc\\_techinfo\\_e.pdf](http://www.hamamatsu.com/resources/pdf/ssd/mppc_techinfo_e.pdf).
- [107] *Vikuiti Enhanced Specular Reflector (Data sheet)*. 3M Optical Systems, 2010.
- [108] I. Braun *et al.* Solid Light Concentrators for Cherenkov Astronomy. *Proceedings of the 31st ICRC in Łódź, Poland*, 1248, 2009. URL <http://icrc2009.uni.lodz.pl/proc/pdf/icrc1248.pdf>.
- [109] S. Ritt. The DRS2 chip: a 4.5 GHz waveform digitizing chip for the MEG experiment. In *Nuclear Science Symposium Conference Record*, volume 2, pages 974–976, October 2004. doi: 10.1109/NSSMIC.2004.1462369.

- 
- [110] Q. Weitzel *et al.* A Novel Camera Type for Very High Energy Gamma-Astronomy. *Proceedings of the 31st ICRC in Łódź, Poland*, 1074, 2009. URL <http://icrc2009.uni.lodz.pl/proc/pdf/icrc1074.pdf>.
- [111] P. Vogler. Development of a trigger system for a Cherenkov Telescope Camera based on Geiger-mode avalanche photodiodes. *Master thesis, ETH Zürich*, 2010. URL [http://ihp-1x2.ethz.ch/pub/dipl/Master\\_Vogler\\_Patrick.pdf](http://ihp-1x2.ethz.ch/pub/dipl/Master_Vogler_Patrick.pdf).
- [112] H. Anderhub *et al.* A G-APD based Camera for Imaging Atmospheric Cherenkov Telescopes. *Nuclear Instruments and Methods in Physics Research Section A*, 628(1):107–110, 2011. ISSN 0168-9002. doi: 10.1016/j.nima.2010.06.296. URL <http://www.sciencedirect.com/science/article/pii/S0168900210014865>.
- [113] T. Bretz and D. Dorner. MARS–The Cherenkov Observatory edition. *AIP Conference Proceedings*, 1085(1):664–667, 2008. doi: 10.1063/1.3076762. URL <http://link.aip.org/link/?APC/1085/664/1>.
- [114] T. Bretz *et al.* MARS - CheObs goes Monte Carlo. *Proceedings of the 31st ICRC in Łódź, Poland*, 1259, 2009. URL <http://icrc2009.uni.lodz.pl/proc/pdf/icrc1259.pdf>.
- [115] *Sky Quality Meter - L (Instruction Sheet)*. Unihedron, Canada, February 2008. URL [http://unihedron.com/projects/sqm-l/Instruction\\_sheet.pdf](http://unihedron.com/projects/sqm-l/Instruction_sheet.pdf).
- [116] ASTM Standard G173-03. *Reference Solar Spectral Irradiances: Direct Normal and Hemispherical on 37° Tilted Surface*. ASTM International, West Conshohocken, PA, 2003 (2012). doi: 10.1520/G0173-03R12. URL <http://www.astm.org>.
- [117] R. Winston. *Nonimaging Optics*. Elsevier Academic Press, 2004.
- [118] A. Okumura. Optimization of the collection efficiency of a hexagonal light collector using quadratic and cubic Bézier curves. *Astroparticle Physics*, 38(0):18–24, 2012. ISSN 0927-6505. doi: 10.1016/j.astropartphys.2012.08.008. URL <http://www.sciencedirect.com/science/article/pii/S0927650512001624>.
- [119] I. Braun. Private communication. 2009–2012.
- [120] B. Huber *et al.* Solid light concentrators for small-sized photosensors used in Cherenkov telescopes. *Proceedings of the 32nd ICRC in Beijing, China*, 136, 2011. doi: 10.7529/ICRC2011/V09/0136.
- [121] B. Huber. Contributions to High Energy and Very High Energy Gamma-Ray Astronomy. *PhD thesis*, 2012.
- [122] Evonik Industries (Germany). Private communication. 2009–2010. URL <http://www.evonik.com>.
- [123] *Product catalog "TL Blacklight Blue"*. Philips Electronics N.V., October 2012. URL <http://www.ecat.lighting.philips.com/1/tl-blacklight-blue/66039/cat/>.
- [124] *EPO-TEK 301 (Technical Data Sheet)*. Epoxy Technology Inc., March 2012. URL <http://www.epotek.com/sscdocs/datasheets/301.PDF>.
- [125] F. Retière. Private communication at the PD09 conference. 2009.



- 
- [126] H. Anderhub *et al.* Design and Operation of FACT – The First G-APD Cherenkov Telescope. 2013. URL <http://arxiv.org/pdf/1304.1710.pdf>.
- [127] S. Ritt. Design and performance of the 6 GHz waveform digitizing chip DRS4. In *Nuclear Science Symposium Conference Record*, pages 1512–1515, 2008. doi: 10.1109/NSSMIC.2008.4774700.
- [128] S. Ritt, R. Dinapoli and U. Hartmann. Application of the DRS chip for fast waveform digitizing. *Nuclear Instruments and Methods in Physics Research Section A*, 623(1): 486–488, 2010. ISSN 0168-9002. doi: 10.1016/j.nima.2010.03.045. URL <http://www.sciencedirect.com/science/article/pii/S0168900210006091>.
- [129] Web page of the DRS chip, accessed on June 07, 2013. URL <http://www.psi.ch/drs/history>.
- [130] D. Hanna, A. McCann, M. McCutcheon and L. Nikkinen. An LED-based flasher system for VERITAS. *Nuclear Instruments and Methods in Physics Research Section A*, 612(2):278–287, 2010. ISSN 0168-9002. doi: <http://dx.doi.org/10.1016/j.nima.2009.10.107>. URL <http://www.sciencedirect.com/science/article/pii/S0168900209020580>.
- [131] T. Krähenbühl *et al.* Calibrating the camera for the First G-APD Cherenkov Telescope (FACT). *Proceedings of the 32nd ICRC in Beijing, China*, 529, 2011. doi: 10.7529/ICRC2011/V09/0529.
- [132] N. Akchurin and H. Kim. A study on ion initiated photomultiplier afterpulses. *Nuclear Instruments and Methods in Physics Research Section A*, 574(1):121–126, April 2007. ISSN 0168-9002. doi: 10.1016/j.nima.2007.01.093. URL <http://www.sciencedirect.com/science/article/B6TJM-4MXJ3RK-1/2/2abacc7657308fb4dd58ea3e5f1003a1>.
- [133] M. Calvi *et al.* Aging and time resolution measurements for the Hamamatsu R7600 multi-anode photomultiplier tube. In *Nuclear Science Symposium and Medical Imaging Conference*, pages 1638–1641, 2011. doi: 10.1109/NSSMIC.2011.6154651.
- [134] S. Aiello *et al.* Aging characterization on large area photo-multipliers. *Nuclear Instruments and Methods in Physics Research Section A*, 725(1):151–154, October 2013. ISSN 0168-9002. doi: 10.1016/j.nima.2012.11.130. URL <http://www.sciencedirect.com/science/article/pii/S0168900212014775>.
- [135] F. Aharonian *et al.* Calibration of cameras of the H.E.S.S. detector. *Astroparticle Physics*, 22(2):109–125, 2004. ISSN 0927-6505. doi: DOI:10.1016/j.astropartphys.2004.06.006. URL <http://www.sciencedirect.com/science/article/B6TJ1-4D62YDC-1/2/2f28afd39a67cf979313af91b7afab39>.
- [136] T. Schweizer, E. Lorenz, M. Martinez, A. Ostankov and D. Paneque. The optical calibration of the MAGIC telescope camera. In *Nuclear Science Symposium Conference Record*, volume 1, pages 437–441, 2001. doi: 10.1109/NSSMIC.2001.1008494.
- [137] D. Hanna *et al.* Calibration of the VERITAS Gamma-ray Telescopes. *Proceedings of the 30th ICRC in Merida, Mexico*, 702:1417–1420, 2007.

- 
- [138] S. España *et al.* Performance evaluation of SiPM photodetectors for PET imaging in the presence of magnetic fields. *Nuclear Instruments and Methods in Physics Research Section A*, 613(2):308–316, 2010. ISSN 0168-9002. doi: DOI:10.1016/j.nima.2009.11.066. URL <http://www.sciencedirect.com/science/article/B6TJM-4XV5NTN-3/2/e50853a96d6fc5ce575fef2b5c2a89ca>.
- [139] G. Vacanti *et al.* Muon ring images with an atmospheric Cerenkov telescope. *Astroparticle Physics*, 2(1):1–11, 1994. ISSN 0927-6505. doi: [http://dx.doi.org/10.1016/0927-6505\(94\)90012-4](http://dx.doi.org/10.1016/0927-6505(94)90012-4). URL <http://www.sciencedirect.com/science/article/pii/0927650594900124>.
- [140] A. Rovero *et al.* Calibration of the Whipple atmospheric Cerenkov telescope. *Astroparticle Physics*, 5(1):27–34, 1996. ISSN 0927-6505. doi: DOI:10.1016/0927-6505(95)00054-2. URL <http://www.sciencedirect.com/science/article/B6TJ1-3WN7CXP-2/2/c09fb2c65bd7eb715790d9f9dc3cd9a8>.
- [141] N. Leroy *et al.* Calibration Results for the First Two H.E.S.S. Array Telescopes. In *International Cosmic Ray Conference*, volume 5 of *International Cosmic Ray Conference*, page 2895, July 2003.
- [142] S. LeBohec and J. Holder. The cosmic ray background as a tool for relative calibration of atmospheric Cerenkov telescopes. *Astroparticle Physics*, 19(2):221–233, 2003. ISSN 0927-6505. doi: DOI:10.1016/S0927-6505(02)00201-3. URL <http://www.sciencedirect.com/science/article/B6TJ1-4753K2K-1/2/ac734db12995db8ec30c9a34b730a1af>.
- [143] A. Biland *et al.* First Results from the First G-APD Cerenkov Telescope. *Proceedings of the 32nd ICRC in Beijing, China*, 1125, 2011. doi: 10.7529/ICRC2011/V09/1125.
- [144] *Innovative camera records cosmic rays during full moon*. CERN Courier, December 2011. URL <http://cerncourier.com/cws/article/cern/47816>.
- [145] J. Aleksic *et al.* Performance of the MAGIC stereo system obtained with Crab Nebula data. *Astroparticle Physics*, 35(7):435–448, 2012. ISSN 0927-6505. doi: <http://dx.doi.org/10.1016/j.astropartphys.2011.11.007>. URL <http://www.sciencedirect.com/science/article/pii/S0927650511002064>.
- [146] T. Krähenbühl *et al.* First experience with the FACT camera. *PhotoDet 2012: International Workshop on New Photon-detectors*, 2012.
- [147] T. Bretz *et al.* FACT - How stable are the silicon photon detectors? *Proceedings of the 33rd ICRC in Rio de Janeiro, Brazil*, 683, 2013. URL <http://www.cbpf.br/~icrc2013/papers/icrc2013-0683.pdf>.
- [148] D. Dorner *et al.* FACT - Long-term Monitoring of Bright TeV-Blazars. *Proceedings of the 33rd ICRC in Rio de Janeiro, Brazil*, 686, 2013. URL <http://www.cbpf.br/~icrc2013/papers/icrc2013-0686.pdf>.
- [149] D. Hildebrand *et al.* FACT - Measuring Atmospheric Conditions with Imaging Air Cerenkov Telescopes. *Proceedings of the 33rd ICRC in Rio de Janeiro, Brazil*, 709, 2013. URL <http://www.cbpf.br/~icrc2013/papers/icrc2013-0709.pdf>.

- [150] T. Bretz *et al.* FACT - Threshold prediction for higher duty cycle and improved scheduling. *Proceedings of the 33rd ICRC in Rio de Janeiro, Brazil*, 720, 2013. URL <http://www.cbpf.br/~icrc2013/papers/icrc2013-0720.pdf>.
- [151] A. Biland *et al.* FACT - Towards Robotic Operation of an Imaging Air Cherenkov Telescope. *Proceedings of the 33rd ICRC in Rio de Janeiro, Brazil*, 708, 2013. URL <http://www.cbpf.br/~icrc2013/papers/icrc2013-0708.pdf>.
- [152] C. Benn and S. Ellison. La Palma night-sky brightness. *La Palma Technical Note*, 115, 1998. URL [http://www.ing.iac.es/Astronomy/observing/manuals/ps/tech\\_notes/tn115.ps.gz](http://www.ing.iac.es/Astronomy/observing/manuals/ps/tech_notes/tn115.ps.gz).
- [153] Y. Musienko, S. Reucroft and J. Swain. The gain, photon detection efficiency and excess noise factor of multi-pixel Geiger-mode avalanche photodiodes. *Nuclear Instruments and Methods in Physics Research Section A*, 567(1):57–61, November 2006. ISSN 0168-9002. doi: 10.1016/j.nima.2006.05.214. URL <http://www.sciencedirect.com/science/article/B6TJM-4K8R2VD-1/2/dd9c3102c37e1cab80200b09e6d4feff>.



# Curriculum Vitae

## Personal data

---

Name	Thomas Philipp Krähenbühl
Date of Birth	February 25, 1984
Place of Birth	Langenthal BE, Switzerland

## Education

---

2008 – 2013	PhD student at ETH Zurich in the field of high energy astrophysics with Prof. Felicitas Pauss
2003 – 2008	Studies in Physics at ETH Zurich. Master thesis: “G-APD arrays and their use in axial PET modules” with Prof. Felicitas Pauss
1997 – 2003	Gymnasium with baccalaureate certificate at the Kantonsschule Alpenquai, Lucerne. Focus topics: Physics and Applied Mathematics

## Talks at national and international conferences

---

2009	“Geiger-mode avalanche photodiodes as photodetectors in Cherenkov astronomy”, PD09 conference in Matsumoto, Japan
2009	“Geiger-mode avalanche photodiodes as photodetectors in Cherenkov astronomy”, 31st ICRC in Łódź, Poland
2009	“A Novel Camera Type for Very High Energy Gamma-Astronomy”, Joint Annual Meeting of the SPS, ÖPG and ÖGAA in Innsbruck, Austria
2010	“Results of the Prototype Camera for FACT”, RICH2010 conference in Cassis, France
2010	“Semiconductor photosensors for Cherenkov telescopes”, Annual meeting of the Swiss Physical Society in Basel, Switzerland
2011	“The Calibration of the FACT Camera”, Joint Annual Meeting of the SPS, ÖPG, SGAA and ÖGAA in Lausanne, Switzerland
2011	“G-APDs in Cherenkov astronomy: the FACT camera”, NDIP11 conference in Lyon, France
2011	“Calibrating the camera for the First G-APD Cherenkov Telescope (FACT)”, 32nd ICRC in Beijing, China
2012	“First experience with the FACT camera”, PhotoDet2012 conference in Paris, France

## Main author of peer-reviewed publications

---

- T. Krähenbühl *et al.*: “Geiger-mode avalanche photodiodes as photodetectors in Cherenkov astronomy”, *Proceedings of Science* (2009), PoS(PD09)024.
- T. Krähenbühl *et al.*: “Results of the Prototype Camera for FACT”, *Nuclear Instruments and Methods in Physics Research Section A*, Volume 639, Issue 1 (2011) 55–57.
- T. Krähenbühl *et al.*: “G-APDs in Cherenkov astronomy: the FACT camera”, *Nuclear Instruments and Methods in Physics Research Section A*, Volume 695 (2012) 96–99.